INL/EXT-12-27059

Advanced Test Reactor Core Modeling Update Project

Annual Report for Fiscal Year 2012

David W. Nigg
Kevin A. Steuhm

September 2012

The INL is a U.S. Department of Energy National Laboratory
operated by Battelle Energy Alliance

INL/EXT-12-27059

Advanced Test Reactor Core Modeling Update Project Annual Report for Fiscal Year 2012

Edited by: David W. Nigg, Principal Investigator and Kevin A. Steuhm, Project Manager

September 2012

Idaho National Laboratory
Nuclear Science and Technology Directorate
Idaho Falls, Idaho 83415

http://www.inl.gov

Prepared for the
U.S. Department of Energy
Office of Nuclear Energy
Under DOE Idaho Operations Office
Contract DE-AC07-05ID14517

Nuclear Science and Technology Directorate

Advanced Test Reactor Core Modeling Update Project
Annual Report for Fiscal Year 2012

INL/EXT-12-27059
September 2012

Approval:

David W. Nigg, Principal Investigator

EXECUTIVE SUMMARY

Legacy computational reactor physics software tools and protocols currently used for support of Advanced Test Reactor (ATR) core fuel management and safety assurance, and to some extent, experiment management, are inconsistent with the state of modern nuclear engineering practice, and are difficult, if not impossible, to properly verify and validate (V&V) according to modern standards. Furthermore, the legacy staff knowledge required for application of these tools and protocols from the 1960s and 1970s is rapidly being lost due to staff turnover and retirements. In late 2009, the Idaho National Laboratory (INL) initiated a focused effort, the ATR Core Modeling Update Project, to address this situation through the introduction of modern high-fidelity computational software and protocols. This aggressive computational and experimental campaign will have a broad strategic impact on the operation of the ATR, both in terms of improved computational efficiency and accuracy for support of ongoing DOE programs as well as in terms of national and international recognition of the ATR National Scientific User Facility (NSUF).

The ATR Core Modeling Update Project, targeted for full implementation in phase with the next anticipated ATR Core Internals Changeout (CIC) in the 2014-2015 time frame, began during the last quarter of Fiscal Year 2009, and has just completed its third full year. Key accomplishments so far have encompassed both computational as well as experimental work. A new suite of stochastic and deterministic transport theory based reactor physics codes and their supporting nuclear data libraries (HELIOS, KENO6/SCALE, NEWT/SCALE, ATTILA, and an extended implementation of MCNP5) has been installed at the INL under various licensing arrangements. Corresponding models of the ATR and ATRC are now operational with all five codes, demonstrating the basic feasibility of the new code packages for their intended purpose. Of particular importance, a set of as-run core depletion HELIOS calculations for all ATR cycles since August 2009, Cycle 145A through Cycle 151B, was successfully completed during 2012. This major effort supported a decision late in the year to proceed with the phased incorporation of the HELIOS methodology into the ATR Core Safety Analysis Package (CSAP) preparation process, in parallel with the established PDQ-based methodology, beginning late in Fiscal Year 2012.

Acquisition of the advanced SERPENT (VTT-Finland) and MC21 (DOE-NR) Monte Carlo stochastic neutronics simulation codes was also initiated during the year and some basic applications of SERPENT to ATRC analysis were demonstrated. These two new codes will offer significant additional capability, including the possibility of full-3D Monte Carlo fuel management support capabilities for the ATR at some point in the future. Finally, a capability for rigorous sensitivity analysis and uncertainty quantification based on the TSUNAMI system has been implemented and initial computational results have been obtained. This capability will have many applications as a tool for understanding the margins of uncertainty in the new models as well as for validation experiment design and interpretation.

On the experimental side of the project, a complete statistical analysis of the first four of six planned application-specific ATRC physics code validation measurements based on neutron activation spectrometry was completed in accordance with applicable national and international standards. The validation measurements will continue through 2014 and will include the introduction of additional new experimental hardware to broaden the scope of the validation protocols. Further opportunities to collaborate with various other ongoing experimental campaigns in the ATRC and ATR are also being identified as the Core Modeling Update Project proceeds, with a particular emphasis at the moment on obtaining additional code validation data from a “depressurized” low-power run (Cycle 152A) of the ATR late in 2012.

A second component of the experimental validation campaign involves the possible construction of a system for non-invasive measurement of the burnup of ATR fuel elements *in-situ* in the ATR canal.

Post-irradiation non-invasive ATR fuel burnup measurements can serve as a key fuel depletion model validation tool and also as an aid in improved fuel management. Initial in-canal feasibility measurements to identify appropriate engineering parameters and radiation measurement instrumentation for a system to perform this type of measurement were conducted during 2010 with significant additional progress in 2011 and early 2012. Progress in 2011-2012 included the preparation and transmittal, to the Department of Energy, of a proposal for construction of a permanent system for non-invasive *in-situ* fuel element burnup measurements in the ATR canal, as well as some feasibility studies for remote positioning of the detector used for the measurements.

It is also important to recognize that the ATR Core Modeling Update Project represents not only an investment in new technology. It also represents a key investment in the new generation of INL scientific and engineering staff who will, by demographic necessity, assume leadership roles in the overall ATR enterprise over the next several years. Accordingly, several students and early-career INL Scientific and Engineering staff members are being proactively integrated into the effort and this has accelerated in 2012.

Finally we note that although full implementation of the new computational models and protocols will extend over a period of a few years, interim applications in the much nearer term have already been demonstrated. For example, these demonstrations included an analysis that was useful for understanding the cause of some ATR operational issues in December 2009 that were triggered by a larger than acceptable discrepancy between the measured excess core reactivity and a calculated value that was based on the legacy computational methods. More recently, computational support for the Cycle 152A ATR depressurized run and its supporting ATRC experiments was also provided. Furthermore, the new code system is being used extensively for core design calculations associated with the possible conversion of the ATR to a low-enriched uranium (LEU) type fuel at an appropriate time in the future. As the Core Modeling Update Project proceeds, we anticipate further such interim, informal applications in parallel with formal qualification of the system under applicable INL and external Quality Assurance procedures and standards.

CONTENTS

ACRONYMS

AGR	Advanced Gas Reactor
ANS	American Nuclear Society
ATR	Advanced Test Reactor
ATRC	Advanced Test Reactor Critical Facility
CIC	Core Internals Changeout
CSAP	Core Safety Assurance Package
ENDF	Evaluated Nuclear Data File
NGNP	Next Generation Nuclear Plant
NST	Nuclear Science and Technology
NSUF	National Scientific User Facility
RERTR	Reduced Enrichment for Research and Test Reactors
V&V	Verification and Validation
DHA	Detector Housing Assembly
HPGe	High Purity Germanium
HPXe	High Pressure Xenon
INL	Idaho National Laboratory
$LaBr_3$	Lanthanum Bromide
OSCC	Outer Shim Control Cylinder
ESAP	Experiment Safety Analysis Package
IRPhE	OECD International Reactor physics Experiment Evaluation (Program)
OECD	Organization for Economic Cooperation and Development
QA	Quality Assurance
LEP	(ATR) Life Extension Program
ICSBE	OECD International Criticality Safety benchmark Experiment Evaluation (Program)
DOE	(US) Department of Energy
NR	Naval Reactors
VTT	National Research Centre (Finland)

ACKNOWLEDGEMENTS

The technical team for the ATR Methods Update project would like to gratefully acknowledge Dr. Charles Wemple, Studsvik Scandpower, for his essential assistance in the setup of the various HELIOS models, for the training of key INL staff members in the use of HELIOS, and for his overall review of the HELIOS ATR model effort as it proceeded. Additionally, we also thank Ms. Christine White (INL) for her assistance with many of the graphic illustrations in this report, Mr. Neil Boyce (INL) for the fabrication of new experimental hardware for use in the ATRC and ATR flux traps and Mr. Anthony LaPorta (INL) for provision of the physics measurement data for the ATR "depressurized run" support experiments that were conducted in the ATRC during the year. Finally we wish to thank Dr. John Williams, University of Arizona for his valuable counsel with regard to the least-square adjustment based validation protocols that have been adapted for use with the ATR.

1.0 INTRODUCTION

David W. Nigg

This Annual Report documents the accomplishments of the ATR Core Modeling Update Project during Fiscal Year 2012. A brief overview of the background, rationale, organizational structure, and a basic summary of progress to-date for the project is provided below. Later sections cover additional detail on specific technical accomplishments during the year. Each Section is designed to stand on its own, with its own set of references, to facilitate use of the information presented here in other reports and presentations as needed.

1.1 Description of the Advanced Test Reactor

The Advanced Test Reactor (ATR), located at the Idaho National Laboratory (INL), is one of only a few high-power research reactors of its type in the world, with a variety of missions involving accelerated testing of nuclear fuel and other materials in a very high neutron flux environment, medical and industrial isotope production, and other applications. Along with its companion critical mockup (ATRC), the ATR is one of the key nuclear engineering research and testing facilities within the US Department of Energy (DOE) National Laboratory Complex. The ATR and ATRC also serve as the centerpieces of the recently-formed ATR National Scientific User Facility (NSUF), whose purpose is to facilitate the current trend toward broadening the applications of the ATR beyond its traditional base.

The ATR (Figures 1.1 and 1.2) is a highly-heterogeneous light-water and beryllium moderated, beryllium reflected, light-water cooled system with highly-enriched (93% ^{235}U) plate-type fuel elements arranged in a serpentine pattern. Gross reactivity and power distribution control during operation is achieved through the use of eight pairs of rotating control drums with hafnium neutron absorber plates on one side as can be seen in Figure 1.1. There are several design features incorporated into the ATR and ATRC (Figures 1.3 and 1.4) to optimize experimental capabilities. These features include: a) the use of flux traps to provide high thermal neutron fluxes for irradiation or experiments in nine regions, b) incorporation of special control shim design features to retain axial flux symmetry throughout an ATR fuel cycle; and c) regional power control to provide capability for power shifting between core lobes to optimize the neutron flux distribution for a wide range of simultaneous experiments. The ATR can be operated at powers as high as 250 MW although most routine applications do not require the maximum power. Typical thermal neutron fluxes in the flux traps can be as high as 5.0×10^{14} n/cm^2-s. Typical operating cycle lengths are in the range of 45–60 days. The core fuel configuration and the experiment loadings are usually rearranged between cycles and each fuel element is typically burned for two or three cycles during its useful lifetime.

The ATRC (Figures 1.3 and 1.4) is an open-pool nuclear mock-up of the ATR that typically operates at approximately 600 W and produces a thermal neutron flux levels in the traps that are in the range of 1.0×10^9 n/cm^2-s. As is the case for the ATR, the core consists of a 4-ft-high (122 cm), uniform-width, vertical 40-element fuel annulus shaped in a serpentine fashion between and around nine flux-trap regions located in a three-by-three square array. The cruciform fixture inside the serpentine is called the neck shim housing. The reactivity of the core is controlled by: (a) five vertically withdrawn safety rods that use cadmium as the poison material; (b) 24 vertically withdrawn hafnium neck shim rods; and (c) eight pairs of rotating outer shim control cylinders (OSCCs) that use hafnium poison plates.

ATRC criticality can normally be stably attained at a power as low as 0.25 mW and the maximum rated power is 5 kW. The ATRC facility is typically used with prototype experiments to characterize in advance, with precision and accuracy, the expected changes in core reactivity for the same experiments in the ATR. Useful physics data can also be obtained for evaluating the worth and calibration of control elements as well as thermal and fast neutron distributions.

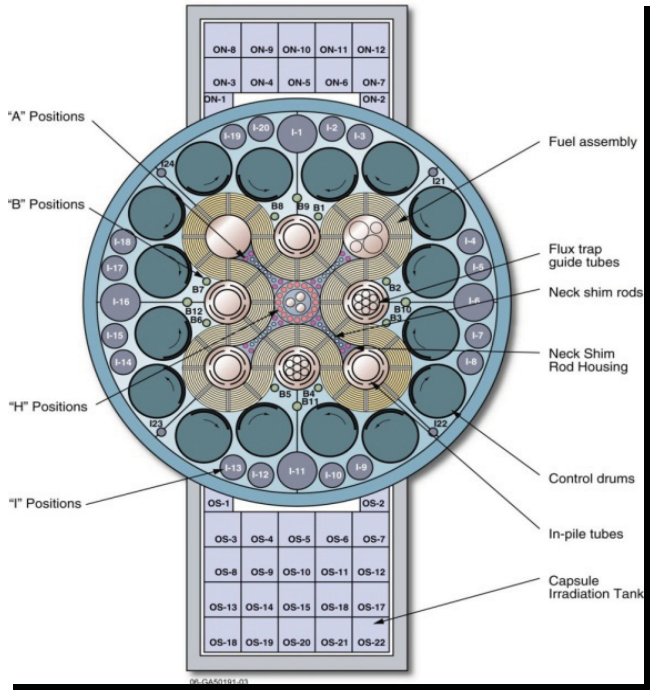

Figure 1.1. Core and reflector geometry of the Advanced Test Reactor.

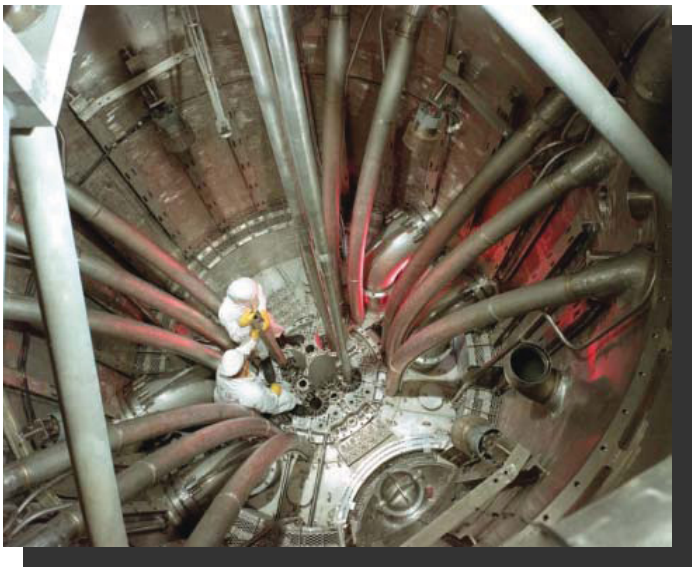

Figure 1.2. View into the ATR pressure vessel (File Photo, ca 1967).

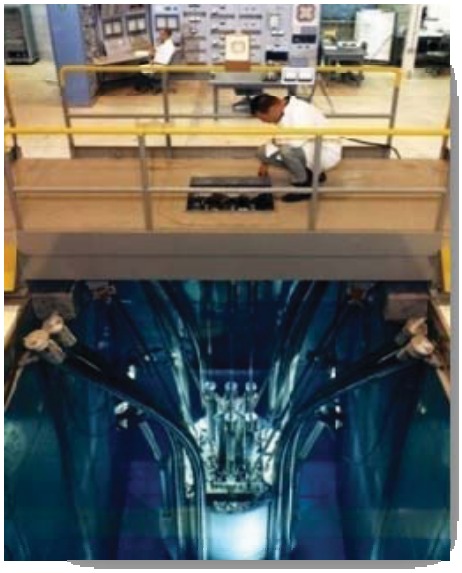

Figure 1.3. The Advanced Test Reactor Critical Facility (File Photo, ca 1967).

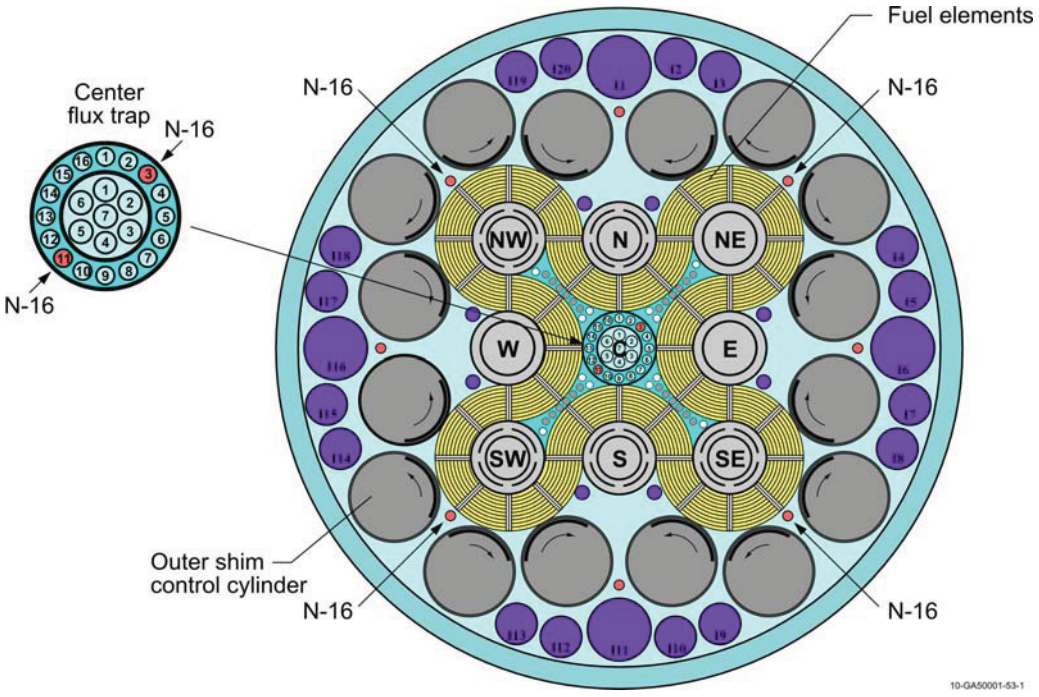

Figure 1.4. ATRC Configuration, showing the NW LIPT Flux Trap and six N-16 positions.

1.2 Rationale for the ATR Core Modeling Update Project

Computational reactor physics modeling is used extensively to support ATR experiment design, operations and fuel cycle management, core and experiment safety analysis, and many other applications. Experiment design and analysis for the ATR is generally supported by very detailed and sophisticated three-dimensional Monte Carlo analysis, typically using the internationally recognized continuous-energy MCNP5 code (Goorley et al., 2004) coupled to extensive fuel isotope buildup and depletion analysis where appropriate. On the other hand, the computational reactor physics software tools and protocols currently used for ATR core fuel cycle analysis and operational support are largely based on four-group diffusion theory in Cartesian geometry (Pfeifer et al., 1971) with heavy reliance on "tuned" nuclear parameter input data. These methods are obsolete and have been superseded in the general reactor physics community by high-fidelity multidimensional transport-theory-based methods. As a result, the historical approach to ATR reactor physics operational support has become inconsistent with the state of modern nuclear engineering practice and the legacy models are nearly impossible to properly verify and validate (V&V) according to modern standards. Furthermore, some aspects of the analysis process are highly empirical in nature, with many "correction factors" and approximations that require very specialized experience to apply. But the staff knowledge from the 1960s and 1970s that is essential for the successful application of these various approximations and outdated computational processes is rapidly being lost due to staff turnover and retirements. Finally, future clients of the ATR NSUF are anticipated to be experienced in the use of modern computational methods available for nuclear systems modeling and are likely to expect corresponding computational support services within the NSUF infrastructure.

Figure 1.5 illustrates one of the challenges experienced recently with the legacy physics computational methods used for ATR operational support. A fueled experiment associated with the DOE Next Generation Nuclear Plant Advanced Gas Reactor (NGNP) development program was scheduled for irradiation in the south flux trap of the ATR as shown. However, uncertainties in the supporting computations were such that it was not possible to determine the neutronics effects of this experiment on neighboring flux traps to sufficient accuracy, and the operational margins of conservatism that were consequently required caused the experiment to be delayed until a later ATR cycle, at significant expense. In a second example of the impact of uncertainty in the current computational methods, some operational issues arose in December 2009 that were triggered by a larger than acceptable discrepancy between the calculated and measured excess core reactivity. These issues were resolved via standard procedures, but schedules were adversely impacted and the root cause was largely traced to problems with the legacy computational model of an experiment in the central flux trap.

In response to this situation, the INL is currently engaged in a major multiyear effort to modernize the computational reactor physics tools and validation protocols needed for support of ongoing ATR operations as well as for new applications, such as the design of suitable LEU fuel elements and corresponding LEU core configurations for the ATR and the ATRC. This aggressive computational and experimental campaign will have a broad strategic impact on the operation of the ATR, both in terms of improved computational efficiency and accuracy for support of ongoing DOE programs as well as national and international recognition of the ATR NSUF. The new computational methods and V&V protocols will be broadly applicable across all programs that use the ATR and ATRC. The developmental effort is in fact already leveraged with several other INL projects including the ATR Life Extension Program (LEP), the DOE Reduced Enrichment for Research and Test Reactor (RERTR) initiative ad noted, and an INL collaboration with Idaho State University (ISU), the Atomic Energy Commission of France (CEA), and the National Atomic Energy Commission of Argentina (CNEA) to evaluate various options for in-core ATR and ATRC instrumentation upgrades under the auspices of the NSUF (Rempe et al., 2010).

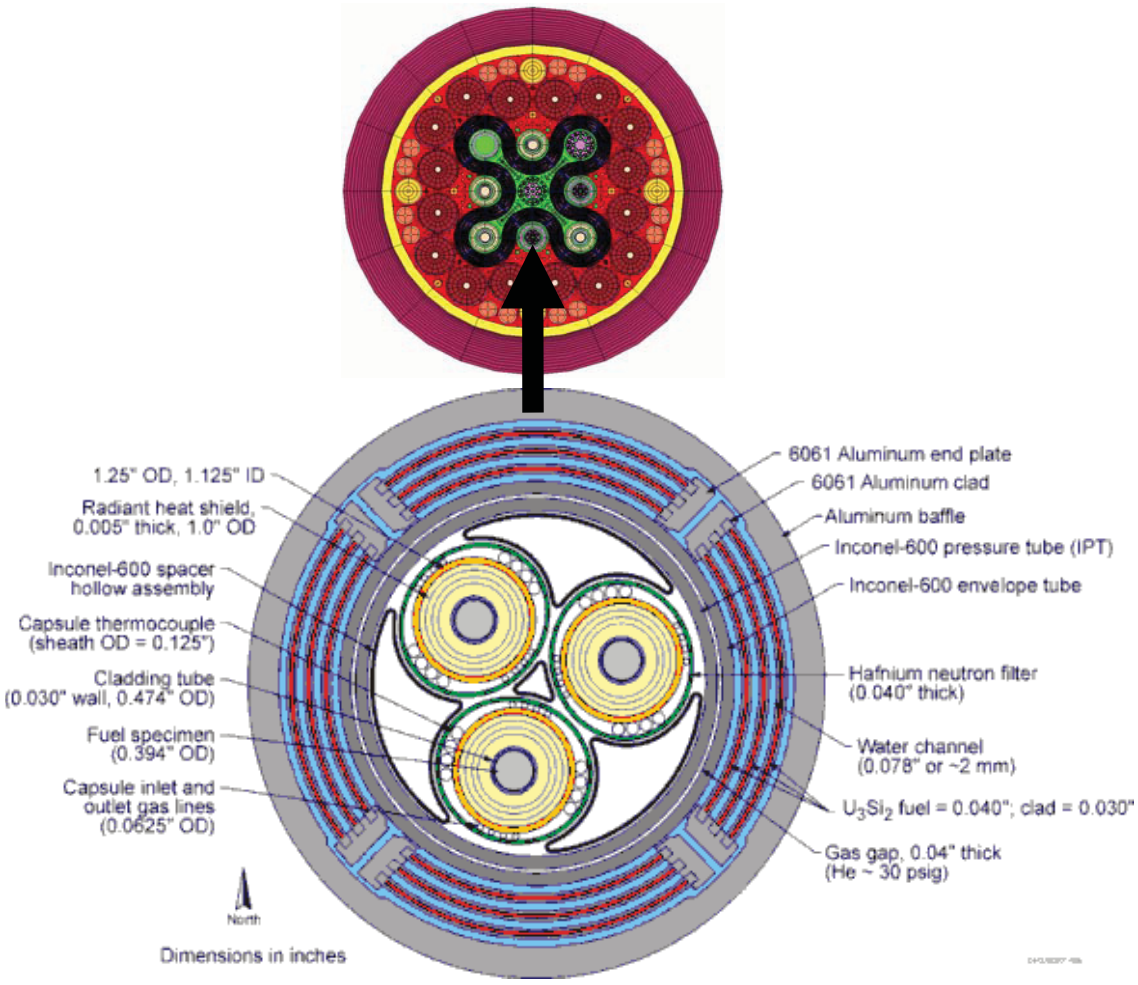

Figure 1.5. Gas Test Loop experiment designed for placement in the ATR south flux trap.

1.3 Technical Objectives of the Core Modeling Update Project

Prior to the initiation of the Core Modeling Update Project in late 2009, the INL was already making a few efforts to modernize ATR reactor physics analysis capabilities using current standard software. Those efforts have produced some important progress, especially for experiment design and analysis as noted earlier. However, this largely had been on an *ad-hoc* basis, and several key tasks remained. Those tasks, which are the basis for the Modeling Update Project included:

- Implementation of complementary, self-consistent multidimensional stochastic and deterministic neutron transport models of the ATR and ATRC cores using well-established and recognized science-based software packages consistent with current practice
- Standardized computational procedures and training, more easily transferred to new staff members

- Additional Verification &Validation, with development of standard apparatus and protocols for detailed neutron flux and power distribution and spectrum validation measurements in the core and selected flux traps that can be adapted as needed for changing experimental conditions and repeated on a regular basis. This also offers an opportunity to make much more effective use of ATRC both within the INL and as a key component of the National Scientific User Facility

Figure 1.6 shows the suite of new tools that will be available and how they generally relate to one another. This illustration is however not a computational flow chart or procedure *per se*. Specific computational protocols using the tools shown in Figure 1.6 for routine ATR support applications will be specified in approved procedures and other operational documentation. These documents will prescribe the geometric modeling input files, nuclear data files, and other aspects of each specific computational protocol. For example there will be a procedure for performance of core-follow calculations and computation of Core Safety Analysis Package (CSAP) physics support data for a particular ATR operational cycle using the new tools.

The most recent release of the Evaluated Nuclear Data Files (ENDF/B Version 7) are used to provide the basic cross section data and other nuclear parameters required for all of the modeling codes. The ENDF physical nuclear data files are processed into computationally-useful formats using the standard publically-available NJOY or AMPX (Radiation Safety Information Computational Center, 2010) codes as applicable to a particular module as shown at the top of the Figure.

As noted earlier, the MCNP5 three-dimensional stochastic simulation code is already used extensively for ATR experiment design and analysis and, to some limited extent, core analysis. Under the Core Modeling Update Project, we are also introducing the KENO stochastic simulation code (Hollenbach et al., 1996). The KENO code is useful both as a stand-alone analysis and verification tool as well as in conjunction with the TSUNAMI (Broadhead et al., 2004, Williams and Rearden, 2008) sensitivity-uncertainty analysis system available with the SCALE nuclear system analysis package (Bowman et al., 2009). Furthermore, during Fiscal year 2012, we also investigated the possibility of incorporating the extremely sophisticated MC21 (Sutton et al., 2007) and SERPENT (Leppänen, 2012) stochastic simulation and depletion codes into the new suite, acquisition of both codes was initiated and some initial demonstrations of applications of the SERPENT code to ATRC validation experiments were completed, and are reported in Section 3.

The right-hand side of Figure 1.6 shows the new high-fidelity deterministic transport computational tools that are being integrated into the system. HELIOS (Studsvik Scandpower, 2008) and ATTILA (McGhee et al., 2006) are commercial grade software products now in place at the INL under permanent sitewide licenses. NEWT (DeHart, 2006) together with its SCALE-based support infrastructure is a well-established and verified software tool developed within the DOE National Laboratory system. All three code packages have various strengths and weaknesses, but taken together they will provide the necessary high-fidelity neutron and gamma transport capability that is required for various aspects of ATR and ATRC core modeling as summarized in Figure 1.6. These aspects are described in much more detail in Sections 2 and 3 of this report.

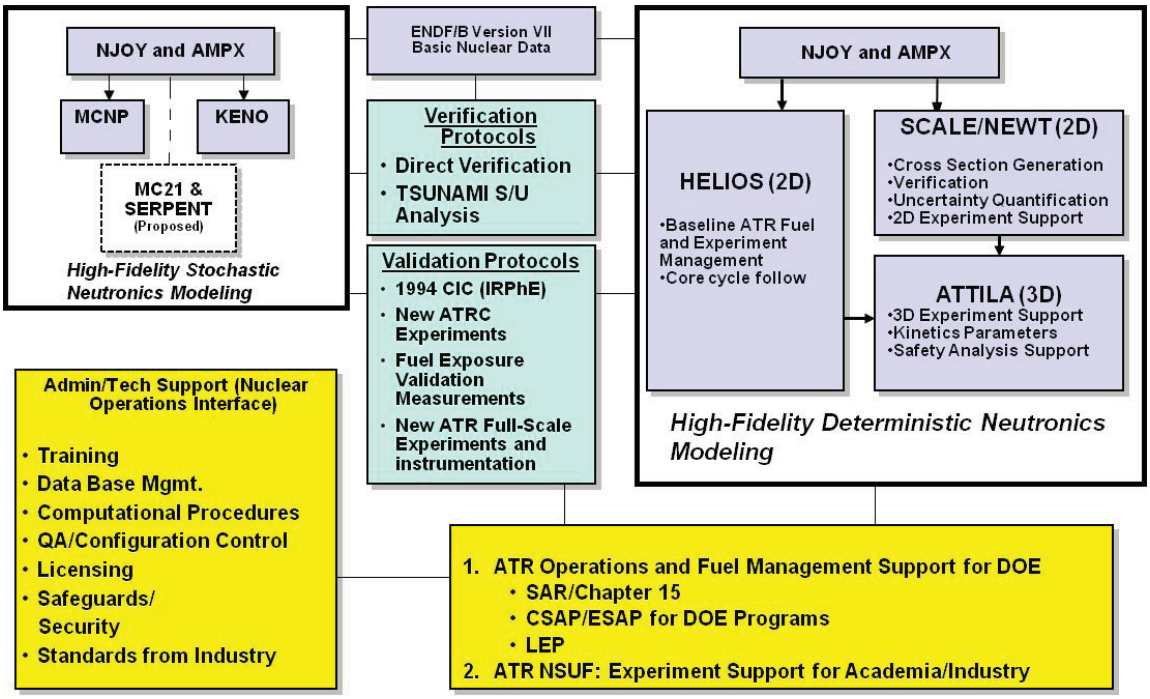

Figure 1.6. Advanced computational tool suite for the ATR and ATRC, with supporting verification, validation and administrative infrastructure.

As always, theory and experiment must be consistent in any scientific or engineering enterprise. The Core Modeling Update Project also includes several activities designed to incorporate historical validation data from earlier ATR and ATRC experiments as well as to develop new validation data specific to the new computational models and protocols. In particular, much of the initial model testing has been based on a very well documented critical experiment conducted as part of the 1994 ATR Core Internals Changeout (CIC) activity (Kim and Schnitzler, 2008), which will be described in detail later. New core flux measurements in both ATRC and ATR are also underway and a complete statistical analysis of the first four ATRC validation experiments per ASTM Standard E944 (ASTM, 2008) was completed and is documented in Section 3 of this report. Additional validation effort in FY-2012 was focused on obtaining initial data from a previously unanticipated "depressurized" low-power run (Cycle 152A) of the ATR late in 2012. This activity will continue in 2013 and additional new validation experiments in the ATRC, described in Section 4, are planned for FY-2013 and FY-2014 as well.

Finally, the Core Modeling Update Project includes a task described in Section 5 to develop non-invasive methods for post-irradiation measurement of exposure (or "burnup") in ATR fuel elements, both as an aid in characterizing the existing inventory of used elements as well as to provide additional validation data for the new ATR core follow and fuel cycle design models.

1.4 Project Structure and Technical Team

The ATR Core Modeling Update project includes 5 technical tasks. It is organized and funded as a part of the larger ATR Life Extension Program (LEP). The five tasks, which also provide the framework for the structure of this Annual Report, are as follows:

Task 1: Project Management: Includes sponsor/Collaborator interface maintenance, project documentation and planning, software licensing, travel, and university interfaces including student support.

Task 2: ATR Model Development and V&V: Includes development, verification, and validation of baseline KENO, HELIOS, NEWT and ATTILA models for current ATR reactor applications, along with testing of SERPENT and MC21 for possible future inclusion in the suite. The workscope includes fuel cycle management and neutronics support to core safety analysis, and limited development of capabilities for experiment analysis to the extent that experiment neutronic effects impact the operation of the reactor overall. (Detailed ATR experiment design and analysis is ordinarily handled separately, as part of the workscope for each individual experiment series, and is not considered to be a part of the Core Modeling Update Project). Details of FY-12 activities and accomplishments in connection with this task are reported in Section 2 of this Annual Report. In FY-2012, these activities were almost exclusively focused on demonstrating feasibility of the HELIOS system as a new primary reactor physics tool to support core fuel loading design and fuel cycle analysis tasks that are required for preparation of CSAP documentation for each ATR cycle.

Task 3: ATRC/ATR Model Development and Applications Specific to V&V: Includes development and application of baseline MCNP, KENO, HELIOS, NEWT, and ATTILA (and in the future, SERPENT and possibly MC21) models for support of ATRC validation experiments pertinent to the Core Modeling Update Project and for the 2012 ATR depressurized run. This task also includes the development and application of new capabilities for rigorous sensitivity studies and statistical analyses pertinent to uncertainty quantification in the new computational models, with a strong emphasis on building protocols that are consistent with applicable national and international standards, especially ASTM-944 (ASTM, 2008). Details of FY-12 activities and accomplishments in connection with this task are reported in Section 3 of this Annual Report.

Task 4: Neutronics Validation Experiments: This task includes the performance and reporting of new validation experiments in ATRC and ATR (as feasible) that are pertinent to quality assurance of the new computational models. It supports development of apparatus and protocols for a standard set of neutron activation spectrometry measurements that can be used on a more routine basis in the future for code validation as dictated by evolving ATR applications. This task also includes collaboration with various other DOE and NSUF projects where there is mutual benefit in terms of new physics validation data. Currently these collaborations include a project funded under the NSUF to investigate the feasibility of various techniques for online neutron flux measurements in the experiment positions as well as several physics experiments involving depressurized operation of the ATR to support ongoing operations.. Details of FY-12 activities and accomplishments in connection with this task are reported in Section 4 of this Annual Report.

Task 5: In-Canal ATR Fuel Exposure Validation Measurements: This task has been focused on development of a non-invasive method and apparatus for measurement of the isotopic composition of used ATR fuel elements to infer the burnup. The effort included a series of scoping measurements conducted in FY-10, with ongoing data analysis through FY-11 and the first part of FY-12. It also includes the specification of a conceptual design for a permanent measurement system that can be installed in the fuel storage canal. Final design, construction and qualification of a permanent measurement system was formally proposed for inclusion in the longer-term scope of the Core Modeling Update Project. Details of FY-12 activities and accomplishments in connection with this task, which was completed in early 2012 are reported in Section 5 of this Annual Report.

The leadership team for the ATR Core Modeling Update Project consists of a Principal Investigator, a Project Manager, and several senior co-investigators who are responsible for various key aspects of each task listed above. It is important to recognize that the ATR Core Modeling Update Project represents not only an investment in new technology. It also represents a key investment in the new generation of INL scientific and engineering staff who will, by demographic necessity, assume leadership roles in the overall ATR enterprise over the next several years. Accordingly, several students and early-career INL Scientific and Engineering staff members are also proactively integrated into the effort, and this will

accelerate in 2013 and beyond. The students supported by the project in 2012 included two from the University of Utah, two DOE Interns from Oregon State University, and one student from RPI.

1.5 Overview of FY-2012 Accomplishments

The Core Modeling Update Project is expected to require approximately 60 months to complete, and is targeted for full implementation in phase with an anticipated ATR Core Internals Changeout (CIC) in the 2014-2015 time frame. The project began during the last quarter of Fiscal Year 2009, and has just completed its third full year. Some key accomplishments in the first 38 months are briefly summarized below, along with a description of planned next steps in several areas during FY-2013 and beyond. Additional technical details are provided in the remainder of this Annual Report.

- HELIOS, NEWT, ATTILA, KENO, and MCNP models of ATR and AT RC are all operational. Initial SERPENT models also have been demonstrated.
- An initial demonstration-level HELIOS model of the ATR with fuel depletion and replacement is operational and "as run" analyses beginning with Cycle 145a and proceeding through Cycle 151B have been completed, with all experiments explicitly represented in the model database. This will provide the basis for more formal acceptance testing and qualification of the core fuel cycle computational models and protocols in 2013 and 2014, with the goal of enabling a decision to rely exclusively on the new computational methods and fuel cycle models by the end of Fiscal Year 2014. The acceptance testing calculations will be continued and refined in 2013 and beyond, with the HELIOS methodology running in parallel with the standard PDQ-based CSAP methodology during this time.
- Initial critical shim rotation for Cycle 152A (Depressurized Physics Testing) was successfully modeled, and informal cycle follow calculations from 152A forward have been initiated.
- Capability for rigorous sensitivity-uncertainty analysis is available
- Validation protocol development and demonstration are underway, with a focus on consistency with ASTM-944. Complete results of statistical validation analyses for the first four (of 6) ATRC irradiations were presented at the 2012 American Nuclear Society (ANS) Reactor Physics Topical Meeting and at the 2012 ANS Annual Meeting.
- In-canal feasibility measurements for construction of a permanent fuel burnup validation system have been completed and proposal for new system construction has been submitted to DOE-NE.
- Students and entry-level INL S&E staff are being integrated into the effort . First PhD degree was completed May 2011.
- Support of possible ATR LEU fuel conversion under RERTR, using the new methods exclusively, has also been initiated.
- Initiated use of additional direct validation data referenced to ATR Cycle 152A ("Depressurized Run") and the corresponding ATRC supporting configurations.
- A new fuel element power fitting algorithm based on least-squares adjustment is now operational and will be applied to support the depressurized operations of the ATR as well as future measurements in the ATRC.
- The INL team received significant national and international attention via refereed publications topical conferences (ANS, ASTM), culminating in an invited special session at the 2012 ANS Annual meeting and an invitation (accepted) for INL to have a representative on ASTM Standards Committee E10.5 (Nuclear Metrology)

- Acquisition of MC21 and SERPENT 3D stochastic simulation codes from DOE-NR and VTT-Finland was initiated and SERPENT is now operational at the INL, with MC21 anticipated to follow. These codes offer significant additional V&V capability now, as well as a potential longer-term route to full 3D Monte Carlo CSAP analysis at an appropriate time in the future.

- The adoption of the Studsvik Scandpower HELIOS code for ATR fuel cycle physics and fuel cycle analysis has significantly advanced the goals of the BEA Center for Nuclear Systems Design and Analysis, a formal collaboration between Studsvik and INL that was established in 2005 under the then-new INL Management and Operations Contract between Battelle Energy Alliance and the US Department of Energy.

1.6 References

ASTM (American Society for Testing and Materials), "Standard Guide for Application of Neutron Spectrum Adjustment methods in Reactor Survieillience", ASTM-E944-08 (2008)

Bowman, S. M. (Ed.), *SCALE: A Modular Code System for Performing Standardized Computer Analyses for Licensing Evaluation*, ORNL/TM-2005/39, Version 6, Vols. I–III, Oak Ridge National Laboratory, Oak Ridge, Tennessee, January 2009. Available from Radiation Safety Information Computational Center at Oak Ridge National Laboratory as CCC-750.

Broadhead, B. L., Rearden, B. T., Hopper, C. M., Wagschal, J. J. and Parks, C. V., "Sensitivity- and Uncertainty-Based Criticality Safety Validation Techniques," *Nucl. Sci. Eng.* **146**, 340–366 (2004).

DeHart, M. D., Advancements in Generalized-Geometry Discrete Ordinates Transport for Lattice Physics Calculations, A154.pdf in Proc. of PHYSOR–2006, American Nuclear Society Topical Meeting on Reactor Physics: Advances in Nuclear Analysis and Simulation, September 10–14, 2006, Vancouver, British Columbia, Canada.

Hollenbach, D.F., Petrie, L.M., Landers, N.F., KENO-VI: A General Quadratic Version of the KENO Program, ORNL/TM-13011, Lockheed Martin Energy Research Corp., Oak Ridge National Laboratory, 1996.

Kim, S. S. and Schnitzler, B. G., Advanced Test Reactor: Serpentine Arrangement of Highly Enriched Water-Moderated Uranium-Aluminide Fuel Plates Reflected by Beryllium" HEU-SOLTHERM-022, *International Handbook of Evaluated Criticality Safety Benchmark Experiments*, NEA/NSC/DOC(95)03, OECD-NEA (2008).

Leppänen, J., 2012b. "Serpent Progress Report 2011", VTT Technical Research Centre of Finland (2012), VTT-R-05444-12.

McGhee, J.M., Wareing, T.A., Barnett, D.J., ATTILA Version 5: User Manual, Transpire Inc., Gig Harbour WA, USA (2006).

Pfeifer, C.J., PDQ Reference Manual II, WaPD-TM-947(L), 1971.

Radiation Safety Information Computational Center, NJOY99- Code System for Producing Pointwise and Multigroup Neutron and Photon Cross Sections from ENDF/B Data and AMPX77- Modular Code System for Generating Coupled Multigroup Neutron-Gamma Libraries from ENDF/B, Oak Ridge National Laboratory (http://www-rsicc.ornl.gov), 2010.

Rempe, J.L., Nigg, D.W., Imel, G. R., Unruh, T., FY-10 Irradiation Experiment Plan for the ATR National Scientific User Facility – Idaho State University Project Evaluating Flux Sensors, PLN-3351, Revision 0, Idaho National Laboratory, 2010.

Studsvik Scandpower, HELIOS Methods (Version 1.10), 2008.

Sutton, T.M., et al., The MC21 Monte Carlo Transport Code, Knolls Atomic Power Laboratory and Bettis Laboratory, LM-06K144, 2007.

Williams, M.L., Rearden, B.T., SCALE 6 Sensitivity/Uncertainty Methods and Covariance Data, *Nucl. Data Sheets* **109** (2008), p. 2796.

2.0 HELIOS MODEL DEVELOPMENT FOR ATR CSAP AND FUEL MANAGEMENT APPLICATIONS

Samuel Bays, Emily Swain, Douglas Crawford, William Skerjanc, Benjamin Chase

2.1 Overview of the ATR/ATRC Model

HELIOS is a general 2D geometry deterministic transport code. Arbitrary 2D geometry is created from user input-specified polyhedral shapes in space. Circular features can be planted within these polyhedral shapes. The code supports property overlays, such as composition, temperature and density, mapped to this arbitrary 2D geometry. Geometry-corrected resonance integrals are calculated on-the-fly for every spatial region (i.e., per single spatial mesh) of the arbitrarily heterogeneous geometry description using the subgroup resonance treatment (Studsvik Scandpower, 2009). Very large and complex geometries are supported by subdividing the geometry into smaller subsystems. These subsystems are solved explicitly via the collision probability transport solution and then current-coupled with adjacent subsystems (Studsvik Scandpower, 2009; Stamm'ler and Abbate, 1983). The code also has a method-of-characteristics option for the transport solution (Studsvik Scadpower, 2009; Vladimirov, 1959; Marchuck, 1961). HELIOS depletes all fissile materials as applicable in any given single spatial region (i.e., meshes are depleted separately). New property overlays can be added during the course of the depletion (e.g., change in control poison configuration, change in temperature, etc.). The code also supports tracking of gamma rays and gamma ray heating of core internals, though this feature has not been explored for the ATR at this time.

The ATR/ATRC HELIOS model (referred to hereafter as "ATR model") is a hierarchical system of input files for supporting core-follow, core-prediction and physics verification and validation. Disparate core modeling applications can be supported using many of the same "SET" input files (i.e., these files have a *.SET suffix). This distributed input file feature paired together with the subsystem current coupling approach allows a large degree of modularity in core modeling without the need for tracking very large input descriptions within a single file. In this way, fuel elements and experiment facilities can be swapped in or out of the model by simply loading them or un-loading them from the model in like-fashion to the way this is physically performed in the actual cores.

Due to this inherent modularity, the overall collection of input SET files will be referred to as the "model". All application-specific models will likely use all (if not nearly all) of the same files used to describe Fuel Elements (FEs), Outer Shim Control Cylinders (OSCCs), safety-rods (SRs), Neck Arms, the Be reflector and miscellaneous core internals. These common files shall hereby be referred to as the "base model", as they are the prerequisite foundation (or base) for constructing any given application-specific model. An example of an application-specific input SET file would be a file that contained the geometry and material overlay definitions for an experiment flux trap. These SET files are called by an application-specific input file that defines the base model as well as any of the application-specific components of the model. The application-specific input file is hereby referred to as the "short input file" as this file is: 1) the piece of input used to define the problem setup for the HELIOS simulation, and 2) is many times shorter in brevity than if a user were to embed all the contents of the model in a single input file.

2.1.1 Distributed Input Descriptions

In the ATR HELIOS model, the base model SET files are stored in a directory called /BaseModel (See Figure 2.1). The /BaseModel directory also contains default ATRC SET files for describing the ATRC beryllium reflector, neck-rods and Mark IV fuel loading. This directory also includes a /Templates sub-directory where example(s) for setting up a model starting from the base model constituents is provided. Also included are essential shell scripts, with examples included in /Scripts), for enabling HELIOS to

locate the base model file hierarchy (/BaseModel and sub-directories) and all relevant experiments from any other arbitrary location within a Unix/Linux operating system.

Another directory called the /EXPR directory is required. This directory includes geometry and material overlay information for defining experiments to be loaded into the application-specific model. Geometry nodes (intersections of polygon line segments) from experiments are connected to nodes in the base model. Neutron currents are traded across the line segments created by connecting nodes.

Unless working with fresh fuel, the composition of each of the 40 fuel elements must be loaded into the ATR HELIOS model. The calculations required for decaying the end-of-cycle compositions from one cycle going into a new cycle are performed in the /CANAL directory. This directory includes a single-fuel-element (SFE) HELIOS model, for performing the decay calculations, and a file repository of end-of and beginning-of-life fuel compositions.

The /CORE directory contains As-Run analyses. This directory may also be where future CSAP analyses are located or alternately a separate high level CSAP directory could be made. The /Benchmarks directory contains ATR and ATRC criticality and flux wire benchmarks as well as the cases used in the OSCC mesh refinement study discussed later.

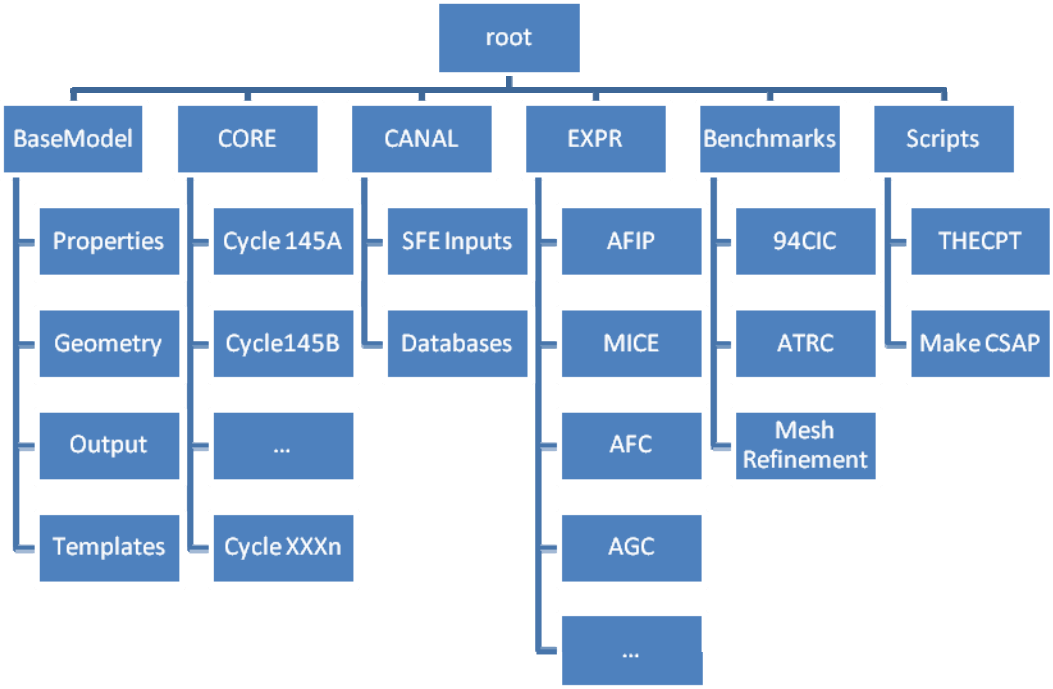

Figure 2. 1 Overview of ATR HELIOS model directory structure.

2.1.2 Neutronic Subsystem Coupling

HELIOS enables division of the problem into geometric regions called structures. These structures can be lumped into subsystems of shared neutronic importance within the model to make the complete system. In this way, the ATR model geometry is essentially a large jig-saw puzzle of connected polygonal structures that comprise the entire system. The subsystem approach allows adjacent geometry structures to neutronically communicate via neutron currents that are traded across the adjoining line-segments.

The subsystem approach also allows for repetitive geometry without requiring a fixed mesh, e.g., triangular or square pitch is not mandated for repetitive geometry. This modularity allows for relatively

simple swap-in/out of one structure for another. An example of this could be swapping in one flux trap for another. Another example is replacing any given fuel element with a new element containing flux wands. An additional example is replacing the standard fuel element model with one that has many more mesh regions for a detailed "Hot-Stripe" heat flux analysis. Hot-stripe analysis is discussed in further detail later.

Two requirements must be respected. First, the outer connecting nodes of the new structure (i.e., exterior nodes of a structure's polygonal shape) must be identical to those of the original structure (See Figure 2.2). In other words, the outer shape of the flux-trap cannot be changed or it would not fit into the jig-saw puzzle that is the entire system. However, the internal nodes can be changed to construct any new geometry. Second, the structure (or subsystem) must be neutronically unique such that the angular quadrature of the current coupling to adjacent puzzle pieces is still valid.

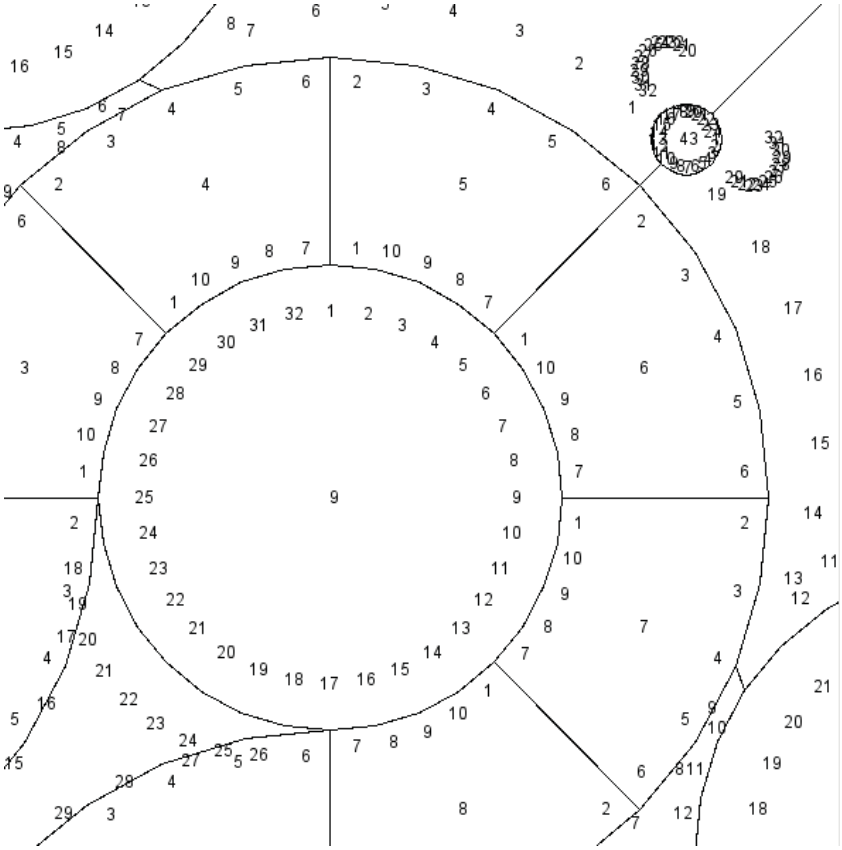

Figure 2.2 Node couplings of the ATR HELIOS model.

2.1.3 Material Overlay Features

HELIOS enables hierarchical overlaying of material (composition, temperature, density) definitions from the system-level down to the individual spatial region (i.e., single mesh). This allows for simulation of shuffling and control material insertion/removal at a mesh-by-mesh fidelity. For instance, the

/BaseModel material overlay and spatial mesh is used to accommodate as little as 3.75° of OSCC rotation. Two OSCC mesh structures are available to allow the user to balance calculation turnaround and model fidelity. The calculation sensitivities to mesh will be discussed in Section 2.3. OSCC rotation is then accomplished by overlaying the absorber material, hafnium, into the appropriate meshes for each new rotation of individual OSCCs during the depletion, Figure 2.3. The Hf overlay method has also been implemented in the model to move each of the 24 neck-shim and regulating rods independently.

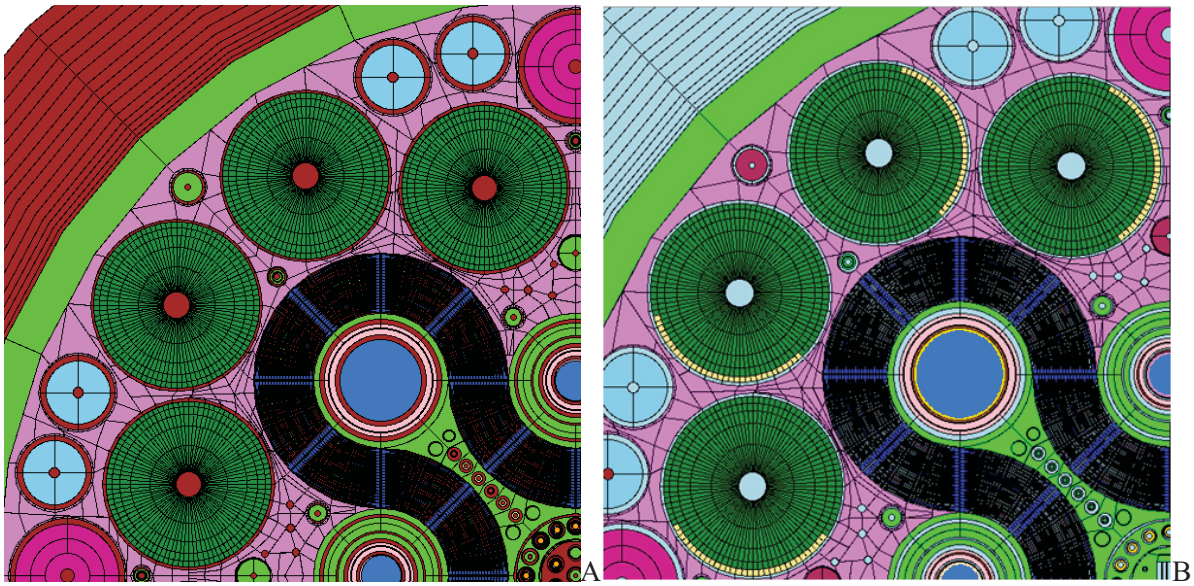

Figure 2.2 Material overlays for OSCCs for: (A) the background state and (B) after hafnium overlay.

Composition Databases. HELIOS provides an information database file format (called HERMES data files) for tracking isotopic information. The isotopic and burnup information dumped (i.e stored) in a HERMES file in one calculation can then be used by a later calculation. An example of this is loading the End-of-Cycle (EOC) composition from a core-follow (As-Run) calculation into the Beginning-of-Cycle (BOC) composition of a subsequent core cycle predictive model. HERMES files are also useful for specifying restart calculations, for example in the case where a cycle has an unplanned shutdown and thus does not follow the originally modeled path.

Embedded Arithmetic Expressions. The input pre-processing code for HELIOS, called AURORA, allows for embedded arithmetic expressions. In other words, numerical constants can be manipulated by algebraic formulas defined within the input files prior to being used in the actual physics calculation. This allows much of the problem definition (e.g., drawing dimensions) to be entered directly into the input files as opposed to being pre-computed by the user. Hence, the traceability of model properties to drawings and tracked documents is much more transparent than in other codes. Any character beyond column 80 in the input file is not read by AURORA. Thus, in the ATR HELIOS model the document reference where the exact numerical constant appears in literature is provided after column 80 to the right of the occurrence of this data in the input file.

2.2 Model Flexibility and Modularity

One short input and four top-level SET files are used to define an application-specific ATR model. The short input is the input file where the problem is defined and all other SETs (and catalogs contained within SETS) can be loaded. A description of these files follows.

1. Short-input (e.g., AsRun.INP): This file defines the HELIOS “CASE” to be run. It is where the OSCC movement, neck-shim pattern, and burnup step definition are defined.

2. Master Set File (e.g., AsRun.SET): This file loads all core internals from the /BaseModel directory. This file allows the user to toggle between ATR and ATRC core internals (i.e., automatically changes the beryllium reflector design, neck-shim design, Hf concentration in the OSCC's, etc.). This file has been co-located with the short-input during development of the HELIOS model system. However, this file could be moved to the /BaseModel as the types of applications (e.g., ATR versus ATRC configuration) becomes fairly routine.

3. EXPR.SET: This file loads all flux trap and capsule experiment geometry from the /EXPR directory. For fresh experiments, this file defines the fresh experiment composition, Hf shroud, Cd basket composition, etc. For previously irradiated experiments, this file loads the BOC composition files (i.e. HERMES files containing database-stored material overlays) via a DBMAT operator. A DBMAT operator can be used to define a material composition (in lieu of a material MAT operator) by telling HELIOS to look in an existing HERMES file. Experiment geometries currently supported are the following: AFC, AFIP, AGC, AGR, LIPT, LOOP2A, MICE, MUCH, NSUF, SIPT, and SPICE. This list is also valid for various experiment facilities (e.g., CDIPT, CIHA), backups, and dummy inserts for the respective experiment programs. Fillers and generic capsules are also provided for experiment positions that do not currently have experiment geometries available.

4. FUEL.SET: This file loads all fuel element geometry from the /BaseModel directory. Current fuel element options are Mark IV fuel, Mark VII fuel, a version of Mark VII fuel with a fine mesh of the fuel meat, and a Mark VII fuel element with three flux wands holding wires near the central rib.

5. INTR.SET: This file loads aspects of the core internals that may change over the life of the core. This file is currently used to augment the composition of poison materials in the reactor internals, namely neck-shim hafnium and the reflector beryllium depletion. It interacts with /BaseModel but can also load-from and dump-to a HERMES file, such as those containing the hafnium compositions from the previous cycle.

2.2.1 Fuel and Experiment Loading.

Fuel shuffling and experiment facility change-out is accomplished by defining each fuel element and experiment as a self-contained polygon structure (defined by the HELIOS STR operator). These HELIOS structures can be repeated as many times as necessary by connecting the outer nodes of these structures to the connecting nodes of other structures within the ATR HELIOS model. Once connected these amalgamated structures comprise a subsystem. Subsystems can be connected with other subsystems or other structures to form the entire system of the problem statement. These node-to-node connections are performed using the HELIOS CNX operator. Figure 2.4 shows the fully connected system of the ATR HELIOS model. Currently the fuel serpentine, outer beryllium reflector containing the OSCC's and the inner beryllium reflector containing the B-positions are contained within subsystems. The green, yellow and blue regions are the outer and inner reflector and fuel serpentine, respectively, and are connected with the remainder of the structures (cyan) to form the entire system. Note the numbering scheme in the figure denotes the position of these features as they appear in the CNX operator used to form each subsystem.

Most experiments can be loaded by swapping structures in and out of the model. The nine flux-traps, B-holes and I-holes structures can be inserted into the model using node connections. So long as the polygon shape matches the opening in the jigsaw puzzle formed by the surrounding structures, these experiment facilities can also be rotated within the ATR model geometry or moved to another flux trap. Figure 2.5 shows an example of two structure definitions describing experiment facilities for the center flux trap. Note that in both structures in the figure the connecting node x-y locations and numbering schemes are identical. The interior of a flux trap STR can contain as much geometric detail as needed, such as an experiment-specific facility, insulation tube, pressure tube, shroud, etc., with marginal need for homogenization in the X-Y plane.

A-positions, H-positions and any other capsule facility are not defined using the STR operator. Given their cylindrical nature, they are specified by the HELIOS CCS (circular-cylindrical-system) operator. CCS features are embedded into a STR by specifying their x-y location within the STR's definition. In the ATR HELIOS model's capsule experiment facilities, a typical CCS contains the pellet, rodlet, capsule, neutron filter and basket (as applicable), respectively.

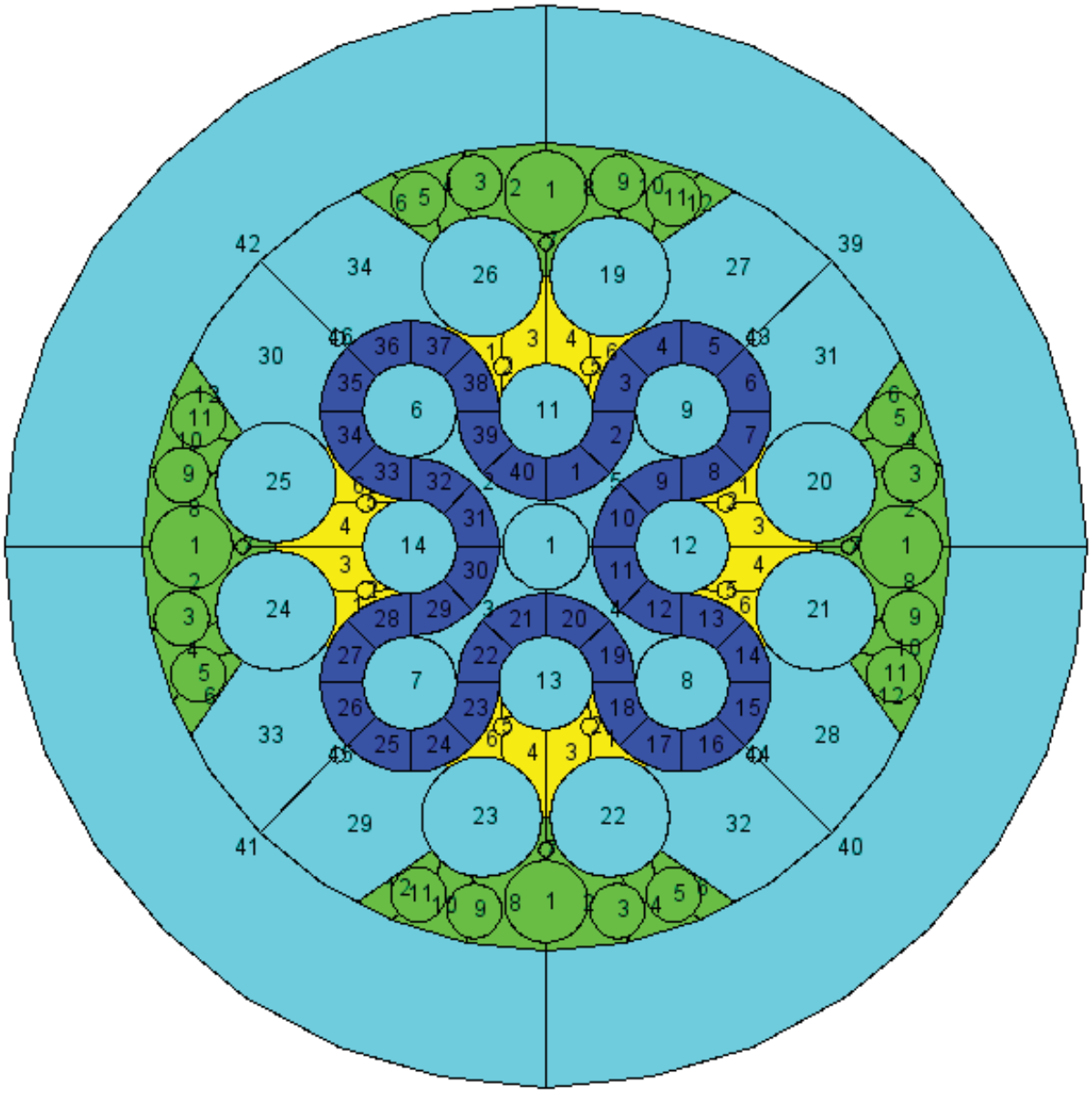

Figure 2.3 ATR HELIOS model full neutronic system comprised of connected subsystems and adjacent structures.

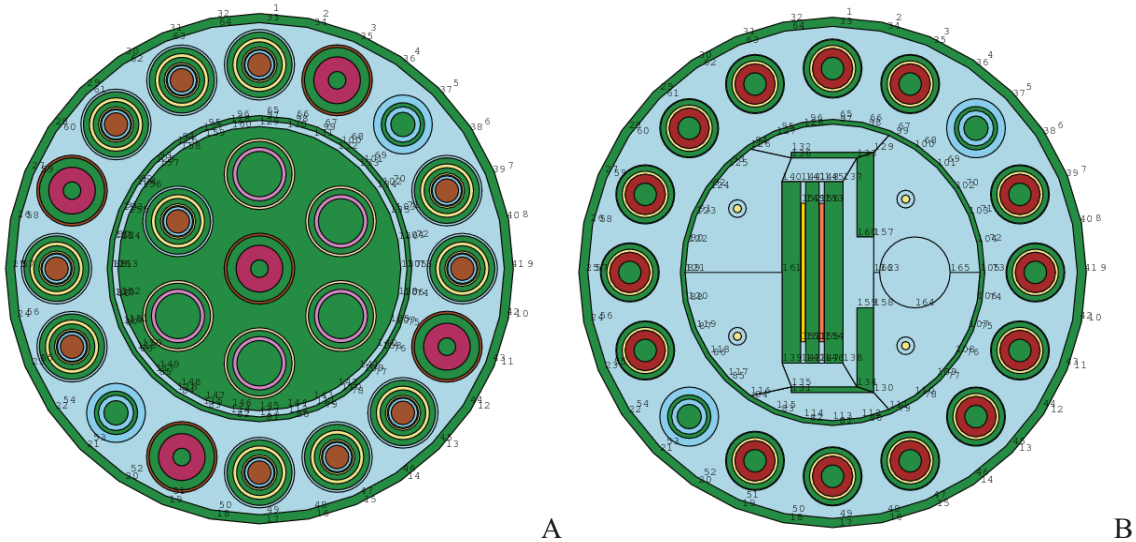

A B

Figure 2.4 Structure mesh for: (A) Center Irradiation Housing Assembly (CIHA), (B) ATR Full-sized-plate In center flux trap Position (AFIP). Both structures are located in the center flux trap for different applications.

2.2.2. ATR to ATRC Toggling.

As mentioned earlier, the base model also includes alternative SET files for defining the ATRC. The ATRC is a near replica of the ATR, but with a few important differences. The following differences required a different SET definition.

- The ATRC hafnium neck-shims are solid cylinders as opposed to annuli as in the ATR.
- The ATRC beryllium reflector has many more water holes than in the ATR.
- The ATRC does not have four small outboard A-positions in the neck-arms.
- The ATRC does not have Large B- or Small I-positions in the beryllium reflector.
- The ATRC fuel element U-235 loading is 975 grams as opposed to 1075 grams in the ATR.
- The ATRC fuel element B-10 loading is 0.81 grams as opposed to 0.66 grams in the ATR.
- The ATRC B-10 volumetric density is the same in every plate whereas the boron is concentrated in the inner and outer four plates in the ATR model.

To change a model from ATR to ATRC, one simply needs to change the catalog call in the short input to specify ATR versus ATRC internals in the Master SET, which is the change of a single character (i.e., &ATR becomes &ATRC). The only other suggested change is to comment out the Small I, Small A, and Large B catalog calls in EXPR.SET. This ensures that these features are not loaded from the /EXPR directory. Figure 2.6 demonstrates the ability to toggle between core internals and reflector differences while preserving the experiment (and fuel) loading configuration.

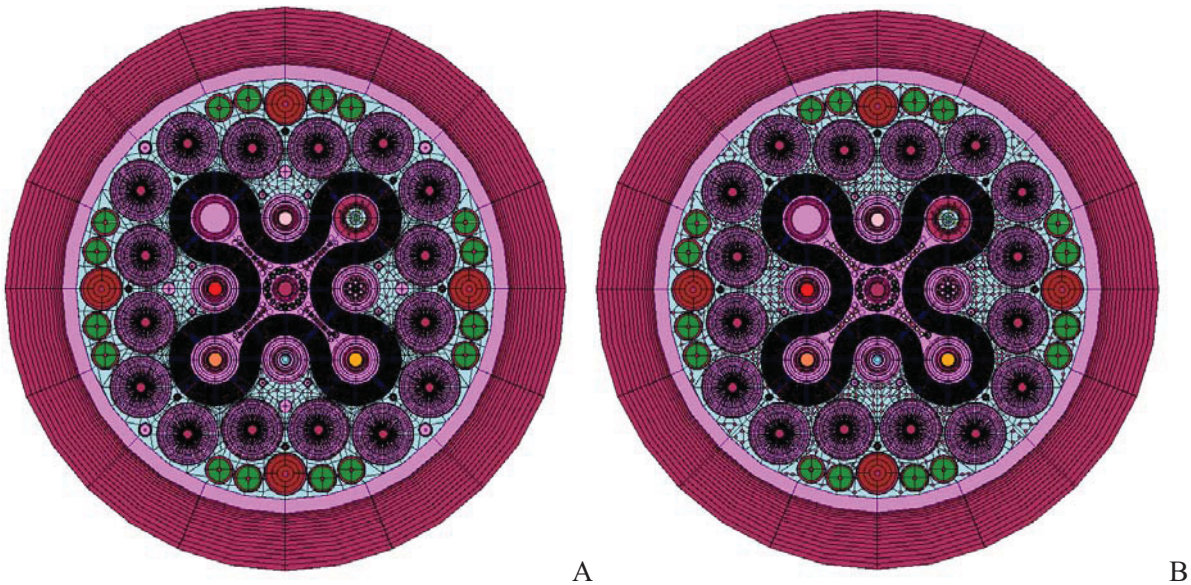

A B

Figure 2.5 Cycle 152A reactor loading pattern for: (A) the ATR, (B) the ATRC

2.2.3. Depletion of Non-Fuel Regions

Hafnium Neck Shim Depletion. Currently two methods of capturing neck-shim burnup are supported. First, the density of the "fresh" hafnium composition is decremented by a fraction ranging from 0 to 1. This is analogous to the current process where a similar fraction produced by the HFBURN code is used to augment the macroscopic Hf cross-section used in the PDQ/HARMONY code suite. PDQ/HARMONY is the software used for core design analysis for the ATR (Caldwell, 1967; Breen et al., 1965). The second method supported is to micro-deplete the Hf composition and store BOC/EOC neck-shim data in HERMES files. We are not currently using this latter approach because to do so we would need to reconstruct the neck-shim fluence history going back to the 2004 Core Internals Change-out (CIC) and this does not appear to be practical. However, this approach can begin to be used after the next CIC, assuming that HELIOS is used to model the fresh neck shims during the needed ATR cycle predictions.

Beryllium Reflector Depletion. HELIOS is not well adapted for beryllium depletion for two primary reasons. First, the code requires a separate depletion calculation for every single mesh region containing burnable material. In other words there is no averaging of fluxes over large areas of the core prior to depletion. Given the enormous number of mesh regions in the beryllium reflector, it is expected that depleting the reflector would greatly increase computer resource requirements. Beryllium depletion contributes a small decrement to core reactivity every cycle (Smith et al, 1990). Therefore, it is likely that the reflector composition can be updated with sufficient accuracy once per cycle via an external depletion calculation. The second reason is that HELIOS does not support all the reaction types necessary to deplete beryllium. Table 2.1 has a list of reactions that need to be modeled in a beryllium depletion chain. Note that HELIOS uses the following neutron reactions to deplete the fuel: (n,γ), (n,f), (n,2n), (n,3n). It does not incorporate (n, p) or (n,α) into its burnup depletion chains.

An initial effort to evaluate a viable external depletion methodology has begun. Such a methodology will need to be coupled to a code currently part of the Core Methods Update Project code suite that can deliver both flux and cross-section data for the reactions given in Table 2.1. Another useful software requirement is a depletion code that allows the individual depletion chains to be tailored for the special problem of beryllium depletion. Finally, it is important for the depletion code to be accurate and stable over a

sufficient range of problem types so that it can be validated by experimental benchmarks more common than beryllium depletion.

Table 2.1. Isotopes, reaction types and depletion chains necessary for depleting the beryllium reflector.

Chain	Reaction/Decay	Reaction/Decay	Comments
1	$^{9}Be + n(th) \rightarrow {}^{10}Be + \gamma$	n,γ	
1	$^{10}Be \rightarrow {}^{10}B + \beta^{-}$	β Decay	
1	$^{10}B + n \rightarrow {}^{7}Li + \alpha$	n,α	
2	$^{9}Be + n \rightarrow {}^{6}He + \alpha$	n,α	^{6}He has no MCNP cross section data
2	$^{6}He \rightarrow {}^{6}Li + \beta^{-}$	β Decay	Assume ^{6}He and ^{6}Li in secular equilibrium
2	$^{6}Li + n \rightarrow {}^{3}H + \alpha$	n,α	
2	$^{3}H \rightarrow {}^{3}He + \beta^{-}$	β Decay	
2	$^{3}_{2}He + n \rightarrow ({}^{3}_{1}H + p) or\ \alpha$	n,p or n,α	The n,α has no other product
3	$^{8}Be + n \rightarrow 2\alpha + 2n$	n,2n	The 2α represents ^{8}Be instantaneous decay.

A likely candidate to meet these requirements is a new code developed at Idaho National Laboratory called Multi-Reactor Transmutation Analysis Utility (MRTAU). MRTAU is a general depletion program written in a modular structure using FORTRAN 95/2003. Two exponential matrix solution methodologies are supported by MRTAU: the Taylor series method and Chebysev Rational Approximation Method (CRAM). The ability to have two different solution types allows for a consistent methodological verification internal to the code. The code allows the user to input a burnup dependent flux and cross-section data set. For each flux and cross-section subset, the code allows the user to arbitrarily control the number of solution time-steps. The code also allows the user to select an arbitrary number of polynomial expansions to either the Taylor or CRAM matrix polynomial expansion. This would be equivalent to a code-to-code verification with all input data identically preserved. The ability to vary the number of time-steps and solution fidelity via polynomial order facilitates convergence testing of both solution types. These capabilities will be important as the code is validated against ATR experiments for the irradiation conditions and transmutation reactions relevant to experiments, but to be used for depletion of beryllium with the flux conditions within the reflector region.

Most importantly, the code does not mandate any reaction type. The number of naming conventions for and the burnup chain linkage between reaction types are controlled by the user in human-readable library files. There is no limit on the number of isotopes defined. The current isotope list contains 182 fission products from Zn-66 to Yb-172 and 49 heavy metals from Pb-206 to Cf-252. The code is not limited to any set library of isotopes. In fact, it may be useful to create a specialized library for just the chains in Table 2.1 rather than append the 231 isotope library. All libraries are in a simple to understand human readable format such that manipulation of nuclear data can be performed by the user or by a coupling code with little expert knowledge of library structure.

All of the reaction types in Table 2.1 are supported by the current library files for MRTAU but at present the beryllium, lithium, tritium and helium reactants and products (other than He-4) are not encoded into these files. Some simplifications to these chains can be made. In chain 2, He-6 is short lived ($T_{1/2}$ = 0.8 sec) such that the ^{9}Be(n,α)^{6}He reaction would likely be modeled as ^{9}Be(n,α)^{6}Li. In chain 3, Be-8 is also very short lived so that the n,2n reaction in chain 3 can be modeled as instantly producing two alpha particles and two neutrons.

A preliminary effort has been undertaken to couple MCNP to MRTAU using a coupling script/code written in PYTHON 2.7. The MCNP/MRTAU Python script creates flux and flux cross-section

multiplier tallies in the MCNP file and then computes one-group cross-sections and fluxes from the MCNP output. The code then inputs these fluxes and cross-sections for each depletable region into the MRTAU input file. A preliminary depletion benchmark of the AFIP-3 experiment in Cycle 144A has been performed. AFIP-3 was a reduced enrichment plate-type fuel experiment previously tested in the ATR (See Appendix A). The experiment consisted of two prototypic plates containing low-enriched uranium in a molybdenum alloy which were stacked axially in a plate frame assembly and then loaded into the Center Flux Trap of the ATR. The MCNP/MRTAU results were compared with Post Irradiation Examination (PIE) data in the form of axial gamma scans across the plates as well as chemical dissolution analysis of two specimens sampled at two different axial locations within the plates. When compared to the PIE data, the average bias between MCNP/MRTAU and PIE over all four samples for end of life U-235 concentration was about 4%. The average bias for the Cs134/Cs137 ratio as about 5.6%. The agreement between the MCNP/MRTAU and the Monte Carlo With Origen (MCWO) script system, currently used for AFIP experiment analysis, was within 2% (See Figure A-3)

2.2.4 Single Fuel Element Model and Decay Calculations.

The composition data corresponding to each fuel element is stored in a respective HERMES data file. The file handle given to this HERMES file contains the location along the ATR fuel serpentine, fuel element serial number, core cycle number and BOC or EOC state. This data file system is then used to track the entire life-cycle of a fuel element while either in the ATR or the ATR canal. A new software utility called Total Heuristic Evaluator – Critical Process Transformer (THECPT) has been written in FORTRAN90. THECPT automates preparation of input files for single fuel element decay in the ATR canal. THECPT also serves as a post-processor of output files. THECPT reads and writes all necessary information for transferring fuel elements burned in cycle A and going to cycle B. It maintains all pertinent information for HELIOS DUMP and DBMAT operators in a comma separated variable file called ATRFUE.csv. Comma separated variable files can be interpreted as text I/O by any given computer language, but can also be opened by standard text editors and recognized by MS-EXCEL as a spreadsheet file. ATRFUE.csv then becomes a living record maintained by THECPT of fuel inventory data (stored in HERMES data files) for the purpose of use in HELIOS.

The HELIOS DUMP operator is responsible for saving composition and burnup material into a HERMES file during a depletion calculation. Not only is the EOC information stored in HERMES files but also all depletion steps specified by the user along the course of the depletion are written to the HERMES file. The HELIOS DBMAT operator is responsible for loading the compositions found in a HERMES file.

THECPT's primary function is to track all pertinent information for the DUMP and DBMAT operators to perform a single-fuel-element HELIOS calculation (Figure 2.7). THECPT determines whether a decay calculation is being requested and writes a short input file for that fuel element with the decay time requested by the user. If no decay calculation is needed, THECPT still writes a short input with a one hour decay time. A HELIOS transport calculation then is performed on every fuel element candidate listed in the THECPT input file to provide the user with reactivity data that can facilitate fuel loading pattern decisions. Upon completion of these single fuel element runs, THECPT is then used to update or append ATRFUE.csv. If ATRFUE.csv contains a record with the same cycle number, serial number and BOC or EOC condition, that record is updated with the new k-inf. If ATRFUE.csv does not contain a pre-existing record, THECPT appends ATRFUE.csv with a new record containing the recently calculated k-inf. Following an As-Run calculation, THECPT reads the HELIOS output and updates ATRFUE.csv with fuel element lobe powers, exposures, various isotopic data, the core position where the element resided, end-of-cycle date, and various needed HELIOS data values for creating a DBMAT operator in the single fuel element model.

The short input used to perform the single-fuel-element transport calculation loads exactly the same fuel element structure used in the base model but loads it into its own system with infinite reflective boundary conditions. The infinite reflective boundary condition is useful for determining the k-inf value for each

individual fuel element. HELIOS does not allow a pure-decay calculation absent of a depletion calculation. Thus, a fallacious power level of approximately 30.5 Watts is used to burn the fuel element for one hour, modeling a negligible burnup, so as to not affect the composition in any significant way. The 30.5 Watts burned for one hour divided by the heavy metal mass of one fuel element (1156 gm) yields a burnup of 0.0011 megawatt-days per Metric Tonne (MWD/MT). Note that the minimum burnup allowed in HELIOS is 0.001 MWD/MT. These single fuel element calculations result in a dumped HERMES file that is to be loaded into the ATR model as the BOC state. Following full core cycle depletion, the 40 fuel element compositions are dumped again into new HERMES files representing the EOC.

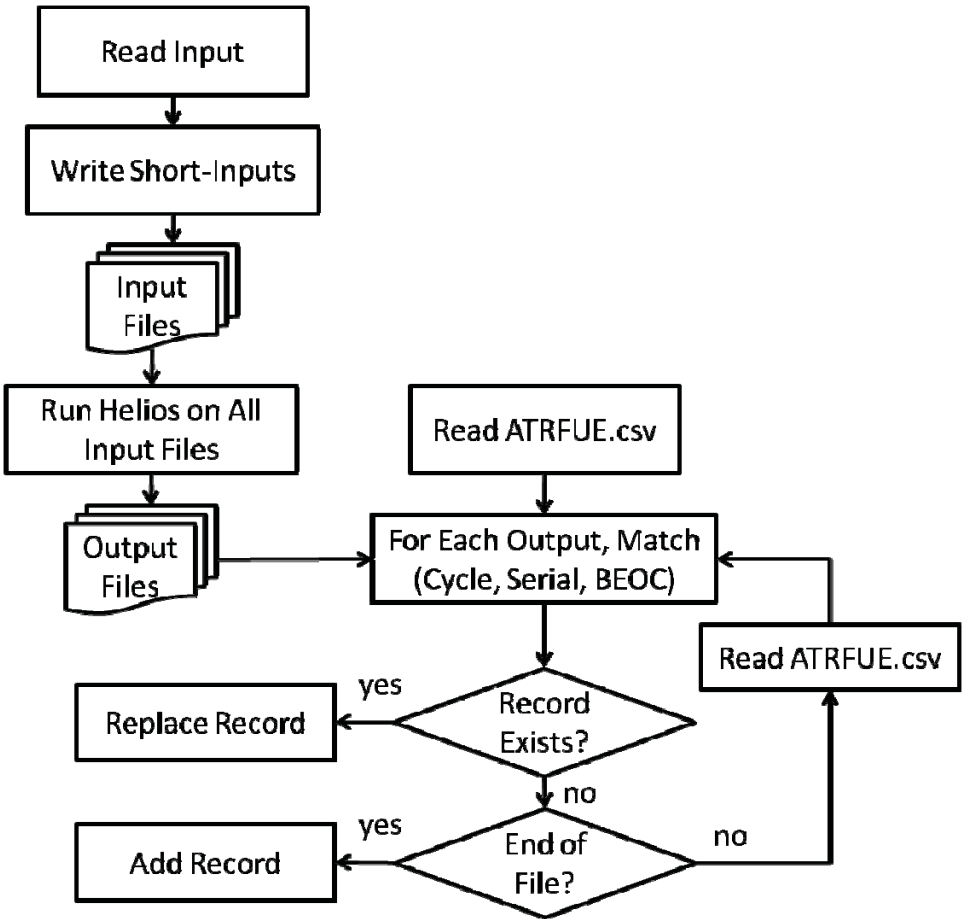

Figure 2.6. Flow diagram describing general process followed by THECPT for creating single-fuel-element inputs, performing decay (and decayless) calculations and storing the new k-inf values in ATRFUE.csv.

2.3 Model Fidelity and Convergence Tests

2.3.1 Angular Coupling Parameter Sensitivity

A model fidelity study was performed to assess the computed transport eigenvalue's sensitivity to the current coupling parameter (k) which controls the angular discretization of current being passed from one structure and/or subsystem to another (Studsvik Scandpower, 2009). The angular discretization was varied over combinations of two to five azimuthal angles with one to two polar angles (See Figure 2.8). The default used in the above benchmark was four azimuthal angles confined to only one polar angle in the 2D plane (i.e., k=4). As can be seen from visual inspection of Figure 2.9, the value of k=4 is sufficiently converged to be considered adequately precise enough for regular usage of the model. The change in computed eigenvalue from two azimuthal angles (k=2) to three (k=3) was 0.19%, whereas the change from three (k=3) to four angles (k=4) was only 0.10%. The change from four (k=4) to five (k=5) angles was only 0.05%. Generally, these changes are smaller than uncertainties that can be attributed to random error for most cases. Therefore, perhaps k=2 would be sufficient for most applications. Nevertheless, it was found that k=4 to k=5 can offer more precision with negligible added computational cost.

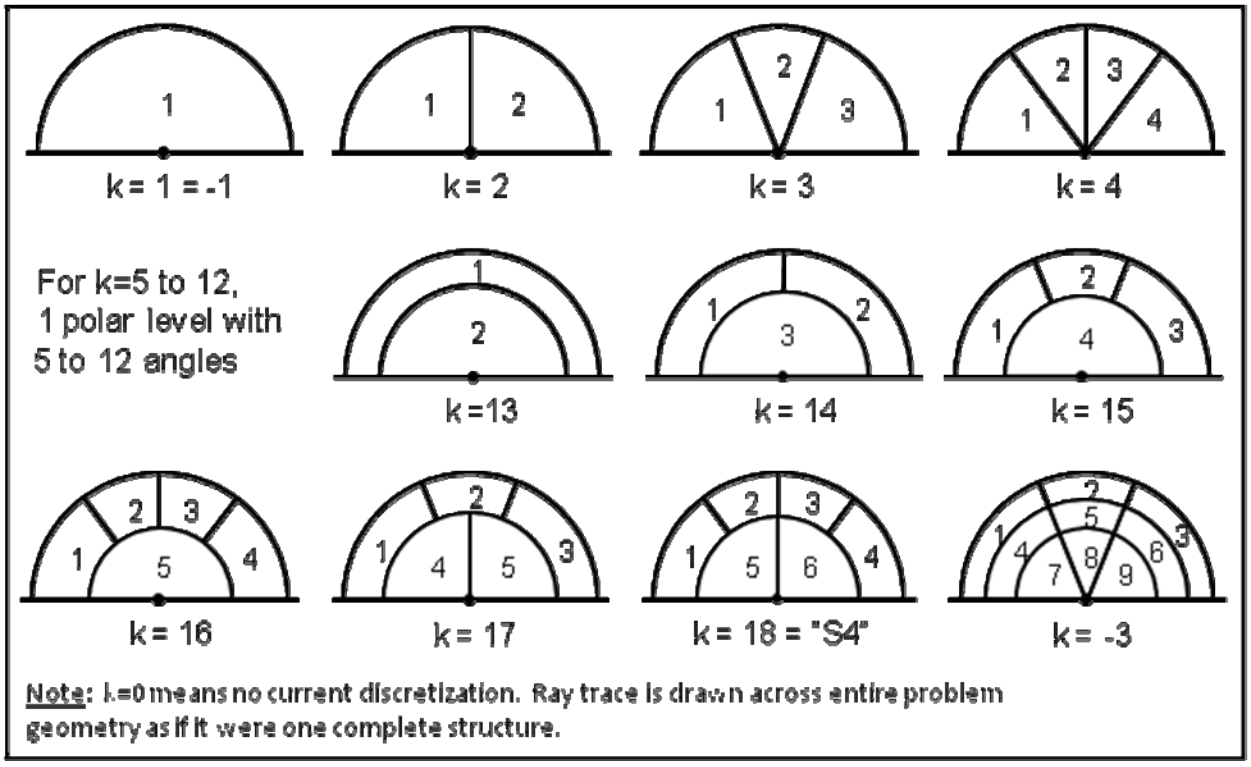

Figure 2.7 Angular current coupling schemes available in HELIOS (Studsvik Scandpower, 2009).

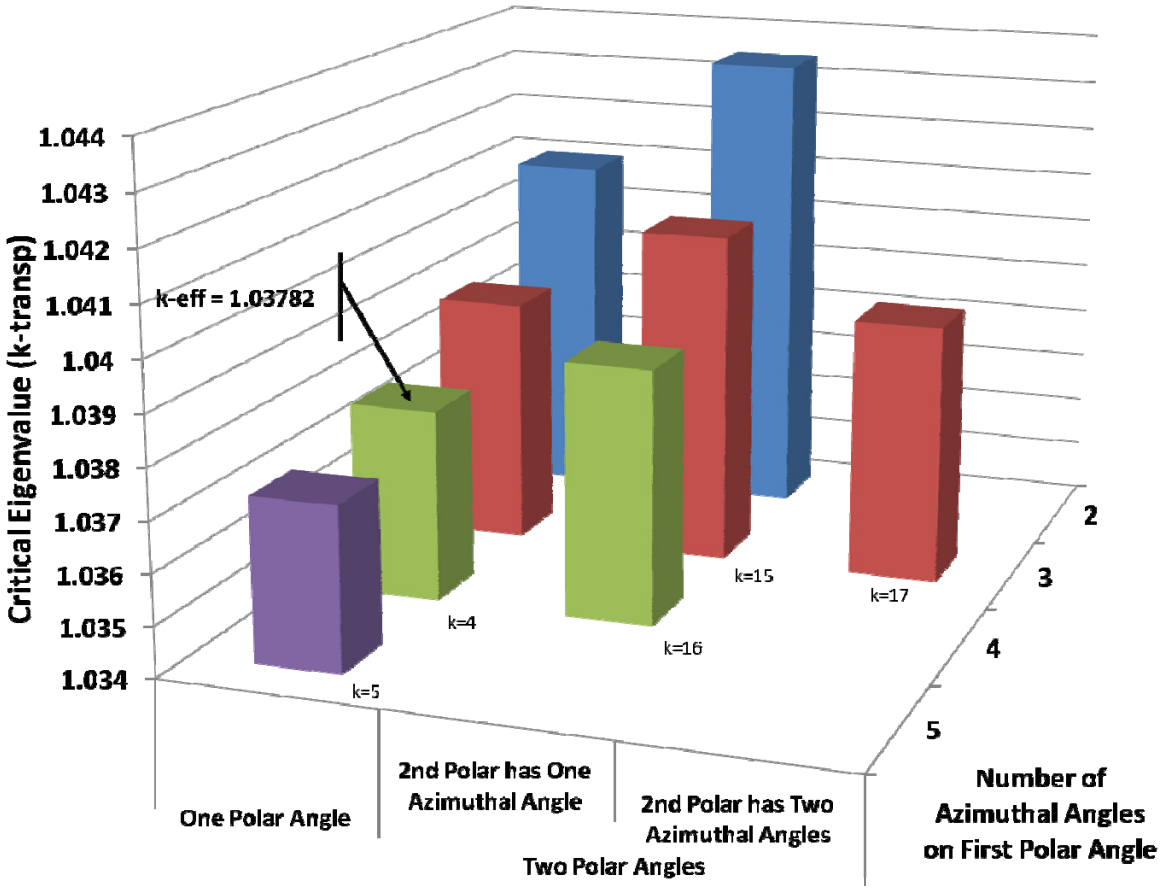

Figure 2. 8 Computed transport eigenvalue (2D k-transp) per angular discretization of the inter-structure/subsystem current coupling parameter, "k".

2.3.2 Outer Shim Control Cylinder mesh Refinement

A mesh refinement parameterization study was performed on the ATR OSCCs to demonstrate that the model has attained sufficient precision to quantify bias between the HELIOS prediction of criticality and a known (i.e, measured) critical state. Without knowing the precision, determination of bias could be misinterpreted as the level of accuracy when in reality it could be error associated with un-quantified effects, such as poor solution fidelity and/or statistical variations. Additionally, this study provides the framework for quantifying the general precision of ATR models and juxtaposing the intended precision against the use of the data and the time required by the program to obtain the data. Thus, the ATR models will contain mesh refinement options that would suit the various needs of the users.

Radial Mesh Refinement. The radial refinement study of the OSCC meshing utilized an OSCC model that consisted of a CCS representing the 120° Hf blade arc attached to an OSCC, the beryllium structure of the OSCC, and the center coolant hole of the OSCC (Figure 2.10). The outermost ring of the OSCC model was azimuthally segmented into 96 different regions, while the remainder of the OSCC was only segmented in the radial direction. The azimuthal segmentation of the outer ring enabled the model to simulate rotation of the outer shims via the use of material overlays. Material overlays are used to specify that the hafnium blade material be placed in specific regions. Changing the specified regions effectively

rotates the hafnium blade location. Thus, this model could be used to easily study the effect of mesh refinement in the radial direction by changing the number of rings used to represent the beryllium within the outermost ring while having no effect upon the representation of the hafnium blade or rotational position of the OSCCs.

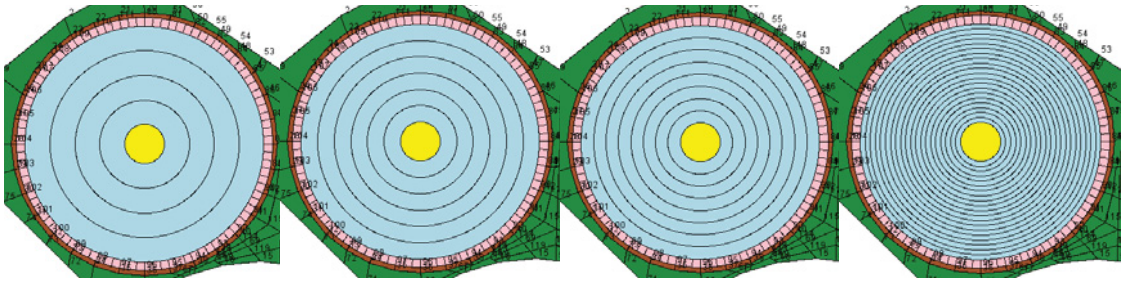

Figure 2.9 Refinement in the radial direction of the OSCCs

Data was collected from the same depletion time step (representing about 6 days from the start of the cycle) for four separate cases. This time step was selected with the intent to include the effects of error propagation over the course of depletion in the analysis, although this assumption has not been verified. The cases consisted of OSCC meshing between the outermost ring and the center coolant hole that were created by evenly spaced radii that form radial rings. The cases contained 4, 6, 8, and 20 radial rings, respectively (not including the water hole or the outermost hafnium-containing ring). The change in lobe powers between these cases was undetectable, indicating a change on the order of less than 0.02%. Additionally, the change in runtime between these cases behaved in a very linear manner.

Figure 2.11 shows the fractional change in computed eigenvalue relative to the case with 20 rings as a function of ring refinement. In this plot, k-transp stands for the eigenvalue solution of the HELIOS converged inner (flux) and outer (source) iterations. K-inputB stands for the eigenvalue of the transport solution using the input buckling specified by the user. K-inf stands for the infinite multiplication factor for the system. K-infcrit stands for the infinite multiplication factor of the system in the critical spectrum. The change in eigenvalue between these cases was on the order of 0.005% or less.

When compared to the runtime results of this analysis, the eigenvalue results show that an increase in precision is very expensive with respect to execution time of the program when refining the OSCC mesh in the radial direction only. The eigenvalue trends also suggest that a mesh refinement of about 8 radial rings or more increase the precision of the calculations at a slower rate than the precision obtained from 4 or 6 radial rings. This data suggests that a refinement above 8 radial rings is most likely an inefficient use of computational resources.

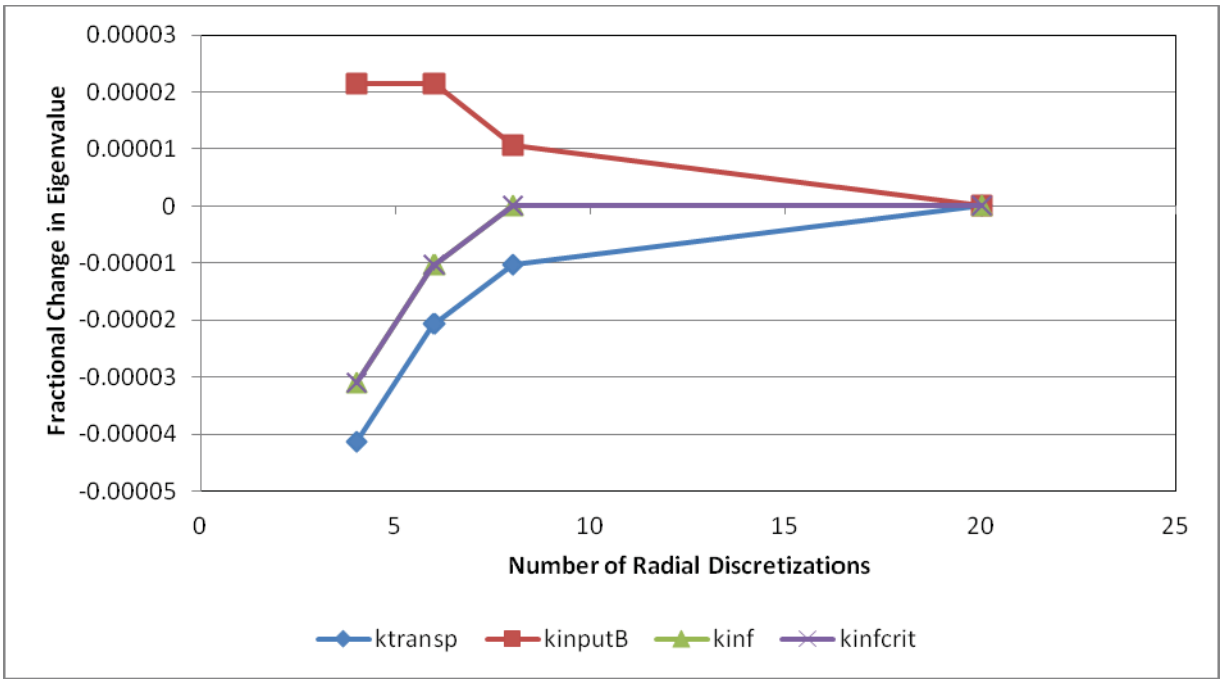

Figure 2.10 Fractional change in eigenvalue precision to OSCC radial refinement

Azimuthal Mesh Refinement. The azimuthal refinement study of the OSCC meshing utilized an OSCC model that consisted of the same general CCS structure as the radial refinement model, but with some key differences (2. 12), namely the number of azimuthal meshes, which greatly affected the operation of material overlays in the outermost Hf containing ring. Also, the radial rings were defaulted to the dimensions of the ATR Version0 model from the previous year of this project (Nigg and Steuhm, 2011).

In HELIOS, only one azimuthal meshing can be applied to each CCS. Thus, a coarse azimuthal mesh in the inner CCS representing an OSCC and a 96 azimuthal mesh in the outer ring of a CCS is not possible within the confines of the code. If the azimuthal meshing in the outer ring was simply changed to a meshing other than a 96 azimuthal mesh, then the OSCCrotat.SET file that specifies the appropriate location of the OSCC material overlay via a mesh numbering scheme would no longer function properly. To utilize the same mesh number-based material overlay methodology, a SET file containing a new numbering scheme specifically created for each azimuthal mesh analyzed in the study would become necessary.

To avoid this complication, the azimuthal refinement model represents OSCC position changes through the simple use of CCS rotation within the geometry of the model. CCS rotation allows the material applied to a CCS to remain stationary relative to the CCS, while still modeling the physical rotation of the OSCCs. To accomplish this methodology change, the hafnium arc (pink area in outermost ring of Figure 2.12) and the outermost beryllium regions of the OSCCs (blue area in outermost ring of 2. 12) are defined by region name versus the region number definition required by the material overlay methodology. The use of the OSCCrotat.SET file is completely circumvented, creating an accurate model without erroneous material placement.

Because of the generation of new “hidden nodes” (created by HELIOS to couple the STR to the CCS) during the rotation of a CCS, changing the geometry of the model increases the run time of a time step

when compared to the use of a material overlay methodology. Thus, the azimuthal refinement runtime analyses cannot be directly compared to runtime analyses performed for other mesh refinement studies. Furthermore, HELIOS does not allow the CCS rotation to be redefined in the middle of a calculation, as this would constitute re-meshing the problem geometry. Changing the geometry of the model via several serial calculations significantly increases the run time of multiple time steps when compared to the use of a material overlay methodology since restart calculations utilizing composition dumps would need to be performed. Therefore, using the CCS rotation feature is not considered a viable method for OSCC rotations unless the core designer finds the representation of one core state (one core control/power configuration) per HELIOS calculation useful for his/her analysis and design process. Note that the primary method for representing OSCC positions will remain the material overlay method.

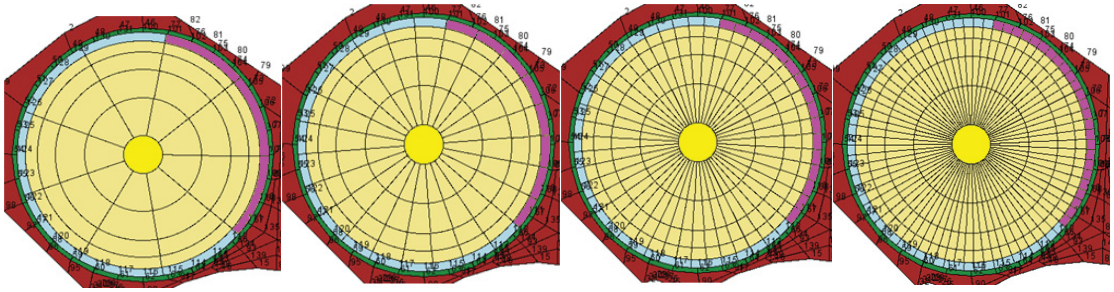

Figure 2.11 Refinement in the azimuthal direction of the OSCCs.

Data was collected from the CCS-rotation method for a single time step (representing the ATR with a balanced position of all of the OSCCs at a 90° rotation) for six separate cases. These cases utilized the Version0 model OSCC radial meshing, in addition to the specific azimuthal discretization used for each case. Note that the single time step used in this portion of the study does not include the effects of error propagation in the analysis. A single time step was performed to reduce the complexity associated with the change in OSCC rotation methodology. The azimuthal refinement cases contained 3, 9, 24, 48, 72, and 75 evenly-spaced azimuthal discretizations of the hafnium arc, respectively. Note that the geometry change methodology created program limitations that did not allow refinement above 75 azimuthal discretizations.

Figure 2.13 and Figure 2.14 give the fractional change in corner lobe powers and center lobe power, respectively, for the azimuthal refinement study. The change in corner lobe powers between these cases was 3.5% or less, although the change decreased to 1% or less when 24 or more azimuthal discretizations were used. The change in center lobe power between these cases was 10% or less, although the change decreased to 2% or less when 24 or more azimuthal discretizations were used.

Figure 2.15 shows the fractional change in the eigenvalue, specifically k-transp, versus the number of azimuthal discretizations. The change in eigenvalue between these cases was 3% or less, although the change decreased to 0.5% or less when 24 or more azimuthal discretizations were used. The decrease in runtime relative to the case with the most azimuthal discretizations reached 35% or less. These results show that a noticeable increase in precision is fairly inexpensive with respect to execution time of the program when refining the OSCC azimuthal mesh from 3 to 24 azimuthal discretizations (assuming the use of this discretization over the four radial rings used in the Version0 model). The trends also suggest that a mesh refinement above 24 discretizations has little effect on the precision of the model. Note that the use of a material overlay methodology may change these results, but the runtime trend results can provide insight into the level of refinement needed to appropriately represent the ATR.

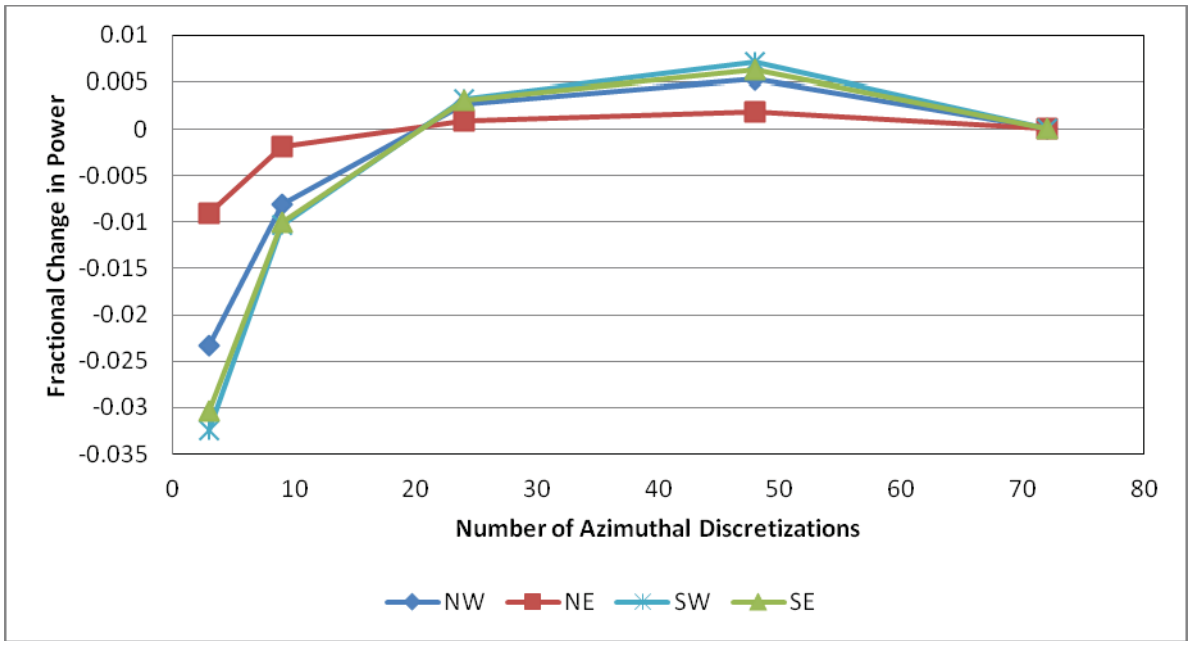

Figure 2.12 Fractional change in corner lobe power precision due to OSCC azimuthal refinement.

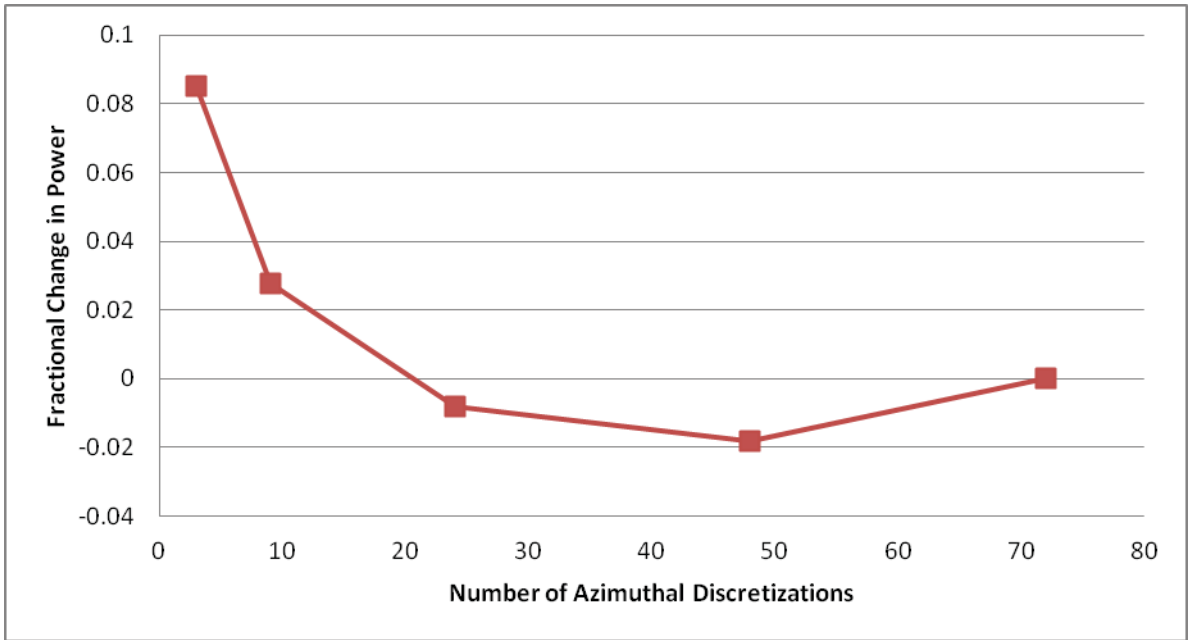

Figure 2.13 Fractional change in center lobe power precision due to OSCC azimuthal refinement.

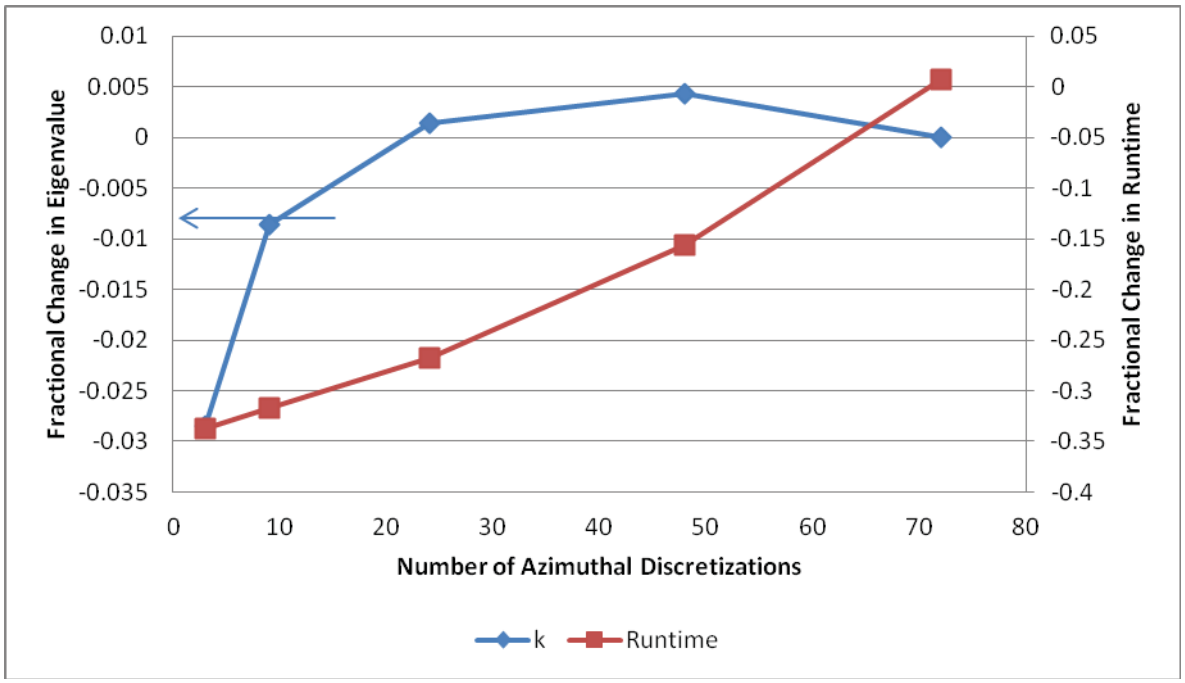

Figure 2.14 Fractional change in transport eigenvalue precision and runtime due to OSCC azimuthal refinement.

Concentric Ring Mesh Refinement. The concentric ring refinement study utilizes an OSCC model that consisted of the same general CCS structure as the radial refinement model. The concentric ring model contained seven equally spaced radial rings (not including the water hole or the outermost hafnium containing ring) and utilized 96 azimuthal discretizations (Figure 2.16). Unlike the azimuthal refinement study, only a subset of the radial rings is discretized. The concentric ring study applies the azimuthal discretization for an increasing number of concentric azimuthally meshed rings starting outwards and progressing inwards. The rings inside the azimuthally discretized rings contain only the radial discretization created by the equally spaced radial rings (i.e., no azimuthal discretization).

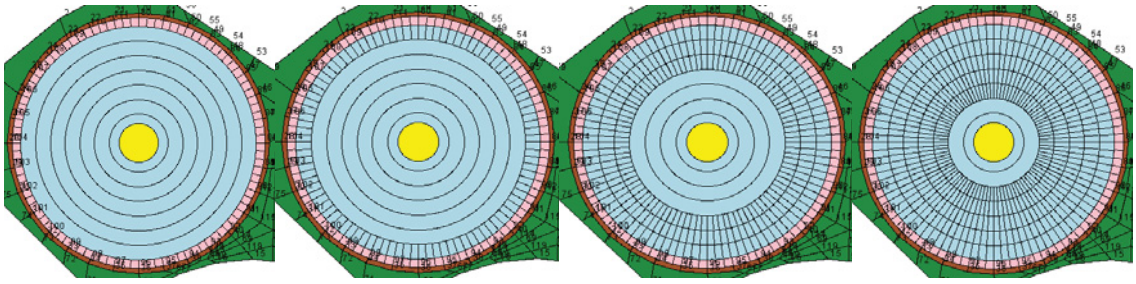

Figure 2. 15 Refinement in the azimuthal direction of concentric rings in the OSCCs.

The consistent azimuthal segmentation of the rings enabled the model to simulate rotation of the outer shims via the use of material overlays, just as was done for the radial refinement study. Data was collected from the same time step (representing about 38 days from the start of the cycle) for seven separate cases. This time step was selected to include a more significant portion of the effects of error propagation due to depletion modeling in the analysis. The cases contained 0, 1, 2, 3, 4, 5, and 6 azimuthally discretized radial rings, respectively.

Figure 2. 17 and Figure 2.18 gives the fractional change in corner lobe powers and center lobe power, respectively, for the concentric ring study. The change in corner lobe powers between these cases was 10% or less, although the change decreased to 1% or less when five or more azimuthally discretized radial rings (which create a total of 482 regions between the outermost ring and the center coolant hole) were used. The change in center lobe power between these cases was 25% or less, although the change decreased to 2% or less when five or more azimuthally discretized radial rings were used. Note that the center power trend suggests that the cases presented here have not attained the minimum precision possible by the code when performing concentric ring refinement. Thus, increased center power precision can be expected, although it will likely sacrifice execution time.

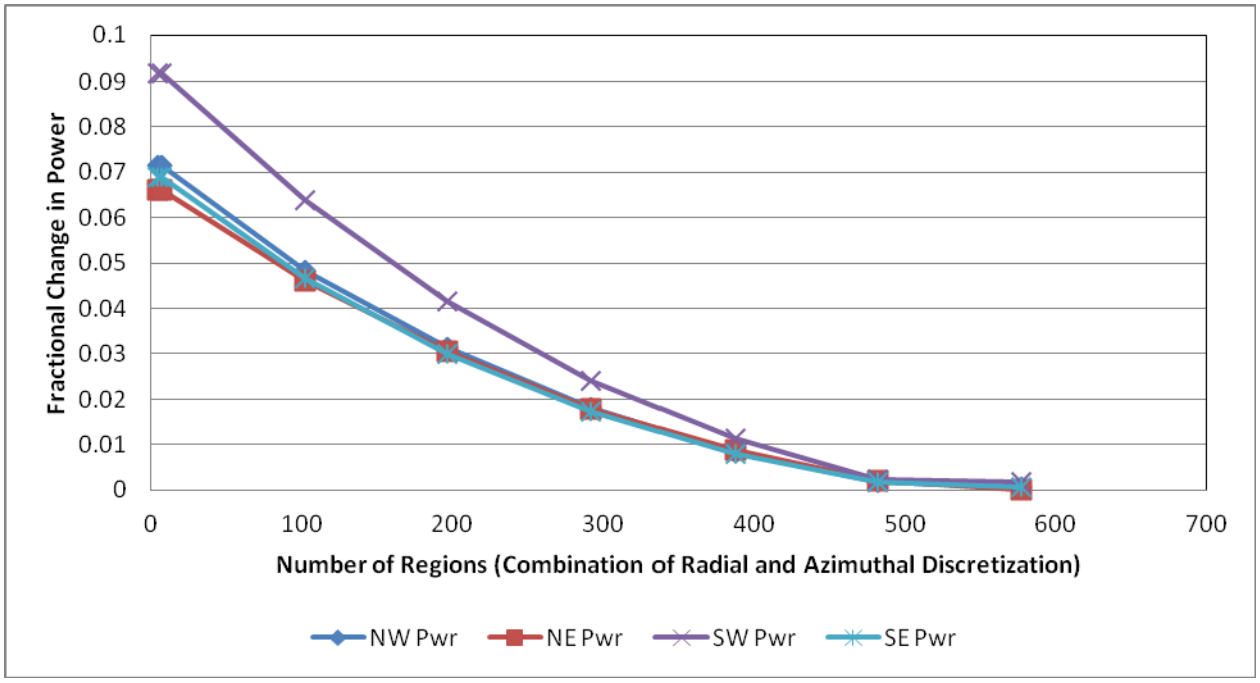

Figure 2.16 Fractional change in corner lobe power precision due to OSCC concentric ring refinement.

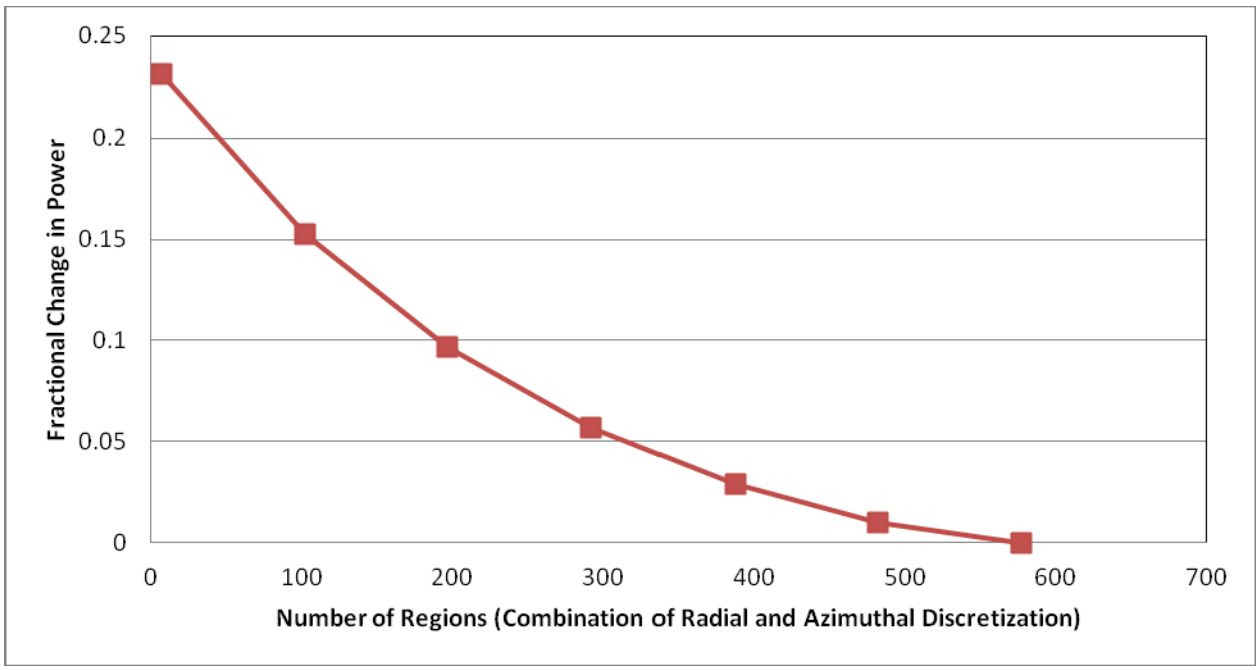

Figure 2.17 Fractional change in center lobe power precision due to OSCC concentric ring refinement.

Figure 2.19 shows the fractional change in k-transp versus the number of azimuthal discretizations. The change in eigenvalue between these cases was nearly 10%, although the change decreased to 1% or less when four or more azimuthally discretized radial rings (which create a total of 387 regions between the outermost ring and the center coolant hole) were used. The decrease in runtime relative to the case with the most azimuthally discretized radial rings reached 85% or less. These results show that a noticeable increase in precision is fairly inexpensive with respect to execution time of the program when refining the OSCC azimuthal mesh from zero to four azimuthally discretized concentric rings. The trends also suggest that a mesh refinement above four azimuthally discretized radial rings becomes increasingly more expensive with respect to execution time of the program, but the precision of the model will increase. Thus, it would be up to the discretion of the user whether increased execution time due to additional azimuthally discretized radial rings is needed for the data.

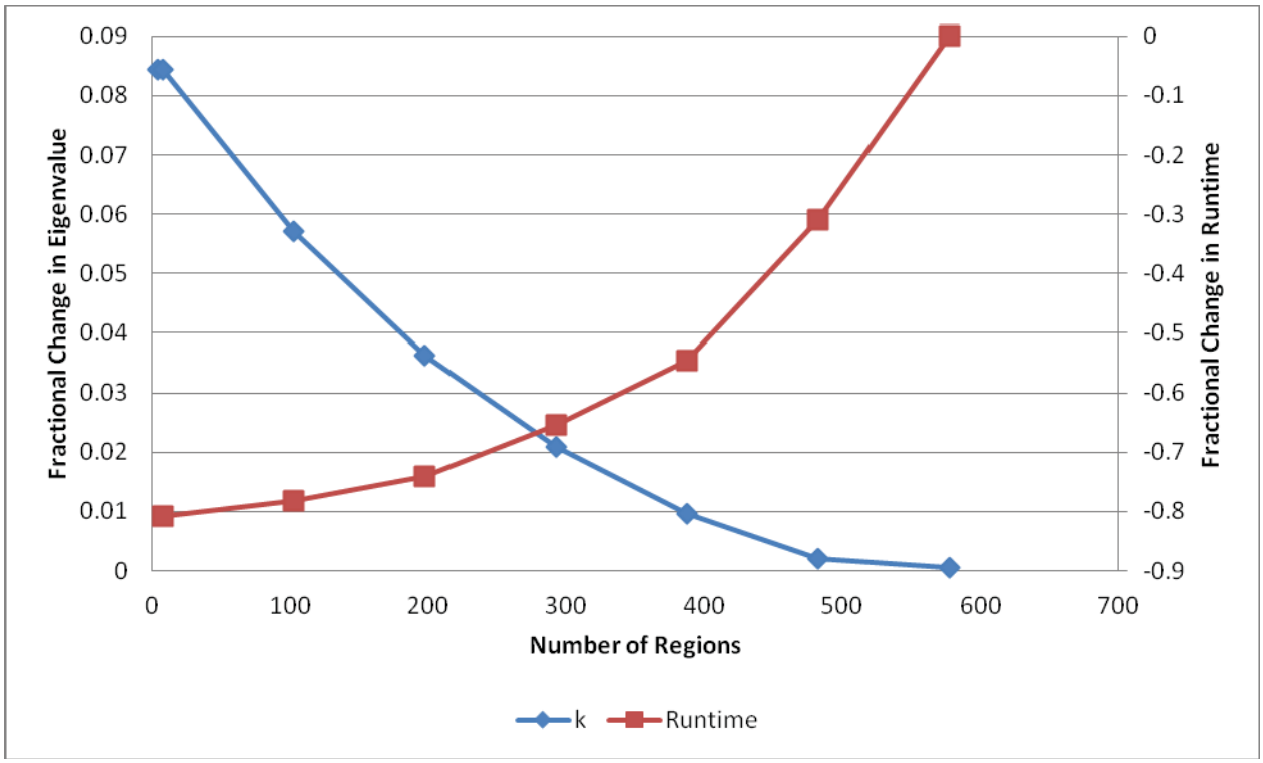

Figure 2.18. Fractional change in eigenvalue precision and runtime due to OSCC concentric ring refinement.

Expectations. Based on the parameterization study performed, it can be expected that models that utilize four radial rings between the center water hole and the outermost ring that are fully discretized by 96 azimuthal discretizations have sufficient precision that the results are useful when making engineering judgments. The benchmark models used in the validation results of this report are based on four radial rings (between the central water hole and the outermost ring containing the hafnium arc) that utilize 96 azimuthal discretizations. It is expected that the precision of data, such as center lobe power, can be increased if a change in OSCC mesh refinement is made to the model.

Each of the OSCC mesh options added to the Version0 model contain 96 azimuthal discretizations so that the material overlay option can perform OSCC rotations at 3.75° per region in the outermost ring. This azimuthal discretization is expected to provide the best precision possible within the azimuthal discretization options available. However, the flexibility in OSCC rotation angle sacrifices the execution time of the program. Unlike azimuthal refinements, the radial mesh refinements proved to have little effect upon the precision of the model. Instead, the radial meshing can be used to select the placement of the azimuthally discretized radial rings so that options with variable execution times and precision levels can be provided to the user. The execution times provided by the concentric ring refinement may be able to offset the increased execution time required by the 96 azimuthal discretizations needed for OSCC rotation flexibility.

An option has been made available that uses two radial rings between the center water hole and the outermost ring and that are fully discretized by 96 azimuthal discretizations. The option produces slightly less precise data than the Version0 model, but in a fraction of the Version0 model execution time of the

program. This option will be a very useful tool when performing initial physics analyses for cycle design predictive calculations. An additional option has been provided that uses four radial rings between the center water hole and the outermost ring and that are fully discretized by 96 azimuthal discretizations. The option produces slightly more precise data than the Version0 model, but has an increased execution time of the program. This option will be a very useful tool when performing model validation and when performing detailed cycle prediction and as-run calculations. Further refinement studies can be used to select the OSCC meshing options that are likely to be utilized by the user based upon optimized precision, optimized execution time, or a combination of these two parameters, as determined during the parallel calculations phase of the project.

2.3.3 Fuel Element Mesh Refinement

A mesh refinement study was performed on the fuel element model to determine if there was sufficient model fidelity to capture finely resolved power distributions, particularly at the azimuthal edges near the side-plates. This region is referred to as the "hot stripe" and is a region of interest for assessing local peak power/thermal constraints. In the hot stripe, the localized azimuthal heat flux along the fuel serpentine could result in a coolant enthalpy rise in excess of the safety margin (Polkinghorne, et al., 1994). The hot stripe is analogous to the fuel pin containing the highest power peaking in a commercial reactor. Though the hot stripe is generally considered to be an azimuthal region near the side plate, it could potentially be defined as any azimuthal segment along a plate. However, it has been shown that under most bounding analyses the hot stripe exists in the first 5% or 10% of arch length along a plate from the fuel element side plate (Polkinghorne et al, 1994). The course and fine mesh FE models are depicted in

Figure 2.20.

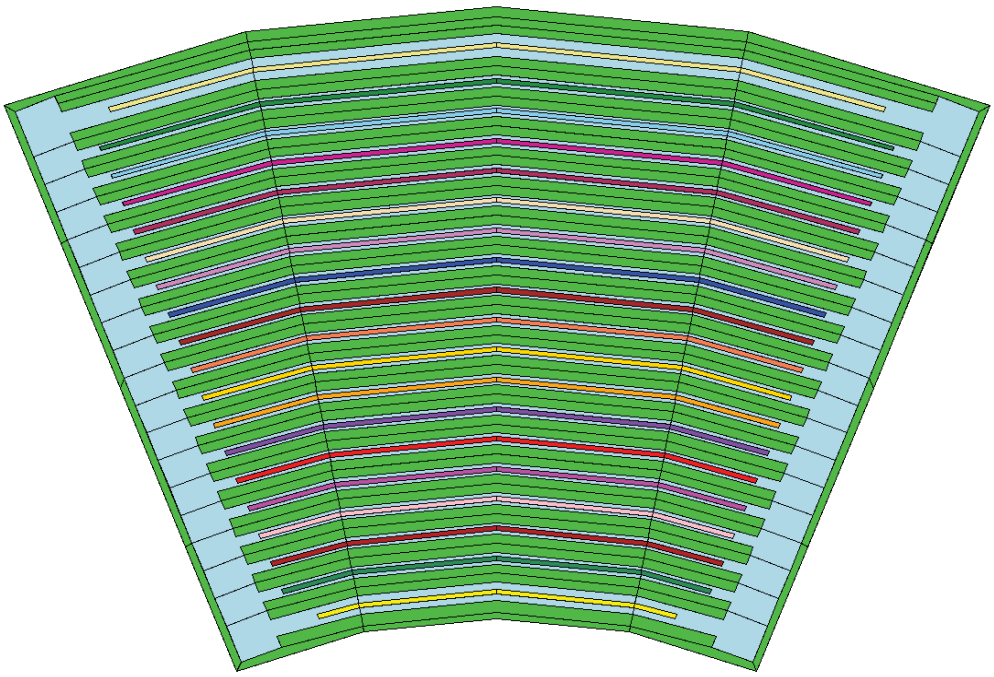

Figure 2.19a Single fuel element model for a course fuel meat mesh.

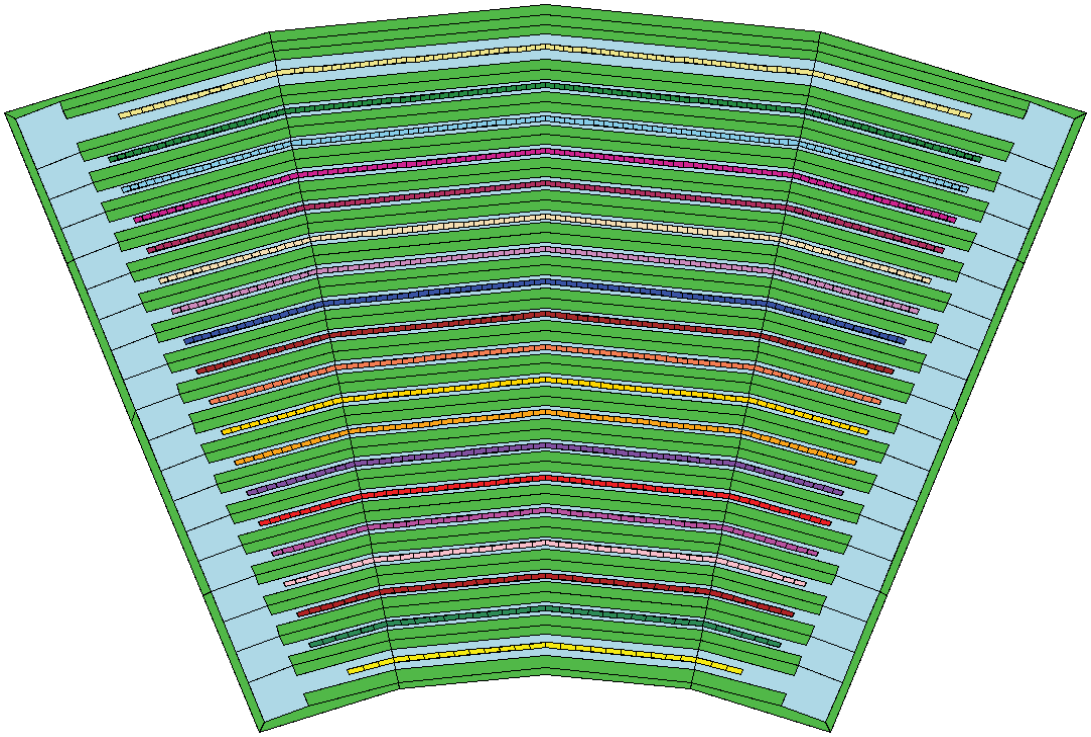

Figure 2.20b Single fuel element model for: a fine fuel meat mesh.

The mesh-refinement study also indicates the degree of spatial self-shielding necessary to capture the true power shape of the FE. To do this, a single fuel element model with reflective boundary conditions was used. The spatial mesh resolution in the fuel meat was increased plate by plate, starting from the inner plate and working outward. The calculated k-transp (equivalently k-inf for the SFE model) as a function of regions in the model is given in

Figure . No discernible convergence trend was found as the number of regions increased in the SFE model, suggesting that the course mesh model is sufficiently meshed to capture spatial shielding within the SFE.

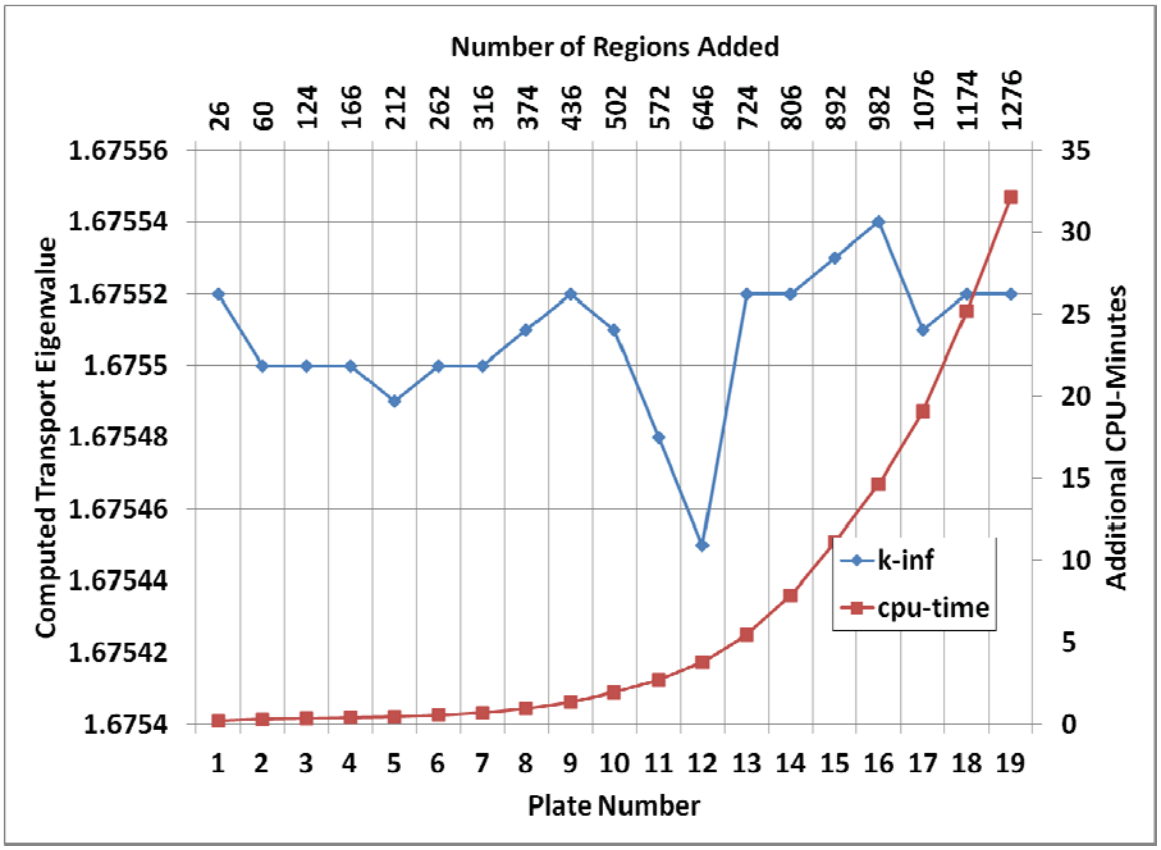

Figure 2.21 k-inf as a function of increasing fuel meat mesh regions in an infinitely reflected single fuel element model

2.4 Model Testing Against Historical Data

Although formal validation of HELIOS and other codes in the suite for ATR/ATRC applications will be largely based on experimental protocols and statistical analysis protocols specifically developed for this purpose (see Chapter 3 of this report), the initial development and testing of the HELIOS model was, by practical necessity, done using historical ATR operations data, especially the published data for the well-known 1994 Core Internals Changeout (CIC) Benchmark that is well-documented in the open literature. In addition, it was essential to test the model against recent "as-run" cycle depletion data, both for development purposes as well as to build a library of isotopic content data for recently-used fuel elements that are the most likely candidate elements for additional use in future cycles (fuel elements are often used two or even three times in the ATR before being taken out of service due to ^{235}U burnout and cladding exposure limits.

2.4.1 Cycle 103A Nuclear Requalification Tests

1994 CIC Benchmark. The original ATR HELIOS model was based solely on a description of the low power physics tests following the core internals change-out prior to cycle 103A-2 in 1994. This critical

experiment was eventually included as an internationally peer reviewed criticality benchmark in the 2005 publications of the International Handbook of Evaluated Reactor Physics Benchmark Experiments (IRPhE) and International Handbook of Evaluated Criticality Safety Benchmark Experiments (Kim et al., 2005). The ATR HELIOS model and a companion MCNP model have since been brought current with Rev 4 of this publication. Additional corrections (Bays et al., 2011) to the model (pertaining to the geometry description of the two regulating rods in the 1994 CIC) have also been performed (Figure 2.21).

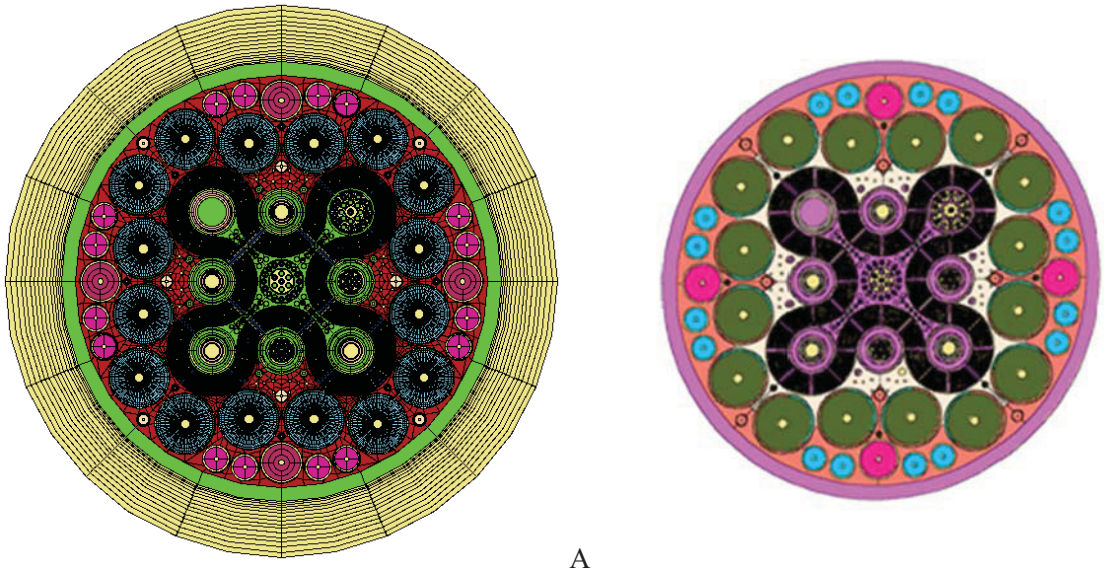

A B

Figure 2.21 Benchmark of the 1994 CIC IRPhE Benchmark done with: (A) HELIOS, (B) and MCNP.

Critical Eigenvalue. The critical eigenvalue assessment was performed last year and it was determined that the 2D version of the 3D IRPhe MCNP model resulted in a 2D k-trasp of 1.03591 ± 0.00014. The HELIOS 2D k-transp was predicted to be 1.04120 at that time. Since then a typographical error by one azimuthal mesh (3.75^{o} of rotation) was found and corrected in the HELIOS model describing the OSCC critical position. The resulting HELIOS 2D k-transp is 1.03723.

Table 2.2 shows a breakdown of the 3D/2D modeling bias with MCNP. The bias was computed by the equation $\rho=(k_1-k_2)/(k_1\times k_2)$. Using this equation the reactivity worth of the 3D/2D effect is 3.3%. Also using this equation, the overall bias between the two codes and models is 0.12%. This level of bias is considered reasonable considering that the standard deviation in k-eff attributable to cross-section uncertainty aloe is 0.4789±0.0001% Δk/k (Aryaeinejad et al., 2010). This standard deviation was computed by a past study conducted by the Core Modeling Update Project in 2010 using the SCALE 44 group covariance data and the SCALE TSUNAMI code (Bowman, 2009).

Table 2.2 IRPhE benchmark, MCNP versus HELIOS modeling biases.

Case	k-eff	Stdev	% Bias
MCNP 3D	0.99935	0.00014	--
MCNP 2D	1.03591	0.00014	3.3%
HELIOS 2D	1.03723		0.12%

Fuel Element Powers. The Cycle 103A-2 power distribution test (Nuclear Test-3) was never included with the ICSBE/IRPhE Evaluations. NT-3 had 25 fission wires placed in all 40 of the ATR fuel elements (FE). Using the exposure data in the fission wires, the local fuel element power can be found, as will be described in more detail in Chapter 3 of this report. However, FE 16-19 gave inconsistent results compared with elements on the opposite side of the lobe. It was believed that the relative location of these outlier FEs to the ATR startup source (the small B-4 position) was the cause for the fission wire exposures to be erroneous. In the follow-up report for these tests, the authors considered FE 16-19 "compromised" and replaced this data with the element powers in position 12-15 assuming a symmetric lobe-power distribution across the south east lobe. Figure 2.22 shows the power distribution for NT-3 as predicted by the ATR HELIOS model. Also shown in the figure are the element powers calculated by PDQ at the time, along with the experimental results included in the Nuclear Test-3 follow-up report. Additionally, the results of an identical experiment performed in the ATRC 94-3 flux run, which was performed as part of these requalification tests, are shown.

In general there is good agreement between the HELIOS and PDQ calculations and the ATR and ATRC measurements. Note that this plot assumes FE 16-19 in ATR NT-3 have the same powers as the corresponding elements in the 12-15 positions, as mentioned before. The highest error between HELIOS and ATR NT-3 was FE 5. Coincidentally, this element shows the highest error value between the ATR NT-3 and the ATRC 94-3 flux run. The follow-up report assigns this error to a "difference in critical shim positions between the two reactors."

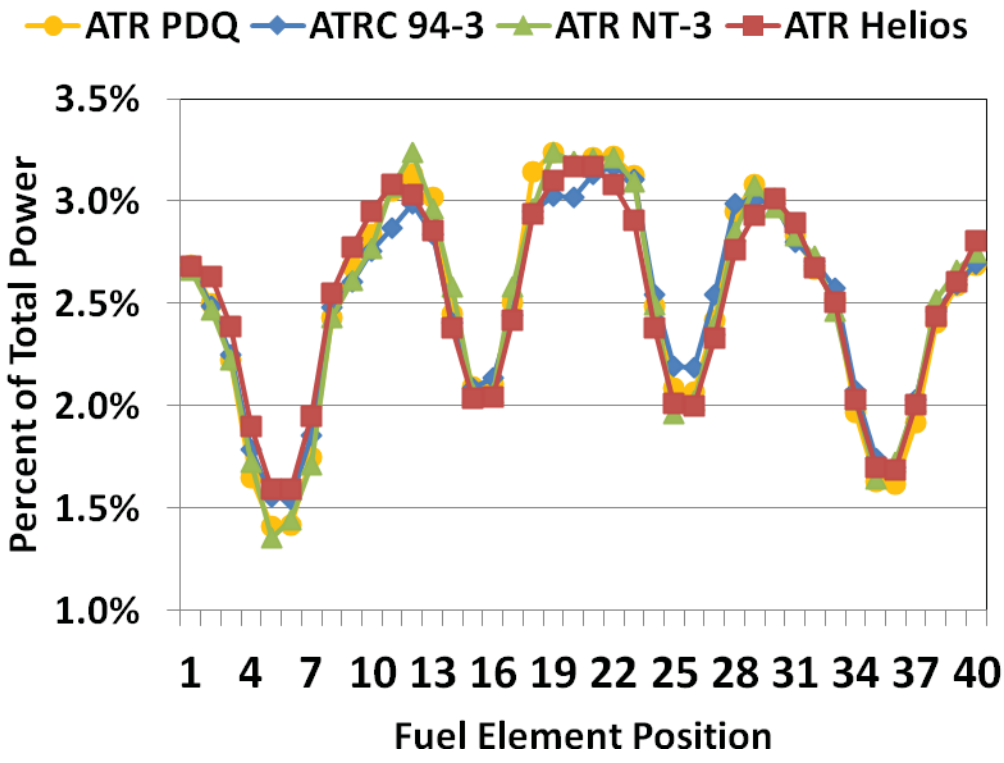

Figure 2.22 Nuclear requalification low power physics tests following the 1994 CIC including ATR (NT-3), the ATRC equivalent of NT-3 and the PDQ and HELIOS predictions of ATR (NT-3).

2.4.2 Cycle 145A to Cycle 151B As-Run Results

Core-Follow Methodology, Core follow (i.e., As-Run) calculations have been performed for cycles 145A through 151B (August 2009 to May 2012) using the HELIOS model. These core follow calculations serve two purposes. First, the As-Run cycles are being used to test the ATR model against the Reactor Data Acquisition System (RDAS) which is the computer system used by the ATR control room to collect total core power and lobe-power information. The RDAS lobe-power readout is computed from a least squares correlation of the N-16 readings from ten flow tubes throughout the ATR reflector (Mesina et al., 2002). RDAS reads the ion-chamber signal for each of these flow tubes and performs the least squares calculation. The N-16 is produced as a result of a $^{16}O(n,p)^{16}N$ reaction. N-16 decays by beta-gamma back into O-16 with a half life of 7.13 sec.

The coefficient matrix for the least squares correlation is generated as part of the nuclear requalification tests after every CIC. Also, an 11^{th} equation representing the total core power as measured by the ATR water power calculator is added to this system with a higher weight (lower covariance) assigned to it than is the case for the N-16 equations, thus ensuring that total power always agrees with the water power calculator instrumentation. The water power calculator is a system that uses the temperature rise between core inlet and outlet conditions to measure total enthalpy rise in the core.

The second purpose of the As-Run calculations is to generate a fuel database (i.e., end-of-cycle isotopic information stored in HERMES files for use in later cycles) going back to 2009. The HERMES file names are one of the data types stored in ATRFUE.csv and managed by THECPT. This effort will ultimately culminate in a composition file repository with a complete HELIOS pedigree; thus allowing future HELIOS core analysis to be performed completely independent of any information provided by the PDQ legacy code.

The only isotopes tracked explicitly in PDQ are U-235, U-236, U-238, Pu-239, Pu-240, Pu-241, B-10, I-135, Xe-135, Xe-135m, Nd-147, Pm-148, Pm-148m, Pm-149, and Sm-149 (Holm, 1978; Brown and Smith, 1990). The remaining fission products are combined into a lumped fission product which carries the same neutronic relevance as the combined miscellaneous fission products. By comparison, HELIOS tracks 350+ isotopes in total. Thus, the neutronic sink of the remaining fission products modeled by PDQ as a lumped fission product is not accounted for in the HELIOS initial As-Runs. However, following each As-Run cycle, more FEs of initial PDQ pedigree are replaced by fresh fuel. Hence, fewer FE compositions are of a PDQ pedigree with each successive cycle.

The general process for creating a HELIOS As-Run cycle consists of the following:

1. Acquire lobe-power, control configuration, and power level from the RDAS surveillance reports for every 1hr of operation.

2. Discretize the 1hr data into so many days in order to capture significant control or power changes throughout the cycle. Model all control maneuvers as “STATES” and build the depletion “PATH”.

3. Acquire PDQ isotopic data for all FE’s. These isotopics will be used when a pre-existing HERMES file is not available. Perform decay calculations for the in-Canal time for each FE. This requires 40 SFE input files to be created and run through HELIOS, thus the process is expedited using THECPT.

4. Acquire relevant experiment test plans and Navy “Letters” and create flux trap and capsule models as independent “SET” files. Only the nine flux traps have been modeled in great detail in the ATR HELIOS model thus far. As part of the center flux trap, the H-position cobalt, dummy, and reactivity shim capsules have been modeled in detail. The A, B, and I-positions were modeled with cobalt capsules, solid flow restrictors, plugs and dummies as appropriate for each individual position. Wherever possible the dimensions were taken

from drawings at the active-fuel mid-plane. The exception to this is where the dimensions of the experiment changed axially. However, in most of these circumstances the mid-plane (or an aggregate at multiple axial levels) gave an acceptable representation of the axial changes. Since HELIOS is a two-dimensional code, axial composition changes have to be homogenized into a single composition.

5. Determine depletable materials that should be tracked cycle to cycle. One important model detail worth tracking from one As-Run to the next is the depletion of the experiments. This is done via the DUMP and DBMAT operator to single experiment HERMES files. These HERMES files are not decayed as is done with the single fuel element files. Another important model detail to track from one As-Run to the next is the depletion of hafnium and cadmium shrouds and baskets. In particular, the cadmium baskets surrounding drop-in capsules for the AFCI program are generally replaced every two cycles since the depletion of these baskets is significant.

6. Run calculation and analyze results.

A list of flux trap and capsule facility geometry features currently available for the model is provided.

a. Advanced Fuel Cycle (AFC)-C,D,E capsules – Advanced fuel cycle fuels containing transuranics and uranium in either metallic or oxide form.

b. ATR Full Size Plate in Center Flux Trap (AFIP)-4,6,7 – Prototype experiment for low enriched uranium molybdenum based plate fuels. Note that the collar containing the H positions is also modeled with this experiment.

c. Advanced Graphite Creep (AGC)-1,2 – Instrumented Lead Experiment to study fuel performance of graphite based fuels.

d. Advanced Gas Reactor (AGR)-3/4 – Instrumented Lead Experiment to study material performance of graphite reactor materials.

e. East and South Irradiation Housing Assembly – Capsule facility for the East and South Flux Trap that provides 7 capsule positions. This facility fits within a Chopped Dummy In-Pile Tube (CDIPT). The CDIPT fits within the annular Safety Rod Assembly (SRA).

f. Center Irradiation Housing Assembly (CIHA) – Capsule facility for the Center Flux Trap that provides 7 capsule positions. Note that the collar containing the H positions is also modeled with this facility.

g. Gadolinium Production Capsule – Erbium targets for production of gadolinium for Pacific Northwest National Laboratory

h. Gas Fast Reactor (GFR) capsule – Advanced materials for Gas Fast Reactors

i. Large In-Pile Tube (LIPT) – Large pressurized water loop in the Northwest Flux trap representing Naval Reactors experiments, modeled with and without the Dual Holder, also has a model for the Backup.

j. LOOP2A – A Standard In-Pile Tube located in the center flux trap. Note that the collar containing the H positions is also modeled with this facility.

k. Multiple Irradiation Capsule Experiment (MICE) – A capsule irradiation facility for the Northeast Flux Trap that provides four experiment positions occupied by Naval Reactors experiments.

l. Maximum Useful Capacity Holder (MUCH) – A specialized in-pile tube with no flow tube.

m. National Scientific User Facility (NSUF) capsules: Capsule experiments supported by universities. Modeled experiments include University of Wisconsin Pilot Project, North Carolina State University Nano-structured Alloys, and Drexel MAX alloy nanolaminates.

n. Standard In-Pile Tube (SIPT) – A pressurized in-pile tube containing Naval Reactors experiments co-located within the annular safety rod assembly.

o. South Position Irradiation Capsule Experiment (SPICE) – A single capsule surrogate for the Multiple Irradiation Capsule Experiment

Critical Eigenvalue. Thirteen cycles of the ATR have been depleted using the above methodology. Figure 2.23 shows the transport eigenvalue for every core state of these depletions, including SCRAMs. In the figure, every red circle represents a HELIOS transport calculation that was performed. As can be seen in the k-eff trends, the model with no axial buckling correction to the calculated eigenvalue (shown as 'k-eff pure 2D') is consistently close to the transport solution critical eigenvalue (i.e., no axial buckling correction) reported by the 1994 CIC HELIOS model. HELIOS allows for an axial geometric buckling adjustment. It is not used in the transport solution algorithm but applied ad hoc to correct the multi-group spectrum used by the depletion algorithm. The ATR value of $Bg^2=5.33\times10^4$ corrects the neutron spectrum used by the depletion algorithm for axial leakage effects. This value is calculated from the standard approximation of axial geometric buckling $(\pi/H)^2$ where H is the height of the core (48 inches) plus an extrapolation distance of $0.71\lambda tr$. $\lambda^{tr} = 1/\Sigma^{tr}$ is calculated assuming an approximate value for the transport cross-section (Σ_{tr}) of $0.1cm^{-1}$. The Bg^2 corrected eigenvalues are indeed near 1.0 (shown as 'k-eff Bsq corrected' in Figure 2.23.

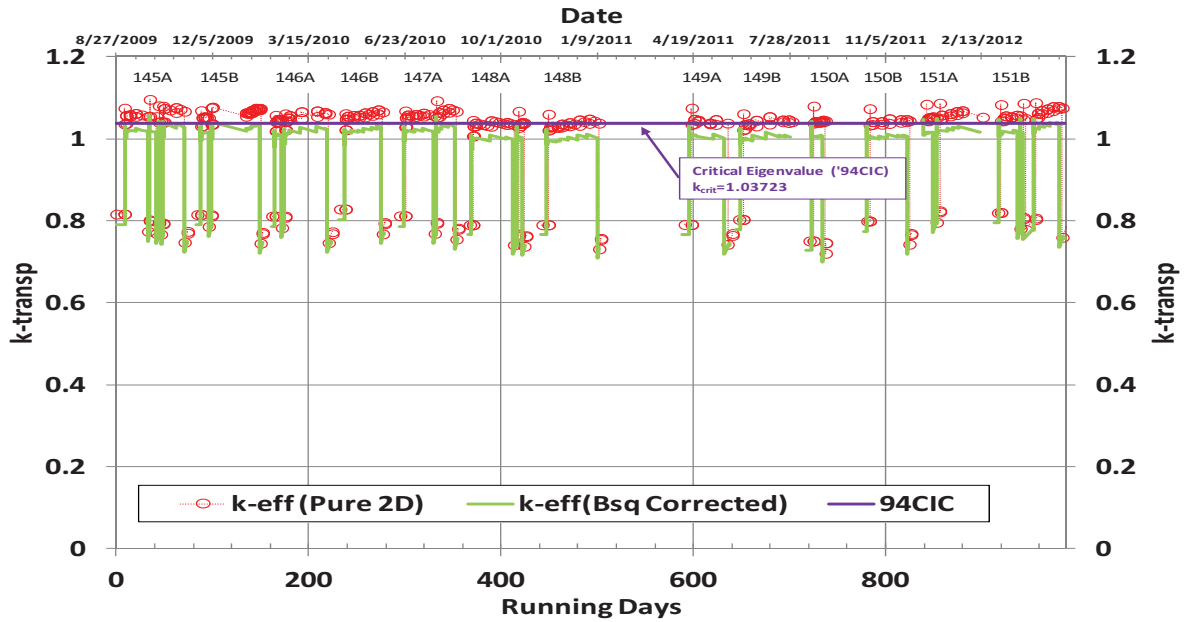

Figure 2.23 k-eff values as a function of calendar days for the ATR HELIOS As-Run calculations.

Lobe Power Comparison. Overall, the ATR HELIOS model has demonstrated remarkable *a priori* consistency with the RDAS reported data for lobe powers. A strip chart style plot for all of the 13 cycles comparing HELIOS against the RDAS data is provided in Figures 2.25-2.29. The interested reader is referred to Appendix B for a more detailed description of each of the 13 As-Run cycles.

As can be seen from the plots, there is an apparent bias between the ATR HELIOS model and RDAS upwards of 15% on occasion, particularly the Northeast Flux Trap. There are multiple possible causes for these differences, which do appear to be statistically significant. Likely the leading cause is a need to provide the exact mass loading of actinides in the core. At the time the As-Run calculations were performed, an approximate mass based on the 1994 CIC beginning of cycle fuel mass was used. HELIOS requires the specific power as opposed to total core power as an input for each core state. The mass discrepancy arises because the mass attributed by experiments was not accounted in the core loading. Also, the fuel actinide loading is assumed fresh when in reality much of the fuel loaded has been depleted in a previous cycle, thus decrementing their initial heavy metal mass. An error in the beginning of cycle initial heavy material loading can propagate into an error in total system power. However, the current version of the model has the ability to use HELIOS to compute the initial mass of the cycle before a detailed As-Run is performed.

Other possible causes for the differences may be lack of accurate experiment capsule descriptions in the A, B and I-positions. Also, the composition of Navy experiments is an approximation based upon the "Letters" communicated by Bettis Atomic Power Laboratory. For example, the exact composition and geometric description of the Medium Reactivity Worth (MRW) capsules in the MICE experiment could potentially alleviate some of the difference in the Northeast lobe as it was loaded in this lobe's flux trap for all but cycles 151A and 151B. Another possible source of systematic bias could be that the coefficient matrix used to correlate N-16 activation rates to lobe-powers may not be perfectly representative of the Cycle 145A to Cycle 151B core configurations.

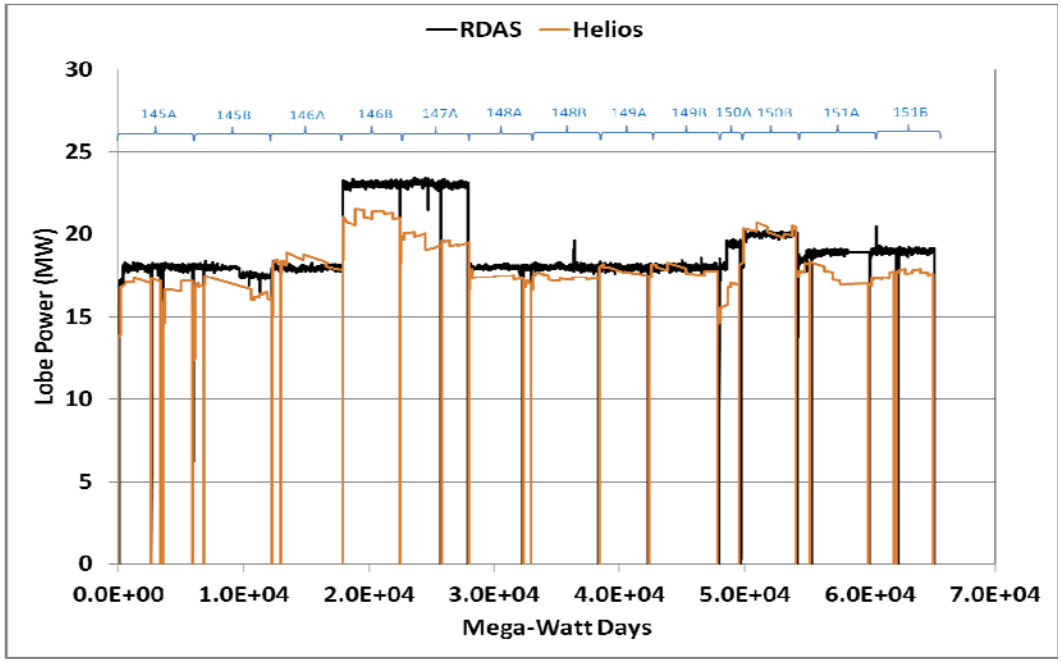

Figure 2.24 Northwest lobe power as a function of operating time expressed in megawatt-days.

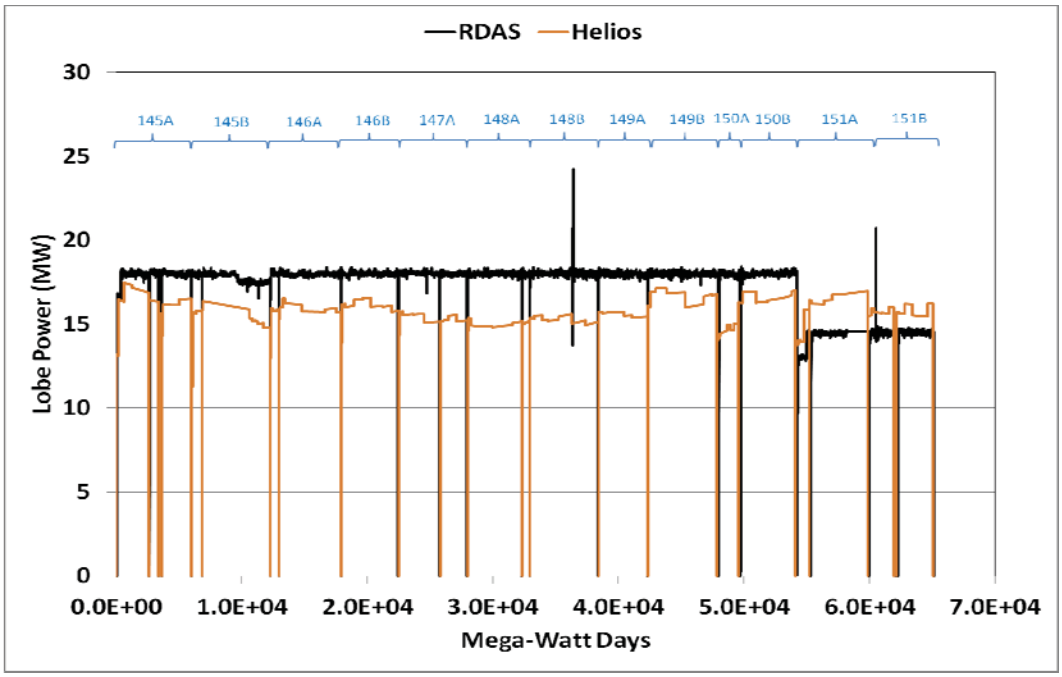

Figure 2.25 Northeast lobe power as a function of operating time expressed in megawatt-days.

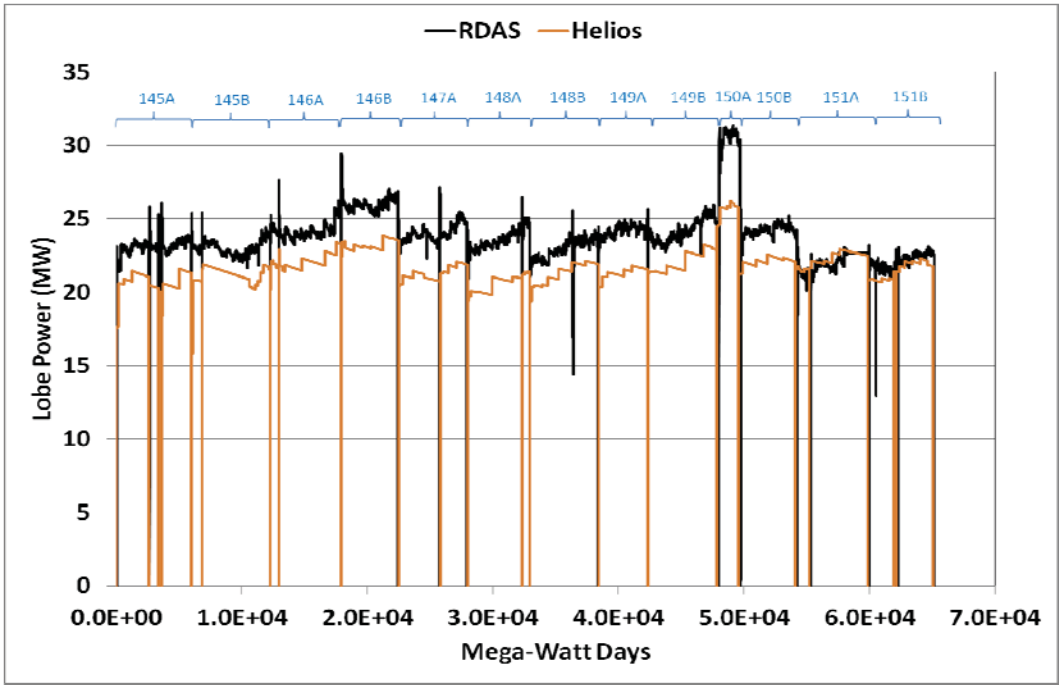

Figure 2.26 Center lobe power as a function of operating time expressed in megawatt-days.

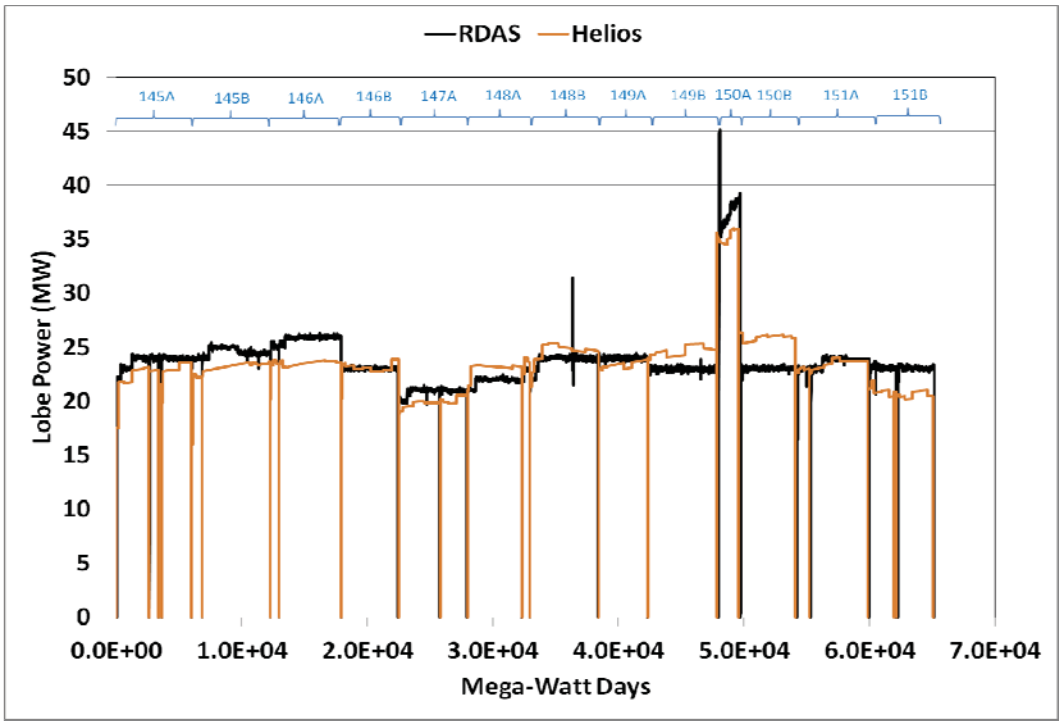

Figure 2.27 Southwest lobe power as a function of operating time expressed in megawatt-days.

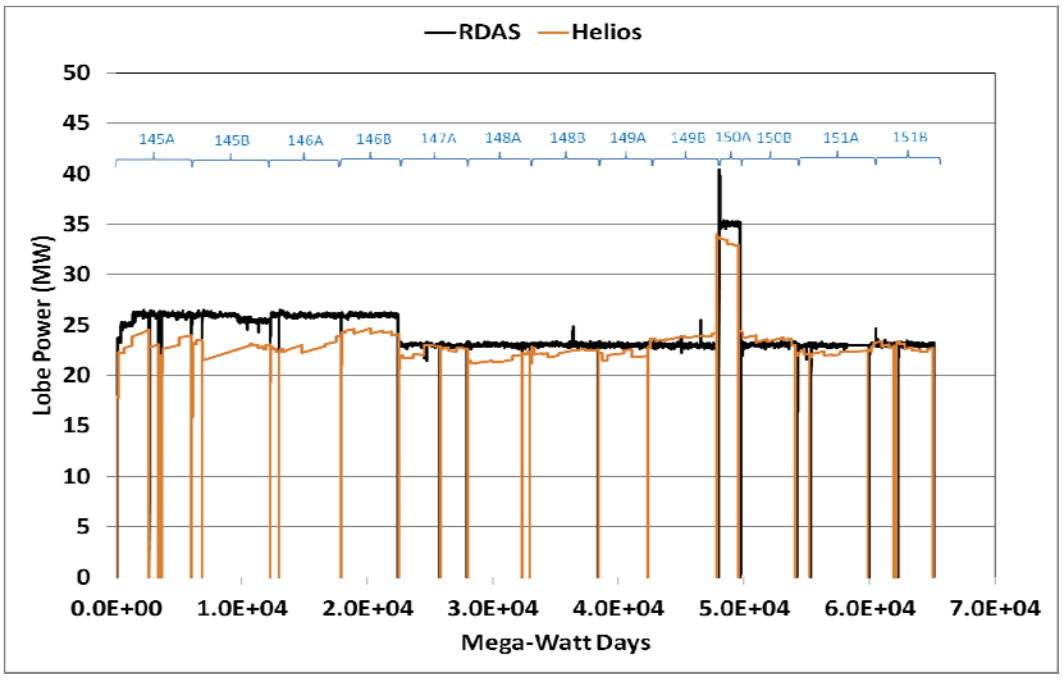

Figure 2.28 Southeast lobe power as a function of operating time expressed in megawatt days.

Fuel Element Depletion. A code-to-code verification was made between HELIOS and PDQ by following a fresh 7F fuel element (XA881T) through three cycles of irradiation (Cycles 148A, 149A, 150B). Fiugre Figure shows the atom density evolution as a function of exposure for U-235, U-236 and U-238. Figure Figure 2.29 shows the atom density evolution for Pu-239, Pu-240, Pu-241, Pu-242. As can be seen from the figures, there is good agreement between the two codes for the major fissile isotopes and less agreement between isotopes of very small concentration. HELIOS and PDQ isotopic results agree within 7% for U235 and Pu239 but worse for plutonium of fairly small concentrations (e.g., Pu-241). The error for the very small concentration isotopes can be attributed to computational differences in the two different depletion methods as well as machine precision to account for rounding error for very small numbers.

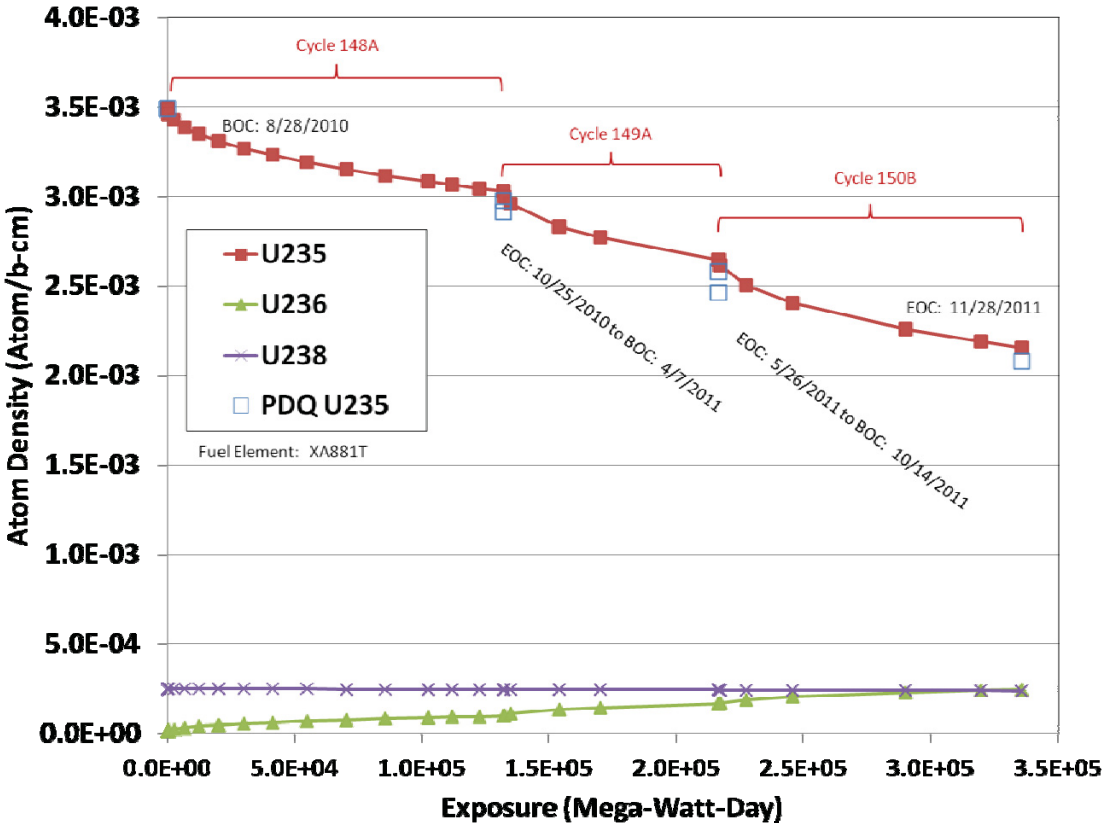

Figure 2.30 Isotopic depletion of uranium isotopes comparison between HELIOS and PDQ.

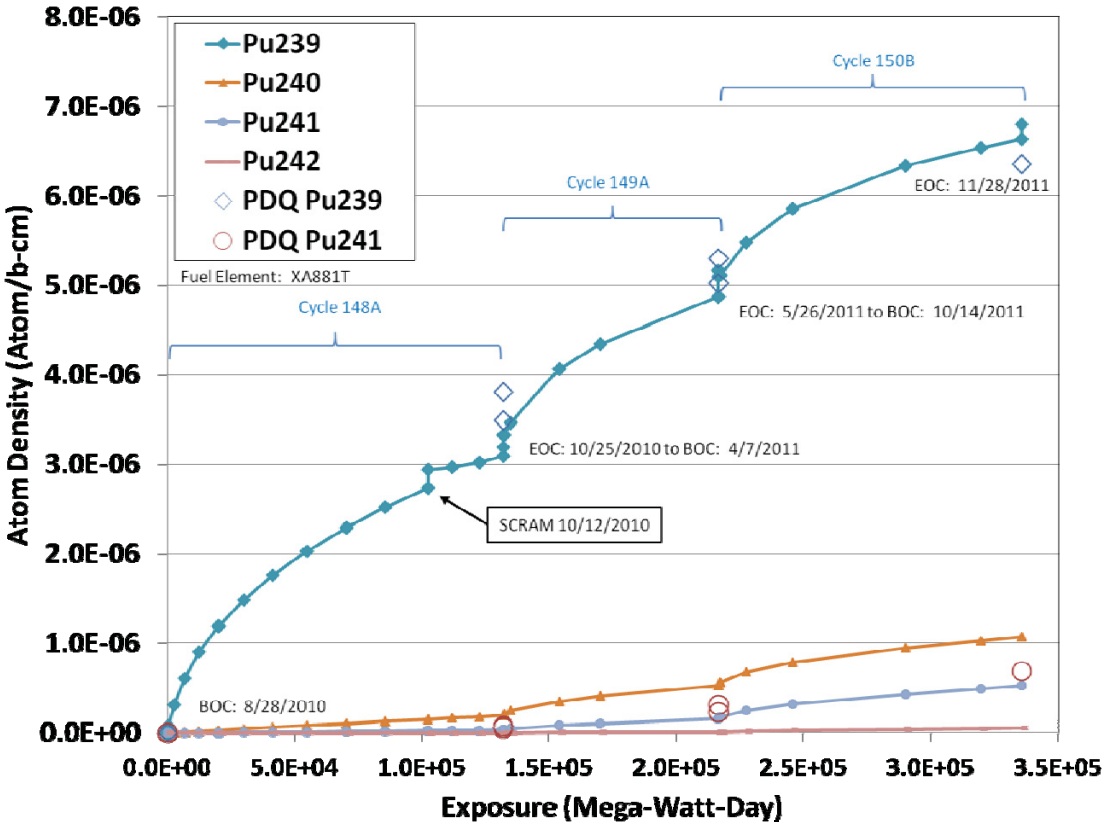

Figure 2.29 Isotopic depletion of plutonium isotopes comparison between HELIOS and PDQ.

2.5 Core Safety Analysis Package (CSAP) Modeling Support Capability

2.5.1 CSAP Description and History

Several different types of physics analyses have previously been identified to satisfy the ATR Updated Final Safety Analysis Report (UFSAR) requirements for each operational cycle. The analyses pertaining to the ATR core as a whole and specifically to the driver fuel are reported in the Core Safety Assurance Package (CSAP). Analyses pertaining to experiments are reported in corresponding documentation created for each experiment. Taken together, this documentation provides DOE with assurance that the UFSAR requirements are being met for each cycle.

A major component of the CSAP documentation consists of physics data produced by the existing suite of codes associated with the diffusion code PDQ. The current effort being undertaken is designed to replace the PDQ physics analysis methodology with an improved methodology capable of calculating and analyzing data that is ultimately reported in the CSAP documentation. Experience gained to date supports a decision that the methodology associated with the HELIOS code will be a suitable replacement for the PDQ methodology presently in place.

In order to completely replace the PDQ physics analysis methodology, the HELIOS code system needs to be capable of representing the neutronics of each ATR cycle. Specifically, the new methodology must be able to track and deplete the driver fuel elements, control surfaces, and beryllium reflector. Also, the total power of the ATR can vary over the course of a cycle, and this must be accommodated in the computations. Reactor physics data such as neutron flux and local fission power must also be available to

compare against component design criteria and predict component lifetimes that are dependent upon neutronic damage. From a practical perspective, the computer time requirements for all calculations defined in the CSAP protocol must also be compatible with the established time schedule for analyses required for a given cycle. The current status of these calculations and capabilities is presented in the sections below.

2.5.2 Power Calculations

Calculation of many of the UFSAR requirements is performed through the use of ZENITH, the postprocessor software used by HELIOS. Like AURORA (the HELIOS preprocessor code), the ZENITH input allows for embedded arithmetic expressions. Therefore, the developer can create formulae within the input file capable of providing virtually any nuclear physics-related output requested. It utilizes user-specified areas to call out unique regions in the ATR geometry. Thus, areas can be used to define individual fuel elements such that key calculations such as power generated within each element can be distinguished from other core components and provided in edits of the output. An example of the output currently generated by ZENITH for element powers is shown in Figure 2.30. Note that this particular example contains two exposure points only. Similar output is also available for power generated in each plate in the core. In support of hot stripe calculations, individual regions within each plate. These powers can also be printed to a file upon user request.

List name : RegPwr
List Title(s) 1) Powers (MW) for each element in core

	pow R-.-1-.-.	pow R-.-2-.-.
0001	1.1763E-06	1.1765E-06
0002	1.3239E-06	1.3234E-06
0003	1.4047E-06	1.4036E-06
0004	1.2602E-06	1.2589E-06
0005	1.1159E-06	1.1147E-06
0006	1.1237E-06	1.1225E-06
0007	1.2870E-06	1.2859E-06
0008	1.4448E-06	1.4439E-06
0009	1.3491E-06	1.3486E-06
0010	1.1769E-06	1.1773E-06
0011	1.2298E-06	1.2302E-06
0012	1.3659E-06	1.3658E-06
0013	1.4623E-06	1.4620E-06
0014	1.4305E-06	1.4302E-06
0015	1.3606E-06	1.3603E-06
0016	1.3638E-06	1.3637E-06
0017	1.4823E-06	1.4822E-06
0018	1.5523E-06	1.5523E-06
0019	1.4362E-06	1.4364E-06
0020	1.2843E-06	1.2850E-06
0021	1.2906E-06	1.2913E-06
0022	1.4441E-06	1.4445E-06
0023	1.5608E-06	1.5611E-06
0024	1.5097E-06	1.5101E-06
0025	1.3612E-06	1.3616E-06
0026	1.3761E-06	1.3765E-06
0027	1.4647E-06	1.4649E-06
0028	1.4635E-06	1.4637E-06
0029	1.3583E-06	1.3586E-06
0030	1.2159E-06	1.2166E-06
0031	1.1488E-06	1.1494E-06
0032	1.1675E-06	1.1674E-06
0033	1.2134E-06	1.2130E-06
0034	1.1099E-06	1.1093E-06
0035	1.0143E-06	1.0136E-06
0036	1.0075E-06	1.0068E-06
0037	1.1198E-06	1.1190E-06
0038	1.2036E-06	1.2029E-06
0039	1.1492E-06	1.1489E-06
0040	1.1531E-06	1.1534E-06

List name : LobePwr
List Title(s) 1) Maximum element powers (MW) for each lobe

	maxNW .-.-E-.-.	maxNE .-.-E-.-.	maxCtr .-.-E-.-.	maxSW .-.-E-.-.	maxSE .-.-E-.-.
0001	1.2134E-06	1.4448E-06	1.2906E-06	1.5608E-06	1.5523E-06
0002	1.2130E-06	1.4439E-06	1.2913E-06	1.5611E-06	1.5523E-06

Figure 2.30 ZENITH output of element powers as well as maximum element powers for each lobe by exposure point.

Figure 2.31 provides an example of the lobe power output currently provided by default from ZENITH. Note that the user is able to select whether these tables are presented in watts (for low power cycles) or in megawatts. The power generated in each of the eight elements in a lobe for each exposure point has been summed and placed within this table for each time step calculation specified within the short input file. In addition, the five lobe powers have also been summed and placed in this table. The total core power provided in this table also takes into account the power produced by fueled experiments in the ATR experiment positions. This is done by defining an area that encompasses the entire core and determining the power generated within that area. Thus, lobe power predictions can be obtained from these tables for each state of the core described by the short input deck.

List name : LobePwr
Labels Array : uburn
List Title(s) 1) Lobe powers (MW) - NW, NE, Center, SW, SE, Total

(R) Area/Face names : unlabeled
(I) Isotope Identifiers : unlabeled
(E) Path (State) idents : *
(G) Group name : unlabeled
(O) Originating Group : unlabeled

Label E	NWpow	NEpow	Ctrpow	SWpow	SEpow	ElementTotPow	TotalPower
0001 AsRun(stSD):0	0.00	0.00	0.00	0.00	0.00	0.00	0.00
0002 AsRun(stSD):0	0.00	0.00	0.00	0.00	0.00	0.00	0.00
0003 AsRun(stSD):0	0.00	0.00	0.00	0.00	0.00	0.00	0.00
0004 AsRun(st08):0	10.13	11.38	14.52	13.22	12.67	61.92	62.57
0005 AsRun(st08):0	10.16	11.37	14.49	13.22	12.68	61.91	62.57
0006 AsRun(st08):2613	10.26	11.30	14.55	13.20	12.60	61.91	62.57
0007 AsRun(st14):2613	17.65	21.91	23.36	22.41	23.61	108.94	109.99
0008 AsRun(st14):2613	17.65	21.88	23.41	22.41	23.59	108.93	109.99
0009 AsRun(st14):15249	18.01	21.53	23.34	22.57	23.48	108.93	109.99
0010 AsRun(st14):27886	18.00	21.27	23.16	22.79	23.72	108.94	109.99
0011 AsRun(st14):40522	17.89	21.05	22.98	23.00	24.02	108.94	109.99
0012 AsRun(st14):53159	17.78	20.85	22.80	23.19	24.33	108.94	109.99
0013 AsRun(st60):53159	18.71	20.67	23.95	22.65	22.94	108.92	109.99
0014 AsRun(st60):53159	18.71	20.67	23.95	22.65	22.94	108.92	109.99
0015 AsRun(st60):89017	18.49	20.33	23.39	23.09	23.62	108.92	109.99
0016 AsRun(st60):124874	18.33	20.11	22.86	23.44	24.20	108.93	109.99
0017 AsRun(st60):124874	18.35	20.15	22.72	23.48	24.26	108.95	109.99

Figure 2.31 ZENITH output of lobe powers as well as total power generated specifically by fuel elements and total core power (including power generated by experiments) by exposure point.

The accurate forecasting of the center lobe power is intimately tied to the accuracy of the model used to determine the lobe powers. The geometry construction within HELIOS is very flexible, so it is able to model the driver fuel elements and complex experiments in great detail. The code also utilizes material definitions, temperatures, and densities that can be easily overlaid on a complex geometry. Additional flux calculations than those used during preliminary cycle design can be used to reduce error. Thus, it is expected that HELIOS will be able to accurately model the center lobe power at any point in a cycle. The initial validation results demonstrate that HELIOS is capable of reasonably modeling center lobe power during initial startups, normal operation, and shutdowns.

It is apparent that the center lobe power is very sensitive to OSCC position, so precision in OSCC position likely leads to greater precision in center lobe power prediction. Due to the addition of analog rotation of the OSCC, it is possible to rotate the entire OSCC component to a precise position and thus increase the accuracy of center lobe power predictions. The use of analog rotation may be of particular

importance to the prediction of the center lobe power at startup, since peak center powers tend to be seen at this point in the cycle.

Some additional work related to power calculations has been identified. For instance, more detailed cycle modeling will be needed to evaluate and quantify the accuracy of center lobe power forecasting. Additional experiments will need to be modeled so that known errors in the model are decreased. Smaller time steps during restarts with very steep ramp rates will be needed to determine the peak center power that is predicted during these transient states. A comparison of the accuracy and bias associated with PDQ analyses and HELIOS analyses will provide valuable confidence that sufficient accuracy is provided by the HELIOS code. Finally, future work is expected to influence core state simplification such that lobe power identification work may be affected.

2.5.3 Isotopics Calculations

Driver Fuel Isotopics. The user-specified areas that define individual fuel elements during power generation are also used to determine the isotopic makeup associated with each element. The set of isotopes used by HELIOS presents a more complete picture of the makeup of materials, unlike PDQ which must use of a mock lumped fission product isotope to properly account for all of the neutronic effects experienced by the ATR core. HELIOS has an up-to-date isotopic library that has been adjusted specifically for use with the ATR reactor.

Stored isotopics of a fuel element are used to transfer the entire isotopic profile into depletion calculations that simulate decay of nuclides while the element is in the canal. After canal decay, the isotopics for the needed fuel elements are transferred to the cycle being analyzed. Post-processing of these isotopics is performed to determine the BOC and EOC fuel loadings associated with uranium, plutonium, and boron. This data is printed to a file so that experiment modeling outside of HELIOS is able to use appropriate fuel isotopics. It also transfers needed fuel processing information to the appropriate facility within the INL complex. The user can choose to list portions of these isotopics in a table. An example of an isotopic table, shown in

Figure 2.32, is used to confirm that the correct fuel loading is being modeled at the beginning of the cycle being analyzed.

List name : InitialLoading
List Title(s) 1) Initial Assembly and Core Loading

	U235MassBOC R-1-.-.-.	U238MassBOC R-1-.-.-.	B10MassBOC R-.-.-.-.
0001	7.8860E+02	7.5430E+01	6.4595E-02
0002	1.0844E+03	7.7856E+01	1.3261E-16
0003	1.0870E+03	7.8047E+01	1.3261E-16
0004	1.0320E+03	7.4094E+01	5.2297E-01
0005	8.8068E+02	7.2947E+01	1.5973E-01
0006	8.8630E+02	7.6234E+01	1.5440E-01
0007	1.0320E+03	7.4094E+01	5.2297E-01
0008	1.0870E+03	7.8047E+01	1.3261E-16
0009	1.0844E+03	7.7856E+01	1.3261E-16
0010	7.4233E+02	7.1581E+01	4.5198E-02
0011	8.1893E+02	7.2336E+01	9.6752E-02
0012	1.0844E+03	7.7856E+01	6.6747E-01
0013	1.0870E+03	7.8047E+01	6.6756E-01
0014	1.0851E+03	7.7911E+01	6.6642E-01
0015	1.0874E+03	7.8072E+01	6.7082E-01
0016	1.0342E+03	7.4253E+01	5.2730E-01
0017	1.0851E+03	7.7911E+01	6.6642E-01
0018	1.0870E+03	7.8047E+01	6.6756E-01
0019	1.0844E+03	7.7856E+01	6.6747E-01
0020	8.1285E+02	7.2261E+01	8.8339E-02
0021	8.2524E+02	7.2073E+01	1.0655E-01
0022	1.0844E+03	7.7856E+01	6.6747E-01
0023	1.0870E+03	7.8047E+01	6.6756E-01
0024	1.0851E+03	7.7911E+01	6.6642E-01
0025	8.9005E+02	7.6335E+01	1.5348E-01
0026	8.9066E+02	7.6126E+01	1.3261E-16
0027	1.0851E+03	7.7911E+01	6.6642E-01
0028	1.0870E+03	7.8047E+01	6.6756E-01
0029	1.0844E+03	7.7856E+01	6.6747E-01
0030	8.1552E+02	7.5624E+01	8.3730E-02
0031	7.6627E+02	7.1792E+01	6.2424E-02
0032	9.4569E+02	7.6607E+01	2.5715E-01
0033	9.1889E+02	7.6442E+01	1.9700E-01
0034	8.7039E+02	7.6026E+01	1.3302E-01
0035	8.8708E+02	7.6183E+01	1.5442E-01
0036	8.8522E+02	7.6039E+01	1.6264E-01
0037	9.1279E+02	7.6407E+01	1.8695E-01
0038	9.2290E+02	7.6501E+01	2.0470E-01
0039	9.2903E+02	7.6543E+01	2.1507E-01
0040	7.9073E+02	7.5421E+01	6.5527E-02

Figure 2.32 ZENITH output of BOC fuel loading for U-235, U-238, and B-10.

Control Surface Isotopics. Tracking of isotopics for the various control surfaces in the ATR core is complicated by the dependence upon the specific control surface of interest. The movement of control surfaces must be integrated into operation of the model, and thus influences how isotopics are tracked. Control surface movement is accomplished through the use of material overlays, density overlays, and/or geometry changes to the model. For instance, material overlays are used to simulate neck shim movement by filling the position with either absorbable material or aluminum.

Isotopic data for each neck shim absorber material can be stored and tracked so that the neck shims are appropriately depleted over their lifetime. To account for neck shim depletion that has occurred prior to HELIOS modeling and thus it has not been explicitly tracked by HELIOS, density overlays are used to artificially decrease the fresh material of a neck shim in proportion to the worth of the neck shims. Thus, this treatment does not include direct isotope tracking in the neck shims. In a similar manner to the density overlay treatment of the neck shims, the safety rods in the ATR core always use non-depleting material overlays which do not include direct isotope tracking. This treatment is due to the small fluence seen by these components. In other words, safety rods are fully withdrawn from the 2D HELIOS model for all but the shut down state; therefore there is little need to model their depletion. Regardless of the method used to rotate the OSCCs (i.e. the material overlay method or the geometry-changing analog rotation method), isotopics in the hafnium blade are not explicitly tracked. OSCC hafnium depletion may be the subject of future work.

Not only can ZENITH produce a table of depleted control compositions, it also uses isotopic compositions as a logical check to confirm the positions of both the OSCCs and neck shims. Area definitions are used to explicitly specify each of these control surfaces. The existence and/or location of regions containing hafnium isotopes are processed, and the results are output to the user.

Figure 2.33 contains an example of a table of neck shim positions presented to the user in a concise manner. Each neck shim is represented by a single number. The ability to use this form of representation is due to the discrete nature of the neck shim positions (i.e. either inserted or withdrawn).

Figure 2.34 is an example of a table containing each of the 16 OSCC positions. These positions are a precise representation of the positions being modeled. Note that slight differences occur between the positions input by the user and the positions that HELIOS is able to model using the overlay method, since the zero position of the OSCCs does not generally align with the azimuthal segmentation that is assumed by the overlay method. Note that the use of the OSCC position table with the analog rotation method has not currently been implemented in the model.

```
List name       : NeckShims
Labels Array    : uburn
List Title(s)  1) Neck Shim Positions by Time Step
               2) Position Number = Inserted, 0 = Withdrawn, -1 = Reg Rod

(R) Area/Face names     :   unlabeled
(I) Isotope Identifiers :   unlabeled
(E) Path (State) idents : *
(G) Group name          :   unlabeled
(O) Originating Group   :   unlabeled

                      NW NW NW NW NW NW -- NE NE NE NE NE NE -- SW SW SW SW SW SW -- SE SE SE SE SE SE
 0001 AsRun(stSD):0    1  2  3  4  5  6  0  1  2  3  4  5  6  0  1  2  3 -1  5  6  0  1  2  3 -1  5  6
 0002 AsRun(stSD):0    1  2  3  4  5  6     1  2  3  4  5  6     1  2  3 -1  5  6     1  2  3 -1  5  6
 0003 AsRun(stSD):0    1  2  3  4  5  6     1  2  3  4  5  6     1  2  3 -1  5  6     1  2  3 -1  5  6
 0004 AsRun(st08):0    1  2  3  4  5  6     1  2  3  4  5  6     1  2  3 -1  5  6     1  2  3 -1  5  6
 0005 AsRun(st08):0    1  2  3  4  5  6     1  2  3  4  5  6     1  2  3 -1  5  6     1  2  3 -1  5  6
 0006 AsRun(st08):2613 1  2  3  4  5  6     1  2  3  4  5  6     1  2  3 -1  5  6     1  2  3 -1  5  6
 0007 AsRun(st14):2613 1  2  3  4  5  6     1  2  3  0  0  0     1  2  3 -1  5  6     1  2  3 -1  0  0
 0008 AsRun(st14):2613 1  2  3  4  5  6     1  2  3  0  0  0     1  2  3 -1  5  6     1  2  3 -1  0  0
 0009 AsRun(st14):15249 1 2  3  4  5  6     1  2  3  0  0  0     1  2  3 -1  5  6     1  2  3 -1  0  0
 0010 AsRun(st14):27886 1 2  3  4  5  6     1  2  3  0  0  0     1  2  3 -1  5  6     1  2  3 -1  0  0
 0011 AsRun(st14):40522 1 2  3  4  5  6     1  2  3  0  0  0     1  2  3 -1  5  6     1  2  3 -1  0  0
 0012 AsRun(st14):53159 1 2  3  4  5  6     1  2  3  0  0  0     1  2  3 -1  5  6     1  2  3 -1  0  0
 0013 AsRun(st60):53159 1 2  3  0  0  0     0  0  0  0  0  0     1  0  0 -1  0  0     0  0  0 -1  0  0
 0014 AsRun(st60):53159 1 2  3  0  0  0     0  0  0  0  0  0     1  0  0 -1  0  0     0  0  0 -1  0  0
 0015 AsRun(st60):89017 1 2  3  0  0  0     0  0  0  0  0  0     1  0  0 -1  0  0     0  0  0 -1  0  0
 0016 AsRun(st60):124874 1 2 3  0  0  0     0  0  0  0  0  0     1  0  0 -1  0  0     0  0  0 -1  0  0
 0017 AsRun(st60):124874 1 2 3  0  0  0     0  0  0  0  0  0     1  0  0 -1  0  0     0  0  0 -1  0  0
```

Figure 2.33 ZENITH output of neck shim positions for each exposure point, where a zero represents a withdrawn neck shim.

List name : OSCCPositions
Labels Array : uburn
List Title(s) 1) Outer Shim Positions by Time Step
2) NW NE SW SE

(R) Area/Face names : unlabeled
(I) Isotope Identifiers : unlabeled
(E) Path (State) idents : *
(G) Group name : unlabeled
(O) Originating Group : unlabeled

Label E	N1position .-.-E-.-.	N2position .-.-E-.-.	N3position .-.-E-.-.	N4position .-.-E-.-.	E1position .-.-E-.-.	E2position .-.-E-.-.	E3position .-.-E-.-.	E4position .-.-E-.-.
0001 AsRun(stSD):0	-0.58	-0.72	-0.72	-0.58	-0.58	-0.72	-0.72	-0.58
0002 AsRun(stSD):0	-0.58	-0.72	-0.72	-0.58	-0.58	-0.72	-0.72	-0.58
0003 AsRun(stSD):0	-0.58	-0.72	-0.72	-0.58	-0.58	-0.72	-0.72	-0.58
0004 AsRun(st08):0	51.92	51.78	51.78	51.92	51.92	51.78	48.03	48.17
0005 AsRun(st08):0	51.92	51.78	51.78	51.92	51.92	51.78	48.03	48.17
0006 AsRun(st08):2613	51.92	51.78	51.78	51.92	51.92	51.78	48.03	48.17
0007 AsRun(st14):2613	89.42	89.28	93.03	93.17	93.17	93.03	89.28	89.42
0008 AsRun(st14):2613	89.42	89.28	93.03	93.17	93.17	93.03	89.28	89.42
0009 AsRun(st14):15249	89.42	89.28	93.03	93.17	93.17	93.03	89.28	89.42
0010 AsRun(st14):27886	89.42	89.28	93.03	93.17	93.17	93.03	89.28	89.42
0011 AsRun(st14):40522	89.42	89.28	93.03	93.17	93.17	93.03	89.28	89.42
0012 AsRun(st14):53159	89.42	89.28	93.03	93.17	93.17	93.03	89.28	89.42
0013 AsRun(st60):53159	115.67	115.53	115.53	115.67	115.67	115.53	104.28	104.42
0014 AsRun(st60):53159	115.67	115.53	115.53	115.67	115.67	115.53	104.28	104.42
0015 AsRun(st60):89017	115.67	115.53	115.53	115.67	115.67	115.53	104.28	104.42
0016 AsRun(st60):124874	115.67	115.53	115.53	115.67	115.67	115.53	104.28	104.42
0017 AsRun(st60):124874	115.67	115.53	115.53	115.67	115.67	115.53	104.28	104.42

Label E	S1position .-.-E-.-.	S2position .-.-E-.-.	S3position .-.-E-.-.	S4position .-.-E-.-.	W1position .-.-E-.-.	W2position .-.-E-.-.	W3position .-.-E-.-.	W4position .-.-E-.-.
0001 AsRun(stSD):0	-0.58	-0.72	-0.72	-0.58	-0.58	-0.72	-0.72	-0.58
0002 AsRun(stSD):0	-0.58	-0.72	-0.72	-0.58	-0.58	-0.72	-0.72	-0.58
0003 AsRun(stSD):0	-0.58	-0.72	-0.72	-0.58	-0.58	-0.72	-0.72	-0.58
0004 AsRun(st08):0	48.17	48.03	55.53	55.67	55.67	55.53	51.78	51.92
0005 AsRun(st08):0	48.17	48.03	55.53	55.67	55.67	55.53	51.78	51.92
0006 AsRun(st08):2613	48.17	48.03	55.53	55.67	55.67	55.53	51.78	51.92
0007 AsRun(st14):2613	89.42	89.28	93.03	93.17	93.17	93.03	89.28	89.42
0008 AsRun(st14):2613	89.42	89.28	93.03	93.17	93.17	93.03	89.28	89.42
0009 AsRun(st14):15249	89.42	89.28	93.03	93.17	93.17	93.03	89.28	89.42
0010 AsRun(st14):27886	89.42	89.28	93.03	93.17	93.17	93.03	89.28	89.42
0011 AsRun(st14):40522	89.42	89.28	93.03	93.17	93.17	93.03	89.28	89.42
0012 AsRun(st14):53159	89.42	89.28	93.03	93.17	93.17	93.03	89.28	89.42
0013 AsRun(st60):53159	104.42	104.28	104.28	104.42	104.42	104.28	115.53	115.67
0014 AsRun(st60):53159	104.42	104.28	104.28	104.42	104.42	104.28	115.53	115.67
0015 AsRun(st60):89017	104.42	104.28	104.28	104.42	104.42	104.28	115.53	115.67
0016 AsRun(st60):124874	104.42	104.28	104.28	104.42	104.42	104.28	115.53	115.67
0017 AsRun(st60):124874	104.42	104.28	104.28	104.42	104.42	104.28	115.53	115.67

Figure 2.34 ZENITH output of individual Outer Shim Control Cylinder positions in degrees.

Experiment Isotopics. Accurate isotope tracking in experiments is a possibility that is not a part of the PDQ-based methodology. Thus, the storage of experiment isotopic data in concert with the versatility of placement in the core enables capabilities that have not previously been explored. Isotopic storage similar to that of fuel has been implemented with a number of experiments, including the ability to track and appropriately apply experiment isotopics regardless of their core position or their exclusion from the core as various cycles are modeled. Areas have been defined for entire experiment positions (i.e. homogenized experiments) as well as specific components of an experiment (such as flux shaping baskets or test trains containing material coupons and holders). This experience also shows that directly modeling moveable experiments (and their effect on the driver fuel) may be possible.

Beryllium Reflector Isotopics. Although most of the depletion characteristics can be easily modeled by HELIOS, the poisoning of the beryllium reflector may be the exception. Currently, HELIOS does not support beryllium depletion. However, the major result of the beryllium depletion is a cumulative effect from the buildup of neutron poisons such as Li-6, B-10, He-3, H-3 within the blocks (see section 2.2.3). Since the buildup during a single cycle is minor, a tool independent of HELIOS can be used to update the material specifications, assuming an appropriate cycle and outage length is provided to the tool.

The solution to this problem is being explored through the use of the transmutation code MRTAU coupled to MCNP via a Python script. The depletion chain associated with the beryllium reflector has not yet been incorporated into the MRTAU input. However, promising results have been obtained when MCNP/MRTAU data has been compared with the As-Run and PIE analysis of the AFIP-3 experiment. . The details of these results are presented in Appendix A. However, PIE data specifically for beryllium materials has not yet been evaluated. The amount of available PIE data for irradiated beryllium is significantly less than for uranium and plutonium fuel. Therefore, it is likely that MCNP/MRTAU will need to be verified by comparing to PDQ/HARMONY but validated against the PIE of past ATR experiments over a range of flux intensity, fluence, neutron spectrum, etc.

Ultimately, MRTAU may not need to be coupled to MCNP for the purpose of supporting CSAP preparation. The main driving force for MCNP/MRTAU is to consistently verify and validate MRTAU over a range of isotope transmutation scenarios to gain confidence in the code. Ultimately, a direct HELIOS/MRTAU coupling may be possible assuming the (n,γ), (n,p), (n,α) reactions of Table 2.1 are consistently invariant of the level of beryllium burnup. The reason for this is that because HELIOS is historically a fuel depletion code, it does not discern (n,p), (n,α). Therefore for a HELIOS/MRTAU coupling, fluxes would have to be extracted from the appropriate beryllium areas and then applied to a MRTAU cross-section library for ATR beryllium. MCNP would be used to generate the necessary beryllium cross-sections.

Future Work. Additional work related to the functionality of isotopics calculations has been identified. For instance, the OSCC position calculations should be expanded to fully operate with analog rotation of the shims. Driver fuel requirements, such as those described in Appendix C, will need to be satisfied. Modeling of experiment movement needs to be explored and a practical methodology developed. A standard procedure to account for axial variation of experiments should be developed, if possible. The potential use of MRTAU should be further explored and a means of transferring the relevant data should also be developed.

Since HELIOS was originally a code for computation of cross-section data, microscopic and macroscopic cross sections for the defined areas can be retrieved from the output and likely will be useful for comparisons to experimental data, experiment backup comparisons, other program results, etc. Isotopic results from HELIOS should be compared to PIE data, experimental data (such as gamma measurements of driver fuel elements or component worth measurements), etc. to validate the depletion schemes used to model the ATR core. Verification of isotopic data through comparison to other codes should be performed as well. Thus, the accuracy of the model can be further confirmed.

Future work is expected to influence core state simplification such that identification of control surfaces may be affected. Significant improvements to the user experience can be made that could influence how positions are displayed to the user. For instance, a table of average OSCC positions for various groupings may be more informative during preliminary cycle design than a precise representation of each individual OSCC. Table display options can be developed to meet these expectations, as needed.

2.5.4 Iterative Fuel Cycle Design

Preliminary Cycle Design. Preliminary cycle design begins by providing the designer with parameters such as total core power, lobe powers, the intended cycle length, and any other parameters set due to experiment restrictions or operational constraints. Several factors lead to a successful cycle design. These factors include the ability to maintain criticality of each reactor state, confirmation that the cycle length can be met with the fuel loading selected, confirmation that control surface positions determined for each reactor state meet constraints, confirmation of total core power, the ability to obtain the desired lobe powers, and the ability to produce results in a reasonable amount of runtime such that multiple iterations can be performed.

Control surface positions can be confirmed as meeting design parameters and operational constraints for each exposure point via the post-processor output. Core and lobe powers can also be confirmed as meeting design parameters for each exposure point. However, lobe power is not a direct input into the case, so an iterative process is necessary to meet this requirement. A description of the iterative process and the data obtained from ZENITH that aids in the iteration are described below.

During the setup of each case, the user is able to modify the short input deck to specify each time step calculation. The current short input deck allows for individual OSCC position specification in degrees for each time step. The withdrawn neck shims are also individually specified for each time step. Total core power is indirectly specified for each time step, provided an appropriate initial heavy metal mass (MWD/MT) is specified as well. The time step length is also indirectly specified for each time step by providing the code with the core exposure relative to the core initial heavy-metal mass (MWD/MT) corresponding to the time at each time step.

ZENITH currently outputs the core initial heavy-metal mass through the use of the same area generating the total core power in

Figure 2.31. Thus, this output allows the user to fully specify each intended time step and receive corresponding lobe power data output. An example of the initial heavy-metal mass output is provided in Figure 2.35. Note that this example also contains the initial heavy-metal mass value for the fuel elements only.

```
List name      : InitialHM
List Title(s)  1) Initial Heavy-Metal Mass (MT): Total Core, Fuel Elements

          InitialMassAll InitialMassElement
              .-.-E-.-.         .-.-E-.-.
 0001       4.34721E-02       4.26933E-02
```

Figure 2.35 ZENITH output of total core initial heavy-metal mass as well as initial heavy-metal mass in the fuel elements only.

The HELIOS-based methodology is centered on core exposure at each time step relative to the initial heavy-metal mass. The PDQ-based methodology models each time step by directly using the number of days into a cycle the time step represents. Thus, a calculation to convert the exposure-based time step to the days into a cycle must be made. It was determined that the most appropriate definition of days would be that of Effective Full Power Days (EFPD).

The calculation of EFPD is dependent upon the average total core power experienced for the cycle designed. Note that the average total power, and thus EFPD, has no definition when only one time step is modeled. Figure 2.36 provides an example of the output provided for average cycle powers. Figure 2.37 provides an example of the output provided, by request, to compare EFPD to the exposure points used by HELIOS. Thus, a means to determine the number of days into a cycle each exposure point represents is available as the cycle is being designed.

```
List name      : avg
List Title(s)  1) Time-Averaged Cycle Powers (MW)
               2) NW, NE, Center, SW, SE, Total

             avgNW        avgNE        avgCtr        avgSW        avgSE avgElementTot     avgTotal
         .-.-E-.-.    .-.-E-.-.    .-.-E-.-.    .-.-E-.-.    .-.-E-.-.    .-.-E-.-.    .-.-E-.-.
 0001       17.946       20.270       22.787       22.793       23.537      107.333      108.381
```

Figure 2.36 ZENITH output of time-averaged power values derived from lobe powers, total element power, and total core power for each time step in design path.

List name : EFPD
Labels Array : uburn
List Title(s) 1) Core Exposures (MWD/MT) by Exposure Point

(R) Area/Face names : unlabeled
(I) Isotope Identifiers : unlabeled
(E) Path (State) idents : *
(G) Group name : unlabeled
(O) Originating Group : unlabeled

Label E	uburn	tburn	pburn	EFPD
0001 AsRun(st5D):0	0.000	0.001	0.000	0.000
0002 AsRun(st5D):0	0.000	0.001	0.000	0.000
0003 AsRun(st5D):0	0.000	0.001	0.000	0.000
0004 AsRun(st08):0	0.000	0.001	0.000	0.000
0005 AsRun(st08):0	0.000	0.003	0.002	0.000
0006 AsRun(st08):2613	2612.970	2612.975	2612.974	1.080
0007 AsRun(st14):2613	2612.970	2612.973	2612.974	1.080
0008 AsRun(st14):2613	2612.970	2612.976	2612.977	1.080
0009 AsRun(st14):15249	15249.476	15249.466	15249.467	6.302
0010 AsRun(st14):27886	27885.980	27885.986	27885.988	11.525
0011 AsRun(st14):40522	40522.484	40522.469	40522.469	16.747
0012 AsRun(st14):53159	53158.996	53159.000	53159.000	21.970
0013 AsRun(st60):53159	53158.996	53158.984	53159.000	21.970
0014 AsRun(st60):53159	53158.996	53158.988	53159.004	21.970
0015 AsRun(st60):89017	89016.703	89017.281	89017.297	36.790
0016 AsRun(st60):124874	124874.406	124857.477	124857.492	51.602
0017 AsRun(st60):124874	124874.406	124857.477	124857.492	51.602

Figure 2.37 ZENITH output of EFPD vs. exposure point and corresponding core exposure relative to the initial heavy-metal mass.

Figure 2.38 provides an example of the reactivity output currently provided by default from ZENITH. It includes the four defined eigenvalue parameters and the reactivity relative to critical in dollars. This table is used to ensure that control position predictions used during iterative design are able to maintain a critical state for each time step being modeled. This also ensures that sufficient fuel has been loaded into the core such that the desired cycle length can be met. Note that a minimum EOC excess reactivity limit must also be met to confirm that the fuel loading selected is appropriate.

List name : k
Labels Array : uburn
List Title(s) 1) Eigens and Reactivity ($) by Exposure Point

(R) Area/Face names : unlabeled
(I) Isotope Identifiers : unlabeled
(E) Path (State) idents : *
(G) Group name : unlabeled
(O) Originating Group : unlabeled

Label E	ktransp	kinputB	kinf	kinfcrit	Reactivity
0001 AsRun(st5D):0	0.826913476	0.801084280	0.826992452	0.830272675	-33.10775
0002 AsRun(st5D):0	0.827143669	0.801300168	0.827219427	0.830497682	-33.06290
0003 AsRun(st5D):0	0.827058017	0.801214874	0.827129781	0.830408454	-33.08062
0004 AsRun(st08):0	1.057749748	1.021133661	1.057662249	1.057335854	2.75950
0005 AsRun(st08):0	1.021114945	0.985846281	1.021014214	1.020932674	-1.91426
0006 AsRun(st08):2613	1.022271633	0.986939311	1.022163630	1.022074461	-1.76447
0007 AsRun(st14):2613	1.068650007	1.031448364	1.068449736	1.068495631	4.06527
0008 AsRun(st14):2613	1.065614581	1.028521061	1.065411091	1.065464020	3.69736
0009 AsRun(st14):15249	1.063339829	1.026289344	1.063143373	1.063171744	3.41546
0010 AsRun(st14):27886	1.059372544	1.022420645	1.059176564	1.059187531	2.92386
0011 AsRun(st14):40522	1.055988669	1.019118428	1.055796504	1.055789828	2.50130
0012 AsRun(st14):53159	1.052573562	1.015785098	1.052386403	1.052363396	2.07197
0013 AsRun(st60):53159	1.094252467	1.055540562	1.094030738	1.094253063	7.01575
0014 AsRun(st60):53159	1.094455838	1.055733323	1.094232321	1.094454527	7.03881
0015 AsRun(st60):89017	1.082234502	1.043839574	1.082026482	1.082144499	5.59978
0016 AsRun(st60):124874	1.067376018	1.029401422	1.067181826	1.067216516	3.80822
0017 AsRun(st60):124874	1.099194884	1.060030103	1.099018335	1.098938584	7.55074

Figure 2.38 ZENITH output of core eigenvalues (see above for definitions) and reactivity difference from criticality by exposure point.

An additional output option displays the lobe and element powers in the form of a map corresponding to the layout of the ATR core (see Figure 2.39 below). This provides the designer with a visual representation of how each core state distributes the core power for each exposure point. When combined with the neck shim and outer shim positions, a cycle design that distributes the core power appropriately around the core can be iteratively developed.

```
Map of Array   : MapPwr
Coordinates    : R-,-2-,-,

 Minimum=10   Maximum=115   X/Y=X/Y(Map)*1E-01   Value=Value(Map)*1E-07

     X= -297 -249 -200 -151 -102  -53   -4   43   92  141  190  239  288  336
   Y  +----+----+----+----+----+----+----+----+----+----+----+----+----+----++   Y
 317  |       10       11                             13       11        | 317
 295  |                                                                   | 295
 273  |                                                                   | 273
 251  | 10                  12                   14                  11  | 251
 229  |                                                                   | 229
 207  |            90                                        103          | 207
 186  |                                                                   | 186
 164  | 11                   11                 13                  13  | 164
 142  |                                                                   | 142
 120  |       12                        12       12                  14   | 120
  98  |                 12                                  13            |  98
  76  |                                                                   |  76
  54  |                                                                   |  54
  32  |                      11                   12                      |  32
  10  |                                                                   |  10
 -10  |                                     97                            | -10
 -32  |                      12                   12                      | -32
 -54  |                                                                   | -54
 -76  |                                                                   | -76
 -98  |                 14                                  14            | -98
-120  |       15                        13       13                  15   | -120
-142  |                                                                   | -142
-164  | 15                   14                 14                  14  | -164
-186  |                                                                   | -186
-207  |            115*                                      115          | -207
-229  |                                                                   | -229
-251  | 14                   16                   16                  14  | -251
-273  |                                                                   | -273
-295  |                                                                   | -295
-317  |       14       15                             15       14        | -317
   Y  +----+----+----+----+----+----+----+----+----+----+----+----+----+----++   Y
     X= -297 -249 -200 -151 -102  -53   -4   43   92  141  190  239  288  336
```

Figure 2.39 ZENITH output of element and lobe powers at a single exposure point displayed as a map corresponding to the layout of the ATR core.

Mesh Fidelity Options. It is expected that HELIOS calculations can be run on a modern computer in a very reasonable amount of time when compared to the full PDQ-based process currently in use. The mesh refinement studies discussed in Section 2.3.2 provide insight into the runtime expected for each time step determination performed during cycle design. Thus far, this insight has been used to provide the user with multiple options (as shown in Figure 2.40) so that runtime can be appropriately balanced against precision. Thus, preliminary iterations can be obtained relatively quickly by evaluating each case modeled using data from the ZENITH output.

```
! OSCC Meshing !
 ! &'OSCC-precise' = SET('geom/OSCCs/OSCCmesh.hrf'/)!
   &'OSCC-quick'   = SET('geom/OSCCs/OSCCmesh.hrf'/)
 ! &'OSCC-analog'  = SET('geom/OSCCs/OSCCmesh.hrf'/)!
```

Figure 2.40 Short Input OSCC Mesh Selection Options

Future Work. Significant improvements to the user experience can still be made. One such improvement that has been identified is the creation of a sample input deck that can serve as a template for cycle design

modeling. This template would allow the user to directly specify time steps in days, simplify calculations by specifying that fewer calculations are performed for each time step, and directly specify total core power such that the value can be easily used in multiple locations (specific power specification, core exposure specification, etc.) needed by the HELIOS code. Similar to the template proposed for cycle design modeling, a second template could be created that is specifically designed to predict the OSCC positions and lobe powers at reactor startup.

Reducing the number of iterations for cycle design is likely to be an area of concerted effort. The iterative process may be broadened such that multiple depletion paths covering several possible design variants can be explored during the same calculation. For long depletion paths, it may be advantageous for multiple depletion paths to be modeled in a distributed manner such that runtime is minimized (i.e. manually parallelized calculations). Previous work has been performed that provided the user with control surface position estimates in an effort to greatly decrease the number of iterations necessary to develop a cycle design [Peterson, 2010]. This work will need to be evaluated and integrated into the current effort, assuming the work is useful and appropriate for a large range of core designs and experiment loadings. Additional options to reduce runtime will also be explored.

Once a cycle design has been developed, branch calculations such as excess reactivity calculations, safety coefficient calculations, and safety scenario calculations are performed. HELIOS is capable of creating these branching calculations through the use of material, temperature, and density overlays. Preliminary work has begun for many of these branching calculations, but additional work is needed to develop an appropriate methodology for these calculations, research how these calculations are to be performed per the UFSAR, and determine why these calculations are performed.

Parallel calculations with the current PDQ methodology are planned for the near future, which will provide direct feedback from the current users. It is expected that additional direction will be revealed from these parallel calculation observations. For instance, additional OSCC mesh options may be developed based upon user experience to better meet the operational needs of cycle design. The reactor startup template can be used during the parallel calculations phase to evaluate the user experience, as well as prediction results against PDQ-based predictions and operational data. The parallel phase will also provide valuable data about the bias associated with the HELIOS model of ATR. Incorporating this bias into the methodology and updating the bias as new cycles are modeled or experimental data is provided will demonstrate significant strides in operational requirements, in addition to the UFSAR requirements that must be specifically addressed.

2.5.5 Fuel Element Information

The THECPT tool that has been created to track each element composition and place the pertinent information into a database was described previously. The file handle given to the HERMES file containing an element's composition includes the location along the ATR fuel serpentine, fuel element serial number, core cycle number and BOC or EOC state. To fully provide the CSAP and cycle designer with the needed information, additional fuel element information will need to be stored. One subset of this information includes restrictions and notes that aid in fuel shuffling, such as manufacturing restrictions, operational restrictions due to inspection results or physical unavailability, holds due to experimental data collection, UFSAR limit restrictions, etc.

Additional information is calculated by ZENITH and should also be stored with the data previously discussed. For instance, the cumulative fission density at specific locations of particular plates in an element must be tracked in order to comply with UFSAR requirements. Thus, fission density values at these points should be stored with the other needed element information. This data can then be passed as an input to ZENITH so that the fission density calculated for a specific cycle can be added to the previously stored data. Future work will calculate the fission density obtained during an analyzed cycle using ZENITH such that updated cumulative fission density can be loaded into the element information

system, as well as used to determine fission density buildup rates, maximum fission densities in an element, and whether an element can be used again based on UFSAR requirements.

Traditionally, the exposure of each element (in MWD) has not been directly tracked. However, a table containing this information (for the current cycle only) can now be requested by the user. An example of this table, calculated by combining the element powers, is shown in Figure 2.41. Future work may alter this table such that the element exposures displayed are cumulative values. This element exposure information is in contrast to the lobe exposure needed for hot stripe calculations. Lobe exposure is calculated in a similar manner to element exposure, except that lobe powers are used instead of element powers. These lobe exposure values are then applied to each element in that lobe. Like the fission density values, lobe exposures are tracked and a cumulative exposure is calculated. An example table of lobe exposures for each element is shown in Figure 2.42.

List name : ElementBurnup
List Title(s) 1) Element Exposures (MWD) Along Path

	MWD	MWD	MWD	MWD	MWD	MWD	MWD	MWD	MWD	MWD
	R-.-1-.-.	R-.-2-.-.	R-.-3-.-.	R-.-4-.-.	R-.-5-.-.	R-.-6-.-.	R-.-7-.-.	R-.-8-.-.	R-.-9-.-.	R-.-10-.-.
0001	0.0000E+00	0.0000E+00	0.0000E+00	0.0000E+00	0.0000E+00	8.6130E+01	8.6130E+01	8.6131E+01	2.7931E+03	9.2378E+03
0002	0.0000E+00	0.0000E+00	0.0000E+00	0.0000E+00	0.0000E+00	9.0224E+01	9.0224E+01	9.0225E+01	3.0725E+03	1.0203E+04
0003	0.0000E+00	0.0000E+00	0.0000E+00	0.0000E+00	0.0000E+00	8.0652E+01	8.0652E+01	8.0652E+01	2.7984E+03	9.3091E+03
0004	0.0000E+00	0.0000E+00	0.0000E+00	0.0000E+00	0.0000E+00	5.8014E+01	5.8014E+01	5.8014E+01	2.1803E+03	7.3226E+03
0005	0.0000E+00	0.0000E+00	0.0000E+00	0.0000E+00	0.0000E+00	4.3705E+01	4.3705E+01	4.3705E+01	1.8410E+03	6.2416E+03
0006	0.0000E+00	0.0000E+00	0.0000E+00	0.0000E+00	0.0000E+00	4.3861E+01	4.3861E+01	4.3861E+01	1.8532E+03	6.2855E+03
0007	0.0000E+00	0.0000E+00	0.0000E+00	0.0000E+00	0.0000E+00	5.8578E+01	5.8578E+01	5.8578E+01	2.2170E+03	7.4552E+03
0008	0.0000E+00	0.0000E+00	0.0000E+00	0.0000E+00	0.0000E+00	8.1810E+01	8.1810E+01	8.1810E+01	2.8704E+03	9.5676E+03
0009	0.0000E+00	0.0000E+00	0.0000E+00	0.0000E+00	0.0000E+00	9.0971E+01	9.0971E+01	9.0971E+01	3.1231E+03	1.0387E+04
0010	0.0000E+00	0.0000E+00	0.0000E+00	0.0000E+00	0.0000E+00	8.5132E+01	8.5132E+01	8.5132E+01	2.7879E+03	9.2336E+03
0011	0.0000E+00	0.0000E+00	0.0000E+00	0.0000E+00	0.0000E+00	8.8675E+01	8.8675E+01	8.8675E+01	2.8653E+03	9.5023E+03
0012	0.0000E+00	0.0000E+00	0.0000E+00	0.0000E+00	0.0000E+00	9.1208E+01	9.1208E+01	9.1208E+01	3.0880E+03	1.0338E+04
0013	0.0000E+00	0.0000E+00	0.0000E+00	0.0000E+00	0.0000E+00	8.3456E+01	8.3456E+01	8.3456E+01	2.9155E+03	9.8042E+03
0014	0.0000E+00	0.0000E+00	0.0000E+00	0.0000E+00	0.0000E+00	6.7516E+01	6.7516E+01	6.7516E+01	2.4916E+03	8.4367E+03
0015	0.0000E+00	0.0000E+00	0.0000E+00	0.0000E+00	0.0000E+00	5.7199E+01	5.7199E+01	5.7199E+01	2.2745E+03	7.7597E+03
0016	0.0000E+00	0.0000E+00	0.0000E+00	0.0000E+00	0.0000E+00	5.7026E+01	5.7026E+01	5.7026E+01	2.2647E+03	7.7243E+03
0017	0.0000E+00	0.0000E+00	0.0000E+00	0.0000E+00	0.0000E+00	6.9718E+01	6.9718E+01	6.9718E+01	2.5536E+03	8.6498E+03
0018	0.0000E+00	0.0000E+00	0.0000E+00	0.0000E+00	0.0000E+00	8.8754E+01	8.8754E+01	8.8755E+01	3.0497E+03	1.0258E+04
0019	0.0000E+00	0.0000E+00	0.0000E+00	0.0000E+00	0.0000E+00	9.6100E+01	9.6100E+01	9.6100E+01	3.2037E+03	1.0725E+04
0020	0.0000E+00	0.0000E+00	0.0000E+00	0.0000E+00	0.0000E+00	9.2811E+01	9.2811E+01	9.2811E+01	2.9468E+03	9.7734E+03
0021	0.0000E+00	0.0000E+00	0.0000E+00	0.0000E+00	0.0000E+00	9.3747E+01	9.3747E+01	9.3747E+01	2.9113E+03	9.6370E+03
0022	0.0000E+00	0.0000E+00	0.0000E+00	0.0000E+00	0.0000E+00	9.8049E+01	9.8049E+01	9.8049E+01	3.0575E+03	1.0169E+04
0023	0.0000E+00	0.0000E+00	0.0000E+00	0.0000E+00	0.0000E+00	9.1918E+01	9.1918E+01	9.1918E+01	3.0037E+03	1.0054E+04
0024	0.0000E+00	0.0000E+00	0.0000E+00	0.0000E+00	0.0000E+00	7.4713E+01	7.4713E+01	7.4713E+01	2.5623E+03	8.6249E+03
0025	0.0000E+00	0.0000E+00	0.0000E+00	0.0000E+00	0.0000E+00	6.0667E+01	6.0667E+01	6.0667E+01	2.2454E+03	7.6012E+03
0026	0.0000E+00	0.0000E+00	0.0000E+00	0.0000E+00	0.0000E+00	6.1208E+01	6.1208E+01	6.1208E+01	2.2607E+03	7.6424E+03
0027	0.0000E+00	0.0000E+00	0.0000E+00	0.0000E+00	0.0000E+00	7.3033E+01	7.3033E+01	7.3033E+01	2.4871E+03	8.3613E+03
0028	0.0000E+00	0.0000E+00	0.0000E+00	0.0000E+00	0.0000E+00	8.7187E+01	8.7187E+01	8.7187E+01	2.8145E+03	9.4017E+03
0029	0.0000E+00	0.0000E+00	0.0000E+00	0.0000E+00	0.0000E+00	9.3233E+01	9.3233E+01	9.3233E+01	2.8746E+03	9.5421E+03
0030	0.0000E+00	0.0000E+00	0.0000E+00	0.0000E+00	0.0000E+00	8.9294E+01	8.9294E+01	8.9294E+01	2.7281E+03	9.0064E+03
0031	0.0000E+00	0.0000E+00	0.0000E+00	0.0000E+00	0.0000E+00	8.4743E+01	8.4743E+01	8.4743E+01	2.5962E+03	8.5632E+03
0032	0.0000E+00	0.0000E+00	0.0000E+00	0.0000E+00	0.0000E+00	8.1439E+01	8.1439E+01	8.1439E+01	2.5405E+03	8.4161E+03
0033	0.0000E+00	0.0000E+00	0.0000E+00	0.0000E+00	0.0000E+00	7.1949E+01	7.1949E+01	7.1949E+01	2.3686E+03	7.8962E+03
0034	0.0000E+00	0.0000E+00	0.0000E+00	0.0000E+00	0.0000E+00	5.3430E+01	5.3430E+01	5.3430E+01	1.8812E+03	6.3172E+03
0035	0.0000E+00	0.0000E+00	0.0000E+00	0.0000E+00	0.0000E+00	4.3108E+01	4.3108E+01	4.3108E+01	1.6521E+03	5.5929E+03
0036	0.0000E+00	0.0000E+00	0.0000E+00	0.0000E+00	0.0000E+00	4.2852E+01	4.2852E+01	4.2852E+01	1.6478E+03	5.5791E+03
0037	0.0000E+00	0.0000E+00	0.0000E+00	0.0000E+00	0.0000E+00	5.3898E+01	5.3898E+01	5.3899E+01	1.9171E+03	6.4373E+03
0038	0.0000E+00	0.0000E+00	0.0000E+00	0.0000E+00	0.0000E+00	7.1130E+01	7.1130E+01	7.1130E+01	2.3865E+03	7.9527E+03
0039	0.0000E+00	0.0000E+00	0.0000E+00	0.0000E+00	0.0000E+00	7.9884E+01	7.9884E+01	7.9884E+01	2.5312E+03	8.3812E+03
0040	0.0000E+00	0.0000E+00	0.0000E+00	0.0000E+00	0.0000E+00	8.4825E+01	8.4825E+01	8.4825E+01	2.6527E+03	8.7517E+03

Figure 2.41 ZENITH output of driver fuel exposure during the current cycle for each exposure point.

To perform hot stripe calculations, data regarding the canal storage time immediately prior to a cycle should also be evaluated and recorded for each element. Specifically, axial correction factors used in the Effective Plate Power (EPP) definition use canal time catagories. Thus, the category number must be stored prior to executing the associated ZENITH calculations. Future work will automate the

categorization of the available elements and the transfer of this information to a ZENITH input deck. Given the computed HELIOS data for a cycle, ZENITH is able to categorize power states such that canal storage time received during unplanned outages are automatically evaluated and applied. ZENITH output of this categorization process is not currently available to the user. If this information is found to be useful during the parallel calculations phase, this output can be easily added.

List name : ElementLobeExposure
List Title(s) 1) Element Exposures by Lobe (MWD) Along Path

	LobeExposure R-.-1-.-.	LobeExposure R-.-2-.-.	LobeExposure R-.-3-.-.	LobeExposure R-.-4-.-.	LobeExposure R-.-5-.-.	LobeExposure R-.-6-.-.	LobeExposure R-.-7-.-.	LobeExposure R-.-8-.-.	LobeExposure R-.-9-.-.
0001	0.0000E+00	7.2985E-18	7.2985E-18	8.1238E-12	9.6789E-06	1.5711E+01	2.5224E+01	2.5276E+01	1.4708E+02
0002	0.0000E+00	8.5900E-18	8.5921E-18	6.3683E-12	7.5963E-06	1.2202E+01	2.3664E+01	2.3633E+01	1.3570E+02
0003	0.0000E+00	8.5900E-18	8.5921E-18	6.3683E-12	7.5963E-06	1.2202E+01	2.3664E+01	2.3633E+01	1.3570E+02
0004	0.0000E+00	8.5900E-18	8.5921E-18	6.3683E-12	7.5963E-06	1.2202E+01	2.3664E+01	2.3633E+01	1.3570E+02
0005	0.0000E+00	8.5900E-18	8.5921E-18	6.3683E-12	7.5963E-06	1.2202E+01	2.3664E+01	2.3633E+01	1.3570E+02
0006	0.0000E+00	8.5900E-18	8.5921E-18	6.3683E-12	7.5963E-06	1.2202E+01	2.3664E+01	2.3633E+01	1.3570E+02
0007	0.0000E+00	8.5900E-18	8.5921E-18	6.3683E-12	7.5963E-06	1.2202E+01	2.3664E+01	2.3633E+01	1.3570E+02
0008	0.0000E+00	8.5900E-18	8.5921E-18	6.3683E-12	7.5963E-06	1.2202E+01	2.3664E+01	2.3633E+01	1.3570E+02
0009	0.0000E+00	8.5900E-18	8.5921E-18	6.3683E-12	7.5963E-06	1.2202E+01	2.3664E+01	2.3633E+01	1.3570E+02
0010	0.0000E+00	7.2985E-18	7.2985E-18	8.1238E-12	9.6789E-06	1.5711E+01	2.5224E+01	2.5276E+01	1.4708E+02
0011	0.0000E+00	7.2985E-18	7.2985E-18	8.1238E-12	9.6789E-06	1.5711E+01	2.5224E+01	2.5276E+01	1.4708E+02
0012	0.0000E+00	3.1278E-18	3.1285E-18	7.0925E-12	8.4739E-06	1.3609E+01	2.5493E+01	2.5474E+01	1.4798E+02
0013	0.0000E+00	3.1278E-18	3.1285E-18	7.0925E-12	8.4739E-06	1.3609E+01	2.5493E+01	2.5474E+01	1.4798E+02
0014	0.0000E+00	3.1278E-18	3.1285E-18	7.0925E-12	8.4739E-06	1.3609E+01	2.5493E+01	2.5474E+01	1.4798E+02
0015	0.0000E+00	3.1278E-18	3.1285E-18	7.0925E-12	8.4739E-06	1.3609E+01	2.5493E+01	2.5474E+01	1.4798E+02
0016	0.0000E+00	3.1278E-18	3.1285E-18	7.0925E-12	8.4739E-06	1.3609E+01	2.5493E+01	2.5474E+01	1.4798E+02
0017	0.0000E+00	3.1278E-18	3.1285E-18	7.0925E-12	8.4739E-06	1.3609E+01	2.5493E+01	2.5474E+01	1.4798E+02
0018	0.0000E+00	3.1278E-18	3.1285E-18	7.0925E-12	8.4739E-06	1.3609E+01	2.5493E+01	2.5474E+01	1.4798E+02
0019	0.0000E+00	3.1278E-18	3.1285E-18	7.0925E-12	8.4739E-06	1.3609E+01	2.5493E+01	2.5474E+01	1.4798E+02
0020	0.0000E+00	7.2985E-18	7.2985E-18	8.1238E-12	9.6789E-06	1.5711E+01	2.5224E+01	2.5276E+01	1.4708E+02
0021	0.0000E+00	7.2985E-18	7.2985E-18	8.1238E-12	9.6789E-06	1.5711E+01	2.5224E+01	2.5276E+01	1.4708E+02
0022	0.0000E+00	2.9921E-18	2.9925E-18	7.3989E-12	8.8314E-06	1.4255E+01	2.4197E+01	2.4200E+01	1.4227E+02
0023	0.0000E+00	2.9921E-18	2.9925E-18	7.3989E-12	8.8314E-06	1.4255E+01	2.4197E+01	2.4200E+01	1.4227E+02
0024	0.0000E+00	2.9921E-18	2.9925E-18	7.3989E-12	8.8314E-06	1.4255E+01	2.4197E+01	2.4200E+01	1.4227E+02
0025	0.0000E+00	2.9921E-18	2.9925E-18	7.3989E-12	8.8314E-06	1.4255E+01	2.4197E+01	2.4200E+01	1.4227E+02
0026	0.0000E+00	2.9921E-18	2.9925E-18	7.3989E-12	8.8314E-06	1.4255E+01	2.4197E+01	2.4200E+01	1.4227E+02
0027	0.0000E+00	2.9921E-18	2.9925E-18	7.3989E-12	8.8314E-06	1.4255E+01	2.4197E+01	2.4200E+01	1.4227E+02
0028	0.0000E+00	2.9921E-18	2.9925E-18	7.3989E-12	8.8314E-06	1.4255E+01	2.4197E+01	2.4200E+01	1.4227E+02
0029	0.0000E+00	2.9921E-18	2.9925E-18	7.3989E-12	8.8314E-06	1.4255E+01	2.4197E+01	2.4200E+01	1.4227E+02
0030	0.0000E+00	7.2985E-18	7.2985E-18	8.1238E-12	9.6789E-06	1.5711E+01	2.5224E+01	2.5276E+01	1.4708E+02
0031	0.0000E+00	7.2985E-18	7.2985E-18	8.1238E-12	9.6789E-06	1.5711E+01	2.5224E+01	2.5276E+01	1.4708E+02
0032	0.0000E+00	6.9955E-18	6.9956E-18	5.6721E-12	6.7874E-06	1.1085E+01	1.9064E+01	1.9057E+01	1.1352E+02
0033	0.0000E+00	6.9955E-18	6.9956E-18	5.6721E-12	6.7874E-06	1.1085E+01	1.9064E+01	1.9057E+01	1.1352E+02
0034	0.0000E+00	6.9955E-18	6.9956E-18	5.6721E-12	6.7874E-06	1.1085E+01	1.9064E+01	1.9057E+01	1.1352E+02
0035	0.0000E+00	6.9955E-18	6.9956E-18	5.6721E-12	6.7874E-06	1.1085E+01	1.9064E+01	1.9057E+01	1.1352E+02
0036	0.0000E+00	6.9955E-18	6.9956E-18	5.6721E-12	6.7874E-06	1.1085E+01	1.9064E+01	1.9057E+01	1.1352E+02
0037	0.0000E+00	6.9955E-18	6.9956E-18	5.6721E-12	6.7874E-06	1.1085E+01	1.9064E+01	1.9057E+01	1.1352E+02
0038	0.0000E+00	6.9955E-18	6.9956E-18	5.6721E-12	6.7874E-06	1.1085E+01	1.9064E+01	1.9057E+01	1.1352E+02
0039	0.0000E+00	6.9955E-18	6.9956E-18	5.6721E-12	6.7874E-06	1.1085E+01	1.9064E+01	1.9057E+01	1.1352E+02
0040	0.0000E+00	7.2985E-18	7.2985E-18	8.1238E-12	9.6789E-06	1.5711E+01	2.5224E+01	2.5276E+01	1.4708E+02

Figure 2.42 ZENITH output of the exposure of the eight-element lobes for each exposure point and applied to each driver fuel element in that lobe.

2.5.6 Hot Stripe Calculations

A variety of calculations must be performed to properly address peak power concerns along the hot stripe of an element in the ATR core. Some of these calculations have been presented previously, such as the region powers and the canal storage time categorization discussed earlier. Other calculations, such as empirical corrections made to account for axial changes in the core, are under development and need to be evaluated as applicable or replaced with appropriate calculations. A brief discussion of the expected direction of these calculations has been provided in Appendix C.

The axial variations present in experiment test trains present a challenge to both HELIOS and the 2-D PDQ code currently used to perform cycle analyses. An approach similar to that used with PDQ could also be used in the HELIOS-based methodology. A model of the RZ plane was created in PDQ to represent a single lobe of the ATR core. The use of a HELIOS RZ model could allow the user to create a homogenized experiment representation that could be incorporated into the model of the XY plane.

Another solution to this problem may be through the use of an experiment model in the MCNP or ATTILA codes. Note that MCNP is already in use for neutronic analyses performed for the experiment. Further evaluations must be made before a path forward can be chosen.

The actual calculation of Effective Point Power (EPtP) and EPP used to provide the hot stripe analysis of an element also utilizes data such as the maximum lobe powers allowed by the CSAP, instrument error corrections for each of the lobes, plate restrictions for each element, and the conversion of region powers to power density. Future work will add components to the model that have not yet been added, evaluate how the necessary information will be obtained, evaluate the region precision needed to properly calculate these values, and combine these aspects to produce values that can be compared against UFSAR limits.

2.5.7 Additional ATR Physics Calculations

HELIOS provides the capabilities to calculate many parameters that have not previously been computationally analyzed. Experimental measurements of these physical characteristics of the core have been used in the past to estimate parameters such as those listed in Figure 2.43 and Figure 2.44. The ability to calculate parameters such as delayed neutron fraction (β_{eff}), neutron lifetime (λ), fuel temperature coefficient, moderator temperature coefficient, and flux trap void worth allows additional validation against parameters provided by UFSAR calculations. These parameters also expand the possible methodology changes that could be made utilizing the HELIOS code. Additional parameters such as these could be calculated as the need arises during methodology creation or the parallel calculations phase of this project.

List name : List
List Title(s) 1) Beta-effective

	uburn	beff	beff	beff	beff	beff	beff
	.-.-E-.-.	1-.-E-1-.	1-.-E-2-.	1-.-E-3-.	1-.-E-4-.	1-.-E-5-.	1-.-E-6-.
0001	0	1.8415E-04	9.5924E-04	9.2968E-04	2.6487E-03	7.6984E-04	2.7193E-04
0002	0	1.8418E-04	9.5939E-04	9.2982E-04	2.6491E-03	7.6996E-04	2.7197E-04
0003	0	1.8417E-04	9.5933E-04	9.2977E-04	2.6489E-03	7.6991E-04	2.7195E-04
0004	0	2.1025E-04	1.0950E-03	1.0613E-03	3.0237E-03	8.7872E-04	3.1044E-04
0005	0	2.0650E-04	1.0755E-03	1.0424E-03	2.9639E-03	8.6309E-04	3.0491E-04
0006	2613	2.0663E-04	1.0761E-03	1.0430E-03	2.9717E-03	8.6362E-04	3.0510E-04
0007	2613	2.1096E-04	1.0987E-03	1.0649E-03	3.0340E-03	8.8169E-04	3.1150E-04
0008	2613	2.1067E-04	1.0971E-03	1.0634E-03	3.0297E-03	8.8046E-04	3.1106E-04
0009	15249	2.1043E-04	1.0959E-03	1.0622E-03	3.0263E-03	8.7946E-04	3.1069E-04
0010	27886	2.1000E-04	1.0938E-03	1.0601E-03	3.0200E-03	8.7765E-04	3.1003E-04
0011	40522	2.0962E-04	1.0919E-03	1.0582E-03	3.0145E-03	8.7607E-04	3.0946E-04
0012	53159	2.0924E-04	1.0901E-03	1.0563E-03	3.0090E-03	8.7448E-04	3.0887E-04
0013	53159	2.1322E-04	1.1108E-03	1.0764E-03	3.0662E-03	8.9110E-04	3.1474E-04
0014	53159	2.1324E-04	1.1109E-03	1.0765E-03	3.0665E-03	8.9118E-04	3.1477E-04
0015	89017	2.1195E-04	1.1045E-03	1.0701E-03	3.0479E-03	8.8582E-04	3.1282E-04
0016	124874	2.1040E-04	1.0968E-03	1.0624E-03	3.0256E-03	8.7939E-04	3.1049E-04
0017	124874	2.1337E-04	1.1122E-03	1.0773E-03	3.0681E-03	8.9174E-04	3.1485E-04

List name : List
List Title(s) 1) Lambda-effective

	uburn	lambda	lambda	lambda	lambda	lambda	lambda
	.-.-E-.-.	.-.-E-1-.	.-.-E-2-.	.-.-E-3-.	.-.-E-4-.	.-.-E-5-.	.-.-E-6-.
0001	0	1.3520E-01	5.8345E-02	1.3110E-01	7.6913E-02	9.3058E-02	2.4092E-01
0002	0	1.3551E-01	5.8244E-02	1.3080E-01	7.6903E-02	9.3140E-02	2.4143E-01
0003	0	1.3536E-01	5.8291E-02	1.3094E-01	7.6908E-02	9.3103E-02	2.4119E-01
0004	0	1.2265E-01	5.9822E-02	1.3892E-01	7.9541E-02	9.3621E-02	2.2798E-01
0005	0	1.2322E-01	5.9928E-02	1.3889E-01	7.9290E-02	9.3335E-02	2.2806E-01
0006	2613	1.2333E-01	6.0054E-02	1.3910E-01	7.9178E-02	9.3128E-02	2.2775E-01
0007	2613	1.1984E-01	6.1089E-02	1.4263E-01	7.9684E-02	9.2540E-02	2.2217E-01
0008	2613	1.1994E-01	6.1070E-02	1.4255E-01	7.9661E-02	9.2541E-02	2.2230E-01
0009	15249	1.2072E-01	6.2657E-02	1.4536E-01	7.8456E-02	9.0236E-02	2.1835E-01
0010	27886	1.2185E-01	6.4434E-02	1.4836E-01	7.7066E-02	8.7769E-02	2.1436E-01
0011	40522	1.2283E-01	6.5946E-02	1.5088E-01	7.5910E-02	8.5796E-02	2.1117E-01
0012	53159	1.2363E-01	6.7177E-02	1.5291E-01	7.4993E-02	8.4274E-02	2.0870E-01
0013	53159	1.2520E-01	6.6121E-02	1.5017E-01	7.5094E-02	8.5152E-02	2.1242E-01
0014	53159	1.2520E-01	6.6121E-02	1.5017E-01	7.5095E-02	8.5152E-02	2.1242E-01
0015	89017	1.2647E-01	6.8194E-02	1.5360E-01	7.3610E-02	8.2700E-02	2.0827E-01
0016	124874	1.2712E-01	6.9370E-02	1.5555E-01	7.2819E-02	8.1407E-02	2.0601E-01
0017	124874	1.2701E-01	6.9725E-02	1.5627E-01	7.2673E-02	8.1077E-02	2.0514E-01

Figure 2.43 ZENITH output of the six delayed-group beta-effectives and lambda-effectives obtained at each exposure point.

List name : List
List Title(s) 1) Avg. neutron lifetime, inverse velocity

	uburn	life	life	invvel	invvel	bsq	dif	dif	ab	ab
	.-.-E-.-.	.-.-E-1-.	.-.-E-2-.	1-1-E-1-.	1-1-E-2-.	.-.-E-.-.	1-.-E-1-.	1-.-E-2-.	1-.-E-1-.	1-.-E-2-.
0001	0	-8.1777E-02	1.6638E+01	1.3639E-04	2.6222E-01	-3.0032E-03	4.8241E-01	2.4688E+00	-2.1899E-04	2.3174E-02
0002	0	-8.1914E-02	1.6628E+01	1.3639E-04	2.6223E-01	-2.9987E-03	4.8236E-01	2.4687E+00	-2.1855E-04	2.3173E-02
0003	0	-8.1866E-02	1.6629E+01	1.3639E-04	2.6220E-01	-3.0005E-03	4.8238E-01	2.4686E+00	-2.1863E-04	2.3174E-02
0004	0	1.9260E+00	1.3045E+01	1.3644E-04	2.7694E-01	8.5426E-04	4.6480E-01	2.3393E+00	-3.2622E-04	1.9231E-02
0005	0	-7.5545E-01	1.3768E+01	1.3647E-04	2.7716E-01	3.1519E-04	4.6704E-01	2.3392E+00	-3.2784E-04	1.9393E-02
0006	2613	-7.8955E-01	1.3768E+01	1.3646E-04	2.7748E-01	3.3217E-04	4.6687E-01	2.3410E+00	-3.2792E-04	1.9376E-02
0007	2613	2.4822E+00	1.4465E+01	1.3647E-04	2.9730E-01	1.0083E-03	4.6932E-01	2.3892E+00	-4.1824E-04	1.8144E-02
0008	2613	3.8548E+00	1.4526E+01	1.3647E-04	2.9727E-01	9.6449E-04	4.6941E-01	2.3889E+00	-4.1734E-04	1.8161E-02
0009	15249	1.0482E+01	1.4692E+01	1.3647E-04	2.9878E-01	9.3049E-04	4.6963E-01	2.3943E+00	-4.2397E-04	1.8109E-02
0010	27886	-6.4282E+00	1.4898E+01	1.3647E-04	3.0027E-01	8.7197E-04	4.6999E-01	2.3994E+00	-4.3105E-04	1.8063E-02
0011	40522	-2.6616E+00	1.5093E+01	1.3647E-04	3.0176E-01	8.2199E-04	4.7030E-01	2.4045E+00	-4.3786E-04	1.8017E-02
0012	53159	-1.6753E+00	1.5294E+01	1.3647E-04	3.0327E-01	7.7154E-04	4.7062E-01	2.4096E+00	-4.4456E-04	1.7970E-02
0013	53159	7.1469E-01	1.5220E+01	1.3643E-04	3.1324E-01	1.3535E-03	4.6720E-01	2.4154E+00	-4.4147E-04	1.7311E-02
0014	53159	7.0998E-01	1.5216E+01	1.3643E-04	3.1324E-01	1.3563E-03	4.6719E-01	2.4154E+00	-4.4149E-04	1.7310E-02
0015	89017	1.4825E+00	1.5852E+01	1.3643E-04	3.1780E-01	1.1806E-03	4.6830E-01	2.4311E+00	-4.6085E-04	1.7178E-02
0016	124874	-5.4113E+00	1.6607E+01	1.3643E-04	3.2256E-01	9.6764E-04	4.6953E-01	2.4477E+00	-4.7955E-04	1.7054E-02
0017	124874	7.6078E-01	1.5834E+01	1.3642E-04	3.2255E-01	1.4110E-03	4.6797E-01	2.4490E+00	-4.8101E-04	1.6915E-02

Figure 2.44 ZENITH output of the two-group average neutron lifetime, 1/v absorber cross section, material buckling, diffusion ratio, and absorption cross section at each exposure point over the whole core.

Additional ATR physics calculations have been incorporated into the current output options. For instance, fuel temperature coefficient, moderator temperature coefficient, and flux trap void worth calculations have been simplified such that these calculations can be performed for every cycle, if requested. A table can also be requested that states the power as seen from the outer flux trap positions as well. This information has been calculated previously, but the calculation was done separate from the calculations needed to complete the CSAP. The inclusion of a table such as the one shown in

Figure 2.45 as an option in the ZENITH output allows this data to be proactively distributed to experiment analysts and operational personnel charged with evaluating the lifetime of various core components.

List name : SourcePwr
Labels Array : uburn
List Title(s) 1) Source powers (MW) - N, E, S, W

(R) Area/Face names : unlabeled
(I) Isotope Identifiers : unlabeled
(E) Path (State) idents : *
(G) Group name : unlabeled
(O) Originating Group : unlabeled

	Label E	Npow	Epow	Spow	Wpow
		.-.-E-.-.	.-.-E-.-.	.-.-E-.-.	.-.-E-.-.
0001	AsRun(stSD):0	0.00	0.00	0.00	0.00
0002	AsRun(stSD):0	0.00	0.00	0.00	0.00
0003	AsRun(stSD):0	0.00	0.00	0.00	0.00
0004	AsRun(st08):0	12.01	12.86	13.47	12.62
0005	AsRun(st08):0	12.00	12.85	13.46	12.62
0006	AsRun(st08):2613	12.04	12.82	13.45	12.67
0007	AsRun(st14):2613	20.97	22.96	23.12	21.14
0008	AsRun(st14):2613	20.98	22.96	23.13	21.15
0009	AsRun(st14):15249	20.96	22.78	23.13	21.31
0010	AsRun(st14):27886	20.81	22.72	23.22	21.32
0011	AsRun(st14):40522	20.64	22.68	23.33	21.29
0012	AsRun(st14):53159	20.48	22.66	23.44	21.25
0013	AsRun(st60):53159	21.11	22.52	23.18	21.77
0014	AsRun(st60):53159	21.11	22.52	23.18	21.77
0015	AsRun(st60):89017	20.74	22.45	23.37	21.66
0016	AsRun(st60):124874	20.43	22.39	23.50	21.54
0017	AsRun(st60):124874	20.40	22.37	23.49	21.51

Figure 2.45 ZENITH output of the powers seen by the outer flux traps at each exposure point.

Another example of useful information, not related to CSAP preparation, that could be proactively distributed to experiment analysts is the flux multiplier in various capsule positions in the ATR reflector (e.g., the large B position). A flux multiplier calculation would be a branch case at a burn step specified by the experiment analyst that models the predicted flux in a capsule if the OSCC's were drawn out past their nominal hot full power position in order to recover from a SCRAM. Generally, this situation results in an over-power condition in large B positions due to their local reactivity worth being strongly controlled by their close proximity to the OSCC's. This over-power is localized to the capsule and not the fuel and could result in the experiment being damaged.

2.5.8. Summary of Current Status

Although the framework for a replacement CSAP methodology based on the HELIOS system has now been laid, there are details that remain to be thoroughly investigated and incorporated over the remaining two years of the ATR Methods Update project, as the HELIOS model is run in parallel with the PDQ methodology and experience is gained. The methodology to create the needed data is under development. Production and storage of the output from the system is also underway. Sufficient progress has been made to the replacement methodology that the parallel calculations phase can now begin. It can be expected that additional areas of development will be discovered during this phase. However, the current status represents significant progress toward the replacement of the PDQ-based neutronics analysis and offers substantial demonstration that HELIOS will be able to completely replace the current system.

2.6 References

Alfonsi, Andrea, et al., PHISICS Toolkit: Multi-Reactor Transmutation Analysis Utility- MRTAU. Knoxville : American Nuclear Society, 2012.

R. Aryaeinejad, D. Crawford, M. DeHart, G. Griffith, B. Gross, D. Lucas, J. Nielsen, D. Nigg, J. Navarro, J. Parry, J. Peterson, K. Steuhm, "Advanced Test Reactor Core Modeling Update Project – Annual Report for Fiscal Year 2010," Idaho National Laboratory, INL/EXT-10-19940, (September 2010).

S. Bays, B. Curnutt, E. Swain, D. Nigg, "ATR Fuel and Experiment Change-out Methodology and Models using HELIOS, Idaho National Laboratory, ECAR-1769, (December 2011).

S. Bowman (Ed.), SCALE: A Modular Code System for Performing Standardized Computer Analyses for Licensing Evaluation, Oak Ridge National Laboratory, ORNL/TM-2005/39, Version 6, Vols. I–III, January 2009. Available from Radiation Safety Information Computational Center at Oak Ridge National Laboratory as CCC-750.

R. Breen, O. Marlowe, C. Pfeifer, "HARMONY: System for Nuclear Reactor Depletion Computation," Idaho National Laboratory, WAPD-TM-478, (January 1965).

A. Brown, A. Smith, "ATR CSA Physics Model Description and Calculation Guide," Idaho National Laboratory, NRRT-N-90-011, p.p. 2-39 (April 1990).

W. Cadwell, "PDQ-7 Reference Manual," Idaho National Laboratory, WAPD-TM-678, (January 1967).

M. Holm, “Lumped Fission Product Cross Sections for the ATR CSAP PDQ Model,” Idaho National Laboratory, RE-P-78-016, (February 1978).

SS. Kim, B. Schnitzler, M. Neely, R. Lell, D. Lee, “Advanced Test Reactor: Serpentine Arrangement of Highly Enriched Water-Moderated,” OECD/NEA, HEU-MET-THERM-022, (2005).

Lillo, Misti A. and Chang, Gray S. As- Run Neutronic Analysis for the AFIP-3 Experiment Irradiated in the Center Flux Trap of the ATR, Cycles 143B and 144A. Idaho Falls : INL, 2011. ECAR-1441

G. Marchuk, “A Survey of Nuclear-reactor Design Methods,” Atommaya Energiya Vol. 11, No. 4, pp. 356-369, 1961.

G. Mesina, T. Jensen, R. McCracken, S. Smith, “LPCIS N-16 Lobe Power Calculation, Theory and Programming,” Idaho National Laboratory, TRA-ATR-1821, (2002).

D. Nigg, K. Steuhm, “Advanced Test Reactor Core Modeling Update Project – Annual Report for Fiscal Year 2011,” Idaho National Laboratory, INL/EXT-11-23348, (September 2011).

J. Peterson, “The Utilization of Perturbation Theory for the Automation of the Advanced Test Reactor Startup Shim Rotation Prediction,” Ph.D. Dissertation, University of Texas, Austin, Texas, (2011).

Polkinghorne, R. Ambrosek, R. Bennett, J. Durney, “ATR-SINDA and SINDA-SAMPLE Calculations for Chapter 15 of the ATR’s Updated FSAR,” Idaho National Laboratory, TRA-ATR-840, (1994).
Robinson, Adam B. AFIP-3 Post-Irradiation Examination Summary Report. Idaho Falls : INL, 2011. INL/LTD-11-22367.

A. Smith, W. Yoon, D. Auslander, W. Cook, “Reactivity Effect of Beryllium Reflector Poison in the ATR,” Idaho National Laboratory, NRRT-N-90-021, (1990).

R. Stamm’ler and M. Abbate, “Methods of Steady-State Reactor Physics in Nuclear Design,” Academic Press, London, (1983).

Studsvik Scandpower, “HELIOS Methods (Version-2.0),” Studsvik Scandpower, (March 2009).

E. Swain, J. Shatford, “Development of a Computer Model of the RERTR Full-size Element,” Idaho National Laboratory, ECAR-1148, (2011).

V. Vladimirov, “Ph.D. Dissertation,” Stecklova Mathematics Institute, USSR. Quoted by Marchuk 1961, (1959)

X-5 Monte Carlo Team. MCNP- A General Monte Carlo N-Particle Transport Code, Version 5. s.l. : Los Alamos National Laboratory, 2008. LA-UR-03-1987.

3.0 VALIDATION PROTOCOL DEVELOPMENT AND DEMONSTRATION

David W. Nigg, Joseph W. Nielsen, James R. Parry, William F. Skerjanc, Samuel E. Bays, Mark .D. DeHart, D.Scott Lucas

Validation protocols for the various computational ATR physics models are primarily based on neutron activation spectrometry in the near term. Additional validation capabilities using post-irradiation burnup measurements for selected fuel elements as described in Section 5 are anticipated in the longer term as well. Some basic equipment for activation experiments in the ATRC Northwest Large In-Pile Tube (NW LIPT) and in the surrounding NW Lobe core fuel elements as well as in the diametrically opposite SE Lobe fuel elements, was fabricated during FY-2010. Initial scoping measurements to determine neutron flux spectra in these regions were completed during FY-2011. Corresponding fuel element fission power distribution measurements throughout the ATRC core were also completed using standard ATRC protocols. There have been four LEP-specific ATRC validation experiments so far. Complete statistical analyses for all four are presented here, along with initial analysis of some additional measurements made during FY-2012 in the ATRC to support a "depressurized" ATR cycle (152A) that was conducted late in the year. These latter measurements were unanticipated at the beginning of FY-2012, but they provided some additional useful validation data for the overall protocol. Furthermore, one example of a numerical verification procedure used for the HELIOS code, a key part of the overall code suite for ATR, is also provided.

Over the course of the ATR Core Modeling Update Project neutron spectrum measurements in the smaller flux traps and additional measurements in the core fuel elements are also planned. The necessary additional equipment was fabricated and assembled during FY-2012 to enable activation measurements within the southeast flux trap during 2013 and beyond. Ultimately, a complete set of experimental apparatus and associated standard validation measurement protocols using neutron activation spectrometry will be available for future code and model validation measurements as needed in both the ATRC and, when feasible, in the ATR itself. The work described here builds on previous related INL experience at the ATR (e.g. Rogers and Anderl, 1995) as well as at other research reactor and accelerator facilities worldwide (e.g. Nigg et al., 2000). It is also intended that detailed Evaluated Benchmarks based on these measurements will ultimately be published for use by the international community under the auspices of the Organization for Economic Cooperation and Development (OECD, 2012).

3.1 Theoretical Background

Neutron activation spectrometry is based on the fact that different chemical elements (and different isotopes of the same element) placed in a neutron field will exhibit distinctively different neutron capture and scatter interaction spectra. Some elements are primarily sensitive to capture of thermal neutrons. Others have strong, well separated, capture resonances in the epithermal energy range, while others have energy thresholds for inelastic scatter, secondary neutron and charged particle emission, and fission, below which essentially no interactions occur. If the neutron interaction product for a particular nuclide is radioactive, then the induced radioactivity of a sample of that nuclide placed in a neutron field will be largely proportional to the neutron flux at energies where interactions are most likely to occur in the sample. If different materials having different sensitivities to neutrons as functions of energy are activated in the same field, it is ultimately possible to reconstruct a "measured" neutron spectrum from measurements of the induced activities. The level of spectral detail that can be reliably obtained generally corresponds to the number of different materials, and different interactions in the same materials, that are available.

3.1.1 Basic Physics.

As an example to illustrate the underlying physics of activation spectrometry, Figure 3.1 shows the capture cross section for ^{197}Au, which has a relatively high thermal neutron capture component as well as a prominent capture resonance at about 5 electron volts (eV). Capture of neutrons in a small sample (typically a foil or wire) of ^{197}Au produces ^{198}Au, which undergoes beta decay with emission of a prominent 411 keV gamma ray. The intensity of this gamma ray is proportional to the neutron capture rate, which is largely proportional to the flux of neutrons at thermal energies and at 5eV. If the sample is placed inside a cover made of cadmium, which suppresses essentially all thermal neutron interactions, then the interaction rate of the gold sample will be proportional only to the neutron flux above thermal energies, primarily at 5 eV where the resonance occurs. The thermal and above-thermal neutron fluxes can then be separated by converting the measured induced activities to saturation activities (i.e. activation rates per atom), subtracting the activation rate of the cadmium-covered sample from that of the bare sample, and computing the corresponding thermal-neutron and total neutron fluxes. This is the classic "Cadmium Difference" method and in effect it enables the inference of a two-energy group (thermal and above-thermal) neutron spectrum. Elemental gold also exhibits several very useful and convenient threshold interactions for secondary neutron emission. These include (n,2n) up through (n,6n), extending up to about 60 MeV (Nigg et al., 2000).

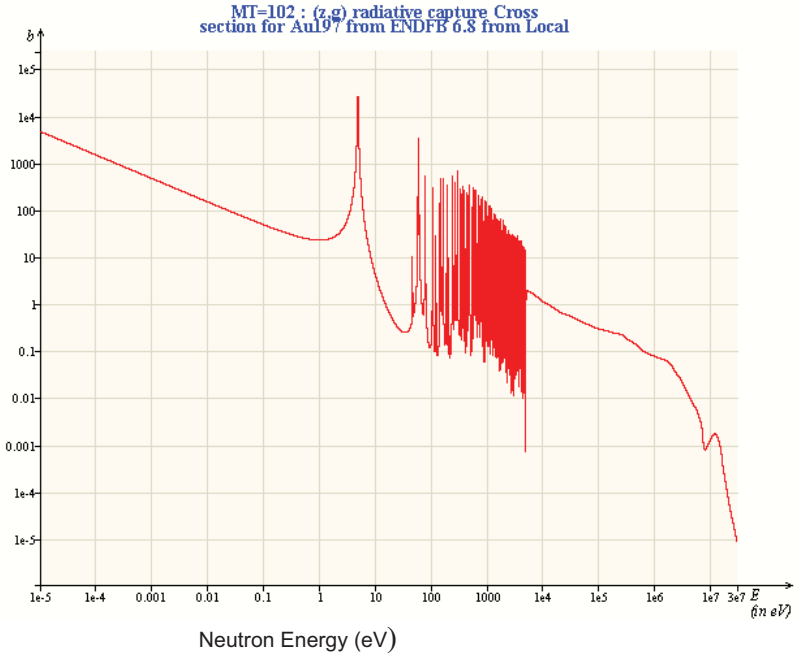

Figure 3.1. Capture cross section (barns) of ^{198}Au. (Source: OECD Janis 2.1)

As another example, cross section data for ^{115}In are shown in Figure 3.2. This nuclide (96% abundance in natural indium) captures thermal neutrons and it also has a strong neutron capture resonance at about 1 eV. In both cases neutron capture produces radioactive ^{116}In, which emits three prominent gamma rays with energies of 416, 1097, and 1293 keV. In addition, it will form an isomer by inelastic scatter of neutrons having energies above about 400 keV. This yields ^{115m}In, which decays back to the ground state by emission of a 336 keV gamma ray. Hence the inelastic scatter rate (and thus the neutron flux above

the 400 keV threshold) is proportional to the measured activity of the 336 keV gamma ray while the activities of the other three gamma rays, which are associated with a different half-life since they are emitted by a different radionuclide (^{116}In), are largely proportional to the neutron flux at thermal energies and at 1 eV. If an indium foil is covered with cadmium, the thermal neutron capture rate is suppressed as described previously for gold. As a result, this single nuclide can be used to obtain information in three different energy ranges of the neutron spectrum under examination.

In the general case, a number of different activation responses (typically at least 8-12) are measured using a variety of nuclides having different sensitivities to neutrons in the thermal, epithermal, and fast energy ranges. This permits the reconstruction of additional spectral detail in the data analysis process. Duplicate and even triplicate foils and wires composed of the same material are also often included to improve statistics in energy ranges of particular interest. Materials found useful for ATRC applications include gold and indium as described above as well as tungsten, manganese, cobalt, copper, and scandium for thermal and epithermal neutron measurements, and several other materials having threshold interactions for fast-neutron measurements, as will be described later.

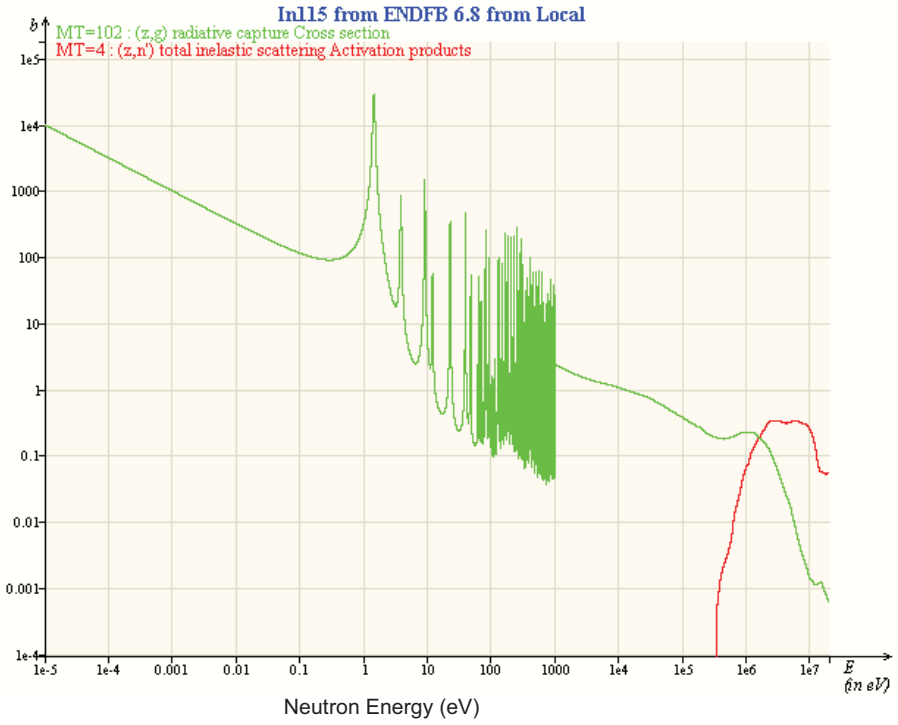

Figure 3.2. Capture (Green) and inelastic scatter (Red) cross sections (barns) of ^{115}In. (Source: OECD Janis 2.1)

3.1.2. General Mathematical Formulation.

We now consider some essential mathematical details of neutron activation spectrometry as specifically applied to the ATR and ATRC in the present work. Although the term "foil or wire" is used here for the dosimeters used to make activation measurements, the method is equally-applicable to any other type of dosimeter, with or without an associated spectral modification shield, for which the neutron response

parameters needed to compute the associated elements of the sensitivity matrices described below can be accurately determined in some manner.

In the following narrative, matrix and vector quantities will generally be indicated by **bold** typeface. In some cases, matrices and vectors will be enclosed in square brackets for clarity. The superscripts, "**-1**" and "**T**" respectively, indicate matrix inversion and transposition.

In general, the volume-average activation rate per atom for a foil or wire dosimeter placed in a neutron flux field may be calculated as:

$$R = \int_0^\infty \sigma_d(E)\, \Psi_d(E)\, dE \tag{1}$$

where $\sigma_d(E)$ is the microscopic activation cross section of interest for the dosimeter material as a function of neutron energy, and $\psi_d(E)$ is the volume-average scalar neutron flux existing within the active dosimeter, as a function of energy, and accounting for self-shielding effects, if any. Equation (1) can also be expressed as:

$$R = \int_0^\infty \sigma_d(E) \left(\frac{\Psi_d(E)}{\Psi(E)} \right) \Psi(E)\, dE = \int_0^\infty \sigma_d(E)\, P_d(E)\, \Psi(E)\, dE \tag{2}$$

where $\psi(E)$ is the unperturbed neutron flux that would exist at the measurement location in the absence of the flux perturbations caused by the dosimeter itself, and any surrounding spectral modification devices or other structures placed in the field (Cd covers, foil and wire positioning devices, etc).

It should be noted here that the function $P_d(E)$ in Equation (2) can be determined independently from $\Psi(E)$ since it is simply a flux ratio. In this case, $\Psi(E)$ on the far right hand side of Equation (2) can be any appropriate *a priori* free-field unperturbed flux estimate that is then modified by the self-shielding function $P_d(E)$.

Equation (2) may be written as a summation rather than as an integral by partitioning the range of the energy variable into a number of discrete contiguous energy groups in the usual manner:

$$R = \sum_{j=1}^{NG} a_j \phi_j \tag{3}$$

where NG is the total number of energy groups, with

$$a_j = \frac{\int_{EL_j}^{EH_j} \sigma_d(E)\, P_d(E)\, \Psi(E)\, dE}{\int_{EL_j}^{EH_j} \Psi(E)\, dE} \tag{4}$$

and

$$\phi_j = \int_{EL_j}^{EH_j} \Psi(E)\, dE. \tag{5}$$

where EL_j and EH_j are the lower and upper energy limits of energy group j.

If additional dosimeter materials are placed in the field, or if a particular material exhibits more than one independent activation response (e.g. gold or indium as noted earlier), then Equation (3) may be written as a system of equations:

$$R_i = \sum_{j=1}^{NG} a_{ij}\ \phi_j \tag{6}$$

where R_i is the total activation rate for interaction i and a_{ij} is the activation constant from Equation (4) for interaction i due to neutrons in energy group j. There will be a total of NF equations, where NF is the total number of activation responses available.

Effective shielded cross sections $\sigma_d(E)$ and the corresponding shielded and unshielded *a priori* neutron fluxes suitable for computing the function $P_d(E)$ in the above equations may be obtained by any of several well-established neutron transport modeling techniques and nuclear data libraries. A typical approach involves computation of application-specific cross sections and *a priori* fluxes for each dosimeter in the neutron field using continuous-energy Monte Carlo techniques, e.g. MCNP. This is crucial if self-shielding or mutual shielding (as in a stack of foils) is significant. It is also sometimes possible to use highly-dilute foils (Auterinen et al., 2004) to avoid the need for shielding corrections, facilitating the direct application of standard dosimetry cross section libraries without further processing. The Monte Carlo calculations for dosimeter packages generally include only the dosimeters and surrounding support structure with a boundary condition that represents the incoming space, angle, and energy-dependent incident neutron source, precomputed using a Monte Carlo or deterministic computational model of the entire reactor. The global reactor computations may be done with MCNP, or with a standard multidimensional discrete-ordinates code such as DORT (Rhodes and Childs, 1988, Wheeler et al., 1990), or in the case of ATR, with any of the more advanced transport codes described earlier.

The system of activation equations (6) may be expanded to yield:

$$\begin{bmatrix} a_{11} & a_{12} & a_{13} & \cdots & a_{1\,NG} \\ a_{21} & a_{22} & a_{23} & \cdots & a_{2NG} \\ a_{31} & a_{32} & a_{33} & \cdots & a_{3NG} \\ \vdots & \vdots & \vdots & & \vdots \\ \vdots & \vdots & \vdots & & \vdots \\ a_{NF1} & a_{NF2} & a_{NF3} & & a_{NF\ NG} \end{bmatrix} \begin{bmatrix} \phi_1 \\ \phi_2 \\ \phi_3 \\ \vdots \\ \phi_{NG} \end{bmatrix} = \begin{bmatrix} R_1 \\ R_2 \\ R_3 \\ \vdots \\ \vdots \\ R_{NF} \end{bmatrix} \tag{7}$$

or, more compactly:

$$\mathbf{A\Phi = R} \tag{8}$$

where **A** is sometimes referred to as the "sensitivity" matrix.

Equation (8) is exactly balanced by definition, provided that the reaction rates R_i, the activation constants a_{ij}, and the group fluxes ϕ_j all correspond to the same self-consistent *a priori* model. If experimentally measured reaction rates for each interaction Rm_i are substituted into Equation (7), a solution of the

resulting new system of equations for adjusted fluxes corresponding to the measured reaction rates may also be obtained under certain conditions. A key assumption at this point is that the detailed *a priori* neutron spectrum used as a weight function to evaluate Equation (4) for the matrix elements $a_{i,j}$ in Equation (7) has a satisfactory degree of physical accuracy over the range of the limits of integration for each energy group defined in the system of adjustment equations (8).

If NF = NG in Equation (7), then the matrix **A** is square, its inverse will ordinarily exist for physically-realistic applications, and the system is thereby fully-determined. Thus the unknown flux vector may immediately be obtained by any standard solution method, provided that the rows of **A** are linearly-independent to a sufficient degree to permit practical machine computation of its inverse. In physical terms, this implies that the response functions (shielded cross sections) for the activation interactions used in the measurement must be selected such that they have sufficiently different shapes as functions of energy when mapped to the adjustment energy group structure that is selected. It may be noted that positive fluxes are not guaranteed to result from this procedure, but if the elements of **A** are computed in a sufficiently valid, physically-realistic manner for the specific measurement configuration, and if the measured reaction rates are accurately and precisely determined, a unique positive solution can generally be obtained.

In practice, the situation where NF is equal to NG is exemplified by the previously-noted cadmium difference method, which can be readily shown to be a special case of Equation (7), with only two rows in the matrix on the left, one for the bare foil and one for the covered foil, with the cadmium cover used as a spectral modifier to force linear independence of the matrix rows. It also typically occurs when measuring pointwise fluxes at resonance energies (e.g. Harker et al., 1992) using stacks of identical foils, and when measuring simple spectra using flux wires composed of alloys of two materials with different spectral responses, such as copper and gold, as is done in the present work.

3.1.3 The Overdetermined Case.

There are two possibilities for the situation where NF, the number of available activation response functions, is not equal to NG, the number of energy groups for which it is desired to obtain adjusted fluxes. If NF > NG the problem is overdetermined and the "extra" information that is thereby available can be incorporated into the direct algebraic determination of a unique best-estimate solution for the adjusted group fluxes and their propagated uncertainties. This is accomplished using a least-squares procedure based on the "normal equations" (Meyer, 1975) as follows.

First, Equation (7) is expanded to yield:

$$\begin{aligned}
&a_{11}\,\phi_1 + a_{12}\,\phi_2 + a_{13}\,\phi_3 \cdots \quad + a_{1\,NG}\,\phi_{NG} = Rm_1 \\
&a_{21}\,\phi_1 + a_{22}\,\phi_2 + a_{13}\,\phi_3 \cdots \quad + a_{2\,NG}\,\phi_{NG} = Rm_2 \\
&\vdots \qquad\quad \vdots \qquad\quad \vdots \qquad\qquad\quad \vdots \\
&a_{NF1}\,\phi_1 + a_{NF\,2}\,\phi_2 + a_{NF\,3}\,\phi_3 \cdots + a_{NF\,NG}\,\phi_{NG} = Rm_{NF}
\end{aligned} \tag{9}$$

where the measured reaction rates Rm_i are now substituted on the right-hand side. An approximation for the flux vector is now sought such that the sum of the squares of the weighted differences between the measured reaction rates and the calculated reaction rates, obtained by substituting the desired approximate solution vector into each row of Equation (9), is minimized. This involves minimization of the quantity Δ, where

$$\Delta = \sum_{i=1}^{NF} \frac{\delta_i^2}{u_i^2} \tag{10}$$

with

$$\delta_i = \left(\mathrm{Rm_i} - (\mathrm{a_{i1}}\phi_1 + \mathrm{a_{i2}}\phi_2 \cdots + \mathrm{a_{iNG}}\phi_{\mathrm{NG}})\right) \tag{11}$$

and where u_i is experimental uncertainty associated with reaction rate i.

Substituting Equation (11) into Equation (10), differentiating the resulting equation successively with respect to each group flux, setting the result to zero in each case and collecting terms yields a new set of equations that can be written as the NG x NG system:

$$\mathbf{A^T[Cov(R_m)]^{-1}A\ \Phi = A^T[Cov(R_m)]^{-1}R_m} \tag{12}$$

Where $\mathbf{A^T}$ is the transpose of **A**, $\mathbf{Cov(R_m)}$ is the NF x NF covariance matrix associated with the measurement vector $\mathbf{R_m}$,and $\mathbf{[Cov(R_m)]^{-1}}$ is its inverse. As a practical matter, $\mathbf{Cov(R_m)}$ often contains only diagonal elements that are the squares of the individual measurement uncertainties. However, if partial correlations between the measurements are important (e.g. correlations arising from the calibration of a common detector system used to measure all of the foil or wire activities), then the appropriate off-diagonal elements of the matrix $\mathbf{Cov(R_m)}$ may also be included. A more detailed derivation of Equation (12) may be found in the 2011 Annual Report of the ATR Methods Update Project (Nigg and Steuhm, 2011).

Equation (12) may be solved by any suitable method to yield a best-estimate adjusted flux vector $\mathbf{\Phi}$ that is optimally consistent with the measured reaction rates. If NF = NG in the first place, the solution of Equation (12) is the same as would be obtained by simply solving Equation (8) without premultiplying through by $\mathbf{A^T[Cov(R_m)]^{-1}}$. The difference between the adjusted flux vector and the *a priori* flux vector then gives a measure of the flux bias of the modeling code of interest, as a function of energy, at the geometric location in the reactor where the validation measurements were made.

It should also be noted that insertion of the adjusted fluxes back into the basic balance equation (7) will not ordinarily produce adjusted reaction rates that are the same as the measured reaction rates, unless of course NF = NG, in which case the adjusted fluxes are forced by definition to produce the measured reaction rates exactly.

It is also useful to note that if Equation (12) is rewritten as:

$$\mathbf{B\Phi = A^T[Cov(R_m)]^{-1}R_m} \tag{13}$$

with

$$\mathbf{B = A^T[Cov(R_m)]^{-1}A} \tag{14}$$

then the inverse of the matrix **B** is the covariance matrix for the adjusted flux vector **Φ**, based on propagation of the measurement uncertainties u_i.

Furthermore, since the solution to Equation (13) may be stated as:

$$\mathbf{\Phi = B^{-1}\ A^{T}[Cov(R_m)]^{-1}R_m} \tag{15}$$

the covariance matrix for the adjusted fluxes may also be equivalently computed from the basic uncertainty propagation formula in matrix algebra:

$$\mathbf{Cov(\Phi) = D\ Cov(R_m)\ D^{T}} \tag{16}$$

where

$$\mathbf{D = B^{-1}\ A^{T}[Cov(R_m)]^{-1}.} \tag{17}$$

Additionally, a vector of adjusted reaction rates **Ra** corresponding to the adjusted flux **Φ** may be computed as:

$$\mathbf{Ra = A\Phi} \tag{18}$$

With corresponding covariance matrix **Cov(Ra)** where:

$$\mathbf{Cov(Ra) = A\ Cov(\Phi)A^{T}.} \tag{19}$$

It is important to recognize at this point that in both the overdetermined case (NF > NG) and in the fully-determined case (NF = NG) no assumptions regarding the uncertainty of the *a priori* flux and its possible group-to-group correlations are required. In effect, the flux can be assumed unconstrained and the least-squares solution procedure yields the "best unbiased estimate" of the adjusted flux and its covariance matrix based only on the measurements and their uncertainties and correlations. However, it is important to recognize that information about the *a priori* flux and its covariance matrix can in fact be included if desired, to provide an additional constraint on the solution as will be described in more detail later.

3.1.4 The Underdetermined Case.

Proceeding further, if NF < NG the problem becomes underdetermined and additional information must be introduced in some manner to permit a realistic solution. Most of the underdetermined adjustment methods involve introduction of the *a priori* flux and its associated covariance matrix into the system of equations, in effect constraining the solution to a single optimum in a least squares sense, just as happens automatically in the overdetermined case. The nuclear cross section parameters $a_{i,j}$ in Equation (7) together with their propagated covariance matrices also can be introduced as additional *a priori* adjustable parameters, to provide further information that may be useful in the determination of the best overall estimate for the adjusted flux spectrum and its uncertainty. Several adjustment codes based on this approach have been developed, e.g. STAY'SL (Perey, 1977), LSL (Stallman, 1986) and FERRET (Schmittroth, 1979). Further mathematical details pertinent to the general application of least-squares methodology to the underdetermined neutron flux adjustment problem of interest here may also be found, for example, in Perey (1978) and Williams (2011). Alternate, somewhat more empirical, iterative adjustment techniques also have been widely used for the underdetermined case, one popular example being the method described by Draper (1971), implemented as an option in the SAND-II code (McElroy

and Berg, 1967) but these latter approaches are no longer generally viewed as being representative of the state of modern practice.

The underdetermined adjustment methods thus allow the estimation of a spectrum having more energy groups (i.e. more detail) than the number of linearly independent activation responses. However, the effective use of all underdetermined methods requires good physical insight, practical experience, and intuition, since the specifics of the input *a priori* spectrum and its covariance, the cross section data vectors and their covariances, as well as the iteration strategy used to produce a solution, can have a significant influence on the results, and opportunities for physically unrealistic results abound.

In the work described here we employ the first approach outlined above for solution of the underdetermined adjustment problem, i.e. direct application of the *a priori* flux and its covariance matrix to produce a relatively simple, but rigorous, algorithm tailored for routine ATR applications. To accomplish this we once again substitute the measured reaction rates Rm_i into Equation (7) and then augment the resulting system, to make it overdetermined, as follows:

$$\begin{bmatrix} a_{11} & a_{12} & a_{13} & \cdots & \cdots & a_{1,\mathrm{NG}} \\ a_{21} & a_{22} & a_{23} & \cdots & \cdots & a_{2,\mathrm{NG}} \\ \vdots & \vdots & \vdots & & & \vdots \\ a_{\mathrm{NF},1} & a_{\mathrm{NF},2} & a_{\mathrm{NF},3} & \cdots & \cdots & a_{\mathrm{NF,NG}} \\ 1 & 0 & 0 & \cdots & \cdots & 0 \\ 0 & 1 & 0 & \cdots & \cdots & 0 \\ 0 & 0 & 1 & \cdots & \cdots & 0 \\ \vdots & \vdots & \vdots & & & \vdots \\ \vdots & \vdots & \vdots & & & \vdots \\ 0 & 0 & 0 & \cdots & \cdots & 1 \end{bmatrix} = \begin{bmatrix} \varphi_1 \\ \varphi_2 \\ \varphi_3 \\ \vdots \\ \vdots \\ \vdots \\ \varphi_{\mathrm{NG}} \end{bmatrix} = \begin{bmatrix} Rm_1 \\ Rm_2 \\ \vdots \\ Rm_{\mathrm{NF}} \\ \varphi_{01} \\ \varphi_{02} \\ \varphi_{03} \\ \vdots \\ \vdots \\ \varphi_{0\mathrm{NG}} \end{bmatrix} = [A][\Phi] = [Z] \qquad (20)$$

where $\varphi_{01}, \varphi_{02}, \ldots\ldots \varphi_{0\mathrm{NG}}$ are the elements of the *a priori* flux vector from the modeling code of interest and the system of equations now has (NF+NG) rows and NG columns.

Note that even if only a single measurement (i.e. NF=1) is available for inclusion in Equation (20), the augmented system will still be overdetermined (albeit by only one row) and some useful spectral adjustment and reduction of uncertainty may occur in the solution. However, if there are no measurements included in Equation (20), then one simply obtains the uninteresting solution where the adjusted flux is identical to the *a priori* flux, with the same covariance.

To complete the statement of the underdetermined problem, we define the covariance matrix for the augmented vector **Z** in Equation (20) as:

$$[\mathrm{Cov}(Z)] = \begin{bmatrix} [\mathrm{Cov}(\mathrm{Rm})] & [0] \\ [0] & [\mathrm{Cov}(\Phi_0)] \end{bmatrix} \qquad (21)$$

where $\mathbf{Cov(\Phi_0)}$ is the covariance matrix for the *a priori* flux vector, computed explicitly by formal sensitivity-uncertainty methods as applied to the modeling code of interest, or synthesized according to any of several generally-accepted prescriptions (e.g. ASTM, 2008) as summarized in Section 3.1.5.

Using the augmented system (20) and the augmented covariance matrix (21), an analogue of Equation (13) can be constructed to yield:

$$\mathbf{B\Phi = A^T\,[Cov(Z)]^{-1}\,Z} \tag{22}$$

with

$$\mathbf{B = A^T\,[Cov(Z)]^{-1}A.} \tag{23}$$

Equation (22) is then solved to yield the adjusted flux vector $\mathbf{\Phi}$. The covariance matrix for the adjusted flux is, as before, the inverse of **B**. Also, since the solution to Equation (22) is:

$$\mathbf{\Phi = B^{-1}A^T[Cov(Z)]^{-1}Z} \tag{24}$$

the covariance matrix for the adjusted fluxes may also be equivalently computed by the standard uncertainty propagation formula, just as in the overdetermined case:

$$\mathbf{Cov(\Phi) = D\ Cov(Z)\ D^T} \tag{25}$$

where

$$\mathbf{D = B^{-1}\ A^T[Cov(Z)]^{-1}\,.} \tag{26}$$

Both methods for obtaining the covariance matrix for the adjusted flux produce the same results, as before, and it will also be observed in practice that the uncertainties of the adjusted fluxes are generally reduced relative to the original flux uncertainties as specified by the diagonal elements of $\mathbf{Cov(\Phi_0)}$.

The vector of adjusted dosimeter reaction rates **Ra** may also be computed from the adjusted flux as before:

$$\mathbf{Ra = A_0\Phi} \tag{27}$$

with corresponding covariance matrix **Cov(Ra)** where:

$$\mathbf{Cov(Ra) = A_0Cov(\Phi)A_0^T,} \tag{28}$$

where in both of the above equations the matrix $\mathbf{A_0}$ is the <u>unaugmented</u> effective cross section matrix, i.e. the first NF rows of the matrix on the left hand side of Equation 20.

Finally, it should be recognized that it is possible to reduce the system represented by Equation (22) to a somewhat more tractable size, producing identical results, by application of the Matrix Inversion Lemma (Williams, 2011), or by use of an equivalent independent derivation by Perey (1978) to yield:

$$\mathbf{\Phi = \Phi_0 + Cov(\Phi_0)\ A_0^T[Cov(Rm) + A_0Cov(\Phi_0)\ A_0^T]^{-1}[Rm - A_0\Phi_0]} \tag{29}$$

with adjusted covariance matrix

$$\mathbf{Cov(\Phi) = Cov(\Phi_0) - Cov(\Phi_0)\, A_0^T [Cov(Rm) + A_0 Cov(\Phi_0)\, A_0^T]^{-1}\, A_0\, Cov(\Phi_0)} \qquad (30)$$

where the matrix $\mathbf{A_0}$ is again the unaugmented effective cross section matrix from Equation (7).

3.1.5. Construction of A Priori Covariance Matrices

As noted earlier, the *a priori* flux covariance matrix used in the various adjustment equations may be computed explicitly by formal sensitivity-uncertainty methods as applied to the modeling code of interest, or synthesized according to physical and mathematical intuition. For the analyses described here, the latter approach is taken, based on a typical generally-accepted prescription (ASTM, 2008 and Schmittroth, 1979). In this formulation, element (i,j) of the *a priori* flux covariance matrix is given by

$$[Cov(\Phi)]_{i,j} = P^2 \varphi_i \varphi_j + R^2 \varphi_i \varphi_j \rho_{i,j} \qquad (31)$$

where:

P = Fractional normalization uncertainty for the *a priori* flux
R = Fractional random uncertainty for the *a priori* flux
φ_i = *A priori* neutron flux in group i
$\rho_{i,j}$ = Correlation coefficient between groups i and j.

The first term on the right hand side of Equation (31) describes a fully-correlated component of the overall covariance matrix and in most reactor physics applications it is typically used to represent the fission power normalization uncertainty. This term is fully-correlated (i.e. all of the group fluxes go up or down by the same factor if the power normalization is changed) and therefore it does not introduce any new spectral information. The second term represents a random uncertainty component that is associated with the computational algorithm used by the reactor physics modeling code of interest. This random component describes the statistical limits within which the shape of the spectrum as a function of energy may reasonably shift as a result of the adjustment.

The second term in Equation (31) may have only diagonal elements representing independent, uncorrelated uncertainties in the group fluxes, or it may (and in practice essentially always does) also contain off-diagonal correlated uncertainties as well, where the correlation coefficients are given by

$$\rho_{i,j} = (1-\Theta)\, \delta_{i,j} + \Theta \exp\left(-(i-j)^2/\Gamma^2\right) \qquad (32a)$$

where:

$\delta_{i,j}$ = Delta function ($\delta_{i,j}$=1 if i=j and $\delta_{i,j}$=0 otherwise)
Θ = Correlation Strength parameter
Γ= Correlation Range parameter ($0 \leq \Gamma \leq (NG-1)$).

Depending on the specific application, the Correlation Strength parameter typically has a value between 0.5 and 1.0. The Correlation Range parameter can vary widely, depending in particular on the neutron

scattering properties of the moderating materials used in the reactor of interest as well as on the specifics of the energy group structure selected for the adjustment. An alternate formulation for the correlation coefficients (ASTM, 2008) that may be more physically realistic in some situations is given by:

$$\rho_{i,j} = (1-\Theta)\,\delta_{i,j} + \Theta \exp\left(-(i-j)/\Gamma\right) \qquad (32b)$$

3.1.6 Additional Considerations

Several notes regarding the ATR-specific protocols developed here are appropriate at this point. First, it is also possible (and not unusual) to further augment Equation (20) so that it also includes the effective shielded cross sections $a_{i,j}$ from Equation (7) and their uncertainties as adjustable parameters of interest as mentioned earlier. In that case, there will be a vector of length NG (composed of the appropriate terms $a_{i,j}$ extracted from the effective cross section matrix) included in **[Z]** on the right-hand side of Equation (14) and a corresponding covariance matrix of dimension NG x NG included on the left-hand side for each dosimeter response Rm included in the analysis. This can be especially important if the uncertainties of the effective cross sections $a_{i,j}$ in Equation (7) are significant in comparison with the uncertainties of the *a priori* fluxes φ_{0j} and the uncertainties of the measured reaction rates Rm. However, for the ATR-specific derivation described here it is assumed at this point that this is not the case, based on some limited earlier experience with detailed neutron activation spectrometric analysis for the ATR using a similar least-squares approach (Rogers and Anderl, 1995). Therefore. only the *a priori* flux and its covariance matrix are currently used in the construction of Equation (20). This assumption may be modified in the future as the ATR validation protocol evolves with application.

Additionally, it is important to recognize that the covariance matrix for the *a priori* flux vector must be constructed in such a manner that it can actually contribute information to the adjustment process, i.e. it must be non-singular, so that its inverse will exist. For example, if the covariance matrix includes only the *a priori* flux normalization uncertainty (which is by definition based on the same fractional multiplier for all groups), it will be fully-correlated (therefore singular) and Equation (22) cannot be solved in a useful manner. Methods for constructing a useful flux covariance matrix are further discussed in Section 3.2, where specific analyses for several ATRC validation experiments are presented. Also, Williams (2011) describes an alternate scheme for constructing the *a priori* flux covariance matrix in situations where the standard matrix is rank-deficient and therefore not invertible, but as a practical matter a standard flux covariance matrix should essentially always be invertible in the case of ATR.

Also, as noted briefly earlier, one can also elect to include the *a priori* flux and its covariance matrix into the analysis via Equation (20) even if the unaugmented system (7) is already fully-determined (NF=NG) or overdetermined (NF > NG). In this case the additional information is factored into the solution in the same variance-weighted manner, and if the covariance matrix entries for the *a priori* flux are set to arbitrarily large values one will obtain the same adjusted flux as would be computed from Equation (13), because with a large covariance specified, the flux is effectively unconstrained and the measured reaction rates drive the solution. Conversely, if the covariance matrix entries are set to arbitrarily small values (but not zero, which creates a singular matrix), the adjusted flux will be numerically equivalent to the *a priori* flux since the vanishing covariance entries imply that the *a priori* flux is already correct and the measurements should have no influence. For this reason the solutions to both the underdetermined and the overdetermined problem (if a flux covariance matrix is supplied) can be highly-dependent on the form and magnitude of the flux covariance data entries, as further illustrated by Williams (2012). Thus the covariance matrices used for the adjustment must be constructed with the same care and attention to physical reality as is required for all of the other input data in the problem.

Neutron activation spectrometry can be applied to any neutron field for which suitable neutron interaction responses can be measured. The general methodology is quite flexible, and in addition to the protocols described here in the context of neutron flux spectrum characterization and modeling code validation, it also can be exercised at ATR in a slightly different manner, for core power distribution studies using direct measurements of local fission rates within the fuel elements, as will be demonstrated in Section 3.3. Activation spectrometry is capable of high overall precision and accuracy ($1\sigma < 5\%$) when uncertainties are carefully managed throughout every step of the process. Precautions to be taken include:

- Use of high-purity, accurately assayed dosimeter materials.
- Careful preparation and handling of the dosimeter packages to ensure accurate knowledge of the foil masses and to avoid contaminants.
- Careful recording of the activation and post-irradiation decay times of the foils.
- Irradiation at constant flux if at all possible, with appropriate corrections for any time-dependence of the flux.
- Accurate, reproducible calibration of gamma spectrometers used for measurement of the foil activities, using certified, traceable standards.
- Use of good techniques for the foil activity measurements in order to minimize uncertainties due to coincidence summing, counting geometry etc.
- Thoughtful selection and application of adjustment techniques.
- Use of multiple adjustment techniques to verify consistency of the data analysis.

It is also important to recognize that activation measurements for code validation, especially in the case of thermal neutron fields, must be planned and interpreted very carefully due to the possibility of large flux gradients that can depend on the specific geometry of the reactor, which can change with time (e.g. as a result of shim rotation in the ATR). As a result, reproducibility can be an issue and self consistent comparison with the calculation being validated is crucial, i.e. be sure you are really calculating the same physical quantity that you are measuring.

3.1.7 Extension of the Adjustment Methodology to the Determination of Element Power Distributions

The least-square methodology represented by Equations (20) and (21) for spectral adjustments is quite general, and in fact can be used to adjust any vector of *a priori* computed parameters against a vector of measured data points that can be related to the parameters of interest through a matrix transform. For example, the ATR has an online lobe power measurement system but it does not have an online individual fuel element power measurement system. Measurements of the element-to-element fission rate distribution are done as needed using activation measurements with small aluminum wires containing milligram quantities of ^{235}U placed at certain locations between the fuel plates of selected fuel elements, as will be described in more detail later. Typically, only the fission rates in the odd-numbered fuel elements are measured in this manner and various empirical assumptions are applied to estimate the fission powers in the intervening even-numbered elements. The least-squares methodology outlined here offers a simple, but mathematically rigorous, approach for estimating the fission powers and their uncertainties in all 40 fuel ATR fuel elements when actual measurements are done only for a subset of the same 40 elements.

We begin by rewriting Equations 20 and 21 as follows:

$$\begin{bmatrix} a_{11} & a_{12} & a_{13} & \cdots & \cdots & a_{1,NE} \\ a_{21} & a_{22} & a_{23} & \cdots & \cdots & a_{2,NE} \\ \vdots & \vdots & \vdots & & & \vdots \\ a_{NM,1} & a_{NM,2} & a_{NM,3} & \cdots & \cdots & a_{NM,NE} \\ 1 & 0 & 0 & \cdots & \cdots & 0 \\ 0 & 1 & 0 & \cdots & \cdots & 0 \\ 0 & 0 & 1 & \cdots & \cdots & 0 \\ \vdots & \vdots & \vdots & & & \vdots \\ \vdots & \vdots & \vdots & & & \vdots \\ 0 & 0 & 0 & \cdots & \cdots & 1 \end{bmatrix} = \begin{bmatrix} P_1 \\ P_2 \\ P_3 \\ \vdots \\ \vdots \\ \vdots \\ P_{NE} \end{bmatrix} = \begin{bmatrix} Pm_1 \\ Pm_2 \\ \vdots \\ Pm_{NM} \\ P_{01} \\ P_{02} \\ P_{03} \\ \vdots \\ \vdots \\ P_{0NE} \end{bmatrix} = [A][P] = [Z] \tag{33}$$

and

$$[\mathrm{Cov}(Z)] = \begin{bmatrix} [\mathrm{Cov}(Pm)] & [0] \\ [0] & [\mathrm{Cov}(P_0)] \end{bmatrix}, \tag{34}$$

where NE is the total number of fuel elements (i.e. 40 for ATR) and NM is the number of these elements for which measurements have been made in the validation experiment of interest. Typically NM=20 for ATR, and only the odd-numbered element fission powers are measured as noted above, but NM may on occasion be any number between 1 and NE. The vector **P** is the desired best least squares estimate for the powers of all 40 fuel elements, the vector **Pm** (first NM entries in [Z]) contains the NM measured powers and the vector $\mathbf{P_0}$ (last 40 entries in [Z]) contains the 40 *a priori* estimates, P_{0i} for the element powers, extracted from the computational model for the validation experiment configuration. The top NM rows of the matrix **A** each contain entries that are equal to zero except for the column corresponding to the element for which the measurement on the right-hand side in that row was made, where the entry would be 1.0. The bottom 40 rows of the matrix **A** correspond to the rows of a 40 x 40 identity matrix as before. Equation 34 includes the NM x NM and NE x NE covariance matrices for the measured power vector and for the *a priori* power estimates respectively. The covariance matrix entries for **[Cov(Pm)]** are based on the uncertainties of the experimental data values in the usual manner. The covariance matrix entries for $\mathbf{[Cov(P_0)]}$ may be computed by the modeling code being validated under certain circumstances, or may be estimated as described previously for the spectral adjustment procedure. The solution of Equations (33) and (34) for the adjusted element power vector **P** and its covariance matrix is obtained in the same manner as described previously for the spectral adjustment equations. Several useful applications of Equations (33) and (34) will be described in Sections 3.3 and 3.5.

3.2 Validation Measurements in the ATRC Northwest In-Pile Tube: Irradiations 1-3

In the initial phase of the experimental campaign described here, various sets of activation foils and wires were irradiated in the NW Large In Pile Tube (LIPT) of the ATRC, with a "balanced "outer shim critical configuration (all drums at the same angular rotation relative to the fuel).

3.2.1 Experimental Methods and Materials.

Three 20-minute ATRC reactor runs at 600 watts were required for this phase. Activation responses included in the measurements are listed in Table 3.1. The first irradiation was targeted on the thermal and epithermal neutron energy range and included duplicate bare Au and Mn foils and duplicate cadmium-covered In, Au, W, Mn, and Cu foil packages. The second irradiation was conducted primarily to experimentally confirm the anticipated small effect of the cadmium-covered foil packages used in Irradiation 1 on the local flux in the NW LIPT. The third irradiation was designed to provide additional spectral detail in the energy range above about 300 keV using a set of In, Ti, Ni, Zn, Fe, and Nb foils contained within a hollow spherical spectral shifting shield composed of boron. The foils were standard 12.7 mm (0.5") diameter foils with thicknesses ranging from 0.0254 mm (1 mil) to 0.127 mm (5 mil).

The foils were positioned within the ATRC NW LIPT insert using specialized insert fittings fabricated for this purpose. Foils used for thermal and epithermal neutron measurements during Irradiation 1 were placed in two covered aluminum strips (Figure 3.3). These strips fit into the middle slots of the square holder shown on the right-hand side of Figure 3.4, which fits, in turn, into the square cavity in the cylindrical LIPT insert on the left hand side of Figure 3.4. The Cd-covered packages were placed in the upper position in the first strip and in the lower position in the second strip. This placement pattern was reversed for the bare foil packages, enabling quantification and averaging of any flux differences that that may exist between the upper and lower positions due to axial gradients. The insert fitting also contains "dummy" strips in the other eight positions as shown in Figure 3.4. These dummy strips are designed so that the fully-assembled insert fitting will have the same metal-to-water ratio as it has in the case of the third irradiation, where a second positioning device, for the boron spectral shield, is substituted in the place of the foil holding strips and dummies used in the first and second irradiations.

Copper/gold (1.55% Au by weight alloyed in natural Cu) flux wires were also placed at specific locations within the strips as shown in Figure 3.3. These wires were 1 mm in diameter and approximately 0.635 cm (0.25") in length. They each contain approximately 45 milligrams of natural copper and 0.7 milligrams of gold. The wires were used to obtain a common measure of the fast and thermal neutron flux in the experiment hardware from one irradiation to another.

Co-normalization of the NW lobe power for the three separate reactor runs was accomplished using the measured activation of the same type of copper/gold flux wires in each of the four even-numbered core fuel elements surrounding the NW flux trap (Elements 32, 34, 36, 38). Each wire was placed in the circled position in the middle of each element as shown in Figure 3.5, at the axial core midplane. Finally, a second set of foil positioning strips was prepared for Irradiation 2, with flux wires in the various positions as before, but without foil packages. This arrangement represents the assumed "unperturbed" LIPT configuration that is associated with the spectral unfolding and adjustment process.

Table 3.1. Activation interactions of interest for ATR model validation applications

Neutron Interaction	Nominal Mass and Composition of Standard Foil	Half-life of Product of Interest	Energy Range of Primary Response	Activation Gamma Energy of Interest (keV)
$^{115}In (n, \gamma)^{116}In$	25 mg, 100% In	54 Minutes	1 eV Resonance	1293,1097, 416
$^{197}Au (n, \gamma)^{198}Au$	60 mg, 100% Au	2.694 Days	Thermal & 5 eV Resonance	412
$^{186}W(n, \gamma)^{187}W$	60 mg, 100% W	23.9 Hours	18 eV Resonance	686
$^{55}Mn(n, \gamma)^{56}Mn$	50 mg, 80% Mn, 20% Cu	2.578 Hours	Thermal & 340 eV Resonance	847
$^{63}Cu (n, \gamma)^{64}Cu$	140 mg, 100%Cu	12.7 Hours	Thermal & 1 keV Resonance	511 (Positron)
$^{115}In (n,n')^{115m}In$	25 mg, 100% In	4.49 Hours	0.5 MeV Threshold	336.3
$^{47}Ti (n,p)^{47}Sc$ $^{46}Ti (n,p)^{46}Sc$ $^{48}Ti (n,p)^{48}Sc$	157 mg, 100% Ti	3.349 Days 83.81 Days 43.7 Hours	1.0 MeV Threshold 3.5 MeV Threshold 5.5 MeV Threshold	159.4 1121,889 984,1312,1038
$^{58}Ni (n,p)^{58}Co$	286 mg, 100% Ni	70.88 Days	1.2 MeV Threshold	811
$^{64}Zn (n,p)^{64}Cu$	117 mg, 100% Zn	12.7 Hours	1.5 MeV Threshold	511 (Positron)
$^{54}Fe (n,p)\ ^{54}Mn$ $^{56}Fe (n,p)\ ^{56}Mn$	132 mg, 100% Fe	312.2 Days 2.578 Hours	1.5 MeV Threshold 5.0 MeV Threshold	834.8 847
$^{93}Nb (n, 2n)^{92m}Nb$	270 mg, 100%Nb	10.13 Days	6.0 MeV Threshold	935

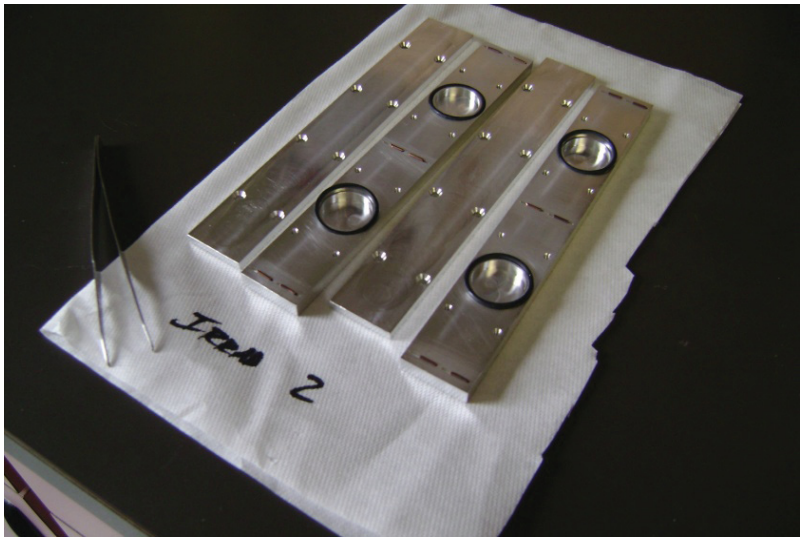

Figure 3.3. Foil positioning strips and covers for the bare and cadmium-covered foil packages. duplicate flux wires are placed in the indented slots at each end and in the middle of each strip.

Figure 3.4. Foil positioning strips and dummy strips mounted in their insert fitting on the right, which is then positioned in the NW LIPT test train insert on the left.

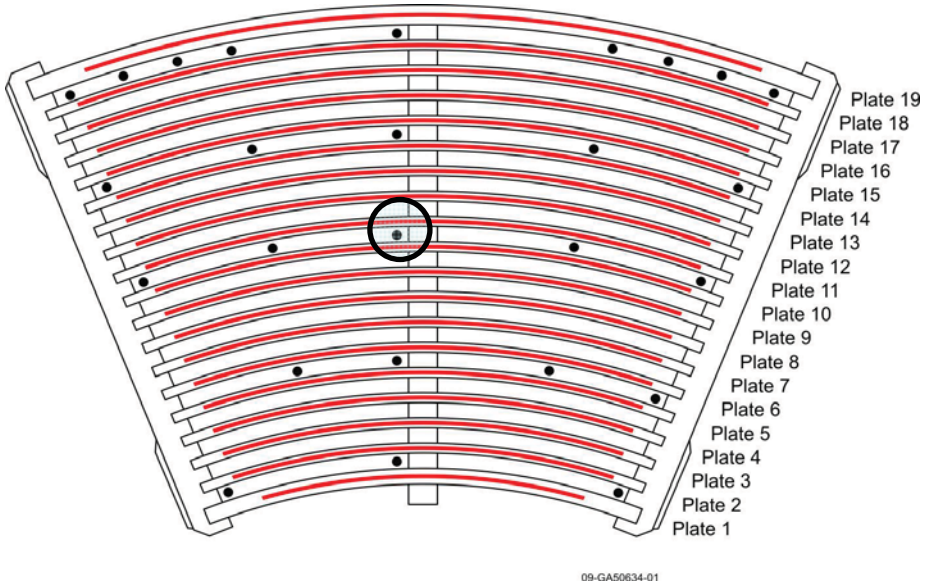

Figure 3.5. Transverse section of an ATRC fuel element showing available flux wire positions. The circled position in the center was used for power normalization in Irradiations 1-3 as discussed in the text.

For the third irradiation, the package of threshold interaction foils was suspended at the center of the boron spectral shifting shield, which was then placed in a second insert fitting as shown in Figure 3.6. The spectral shifter was a hollow sphere of sintered boron, enriched to approximately 90% in ^{10}B, with an inside diameter of approximately 2.5 cm (1”), an outside diameter of 5 cm (2”), and a nominal mass of 115 grams. This device prevents essentially all neutrons having energies of less than about 10 keV from reaching the foil package inside, effectively eliminating interfering interactions from thermal and resonance neutron interactions in the enclosed foils. The insert fitting for Irradiation 3 has 8 positions for flux wires as shown in Figure 3.6.

The cylindrical NW LIPT insert was positioned in a “Test Train”, which consists of the insert with one or the other of its two fittings described previously plus several hollow aluminum spacer sections that are assembled together axially and then put inside of an aluminum shroud that fits inside of the NW LIPT. Figure 3.7 illustrates how each test train is assembled for positioning in the NW LIPT with the center section aligned with the axial active core midplane.

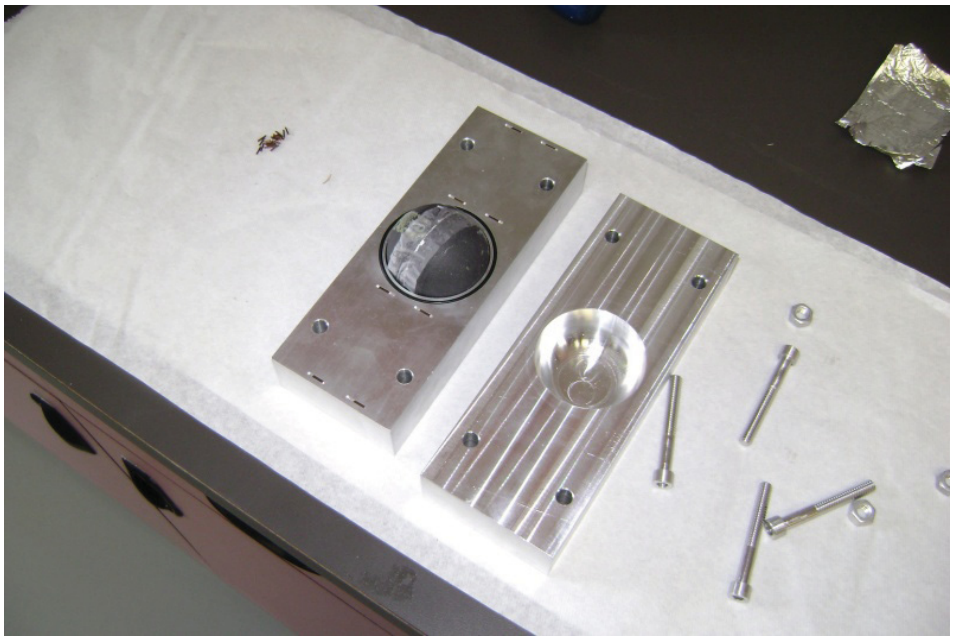

Figure 3.6. Fitting for positioning of boron sphere. Duplicate flux wires are placed in the indented slots at each end, and just above and below the boron sphere. The two halves are then bolted together.

3.2.2 *A Priori* Computational Model

An MCNP5 full-core model of the ATRC was developed for primary support of the validation protocol during the initial stage of development. This model is similar to the published full core ATR1994 Core Internals Changeout (CIC) Benchmark model (Kim and Schnitzler, 2008), but modified to match the current configuration of the ATRC, which is somewhat different from the ATR configuration as a result of evolutionary changes in the ATR over the course of several core internal change-outs (CICs) and fuel design changes. Neutronically, the most significant differences between the cores are the fuel design, operating conditions and the flux trap loadings. ATRC fuel element plates are uniformly loaded with boron, whereas the ATR uses boron for power peaking control only in the four innermost and four outermost plates of the fuel elements. Furthermore, the ATR operates at a high power density with forced cooling under pressurized conditions, while the ATRC is an unpressurized pool type reactor that operates at a power generally less than 1 kW with cooling by natural convection. Hence, ATRC coolant is full density water, and the coolant, moderator (water and beryllium) and fuel can be assumed to remain at room temperature (Bess, 2009). The other significant differences between the ATR and ATRC are related to the contents of the irradiation positions. Flux trap contents can not only influence core reactivity but also the relative power partitioning among the five core lobes. For the experiments discussed here the contents of the NW LIPT were as shown in Figure 3.7. For the remaining flux traps, various INL Test Plan documents and other resources were used to identify the current contents.

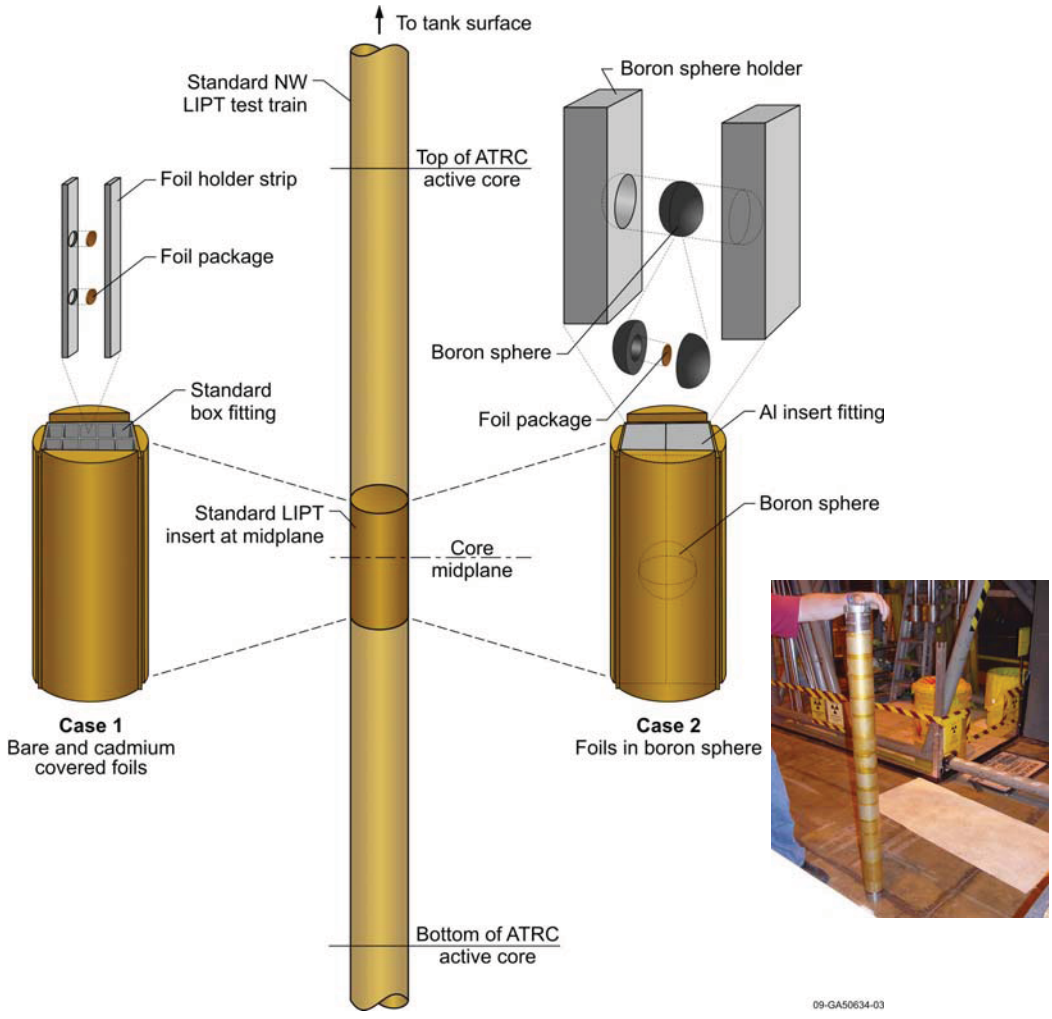

Figure 3.7. Positioning of test train components in the ATRC Northwest Large In-Pile Tube insert. The inset photo shows the entire assembled test train. Case 1 was the configuration for Irradiations 1 and 2. Case 2 was the configuration for Irradiation 3.

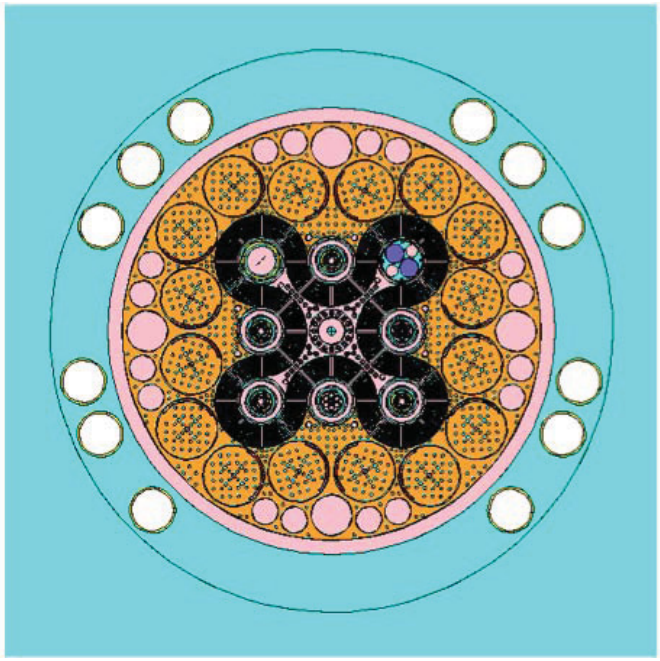

Figure 3.8. MCNP5 ATRC model geometry at the axial core mideplane.

A diagram of the MCNP5 model for Irradiation 1 is shown in Figure 3.8 above. The calculated K_{eff} for this critical configuration was 0.98928 ± 0.00002, where the quoted uncertainty is for the Monte Carlo convergence statistics alone. Separate TSUNAMI analyses indicate that the ATR model is also subject to approximately 0.5% additional uncertainty on the computed eigenvalue due to nuclear data uncertainty propagation. The individual Cu/Au wires and foils were explicitly modeled in their various locations to calculate fluxes and reaction rates at those positions. The reaction rates were tallied using the recent International Reactor Dosimetry File (IRDF) cross-section libraries (Griffin and Paviotti-Corcuera, 2003). The effective microscopic self-shielded and mutually-shielded cross-sections for the foils and wires were then determined by dividing the MCNP5 calculated reaction rate tally by the flux tally. Each tally was partitioned into the 47 energy groups corresponding to the BUGLE series of standard cross section libraries (Roussin, 1980) plus one extra group to cover the highest energy range between 17.3 MeV and 20 MeV. The resulting dosimeter cross-sections were then used for various spectral adjustment analyses described in the following section.

The first two irradiations were successfully conducted in late September 2010 at the ATRC. Irradiation 3 was conducted in late April 2011. The absolute activities of the foils and wires were measured at the INL Radiation Measurements Laboratory (RML) according to standard RML procedures using HPGe gamma spectrometers.

3.2.3 Measured Foil and Wire Responses

Table 3.2 shows the measured saturation activities per atom for all foils whose responses were used in the spectral adjustment procedures reported here. Some of the responses of interest listed in Table 3.1 were too weak to measure accurately, so they were not used since they would effectively be weighted out of the least-squares adjustment algorithm anyway. The measured results are arranged in descending order of

their primary energy range of neutron sensitivity. Total activity measurement uncertainties (counting statistics plus detector calibration) are in the range of 4-6% (1σ) for the foils used in Irradiation 1 and 6-10% for those used in Irradiation 3.

Table 3.2. Measured foil saturation activities – ATRC Irradiations 1 and 3. Measurement uncertainties are as described in the text.

Response	Irradiation	Spectral Modifier	Sensitive Energy Range	Measured σΦ
Nb(n,2n)	3	Boron Sphere	Fast	2.64E-19
Ti-48 (n,p)	3	Boron Sphere	Fast	1.35E-19
Fe-56 (n,p)	3	Boron Sphere	Fast	5.12E-19
Ti-46 (n,p)	3	Boron Sphere	Fast	5.00E-18
Ti-47 (n,p)	3	Boron Sphere	Fast	1.17E-17
Fe-54 (n,p)	3	Boron Sphere	Fast	4.10E-17
Zn-502 (n,p)	3	Boron Sphere	Fast	2.05E-17
Ni-1004 (n,p)	3	Boron Sphere	Fast	5.72E-17
In-(n,n')	3	Boron Sphere	Fast	1.30E-16
In(n,n')	1	Cadmium	Fast	1.24E-16
In(n,n')	1	Cadmium	Fast	1.23E-16
Cu(n,γ)	1	Cadmium	Epithermal	3.44E-16
Cu(n,γ)	1	Cadmium	Epithermal	3.54E-16
Mn(n,γ)	1	Cadmium	Epithermal	9.52E-16
Mn(n,γ)	1	Cadmium	Epithermal	1.01E-15
W(n,γ)	1	Cadmium	Epithermal	2.79E-14
W(n,γ)	1	Cadmium	Epithermal	2.86E-14
Au(n,γ)	1	Cadmium	Epithermal	4.90E-14
Au(n,γ)	1	Cadmium	Epithermal	5.09E-14
In(n,γ)	1	Cadmium	Epithermal	8.03E-14
In(n,γ)	1	Cadmium	Epithermal	8.57E-14
Au(n,γ)	1	None	Thermal	1.07E-13
Au(n,γ)	1	None	Thermal	1.09E-13
Mn(n,γ)	1	None	Thermal	8.74E-15
Mn(n,γ)	1	None	Thermal	8.26E-15

Table 3.3 shows the saturation activities for the Au/Cu flux wires in the NW LIPT hardware as well as in the four surrounding fuel elements in the case of Irradiation 1. The ratio of the gold activity relative to the copper activity for each wire is shown in the last column. This activity ratio, also referred to as a "spectral index" provides a simple indication of the relative "hardness" of the neutron spectrum to which the wire has been exposed. This is based on the fact that copper is relatively more sensitive to thermal neutrons compared to gold, which is roughly equally-sensitive to thermal and above-thermal neutrons.

Table 3.3. Measured flux wire saturation activities – ATRC Irradiation 1.

Wire Location[1]	^{197}Au(n,γ) σΦ (±3%)	^{63}Cu(n,γ) σΦ (±3%)	Spectral Ratio Au/Cu (±5%)
NW LIPT Upper 1L	1.70E-13	3.36E-15	50.41
NW LIPT Upper 1R	1.76E-13	3.29E-15	53.47
NW LIPT Upper 2L	1.74E-13	3.33E-15	52.32
NW LIPT Upper 2R	1.60E-13	3.11E-15	51.53
NW LIPT Middle 1L	1.61E-13	2.62E-15	61.25
NW LIPT Middle 1R	1.58E-13	2.73E-15	57.87
NW LIPT Middle 2L	1.63E-13	2.68E-15	60.60
NW LIPT Middle 2R	1.51E-13	2.65E-15	57.08
NW LIPT Lower 1L	1.75E-13	3.71E-15	47.21
NW LIPT Lower 1R	1.73E-13	3.42E-15	50.63
NW LIPT Lower 2L	1.71E-13	3.56E-15	47.89
NW LIPT Lower 2R	1.83E-13	3.64E-15	50.36
LIPT Average	**1.68E-13**	**3.18E-15**	**52.86**
Fuel Element 32	1.58E-13	1.64E-15	96.23
Fuel Element 34	1.13E-13	1.14E-15	99.06
Fuel Element 36	9.07E-14	8.73E-16	103.84
Fuel Element 38	1.36E-13	1.30E-15	104.40
Core Average	**1.24E-13**	**1.24E-15**	**100.37**

[1] Location "Upper 1L" denotes the wire position at the upper end of Foil Strip 1, Left Side, etc.

In the case of a fully-thermalized neutron field, the spectral index will asymptotically approach the ratio of the Au and Cu cross sections at 2200 m/s, assuming no spatial self-shielding. This asymptotic ratio is approximately 22.1 (i.e. 98.74 barns divided by 4.47 barns). Any physically-realistic departure from the described asymptotic spectral conditions will cause the ratio to increase, primarily due to increased resonance capture in gold. For example, it can be seen from Table 3.3 that the Au/Cu ratio is in the range of 51±3 in the upper and lower wire locations within the NW LIPT hardware since the spectrum is not fully thermalized. In the middle locations of the insert this ratio increases to approximately 60. This is an indication of the axial attenuation by aluminum of thermal neutrons streaming vertically into the NW LIPT insert from the water-filled regions above and below.

Irradiation 2 used the same configuration as Irradiation 1 except that the foil positions were empty - only the Cu/Au wires were installed in the NW LIPT hardware. The resulting wire activities were statistically identical to the corresponding Irradiation 1 activities at all locations in the NW LIPT hardware. This indicates that the presence of the foils and their cadmium covers has only a very small (if any) effect on the absolute flux and spectrum within the NW LIPT hardware.

The activities of the wires in the core fuel elements surrounding the NW LIPT were also essentially identical for the first two irradiations. This confirms that the NW lobe was operating at the same total power for both irradiations, as desired. Finally it is interesting to note from the spectral index data in Table 3 that the neutron spectrum in the core fuel elements is significantly harder than is the case within the NW LIPT. This is as expected, since the contents and surroundings of the NW LIPT provide some moderation of neutrons entering the LIPT region from the fuel.

Table 3.4 shows the wire activities and spectral indices for Irradiation 3. The additional spectral hardening caused by the boron sphere is apparent from the spectral index data in the last column. In addition, it appears from the data for the core flux wires that the NW lobe was operating at a slightly higher power during Irradiation 3 compared to Irradiations 1 and 2, possibly due a slightly higher total reactor power, a slightly greater tilt of the power distribution toward the NW LIPT, or some combination of both. This information was used to renormalize the foil data from Irradiation 3 slightly downward when combining the Irradiation 3 foil activities with the corresponding foil data from Irradiation 1 to obtain a full range adjusted neutron spectrum (the foil activities shown in Table 3.2 reflect this renormalization).

Table 3.4. Measured flux wire saturation activities – ATRC Irradiation 3.

Wire Location[1]	^{197}Au(n,γ) σΦ (±3%)	^{63}Cu(n,γ) σΦ (±3%)	Spectral Ratio Au/Cu (±5%)
NW LIPT Upper L	1.69E-13	3.14E-15	53.96
NW LIPT Upper R	1.69E-13	3.12E-15	54.25
NW LIPT Upper Middle L	1.35E-13	1.99E-15	67.73
NW LIPT Upper Middle R	1.26E-13	1.98E-15	63.57
NW LIPT Lower Middle L	1.32E-13	2.00E-15	66.12
NW LIPT Lower Middle R	1.30E-13	2.02E-15	64.49
NW LIPT Lower L	1.70E-13	3.12E-15	54.59
NW LIPT Lower R	1.73E-13	3.20E-15	53.97
LIPT Average	1.51E-13	2.57E-15	58.58
Fuel Element 32	1.88E-13	1.84E-15	102.06
Fuel Element 34	1.29E-13	1.28E-15	100.52
Fuel Element 36	9.88E-14	1.01E-15	97.96
Fuel Element 38	1.47E-13	1.44E-15	102.37
Core Average	1.41E-13	1.39E-15	101.04
Core Average Irr 3/Irr 1	1.13 (±5%)	1.12 (±5%)	-

[1] Location “Upper L” denotes the upper left-hand flux wire position, etc.

3.2.4 Spectral Adjustment and Code Validation Analysis

Table 3.5 and Figure 3.9 show an 8-group adjusted neutron spectrum for the NW LIPT corresponding to the foil measurement results of Irradiation 1 combined with those of Irradiation 3. The adjusted spectrum was determined using the methodology outlined in Section 3.1 for the overdetermined case with the *a priori* flux covariance matrix included, assuming 10% fully-correlated (normalization) uncertainty, 20% partially-correlated random uncertainty with correlation matrix parameters θ=0.8 and Γ=4 in Equation 32a. The adjustment calculations were performed using an Excel™ spreadsheet implementation based on Equations 22-26, with an independent verification based on Equations 29 and 30, which produces identical results. All 25 measured responses listed in Table 3.2 were used for the adjustment. There were 7 duplicate responses and 1 triplicate response (^{115}In(n,n')), for a net total of 16 responses with sufficient linear independence on the specified 8-group energy structure. The elements of the 25 x 8 coefficient matrix and the *a priori* flux vector for the adjustment procedure were computed using the MCNP5 model of the experimental apparatus described earlier. The nature of the adjustment algorithm is such that the fluxes shown in Table 3.5 represent a variance-weighted least-squares best estimate spatial average flux over the four foil positions in the NW LIPT apparatus, corrected for the perturbing effect of the cadmium covers, the boron sphere, and the foils themselves. The bias of the *a priori* model for the conditions being calculated is the difference between the *a priori* flux and the adjusted flux with its corresponding uncertainty. It can be seen in this case that the adjustment tended to reduce the total flux by about 17% with a concurrent small spectral shape changes that appear to be of limited statistical significance. The chi-squared parameter for the adjustment shows an excellent fit to the experimental data. Table 3.6 shows the measured, *a priori*, and adjusted foil saturation activities for this case. It can be seen that the adjusted activities are very consistent with the corresponding measurements.

Table 3.5. Eight-group neutron flux spectrum from foils – Northwest Large In-Pile Tube, Irradiations 1 and 3 combined, 600W. MCNP5 *a priori.* Combined correlated and uncorrelated uncertainty of the *a priori* fluxes is 22.4%.

Energy Group	Upper E (eV)	Lower E (eV)	*A priori* Flux (n/cm**2-s)	Adjusted Flux (n/cm**2-s)	Propagated Uncertainty (1σ)
1	2.00E+07	1.92E+05	2.95E+08	2.65E+08	2.9%
2	1.92E+05	2.97E+05	8.13E+08	6.49E+08	7.8%
3	2.97E+05	4.54E+02	9.59E+08	7.73E+08	5.3%
4	4.54E+02	3.73E+01	2.95E+08	2.95E+08	5.8%
5	3.73E+01	1.07E+01	1.45E+08	1.34E+08	3.2%
6	1.07E+01	1.86E+00	1.98E+08	1.54E+08	3.3%
7	1.86E+00	4.14E-01	1.81E+08	1.39E+08	3.6%
8	4.14E-01	1.0000E-05	9.64E+08	8.11E+08	2.9%
Total Fast Flux (Groups 1-7)	2.0000E+07	4.1399E-01	2.89E+09	2.41E+09	
Fast/Thermal Ratio			3.00	2.97	

Note: X^2 per degree of freedom = 1.01

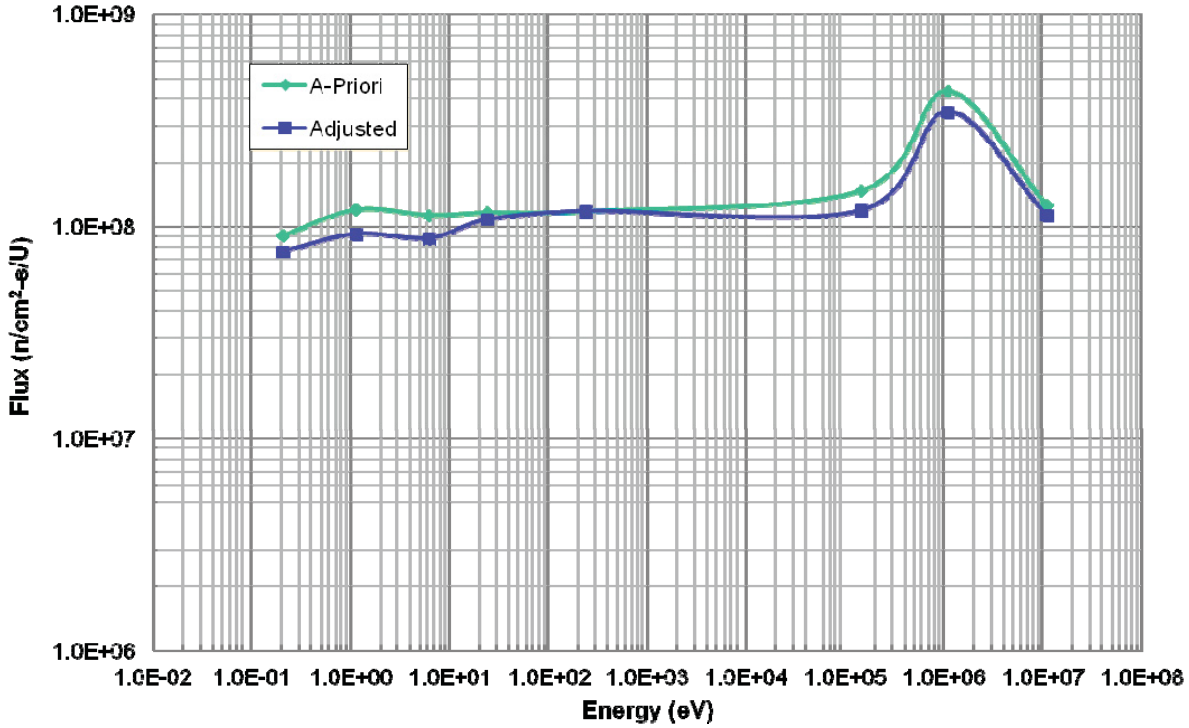

Figure 3.9 Eight-group spectrum adjustment for combined Experiments 1 and 3, corresponding to the group flux data in Table 3.5 (Equation 32a: θ=0.8, Γ=4). The *a priori* normalization uncertainty is assumed to be 10% and the *a priori* random uncertainty is assumed to be 20% . Combined correlated and uncorrelated uncertainty of the *a priori* fluxes is 22.4%.

Table 3.6. Measured, *a priori*, and adjusted foil interaction rates for Irradiations 1 and 3 combined.

Response	Spectral Mod.	Measured σΦ	*A priori* σΦ	Adjusted σΦ
Nb(n,2n)	Boron Sphere	2.64E-19	2.50E-19	2.24E-19
Ti-48 (n,p)	Boron Sphere	1.35E-19	1.62E-19	1.46E-19
Fe-56 (n,p)	Boron Sphere	5.12E-19	6.03E-19	5.41E-19
Ti-46 (n,p)	Boron Sphere	5.00E-18	6.08E-18	5.45E-18
Ti-47 (n,p)	Boron Sphere	1.17E-17	1.14E-17	1.01E-17
Fe-54 (n,p)	Boron Sphere	4.10E-17	4.71E-17	4.22E-17
Zn-502 (n,p)	Boron Sphere	2.05E-17	2.25E-17	2.02E-17
Ni-1004 (n,p)	Boron Sphere	5.72E-17	6.37E-17	5.68E-17
In-(n,n')	Boron Sphere	1.30E-16	1.46E-16	1.26E-16
In(n,n')	Cadmium	1.24E-16	1.48E-16	1.28E-16
In(n,n')	Cadmium	1.23E-16	1.48E-16	1.27E-16
Cu(n,γ)	Cadmium	3.44E-16	4.37E-16	3.53E-16
Cu(n,γ)	Cadmium	3.54E-16	4.42E-16	3.57E-16
Mn(n,γ)	Cadmium	9.52E-16	1.07E-15	9.47E-16
Mn(n,γ)	Cadmium	1.01E-15	1.07E-16	9.43E-16
W(n,γ)	Cadmium	2.79E-14	3.02E-14	2.77E-14
W(n,γ)	Cadmium	2.86E-14	3.11E-14	2.85E-14
Au(n,γ)	Cadmium	4.90E-14	6.42E-14	5.11E-14
Au(n,γ)	Cadmium	5.09E-14	6.24E-14	4.97E-14
In(n,γ)	Cadmium	8.03E-14	1.09E-13	8.41E-14
In(n,γ)	Cadmium	8.57E-14	1.09E-13	8.40E-14
Au(n,γ)	None	1.07E-13	1.31E-13	1.07E-13
Au(n,γ)	None	1.09E-13	1.32E-13	1.08E-13
Mn(n,γ)	None	8.74E-15	1.01E-14	8.52E-15
Mn(n,γ)	None	8.26E-15	1.01E-14	8.49E-15

Table 3.7 and Figure 3.10 illustrate a 36-group (and therefore underdetermined) spectral adjustment using the same *a priori* computational model as before, and the same measured foil interaction data from Table 3.2. Table 3.7 also shows how the *a priori* flux uncertainties are reduced by varying amounts at different neutron energies, depending on how much experimental information is available in each energy group used in the adjustment. Furthermore, it may be noted that the results are consistent with the overdetermined adjustment, well within the adjusted uncertainties. For example, the thermal flux ($E<0.414$ eV) was determined to be $8.11 \pm 2.9\%$ (1σ) by the overdetermined adjustment and $8.05 \pm 3.3\%$ (1σ) by the underdetermined adjustment, where the stated uncertainty in the latter case includes the effects of partial correlation between Groups 35 and 36 in the adjusted covariance matrix.

Table 3.7. 36-group neutron flux spectrum from foils – Northwest Large In-Pile Tube, Irradiations 1 and 3 combined. Reactor Power was 600W. MCNP5 *a priori.*

Group	Lower Energy (eV)	A priori Flux	% Total σ	Adjusted Flux	% Total σ	% Adjustment
1	1.00E+07	7.6283E+05	22.36	7.5662E+05	7.75	-0.81
2	6.07E+06	1.3540E+07	22.36	1.1554E+07	7.32	-14.67
3	3.01E+06	1.1118E+08	22.36	1.0274E+08	5.75	-7.59
4	2.37E+06	8.3249E+07	22.36	7.3001E+07	9.93	-12.31
5	1.92E+06	8.6220E+07	22.36	7.2548E+07	10.30	-15.86
6	1.35E+06	1.6451E+08	22.36	1.3245E+08	10.13	-19.49
7	1.00E+06	1.4458E+08	22.36	1.1495E+08	13.39	-20.50
8	8.21E+05	8.8055E+07	22.36	7.0072E+07	16.43	-20.42
9	7.43E+05	4.5930E+07	22.36	3.6658E+07	18.99	-20.19
10	6.08E+05	1.0305E+08	22.36	8.2680E+07	21.08	-19.77
11	4.98E+05	8.6923E+07	22.36	7.0655E+07	22.64	-18.72
12	3.69E+05	1.0780E+08	22.36	8.8769E+07	23.61	-17.65
13	2.97E+05	7.2473E+07	22.36	6.0403E+07	24.11	-16.65
14	1.83E+05	1.3385E+08	22.36	1.1235E+08	24.35	-16.06
15	1.11E+05	1.0876E+08	22.36	9.1636E+07	24.42	-15.74
16	6.74E+04	8.3888E+07	22.36	7.0567E+07	24.44	-15.88
17	4.09E+04	7.9947E+07	22.36	6.6732E+07	24.42	-16.53
18	3.18E+04	1.3928E+07	22.36	1.1495E+07	24.30	-17.47
19	2.61E+04	4.0372E+07	22.36	3.2784E+07	23.98	-18.80
20	2.42E+04	1.4146E+07	22.36	1.1322E+07	23.26	-19.97
21	2.19E+04	1.4150E+07	22.36	1.1220E+07	21.96	-20.71
22	1.50E+04	4.8421E+07	22.36	3.8361E+07	19.99	-20.78
23	7.10E+03	9.0999E+07	22.36	7.2718E+07	17.41	-20.09
24	3.35E+03	9.0184E+07	22.36	7.3886E+07	14.87	-18.07
25	1.58E+03	9.0728E+07	22.36	7.6717E+07	12.53	-15.44
26	4.54E+02	1.4966E+08	22.36	1.2164E+08	8.29	-18.72
27	2.14E+02	8.8010E+07	22.36	8.9386E+07	6.52	1.56
28	1.01E+02	8.9142E+07	22.36	8.2253E+07	11.57	-7.73
29	3.73E+01	1.1736E+08	22.36	1.0633E+08	11.56	-9.40
30	1.07E+01	1.4531E+08	22.36	1.3425E+08	3.16	-7.61
31	5.04E+00	8.3797E+07	22.36	6.9603E+07	10.76	-16.94
32	1.86E+00	1.1433E+08	22.36	8.7315E+07	5.91	-23.63
33	8.76E-01	8.8463E+07	22.36	6.7178E+07	3.85	-24.06
34	4.14E-01	9.2132E+07	22.36	7.3492E+07	12.97	-20.23
35	1.00E-01	2.6389E+08	22.36	2.1341E+08	12.49	-19.13
36	1.00E-05	7.0027E+08	22.36	5.9208E+08	3.73	-15.45
Total		3.8500E+09		3.2240E+09		-16.26

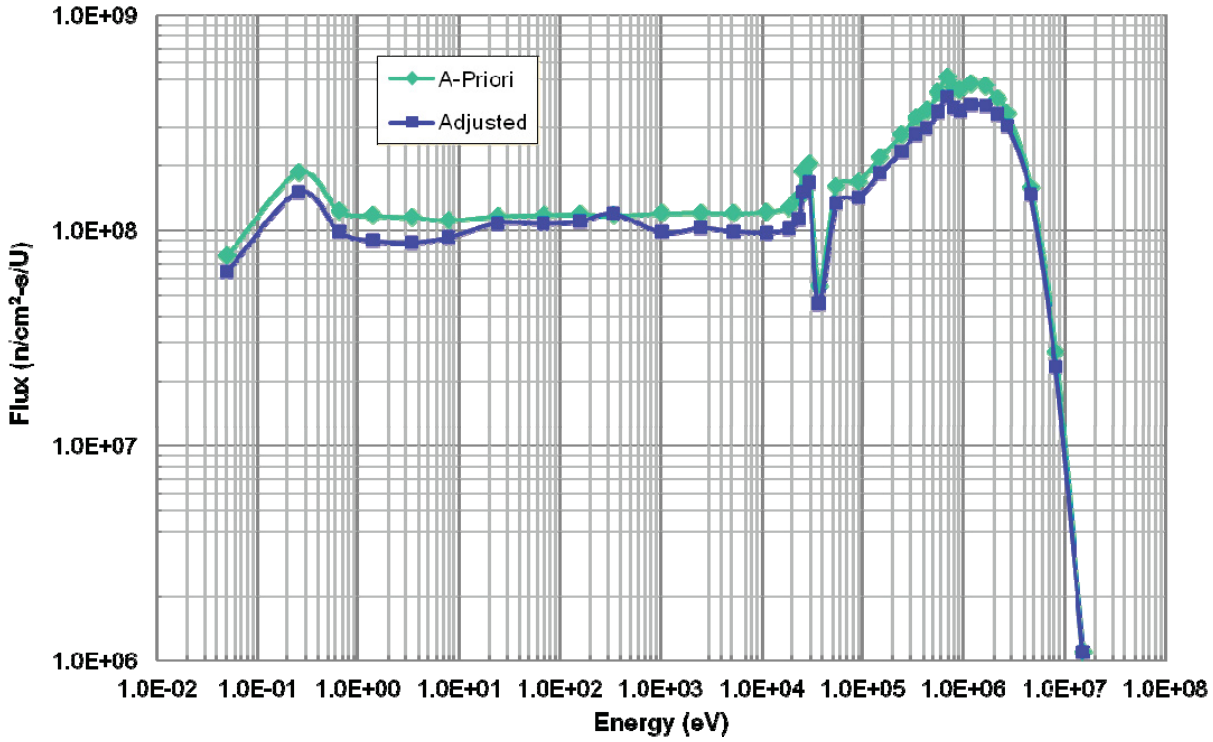

Figure 3.10. 36-group spectrum adjustment for combined Experiments 1 and 3 (Equation 32a: θ=0.8, Γ=4). The *a priori* normalization uncertainty is assumed to be 10% and the *a priori* random uncertainty is assumed to be 20%. Combined correlated and uncorrelated uncertainty of the *a priori* fluxes is 22.4%.

3.3 Initial Validation Measurements in the ATRC Core Fuel Elements: Irradiation 4

Here we describe some selected measurements of the fast (>0.414 eV) and thermal (<0.414 eV) neutron flux within selected core fuel elements surrounding the NW LIPT and the SE IPT as well as fission power measurements made for every other fuel element in the core. These measurements were conducted during February, 2011.

3.3.1 Methods and Materials

In Irradiation 4, activation measurements were made with gold/copper (1.55% Au by weight alloyed in natural Cu) flux wires, the same as described previously, as well as with fission wires composed of 10% by weight ^{235}U in aluminum. The various wires were 1 mm in diameter and approximately 0.635 cm (0.25") in length. The reactor was operated at a power of 720 watts for 20 minutes.

The fission wires were placed in 17 different locations within the cooling channels of each odd-numbered ATRC core fuel element (Figure 3.5), at the core axial midplane. The core fuel element numbering scheme starts with the circled element in Figure 3.11 and proceeds clockwise around the serpentine path of the core. The total measured fission powers for the fuel elements are based on weighted sums of the measured fission rates in the U/Al wires located in each element, computed by the standard protocol used at ATR (Durney and Kauffman, 1967). The uranium fission rates in each wire were measured by the INL RML using a protocol based on gross beta counting.

The Au/Cu flux wires were placed in each of three locations (the innermost, center and outermost radial coolant channels) within fuel elements 12, 14, 16, and 18 in the southeast lobe of the core and fuel elements 32, 34, 36, and 38 in the northwest lobe, again at the axial midplane. Two-group adjusted neutron fluxes were obtained from the measured Au and Cu neutron capture rates (or saturation activities) at each of these 24 locations using the methodology described in Section 3.1. For the initial analysis, the elements of the adjustment matrix and the *a priori* flux vector for each Au/Cu wire were computed using an MCNP5 model of the reactor and experimental apparatus, with nuclear data based on a combination of ENDF/B Version 7 for the transport calculation and IRDF-2002 for the dosimeter interaction rates. Corresponding NEWT, HELIOS and ATTILA models were also developed later for further analysis of Irradiation 4, extending the validation protocols to all codes currently used in the overall suite, with the exception of KENO6, which is used primarily as an uncertainty quantification tool rather than for core design and analysis.

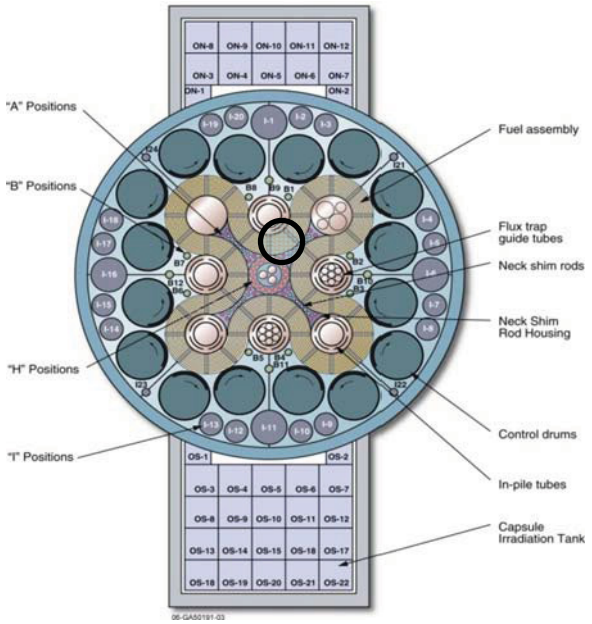

Figure 3.11. Core and reflector geometry of the Advanced Test Reactor. Fuel element number 1 is circled. References to core lobes and in-pile tubes are with respect to reactor north, at the top of the figure.

3.3.2 Fission Power Distributions

Figure 3.12 shows the calculated (MCNP5 *a priori*) fission powers for the 40 ATRC fuel elements and for all five ATRC lobes, along with the measured fission powers based on the fission wire measurements for the odd-numbered elements. The measured lobe powers and the total reactor power were computed using a standard convention based on symmetry: Simply stated, when only the odd-numbered fuel element powers are measured, the power for each even-numbered element is assumed to be equal to the measured power in the odd-numbered element on the opposite side of the same lobe. For example, the power in Element 2 is assumed equal to the power in Element 9, the power in Element 4 is assumed equal to the power in Element 7, and so forth around the core. This assumption may or may not be reasonable, depending on the overall symmetry of the reactor configuration. Of particular interest here

are the results for the SE and NW lobes, comprised of fuel elements 12-19 and 32-39, respectively. MCNP5 yields fission powers that are about 1.5% lower than measured for the SE lobe and about 8% higher than measured for the NW lobe. The corresponding lobe fission power "tilt" (ratio of SE to NW) is then 1.263 for the a priori calculation and 1.385 for the measurements. The difference could be caused by any number of factors, including the possibility of geometric and material composition discrepancies between the as-built reactor and the model representation, possible minor inaccuracies in the exact rotating shim settings at critical, etc.

Figure 3.12 shows the MCNP *a priori* and the measured element powers for Irradiation 4, plotted as a function of element number around the serpentine azimuthal axis of the core. A set of adjusted element powers, calculated for all 40 elements using the available measurements for the 20 odd-numbered elements using the methodology described in Section 3.1.7, is shown in Table 3.8. It can be seen that the adjusted element powers tend to follow the measured powers in the odd-numbered elements. This is a consequence of the fact that the stated uncertainty in the measured element powers (5%) is significantly smaller than the assumed uncertainty of the *a priori* element powers, as estimated by the magnitude of the adjustments needed to obtain consistency with the measured power distribution. The adjusted powers in the even-numbered elements are least-square weighted averages of the neighboring odd-numbered elements with the specific weighting determined by the covariance matrix provided for the adjustment process. All adjustments are seen to be consistent with the stated uncertainty of the *a priori* element powers, as expected, and the adjusted uncertainties for all elements are reduced from the *a priori* uncertainties, again as expected. Figure 3.13 shows the *a priori* and adjusted fuel element fission power distribution, and the corresponding measurements, in graphical form as a function of fuel element number within the serpentine ATRC core.

Table 3.9. shows the *a priori* and measured lobe powers from Figure 3.12, along with the adjusted lobe powers which can be computed simply by summing the adjusted element powers for each lobe, with no further need for the symmetry assumption. It can be seen that the adjustment brings the SE\NW tilt ratio into much better agreement with the measured ratio. Of particular note is the fact that the adjusted lobe powers are also closer to the measured powers, and the total core power is nearly the same.

Table 3.10, Figure 3.14, and Table 3.11 show the same fuel element power distribution information for the case where the NEWT code is used for the *a priori* power distribution calculation. Likewise, Table 3.12, Figure 3.15, and Table 3.13 are for the case where HELIOS is used. Finally, Table 3.14, Figure 3.16, and Table 3.15 are for ATTILA. In all cases, adjustments are within the stated uncertainties and excellent consistency is observed.

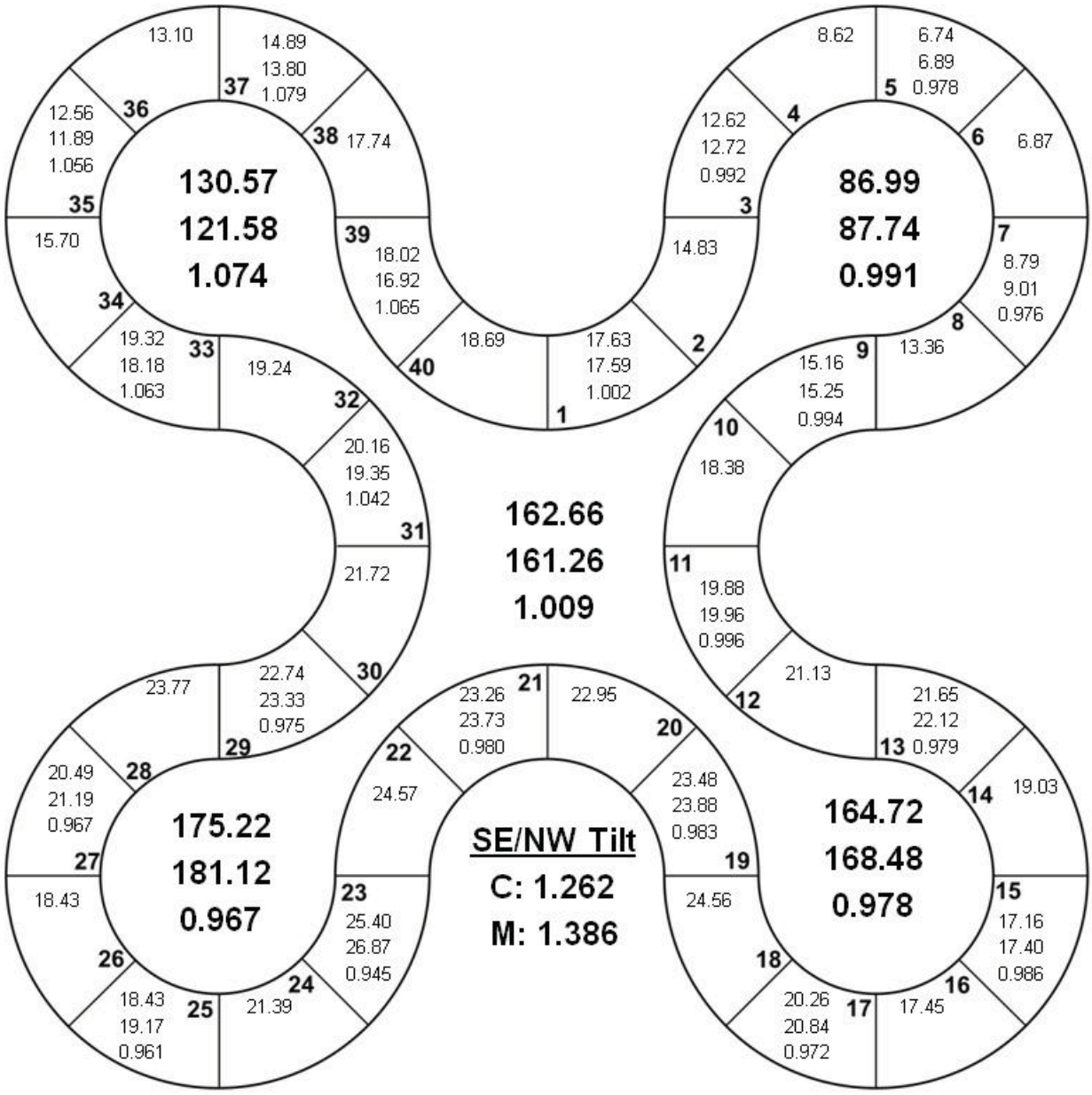

Figure 3.12. MCNP *a priori* (top) and measured (center) total fission powers and the corresponding ratio of the two (bottom) in each fuel element and in each 8-element lobe of the ATRC. Total measured power is 720.2 watts. Uncertainties associated with the measured results are 5% (1σ).

Table 3.8. Fuel element fission rate distribution for Irradiation 4 (MCNP *a priori)*. The *a priori* normalization uncertainty is assumed to be 5% and the *a priori* random uncertainty is assumed to be 10%. Total correlated plus uncorrelated *a priori* uncertainties are listed. Adjustment performed with Equation 32b using θ=1.0 and Γ=1. The adjusted powers are computed using the measured data for only the odd-numbered fuel elements.

Element	*A Priori* Power (W)	Uncertainty % (1σ)	Adjusted Power (W)	Uncertainty % (1σ)	Adjustment Factor	Measured Power (W)
1	17.63	11.18	17.59	3.42	0.998	17.59
2	14.83	11.18	15.12	8.86	1.020	
3	12.62	11.18	12.74	3.41	1.010	12.72
4	8.62	11.18	8.29	9.40	0.962	
5	6.74	11.18	6.81	3.45	1.011	6.89
6	6.87	11.18	6.54	9.51	0.952	
7	8.79	11.18	8.94	3.44	1.017	9.01
8	13.36	11.18	13.86	8.72	1.037	
9	15.16	11.18	15.30	3.41	1.010	15.25
10	18.38	11.18	18.43	9.02	1.003	
11	19.88	11.18	19.97	3.42	1.004	19.96
12	21.13	11.18	21.96	8.70	1.039	
13	21.65	11.18	22.08	3.42	1.020	22.12
14	19.03	11.18	18.44	9.34	0.969	
15	17.16	11.18	17.24	3.45	1.005	17.40
16	17.45	11.18	16.94	9.32	0.971	
17	20.26	11.18	20.66	3.44	1.020	20.84
18	24.56	11.18	25.66	8.66	1.045	
19	23.48	11.18	23.96	3.40	1.020	23.88
20	22.95	11.18	23.32	8.90	1.016	
21	23.26	11.18	23.75	3.41	1.021	23.73
22	24.57	11.18	25.90	8.59	1.054	
23	25.40	11.18	26.81	3.41	1.056	26.87
24	21.39	11.18	21.06	9.20	0.985	
25	18.43	11.18	18.98	3.44	1.030	19.17
26	18.43	11.18	18.01	9.26	0.977	
27	20.49	11.18	21.03	3.44	1.026	21.19
28	23.77	11.18	24.53	8.77	1.032	
29	22.74	11.18	23.37	3.41	1.028	23.33
30	21.72	11.18	21.63	9.07	0.996	
31	20.16	11.18	19.43	3.42	0.964	19.35
32	19.24	11.18	19.35	8.97	1.006	
33	19.32	11.18	18.27	3.42	0.945	18.18
34	15.70	11.18	14.28	9.91	0.909	
35	12.56	11.18	11.87	3.44	0.945	11.89
36	13.10	11.18	11.71	10.09	0.894	
37	14.89	11.18	13.77	3.45	0.925	13.80
38	17.74	11.18	17.41	9.18	0.981	
39	18.02	11.18	17.04	3.41	0.946	16.92
40	18.69	11.18	18.22	9.25	0.975	
Total	720.16	1.83	720.28	1.12		720.18

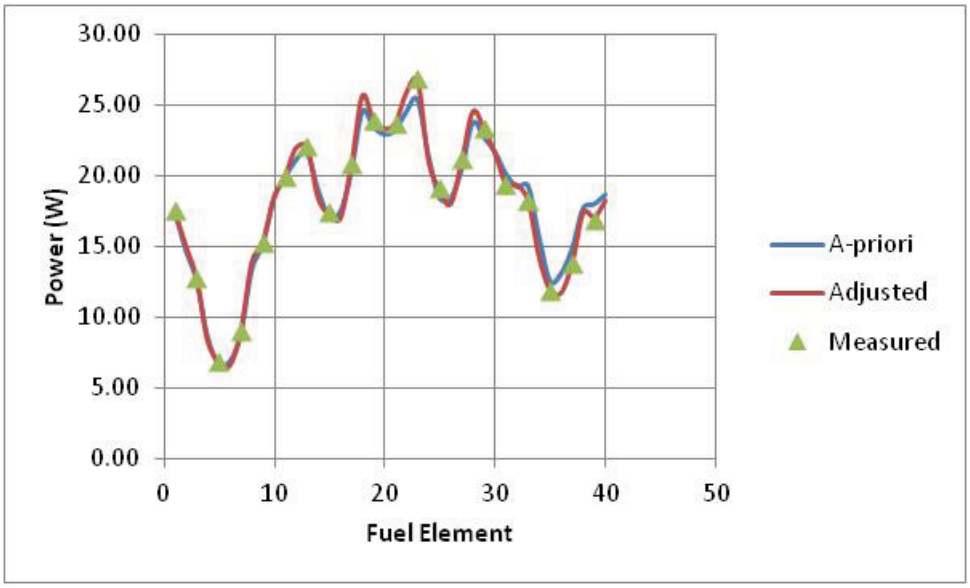

Figure 3.13. Fuel element fission rate distribution for Irradiation 4 (MCNP *a priori).* The *a priori* normalization uncertainty is assumed to be 5% and the *a priori* random uncertainty is assumed to be 10%. Total correlated plus uncorrelated *a priori* uncertainty =11.2%. Adjustment performed with Equation 32b using θ=1.0 and Γ=1. The adjusted powers are computed using the measured data for only the odd-numbered fuel elements.

Table 3.9. Lobe power distributions for Irradiation 4, derived from the data in Figure 3.13 (MCNP *a priori).* *A priori* lobe power uncertainties are in the range of 7% and Adjusted lobe power uncertainties are in the range of 3%.

Lobe	A priori	Measured	C/M	Adjusted	A/M
NE	86.99	87.74	0.991	87.60	0.998
SE	164.72	168.48	0.978	166.95	0.991
SW	175.22	181.12	0.967	179.68	0.992
NW	130.57	121.58	1.074	123.70	1.017
Center	162.66	161.26	1.009	162.34	1.007
Sum	720.16	720.18		720.28	
SE/NW Tilt	1.262	1.386		1.350	

Table 3.10 Fuel element fission rate distribution for Irradiation 4 (NEWT *a priori).* The *a priori* normalization uncertainty is assumed to be 5% and the *a priori* random uncertainty is assumed to be 10%. Total correlated plus uncorrelated *a priori* uncertainties are listed. Adjustment performed with Equation 32b using θ=1.0 and Γ=1. The adjusted powers are computed using the measured data for only the odd-numbered fuel elements.

Element	*A Priori* Power (W)	Uncertainty % (1σ)	Adjusted Power (W)	Uncertainty % (1σ)	Adjustment Factor	Measured Power (W)
1	19.08	11.18	17.53	3.45	0.919	17.59
2	16.04	11.18	15.09	9.59	0.941	
3	13.08	11.18	12.70	3.43	0.971	12.72
4	7.96	11.18	8.28	8.71	1.041	
5	6.02	11.18	6.77	3.43	1.124	6.89
6	6.09	11.18	6.51	8.51	1.069	
7	8.20	11.18	8.90	3.43	1.086	9.01
8	13.83	11.18	13.87	9.01	1.003	
9	16.74	11.18	15.24	3.45	0.911	15.25
10	19.78	11.18	18.40	9.68	0.930	
11	21.42	11.18	19.89	3.45	0.929	19.96
12	22.28	11.18	21.93	9.17	0.984	
13	21.60	11.18	22.02	3.43	1.019	22.12
14	17.33	11.18	18.40	8.55	1.061	
15	15.14	11.18	17.15	3.42	1.133	17.40
16	15.44	11.18	16.88	8.32	1.093	
17	18.53	11.18	20.57	3.42	1.110	20.84
18	24.82	11.18	25.68	8.75	1.035	
19	25.05	11.18	23.87	3.43	0.953	23.88
20	24.54	11.18	23.27	9.51	0.948	
21	25.12	11.18	23.67	3.44	0.942	23.73
22	25.82	11.18	25.86	9.02	1.001	
23	25.66	11.18	26.73	3.42	1.042	26.87
24	19.48	11.18	21.01	8.43	1.078	
25	16.39	11.18	18.88	3.42	1.152	19.17
26	16.23	11.18	17.93	8.24	1.105	
27	18.74	11.18	20.94	3.42	1.117	21.19
28	23.47	11.18	24.53	8.67	1.045	
29	23.96	11.18	23.29	3.43	0.972	23.33
30	23.01	11.18	21.59	9.61	0.938	
31	21.66	11.18	19.35	3.45	0.893	19.35
32	20.40	11.18	19.29	9.52	0.946	
33	19.50	11.18	18.21	3.43	0.934	18.18
34	14.37	11.18	14.29	9.08	0.995	
35	11.62	11.18	11.83	3.43	1.018	11.89
36	11.45	11.18	11.69	8.86	1.021	
37	13.56	11.18	13.73	3.43	1.012	13.80
38	17.77	11.18	17.40	9.21	0.979	
39	19.11	11.18	16.97	3.44	0.888	16.92
40	19.87	11.18	18.18	9.84	0.915	
Total	720.16	1.84	718.30	1.13		720.18

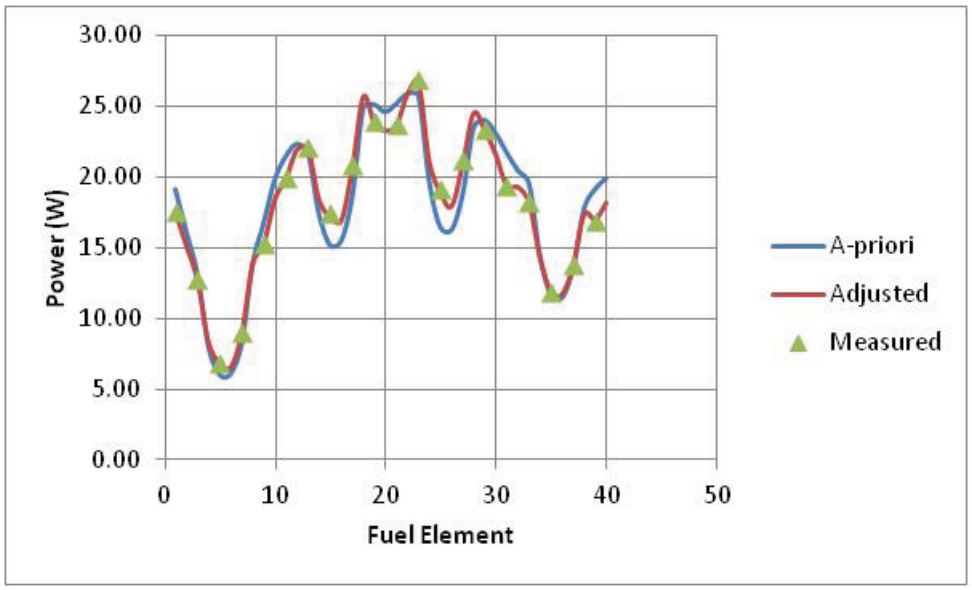

Figure 3.14. Fuel element fission rate distribution for Irradiation 4 (NEWT *a priori).* The *a priori* normalization uncertainty is assumed to be 5% and the *a priori* random uncertainty is assumed to be 10%. Total correlated plus uncorrelated *a priori* uncertainty =11.2%. Adjustment performed with Equation 32b using θ=1.0 and Γ=1. The adjusted powers are computed using the measured data for only the odd-numbered fuel elements.

Table 3.11. Lobe power distributions for Irradiation 4, derived from the data in Figure 3.14 (NEWT *a priori).* *A priori* lobe power uncertainties are in the range of 7% and Adjusted lobe power uncertainties are in the range of 3%.

Lobe	A priori	Measured	C/M	Adjusted	A/M
NE	87.95	87.74	1.002	87.37	0.996
SE	160.18	168.48	0.951	166.49	0.988
SW	169.76	181.12	0.937	179.16	0.989
NW	127.77	121.58	1.051	123.40	1.015
Center	174.49	161.26	1.082	161.88	1.004
Sum	720.16	720.18		718.30	
SE/NW Tilt	1.254	1.386		1.349	

Table 3.12. Fuel element fission rate distribution for Irradiation 4 (HELIOS *a priori).* The *a priori* normalization uncertainty is assumed to be 5% and the *a priori* random uncertainty is assumed to be 10%. Total correlated plus uncorrelated *a priori* uncertainties are listed. Adjustment performed with Equation 32b using θ=1.0 and Γ=1. The adjusted powers are computed using the measured data for only the odd-numbered fuel elements.

Element	*A Priori* Power (W)	Uncertainty % (1σ)	Adjusted Power (W)	Uncertainty % (1σ)	Adjustment Factor	Measured Power (W)
1	17.75	11.18	17.57	3.42	0.990	17.59
2	16.02	11.18	15.10	9.57	0.942	
3	14.17	11.18	12.72	3.45	0.898	12.72
4	10.03	11.18	8.29	10.88	0.826	
5	7.73	11.18	6.82	3.48	0.882	6.89
6	7.98	11.18	6.53	10.97	0.819	
7	11.02	11.18	8.95	3.49	0.812	9.01
8	15.87	11.18	13.83	10.30	0.871	
9	17.35	11.18	15.27	3.45	0.880	15.25
10	19.21	11.18	18.43	9.38	0.960	
11	20.96	11.18	19.94	3.44	0.951	19.96
12	23.00	11.18	21.94	9.46	0.954	
13	22.30	11.18	22.06	3.43	0.989	22.12
14	18.14	11.18	18.44	8.92	1.016	
15	15.38	11.18	17.19	3.42	1.117	17.40
16	15.83	11.18	16.89	8.50	1.067	
17	19.93	11.18	20.64	3.44	1.035	20.84
18	25.32	11.18	25.68	8.91	1.014	
19	25.49	11.18	23.92	3.43	0.938	23.88
20	23.54	11.18	23.31	9.12	0.990	
21	23.46	11.18	23.72	3.42	1.011	23.73
22	25.07	11.18	25.88	8.77	1.032	
23	24.51	11.18	26.78	3.40	1.093	26.87
24	18.86	11.18	21.04	8.16	1.116	
25	15.31	11.18	18.89	3.39	1.234	19.17
26	15.31	11.18	17.92	7.79	1.171	
27	18.55	11.18	20.97	3.41	1.131	21.19
28	22.33	11.18	24.53	8.26	1.099	
29	22.60	11.18	23.34	3.41	1.033	23.33
30	20.84	11.18	21.63	8.71	1.038	
31	19.66	11.18	19.41	3.41	0.987	19.35
32	19.65	11.18	19.29	9.19	0.982	
33	18.98	11.18	18.25	3.42	0.962	18.18
34	14.61	11.18	14.29	9.23	0.978	
35	11.75	11.18	11.85	3.43	1.009	11.89
36	11.81	11.18	11.70	9.11	0.991	
37	14.63	11.18	13.75	3.45	0.940	13.80
38	18.05	11.18	17.40	9.34	0.964	
39	18.63	11.18	17.01	3.43	0.913	16.92
40	18.38	11.18	18.24	9.09	0.992	
Total	720.01	1.82	719.40	1.12		720.18

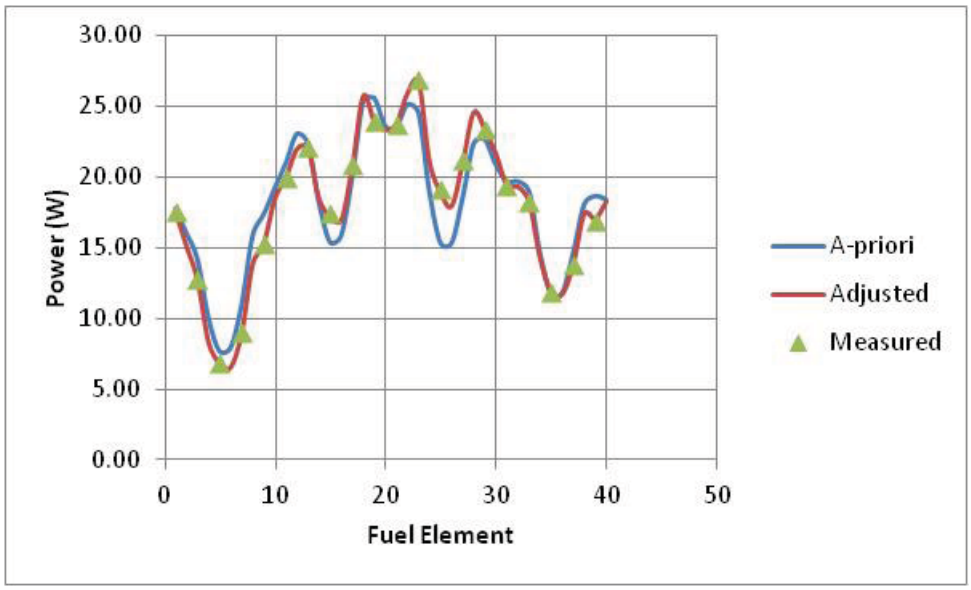

Figure 3.15. Fuel element fission rate distribution for Irradiation 4 (HELIOS *a priori)*. The *a priori* normalization uncertainty is assumed to be 5% and the *a priori* random uncertainty is assumed to be 10%. Total correlated plus uncorrelated *a priori* uncertainty =11.2%. Adjustment performed with Equation 32b using θ=1.0 and Γ=1. The adjusted powers are computed using the measured data for only the odd-numbered fuel elements.

Table 3.13. Lobe power distributions for Irradiation 4, derived from the data in Figure 3.15 (HELIOS *a priori)*. *A priori* lobe power uncertainties are in the range of 7% and Adjusted lobe power uncertainties are in the range of 3%.

Lobe	A priori	Measured	C/M	Adjusted	A/M
NE	100.17	87.74	1.142	87.50	0.997
SE	165.39	168.48	0.982	166.75	0.990
SW	162.54	181.12	0.897	179.37	0.990
NW	128.11	121.58	1.054	123.55	1.016
Center	163.80	161.26	1.016	162.24	1.006
Sum	720.01	720.18		719.40	
SE/NW Tilt	1.291	1.386		1.350	

Table 3.14. Fuel element fission rate distribution for Irradiation 4 (ATTILA *a priori).* The *a priori* normalization uncertainty is assumed to be 5% and the *a priori* random uncertainty is assumed to be 10%. Total correlated plus uncorrelated *a priori* uncertainties are listed. Adjustment performed with Equation 32b using θ=1.0 and Γ=1. The adjusted powers are computed using the measured data for only the odd-numbered fuel elements.

Element	*A Priori* Power (W)	Uncertainty % (1σ)	Adjusted Power (W)	Uncertainty % (1σ)	Adjustment Factor	Measured Power (W)
1	16.81	11.18	17.63	3.40	1.048	17.59
2	15.07	11.18	15.13	9.00	1.004	
3	13.57	11.18	12.76	3.43	0.940	12.72
4	9.47	11.18	8.29	10.29	0.875	
5	7.81	11.18	6.84	3.48	0.876	6.89
6	8.21	11.18	6.57	11.23	0.801	
7	9.91	11.18	8.96	3.46	0.904	9.01
8	14.12	11.18	13.84	9.20	0.980	
9	15.09	11.18	15.33	3.40	1.016	15.25
10	16.67	11.18	18.47	8.17	1.108	
11	18.35	11.18	20.00	3.39	1.090	19.96
12	20.96	11.18	21.97	8.64	1.048	
13	21.73	11.18	22.12	3.42	1.018	22.12
14	19.63	11.18	18.45	9.61	0.940	
15	17.92	11.18	17.28	3.45	0.964	17.40
16	18.22	11.18	16.97	9.69	0.931	
17	20.95	11.18	20.70	3.45	0.988	20.84
18	24.94	11.18	25.66	8.79	1.029	
19	23.23	11.18	24.00	3.40	1.033	23.88
20	20.45	11.18	23.37	7.93	1.143	
21	21.13	11.18	23.80	3.37	1.126	23.73
22	23.81	11.18	25.90	8.34	1.088	
23	25.51	11.18	26.85	3.41	1.053	26.87
24	21.63	11.18	21.07	9.29	0.974	
25	19.01	11.18	19.02	3.45	1.000	19.17
26	18.76	11.18	18.02	9.41	0.961	
27	20.75	11.18	21.06	3.44	1.015	21.19
28	23.90	11.18	24.54	8.81	1.027	
29	22.87	11.18	23.40	3.41	1.023	23.33
30	19.78	11.18	21.68	8.25	1.096	
31	18.90	11.18	19.47	3.39	1.030	19.35
32	19.12	11.18	19.35	8.92	1.012	
33	19.55	11.18	18.29	3.42	0.936	18.18
34	15.53	11.18	14.30	9.77	0.921	
35	13.63	11.18	11.89	3.46	0.872	11.89
36	13.41	11.18	11.72	10.29	0.874	
37	15.08	11.18	13.79	3.45	0.915	13.80
38	17.98	11.18	17.42	9.30	0.969	
39	18.06	11.18	17.07	3.41	0.945	16.92
40	17.26	11.18	18.29	8.52	1.060	
Total	718.78	1.82	721.26	1.11		720.18

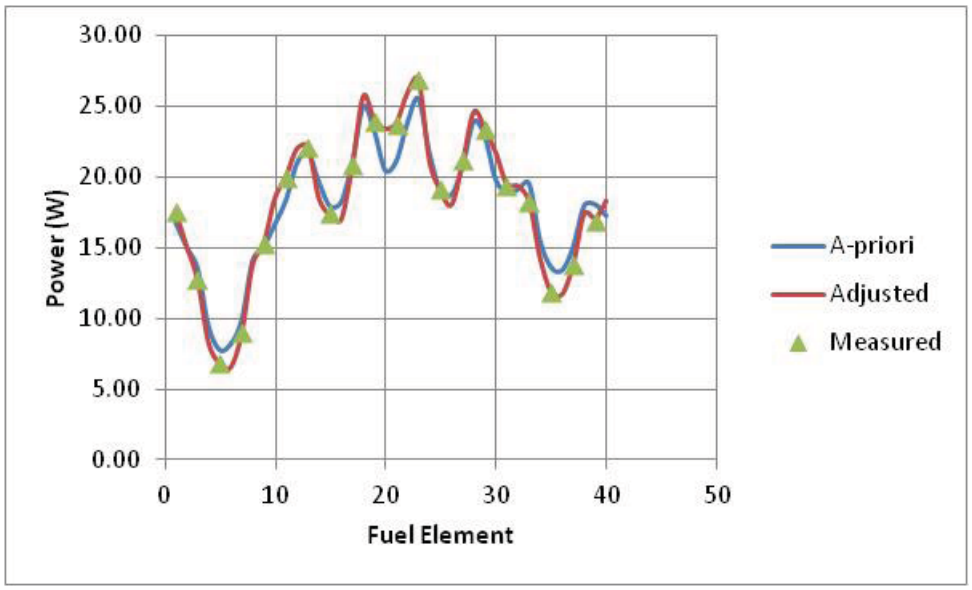

Figure 3.16 . Fuel element fission rate distribution for Irradiation 4 (ATTILA *a priori).* The *a priori* normalization uncertainty is assumed to be 5% and the *a priori* random uncertainty is assumed to be 10%. Total correlated plus uncorrelated *a priori* uncertainty =11.2%. Adjustment performed with Equation 32b using θ=1.0 and Γ=1. The adjusted powers are computed using the measured data for only the odd-numbered fuel elements.

Table 3.15. Lobe power distributions for Irradiation 4, derived from the data in Figure 3.16 (ATTILA *a priori).* *A priori* lobe power uncertainties are in the range of 7% and Adjusted lobe power uncertainties are in the range of 3%.

Lobe	A priori	Measured	C/M	Adjusted	A/M
NE	93.25	87.74	1.063	87.71	1.000
SE	167.58	168.48	0.995	167.14	0.992
SW	176.24	181.12	0.973	179.87	0.993
NW	132.36	121.58	1.089	123.83	1.018
Center	149.35	161.26	0.926	162.72	1.009
Sum	718.78	720.18		721.26	
SE/NW Tilt	1.266	1.386		1.350	

3.3.3 Neutron Flux Spectra and Spectral Indices

We now examine some typical information that can be obtained from the Au/Cu flux wires, in combination with the MCNP *a priori* model. The various discussions are equally applicable to the models based on the other transport codes, and a few selected examples of results from application of the protocol to those codes will be provided as well.

Table 3.16 shows the measured saturation activities for all 24 Au/Cu wires placed in the core fuel elements. These activation rates were used to obtain sets of two-group adjusted neutron fluxes for each wire position as discussed previously.

Table 3.16. Measured activation rates (captures per atom per second) and spectral indices for the Au/Cu wires in the core fuel elements – ATRC Irradiation 4.

Wire	Au (c/atom-s)	Uncertainty % (1σ)	Cu (c/atom-s)	Uncertainty % (1σ)	Au/Cu	Uncertainty % (1σ)
12-2 (Inner)	3.2125E-13	2.56	4.9821E-15	2.96	64.48	3.91
12-11 (Middle)	2.7380E-13	2.92	2.5322E-15	3.74	108.13	4.74
12-19 (Outer)	2.9687E-13	2.80	3.4810E-15	2.66	85.28	3.86
14-2	2.6858E-13	3.00	3.4894E-15	2.78	76.97	4.09
14-11	2.2272E-13	2.63	2.2665E-15	3.22	98.27	4.16
14-19	2.4333E-13	3.08	3.3439E-15	3.46	72.77	4.63
16-2	2.6611E-13	2.60	3.2807E-15	2.92	81.11	3.91
16-11	2.0996E-13	2.72	2.1105E-15	2.99	99.48	4.04
16-19	2.1083E-13	2.69	2.7451E-15	2.72	76.80	3.82
18-2	2.9890E-13	2.61	3.7825E-15	2.73	79.02	3.78
18-11	2.8425E-13	2.59	2.8400E-15	2.91	100.09	3.90
18-19	3.3605E-13	2.59	5.3680E-15	3.27	62.60	4.17
32-2	2.9803E-13	2.58	3.9195E-15	2.66	76.04	3.71
32-11	2.5174E-13	2.84	2.5027E-15	3.29	100.59	4.35
32-19	2.5189E-13	2.61	2.8210E-15	3.15	89.29	4.09
34-2	2.0923E-13	2.69	2.4584E-15	2.92	85.11	3.97
34-11	1.8427E-13	2.85	1.8288E-15	3.49	100.76	4.51
34-19	1.9545E-13	2.71	2.8210E-15	2.86	69.28	3.94
36-2	1.8660E-13	3.14	2.3487E-15	2.88	79.44	4.26
36-11	1.4916E-13	2.88	1.3549E-15	3.39	110.09	4.45
36-19	1.4340E-13	2.76	1.8033E-15	2.93	79.52	4.02
38-2	2.2476E-13	2.55	2.5069E-15	3.12	89.66	4.03
38-11	1.9719E-13	2.67	2.0460E-15	3.39	96.38	4.31
38-19	2.2519E-13	2.86	3.4451E-15	3.19	65.37	4.29

Table 3.17 shows the averages of the a priori and adjusted 2-group neutron fluxes in the NW and SE lobes, based on the data for the 12 Au/Cu wires placed in the listed fuel elements in each lobe. These results are unweighted averages of 2-group flux data for the 12 wire positions in each lobe. They do not represent true volume averages of the fluxes, and they are also not necessarily proportional to the lobe fission powers discussed earlier. Rather, they are based on a representative sample of 12 symmetric, uniformly-distributed, measurement positions in each lobe and they are useful for computing certain ratios of interest.

Table 3.17. A priori (MCNP5) and adjusted average neutron spectrum data for the ATRC SE and NW lobes.

A priori:	Group 1	± (1σ) %	Group 2	± (1σ) %
SE Flux	5.94E+09		9.89E+08	
SE Spectrum	0.857		0.143	
NW Flux	4.85E+09		7.71E+08	
NW Spectrum	0.863		0.137	
Tilt (SE/NW)	1.226		1.282	
Adjusted:	Group 1	± (1σ) %	Group 2	± (1σ) %
SE Flux	5.81E+09	1.16	8.84E+08	1.33
SE Spectrum	0.868	1.54	0.132	1.68
NW Flux	4.50E+09	1.15	6.53E+08	1.37
NW Spectrum	0.873	1.54	0.127	1.71
Tilt (SE/NW)	1.290	1.63	1.353	1.91

It can be seen from Table 3.17 that the adjusted two-group neutron spectra are somewhat "harder" than the a priori spectra, primarily due to a reduction in the thermal flux component by the adjustment process. Of particular additional note is the fact that the adjustment process brings the SE/NW thermal flux tilt more into line with the observed tilt for the element fission powers shown in Figure 3.12. This is consistent with the fact that the fission power in the ATR is primarily proportionate to the thermal neutron flux. The average of the a priori thermal flux over the 12 fuel locations in the Northwest lobe was a factor of 1.18 higher than the corresponding average adjusted flux for the same 12 locations. This is consistent with the results reported in Section 3.2 for the thermal flux inside of the Northwest Large In-Pile tube, which is largely driven by the surrounding fuel elements (Elements 32-39). Similar results are obtained when using the NEWT, HELIOS and ATTILA codes for the *a priori* calculation.

Table 3.18 shows the *a priori* and adjusted spectral indices for each Au/Cu wire along with the measured indices listed earlier. It can be seen that the 2-group adjustment process brings the spectral indices into exact agreement with the measured indices. This results from the fact that in this particular case the adjustment was done using an unconstrained fully determined formulation, i.e. no covariance matrix was included and the uncertainties for the *a priori* fluxes calculated by MCNP were thus effectively assumed to be infinite and the adjustment is totally driven by the measurements. Tables 3.19 and 3.20 show the same spectral index adjustments for the cases where NEWT and HELIOS were used to compute the *a priori* information. In these latter two cases, covariance matrices were in fact included in the adjustment, but with the uncertainty set to an arbitrary 99%, effectively causing the adjustment to again be driven by the measurements only, just as was the case for the calculation with MCNP used for the *a priori*.

Table 3.18 Measured, *a priori,* and adjusted spectral indices for the Au/Cu wires in the core fuel elements – ATRC Irradiation 4 (MCNP *A priori).*

Wire	Measured Au/Cu	*A Priori* Au/Cu	Adjusted Au/Cu
12-2 (Inner)	64.48	69.02	64.48
12-11 (Middle)	108.13	97.35	108.13
12-19 (Outer)	85.28	82.84	85.28
14-2	76.97	70.05	76.97
14-11	98.27	97.38	98.27
14-19	72.77	66.55	72.77
16-2	81.11	70.89	81.11
16-11	99.48	92.56	99.48
16-19	76.80	72.71	76.80
18-2	79.02	73.15	79.02
18-11	100.09	99.54	100.09
18-19	62.60	59.40	62.60
32-2	76.04	70.37	76.04
32-11	100.59	96.05	100.59
32-19	89.29	84.08	89.29
34-2	85.11	79.95	85.11
34-11	100.76	98.97	100.76
34-19	69.28	64.78	69.28
36-2	79.44	80.77	79.45
36-11	110.09	97.46	110.09
36-19	79.52	69.69	79.52
38-2	89.66	84.42	89.66
38-11	96.38	96.08	96.38
38-19	65.37	64.83	65.37

Table 3.19 Measured, *a priori,* and adjusted spectral indices for the Au/Cu wires in the core fuel elements – ATRC Irradiation 4 (NEWT *A priori).*

Wire	Measured Au/Cu	*A Priori* Au/Cu	Adjusted Au/Cu
12-2 (I)	64.48	65.92	64.48
12-11 (M)	108.13	89.48	108.07
12-19 (O)	85.28	75.71	85.27
14-2	76.97	67.90	76.95
14-11	98.27	87.16	98.23
14-19	72.77	63.79	72.73
16-2	81.11	67.87	81.08
16-11	99.48	87.75	99.45
16-19	76.80	69.24	76.78
18-2	79.02	69.34	79.01
18-11	100.09	85.67	100.06
18-19	62.60	57.91	62.59
32-2	76.04	68.27	76.03
32-11	100.59	89.98	100.56
32-19	89.29	80.10	89.27
34-2	85.11	74.01	85.08
34-11	100.76	87.66	100.72
34-19	69.28	63.07	69.27
6-2	79.44	73.72	79.43
36-11	110.09	88.45	110.03
36-19	79.52	69.20	79.50
38-2	89.66	74.69	89.63
38-11	96.38	87.09	96.35
38-19	65.37	62.28	65.36

Table 3.20 Measured, *a priori,* and adjusted spectral indices for the Au/Cu wires in the core fuel elements – ATRC Irradiation 4 (HELIOS *A priori).*

Wire	Measured Au/Cu	*A Priori* Au/Cu	Adjusted Au/Cu
12-2 (I)	64.48	71.29	64.49
12-11 (M)	108.13	91.20	108.06
12-19 (O)	85.28	82.04	85.27
14-2	76.97	73.64	76.96
14-11	98.27	88.78	98.23
14-19	72.77	67.77	72.75
16-2	81.11	72.94	81.10
16-11	99.48	89.77	99.45
16-19	76.80	76.47	76.80
18-2	79.02	75.90	79.01
18-11	100.09	88.70	100.05
18-19	62.60	66.02	62.61
32-2	76.04	72.73	76.03
32-11	100.59	91.88	100.55
32-19	89.29	87.30	89.27
34-2	85.11	81.46	85.10
34-11	100.76	89.49	100.71
34-19	69.28	67.43	69.28
36-2	79.44	80.86	79.45
36-11	110.09	90.71	110.02
36-19	79.52	76.57	79.51
38-2	89.66	82.56	89.63
38-11	96.38	89.94	96.34
38-19	65.37	69.47	65.37

The results given above were based on simple 2-group adjustment analyses, as noted. However, detailed full-range spectral adjustments also can be useful, even in the situation described here where the Au/Cu flux wires provide only two linearly-independent measurements at each core location. For example, Table 3.21 and Figure 3.17 show the results of a 49-group underdetermined spectral analysis for the center flux wire location of Fuel Element 12. In this case the first two rows of Equations 20 and 21 reflect the Au and Cu measurements, respectively, and the other 47 rows contain the *a priori* information. As expected, the adjustment shows a hardening of the spectrum (relative reduction of the thermal neutron flux), consistent with the fact that the measured spectral index for this position was 108.13 while the *a priori* index was 97.35. The adjusted index for the 47-group adjustment was 106.55, reflecting the fact that the adjustment was constrained by a covariance matrix based on a fully correlated normalization uncertainty that was assumed to be 10% and partially-correlated random uncertainties assumed to be 20%. Thus the adjustment was largely driven by the measurement uncertainties listed in Table 3.16, but the *a priori* flux uncertainty still had some effect, reflecting the fact that the computational model does in fact provide some useful information (i.e. the computational uncertainty is not infinite, which would imply that the computations are useless, which is not the case). Finally we note that the uncertainties for the adjusted fluxes remain unchanged above approximately 1 keV, reflecting the fact that the copper and gold activity measurements contribute little information above this energy. However, the uncertainties are substantially reduced below this energy where resonance and thermal neutron capture interactions in gold and copper do contribute useful information.

Table 3.21. 49-group spectrum adjustment results for Fuel Element 12, Center Position (Equation 32a, θ=0.8, Γ=4) using Cu/Au wire activation (MCNP *a priori)*. The *a priori* normalization uncertainty is assumed to be 10% and the *a priori* random uncertainty is assumed to be 20%.

Group	Upper Energy (eV)	A priori Flux	% Total σ	Adjusted Flux	% Total σ	% Adjustment
1	2.0000E+07	5.4355E+04	22.36	5.2412E+04	22.49	-3.57
2	1.9000E+07	9.9327E+04	22.36	9.5775E+04	22.49	-3.58
3	1.7300E+07	1.7984E+05	22.36	1.7340E+05	22.49	-3.58
4	1.4200E+07	9.8319E+05	22.36	9.4797E+05	22.49	-3.58
5	1.2200E+07	3.6484E+06	22.36	3.5176E+06	22.49	-3.59
6	1.0000E+07	6.6768E+06	22.36	6.4370E+06	22.49	-3.59
7	8.6100E+06	1.3253E+07	22.36	1.2776E+07	22.49	-3.60
8	7.4700E+06	4.2104E+07	22.36	4.0586E+07	22.49	-3.61
9	6.0700E+06	8.7469E+07	22.36	8.4308E+07	22.49	-3.61
10	4.9700E+06	2.1702E+08	22.36	2.0916E+08	22.49	-3.62
11	3.6800E+06	1.9759E+08	22.36	1.9041E+08	22.49	-3.63
12	3.0100E+06	1.2456E+08	22.36	1.2002E+08	22.49	-3.64
13	2.7300E+06	1.2363E+08	22.36	1.1911E+08	22.50	-3.66
14	2.4700E+06	6.3325E+07	22.36	6.1001E+07	22.50	-3.67
15	2.3700E+06	1.2814E+07	22.36	1.2342E+07	22.50	-3.69
16	2.3500E+06	7.5301E+07	22.36	7.2508E+07	22.50	-3.71
17	2.2300E+06	2.1212E+08	22.36	2.0419E+08	22.50	-3.74
18	1.9200E+06	2.2429E+08	22.36	2.1585E+08	22.51	-3.76
19	1.6500E+06	2.9692E+08	22.36	2.8566E+08	22.51	-3.79
20	1.3500E+06	4.0284E+08	22.36	3.8743E+08	22.51	-3.83
21	1.0000E+06	2.3037E+08	22.36	2.2150E+08	22.52	-3.85
22	8.2100E+05	1.3249E+08	22.36	1.2735E+08	22.52	-3.88
23	7.4300E+05	2.3724E+08	22.36	2.2797E+08	22.52	-3.91
24	6.0800E+05	2.0496E+08	22.36	1.9689E+08	22.52	-3.94
25	4.9800E+05	2.3209E+08	22.36	2.2286E+08	22.53	-3.98
26	3.6900E+05	1.7513E+08	22.36	1.6809E+08	22.53	-4.02
27	2.9700E+05	3.1938E+08	22.36	3.0634E+08	22.53	-4.09
28	1.8300E+05	2.3390E+08	22.36	2.2416E+08	22.54	-4.16
29	1.1100E+05	2.0559E+08	22.36	1.9680E+08	22.55	-4.28
30	6.7400E+04	1.6503E+08	22.36	1.5771E+08	22.56	-4.44
31	4.0900E+04	7.3375E+07	22.36	6.9963E+07	22.56	-4.65
32	3.1800E+04	6.6091E+07	22.36	6.2840E+07	22.56	-4.92
33	2.6100E+04	2.2177E+07	22.36	2.1019E+07	22.54	-5.22
34	2.4200E+04	2.7291E+07	22.36	2.5786E+07	22.50	-5.51
35	2.1900E+04	1.0933E+08	22.36	1.0306E+08	22.42	-5.73
36	1.5000E+04	2.0673E+08	22.36	1.9473E+08	22.27	-5.81
37	7.1000E+03	1.9624E+08	22.36	1.8530E+08	22.00	-5.57
38	3.3500E+03	1.9145E+08	22.36	1.8173E+08	21.54	-5.08
39	1.5800E+03	2.9105E+08	22.36	2.7746E+08	20.80	-4.67
40	4.5400E+02	1.7897E+08	22.36	1.7332E+08	19.53	-3.16
41	2.1400E+02	1.8566E+08	22.36	1.8126E+08	17.88	-2.37
42	1.0100E+02	2.3080E+08	22.36	2.2629E+08	15.81	-1.96
43	3.7300E+01	2.5794E+08	22.36	2.5157E+08	14.01	-2.47
44	1.0700E+01	1.5861E+08	22.36	1.5356E+08	11.53	-3.18
45	5.0400E+00	2.1063E+08	22.36	2.0366E+08	4.59	-3.31
46	1.8600E+00	1.5148E+08	22.36	1.3849E+08	11.97	-8.58
47	8.7600E-01	1.6502E+08	22.36	1.4603E+08	12.38	-11.51
48	4.1400E-01	3.4508E+08	22.36	2.9407E+08	11.92	-14.78
49	1.0000E-01	4.4503E+08	22.36	3.6329E+08	8.66	-18.37
Total		7.7540E+09		7.3297E+09		-5.47

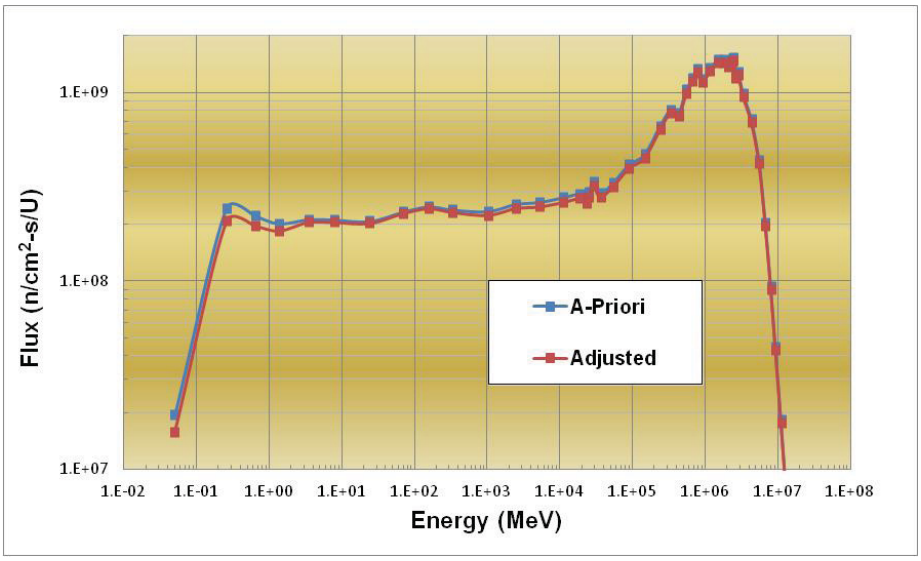

Figure 3.17. 49-group spectrum adjustment for Fuel Element 12, Center Position (Equation 32a, θ=0.8, Γ=4) using Cu/Au wire activation (MCNP *a priori)*. The *a priori* normalization uncertainty is assumed to be 10% and the *a priori* random uncertainty is assumed to be 20%.

Further demonstrating the use of HELIOS for spectral computations in particular, Figure 3.18 shows the computed spectra for all three measurement locations in Fuel Element 12. HELIOS uses a pre-generated 49-group cross section library that has 11 energy groups in the thermal energy range below approximately 0.5 eV, which allows very detailed analyses of spectral shifts throughout the ATR fuel element structure. Thus the computed spectra shown in Figure 3.18 for the three measurement locations clearly show why the spectral indices differ, with the largest measured index being observed in the center of the fuel element. The neutron spectrum tends to harden in the interior of the fuel element because the fuel is under moderated, and the beryllium reflector tends to preferentially soften the spectrum near the inner and outer radii of the element. In addition, the fuel plates contain boron, which also tends to shield the center of the fuel element from thermal neutrons originating in the surrounding beryllium reflector.

As indicated earlier, the validation protocols illustrated here are applicable to any of the codes in the ATR suite. To further demonstrate this, we repeat the spectral adjustment procedure for the center location of Fuel Element 12 using HELIOS rather than MCNP to compute the *a priori* flux information. Figure 3.19 shows the computed perturbed and unperturbed *a priori* neutron spectra at this location, i.e. $\psi_d(E)$ and $\psi(E)$ in Equation(2), respectively. The self shielding of the 5 eV capture resonance in gold is clearly evident. Figure 3.20 then shows the *a priori* and adjusted neutron spectra for this location using the same adjustment parameters as were assumed for the earlier adjustment (Figure 3.17), where MCNP was used for the *a priori* calculation. The results of the two different adjustments are very consistent, and the additional detail that the HELIOS application provides in the thermal energy range can be seen. Such fine detail could also be obtained by tallying the MCNP flux over a finer group structure, but this would require a significant increase in computer time to obtain satisfactory Monte Carlo statistics. Finally, Table 3.22 shows the *a priori* and adjusted Au and Cu responses corresponding to the spectra in Figure 3.20, along with the measured activation rates for reference. Once again, the adjustment process has produced excellent consistency even in such an extreme underdetermined case.

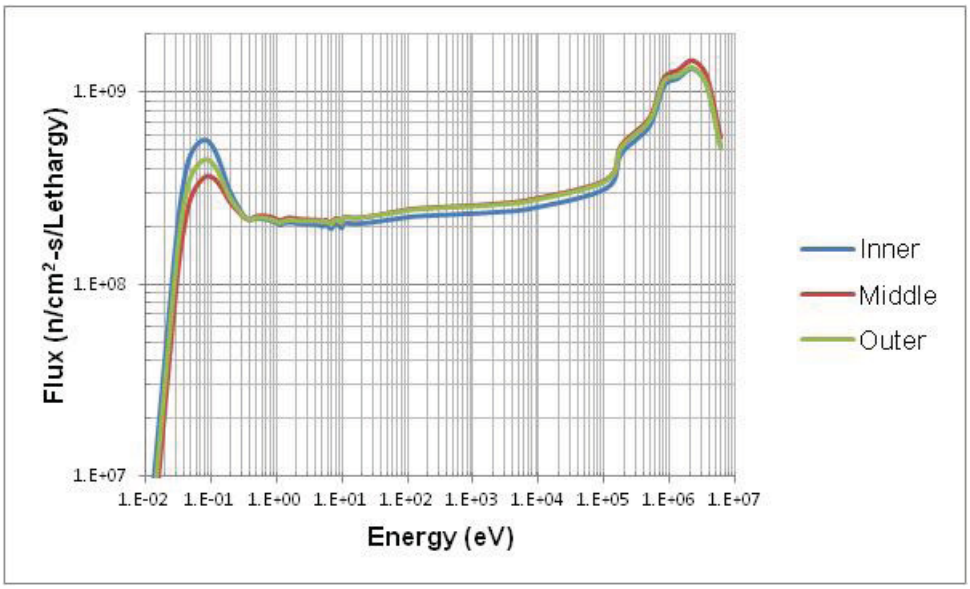

Figure 3.18. Calculated Neutron Spectra for the Measurement Positions in Element 12, ATRC Irradiation 4 (HELIOS *A Priori).* Measured spectral Index Values are 64.48, 108.13 and 85.28 for the Inner, Middle and Outer Positions, Respectively.

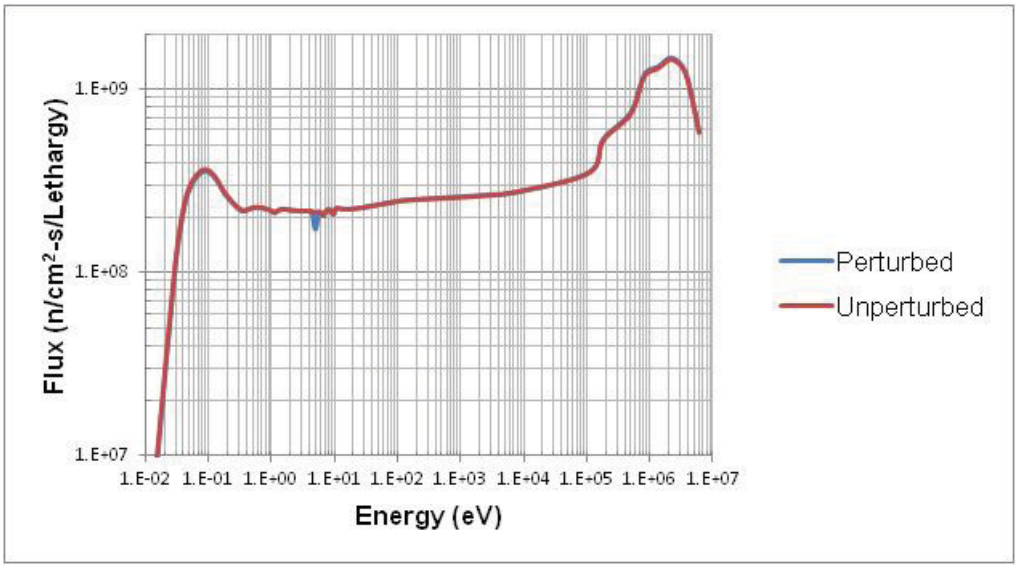

Figure 3.19. Calculated Unperturbed and Perturbed Neutron Spectra at the Position of the Center Wire, Element 12, ATRC Irradiation 4 (HELIOS *A Priori).*

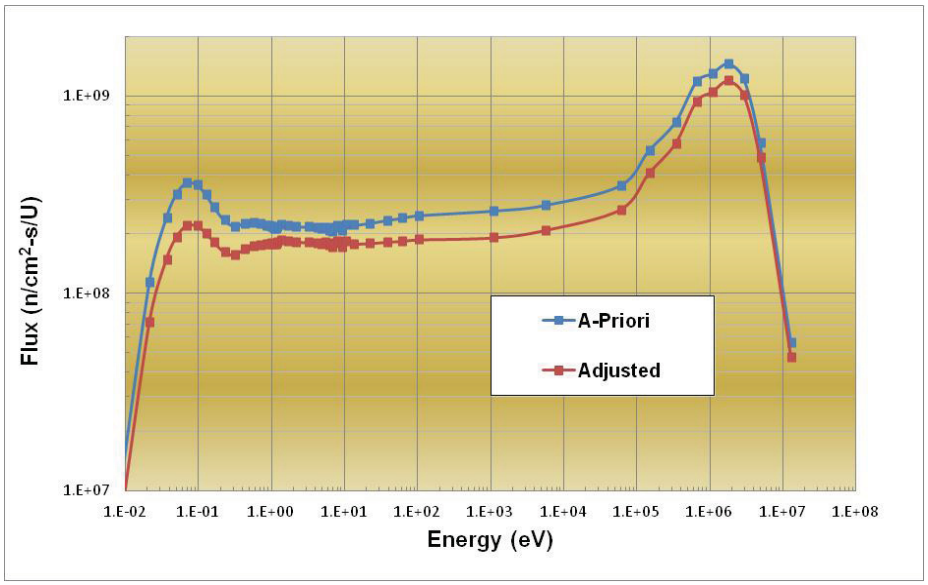

Figure 3.20. 49-group spectrum adjustment for Fuel Element 12, Center Position (Equation 32a, θ=0.8, Γ=4) using Cu/Au wire activation (HELIOS *a priori)*. The *a priori* normalization uncertainty is assumed to be 10% and the *a priori* random uncertainty is assumed to be 20%.

Table 3.21. A *priori* and adjusted gold and copper activation rates corresponding to the *a priori* and adjusted spectra in Figure 3.20, Fuel Element 12, Center Position (HELIOS *a priori)*. Measured data are shown in the bottom rows.

Response	A priori	% Total σ
Au	3.43E-13	17.90
Cu	3.77E-15	14.97
Au/Cu	91.06	
Response	Adjusted	% Total σ
Au	2.74E-13	2.89
Cu	2.57E-15	3.62
Au/Cu	106.72	
Response	Measured	% Total σ
Au	2.74E-13	2.92
Cu	2.53E-15	3.74
Au/Cu	108.13	

3.4 Demonstration of a Semi-Analytic Verification Protocol for HELIOS

The various codes incorporated into the new ATR reactor physics suite are either industry standard tools (e.g. HELIOS) or mature National Laboratory codes (e.g. MCNP). All have been subjected to extensive verification testing for mathematical accuracy and portability among computer hardware operating systems, compilers etc. Nonetheless, just as is the case for validation, verification is also an ongoing process as applications for the various computational tools evolve. Accordingly, the ATR Core Modeling Update project includes a small component that is dedicated to development of a few ATR-specific verification benchmarks that can be used for additional software quality assurance. Appendix A describes a key benchmark that was developed during FY-2012 and its application to the HELIOS code. In this benchmark, a semi-analyic solution to the neutron slowing down and thermalization problem in a medium representative of ATR core fuel elements is established for verification against the HELIOS solution. Figure 3.21, below shows a key result from this exercise, where the benchmark spectrum for a particular case is directly compared to the result produced by the corresponding HELIOS calculation. Excellent agreement is apparent. Further details are provided in Appendix A.

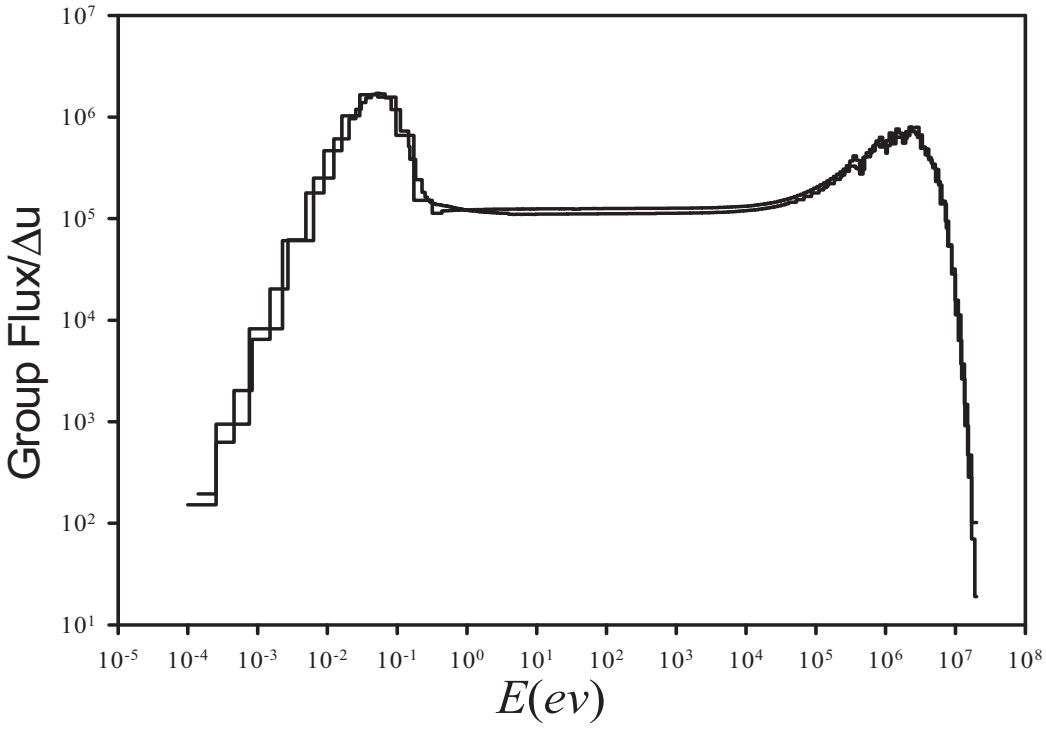

Figure 3.21. Comparison of HELIOS flux and semi-analytic benchmark flux for an infinite medium of water and uranium (B.D. Ganapol, D.S. Crawford, Appendix A).

3.5 Initial Validation Measurements in the ATRC Core: ATR Depressurized Operations Support

In an unanticipated development during FY-2012, it was separately determined that additional core physics measurements would be required to support an operational cycle (152B) that was planned for startup late in the year. These measurements were incorporated into a "depressurized" ATR cycle (152A), to be run prior to startup of Cycle 152B. In depressurized operations, the ATR is brought to a critical state at a very low power, well below the level that requires significant fission heat removal, permitting access to the core for more detailed neutronics than are normally done to support startup of each cycle. In particular, fission power measurements can be made in selected fuel elements using the fission wire technique described earlier. Detailed control shim reactivity worth measurements can also be performed.

In the case of Cycle 152A, the ATR was loaded with 40 fresh fuel elements and the various experiment locations were loaded in a manner that was as close to what will be the case for the follow-on high-power Cycle (152B). In addition, the ATR Critical Facility was also loaded with 40 fresh fuel elements of the same type that are used in the ATR. (Ordinarily the ATRC has its own set of standard fuel elements that are geometrically identical to ATR elements, but the fuel composition and boron content in each plate are slightly different). In addition, the experiment locations in the ATRC were loaded with surrogate experiments that were as neutronically identical to the actual experiments loaded in the ATR itself.

Because of the timing, it was not possible to include an analysis of the actual ATR depressurized operations data in this Annual Report. However, it was possible to include some analysis of one of the supporting ATRC experiments used to plan the corresponding ATR depressurized operation that was scheduled somewhat later. This experiment, referred to as ATRC Support Test 12-5 here, involved a detailed measurement of the fission power in all 40 fuel elements, rather than only the odd-numbered elements as is the usual practice. This offered an excellent opportunity for some additional validation of the various ATRC models using several different codes of interest, with a relatively complicated set of experiments loaded into the flux traps. It also permitted a valuable test of the proposed least-squares algorithm for estimating powers for all 40 elements when measurements are made only for some subset of all 40 elements.

Figure 3.22 shows the computed (MCNP) and measured powers for all 40 elements. These are plotted in Figure 3.23, along with the adjusted power distribution computed from Equations 31 and 32b. Figures 3.24-3.26 show the same information for the cases where HELIOS, NEWT and SERPENT, respectively, were used for the *a priori* calculation. Figure 3.26 represents the first-ever application of the new SERPENT code for ATRC (or ATR) analysis. Table 3.23 provides all of the data for the four codes in numerical form. The results differ in the details, but all show good consistency within the stated uncertainties.

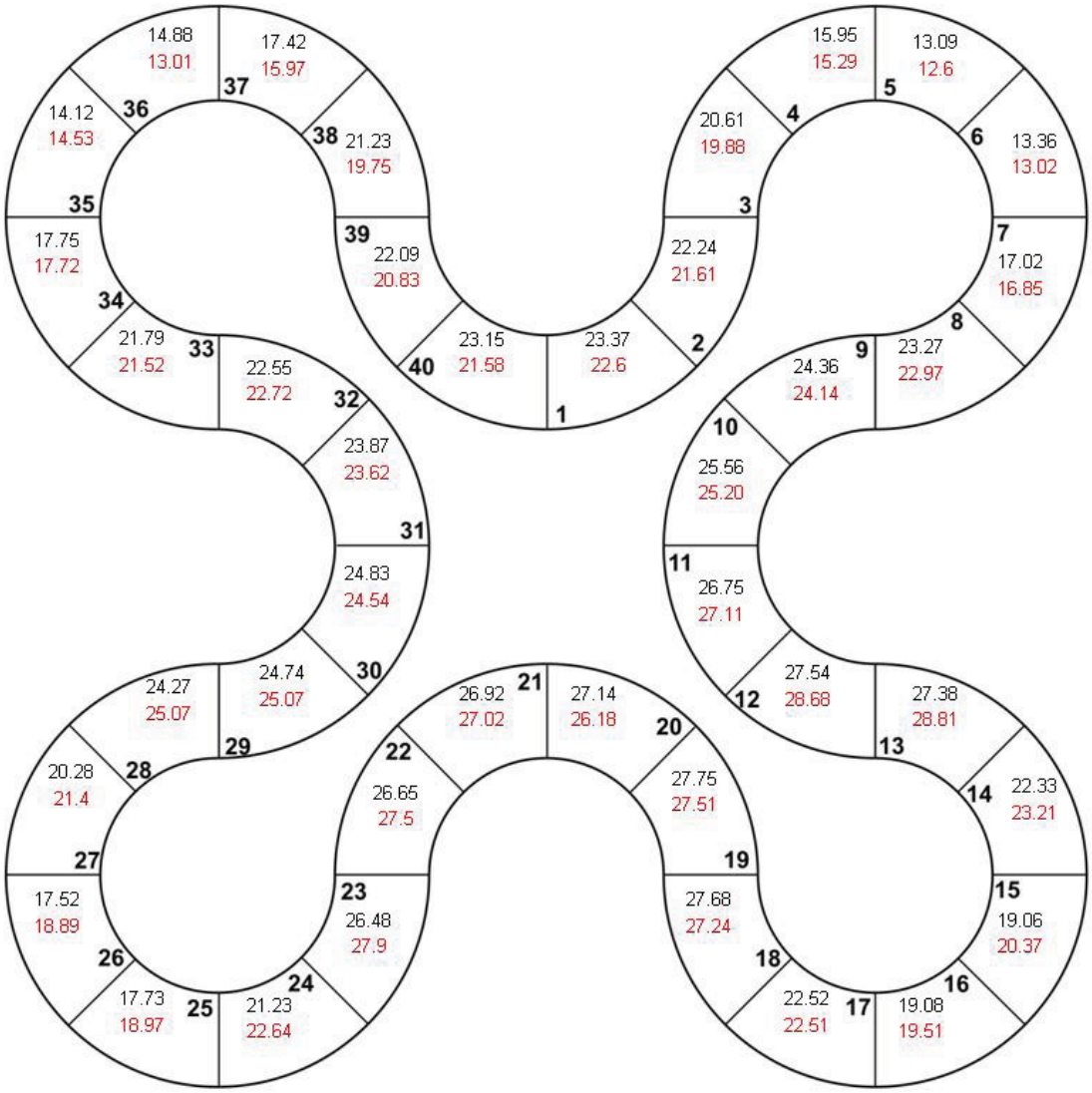

Figure 3.22. Fuel element fission rates for ATRC Depressurized Run for Support Test 12-5 (MCNP *A Priori)*. Top number is the *a priori* result, bottom number is the measurement. Total measured power is 875.5 watts. Uncertainties associated with the measured results are 5% (1σ) or smaller.

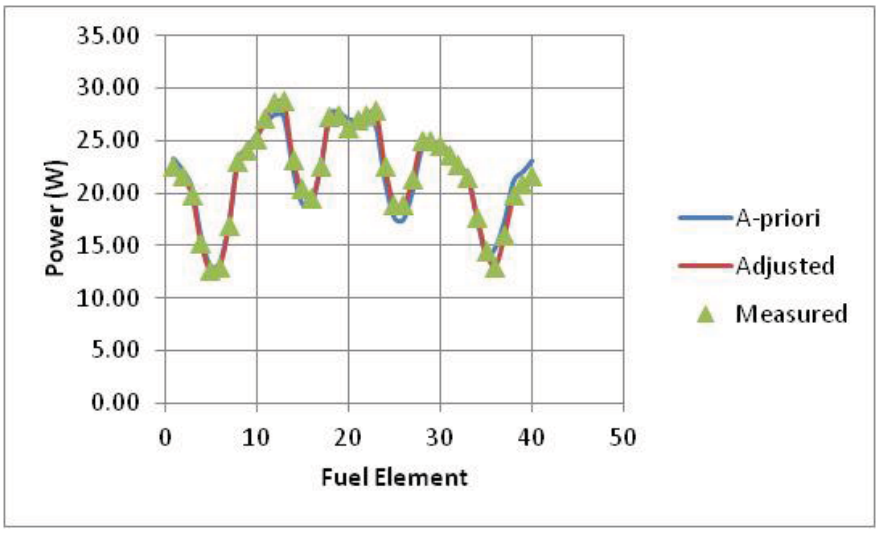

Figure 3.23 . Fuel element fission rate distribution for ATRC Depressurized Run Support Test 12-5 (MCNP *a priori).* The *a priori* normalization uncertainty is assumed to be 5% and the *a priori* random uncertainty is assumed to be 10%. Total correlated plus uncorrelated *a priori* uncertainty =11.2%. Adjustment performed with θ=1.0 and Γ=1. Reduced uncertainties for the adjusted powers are in the range of 3.4% for all elements.

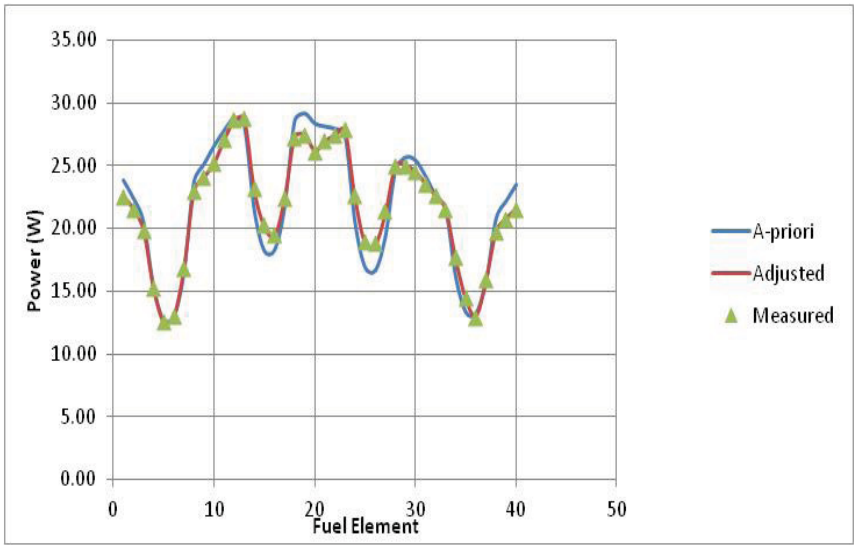

Figure 3.24 . Fuel element fission rate distribution for ATRC Depressurized Run Support Test 12-5 NEWT *a priori).* The *a priori* normalization uncertainty is assumed to be 5% and the *a priori* random uncertainty is assumed to be 10%. Total correlated plus uncorrelated *a priori* uncertainty =11.2%. Adjustment performed with θ=1.0 and Γ=1. Reduced uncertainties for the adjusted powers are in the range of 3.4% for all elements.

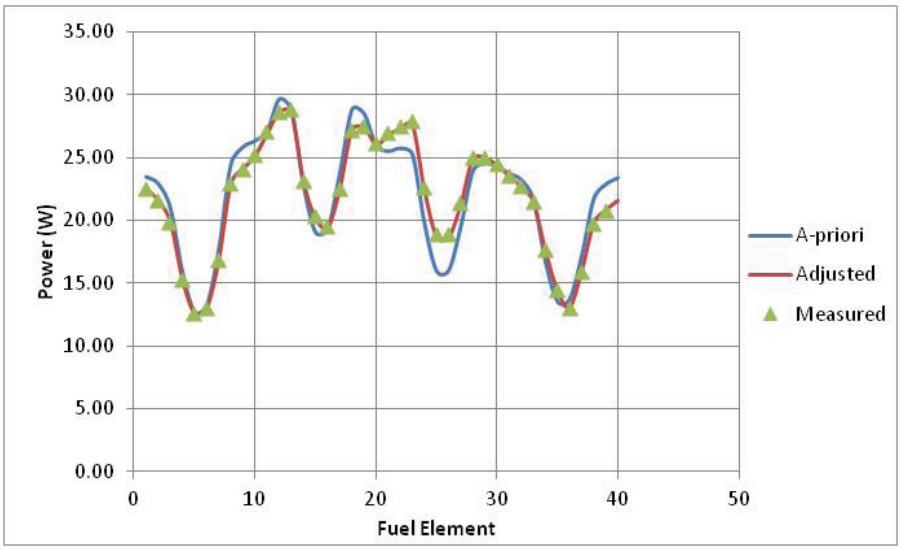

Figure 3.25. Fuel element fission rate distribution for ATRC Depressurized Run Support Test 12-5 (HELIOS *a priori).* The *a priori* normalization uncertainty is assumed to be 5% and the *a priori* random uncertainty is assumed to be 10%. Total correlated plus uncorrelated *a priori* uncertainty =11.2%. Adjustment performed with θ=1.0 and Γ=1. Reduced uncertainties for the adjusted powers are in the range of 3.4% for all elements.

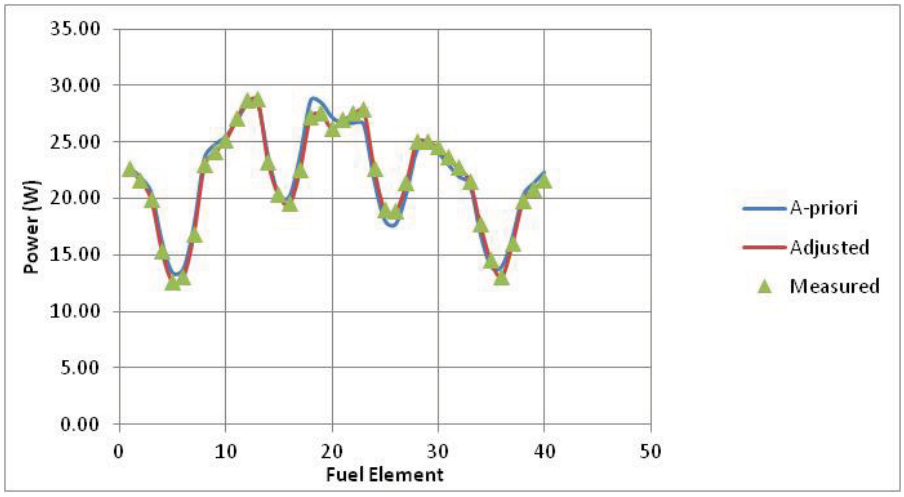

Figure 3.26 . Fuel element fission rate distribution for ATRC Depressurized Run Support Test 12-5 SERPENT *a priori).* The *a priori* normalization uncertainty is assumed to be 5% and the *a priori* random uncertainty is assumed to be 10%. Total correlated plus uncorrelated *a priori* uncertainty =11.2%. Adjustment performed with θ=1.0 and Γ=1. Reduced uncertainties for the adjusted powers are in the range of 3.4% for all elements.

Table 3.23. Fuel element fission rate distributions for ATRC Depressurized Run Support Test 12-5 for all four physics codes tested. The *a priori* normalization uncertainty is assumed to be 5% and the *a priori* random uncertainty is assumed to be 10% . Total correlated plus uncorrelated *a priori* uncertainty =11.2% in all cases. Adjustment performed with θ=1.0 and Γ=1. Total correlated plus uncorrelated adjusted uncertainty = 3.4% in all cases.

Element	*A Priori* Power MCNP	Adjusted Power MCNP	*A Priori* Power NEWT	Adjusted Power NEWT	*A Priori* Power HELIOS	Adjusted Power HELIOS	*A Priori* Power SERPENT	Adjusted Power SERPENT	Measured Power (W)
1	23.37	22.57	23.83	22.55	23.47	22.50	22.64	22.55	22.60
2	22.24	21.59	22.40	21.55	22.91	21.59	21.80	21.58	21.61
3	20.61	19.88	20.51	19.85	20.98	19.85	20.44	19.88	19.88
4	15.95	15.29	15.37	15.22	15.85	15.25	16.10	15.31	15.29
5	13.09	12.60	12.74	12.57	12.72	12.54	13.38	12.62	12.60
6	13.36	13.01	13.01	12.98	13.22	12.96	13.71	13.03	13.02
7	17.02	16.82	16.47	16.73	17.73	16.82	17.52	16.86	16.85
8	23.27	22.95	23.68	22.95	24.48	22.94	23.52	22.95	22.97
9	24.36	24.10	25.10	24.09	25.83	24.12	24.72	24.15	24.14
10	25.56	25.20	26.54	25.19	26.33	25.15	25.43	25.19	25.20
11	26.75	27.05	27.77	27.03	27.14	26.94	26.74	27.05	27.11
12	27.54	28.57	28.75	28.59	29.66	28.66	28.26	28.63	28.68
13	27.38	28.68	28.16	28.71	28.77	28.68	28.40	28.73	28.81
14	22.33	23.16	21.44	23.02	22.80	23.12	23.66	23.24	23.21
15	19.06	20.23	18.22	20.13	19.04	20.15	20.24	20.30	20.37
16	19.08	19.47	18.28	19.40	19.34	19.42	20.14	19.52	19.51
17	22.52	22.48	21.67	22.35	23.72	22.50	23.72	22.55	22.51
18	27.68	27.23	28.52	27.25	28.80	27.21	28.62	27.27	27.24
19	27.75	27.45	29.12	27.46	28.50	27.46	28.42	27.50	27.51
20	27.14	26.23	28.33	26.21	25.98	26.07	27.14	26.23	26.18
21	26.92	26.96	28.09	26.95	25.51	26.81	26.61	26.94	27.02
22	26.65	27.41	27.90	27.43	25.73	27.33	26.62	27.43	27.50
23	26.48	27.78	27.40	27.83	25.27	27.67	26.50	27.79	27.90
24	21.23	22.53	20.45	22.40	19.77	22.40	21.52	22.57	22.64
25	17.73	18.88	16.92	18.80	15.99	18.70	17.99	18.91	18.97
26	17.52	18.78	16.66	18.68	15.99	18.60	17.67	18.79	18.89
27	20.28	21.32	19.32	21.18	19.50	21.25	20.33	21.33	21.40
28	24.27	25.00	24.57	25.00	23.93	24.94	24.18	25.00	25.07
29	24.74	25.01	25.63	25.03	24.54	24.96	24.60	25.04	25.07
30	24.83	24.53	25.40	24.50	24.29	24.43	24.01	24.50	24.54
31	23.87	23.60	24.14	23.57	23.73	23.53	22.92	23.56	23.62
32	22.55	22.65	22.59	22.61	23.23	22.67	21.86	22.63	22.72
33	21.79	21.52	21.46	21.51	21.71	21.48	21.19	21.52	21.52
34	17.75	17.70	16.14	17.52	16.73	17.57	16.82	17.63	17.72
35	14.12	14.40	13.37	14.38	13.54	14.36	13.92	14.44	14.53
36	14.88	13.12	13.29	13.03	13.70	13.02	13.94	13.09	13.01
37	17.42	15.98	15.83	15.86	17.17	15.95	16.48	15.96	15.97
38	21.23	19.77	20.79	19.75	21.72	19.75	20.18	19.74	19.75
39	22.09	20.83	22.19	20.80	22.87	20.82	21.30	20.82	20.83
40	23.15	21.63	23.47	21.60	23.38	21.57	22.27	21.61	21.58
Total	875.56	873.97	875.53	872.25	875.56	871.74	875.53	874.45	875.54

Figure 3.27 shows the result of an adjustment of the MCNP *a priori flux* where only the powers of the odd-numbered fuel elements in Test 12-5 were included in the analysis. This simulates the most-often used protocol for element power measurements, but with the least-square adjustment used to determine the powers in the even-numbered elements rather than the symmetry assumption. Figure 3.28 shows an adjustment where only the measured powers for Elements 8, 18, 28, and 38 were included in the analysis. This arrangement simulates the measurements that were planned for the ATR itself during depressurized operations at the time of publication of this report. The data plotted in Figures 3-23, 3.27 and 3.28 are shown in numerical form in Table 3.24. Once again the results are self-consistent within the stated uncertainties, and it can be clearly seen how the uncertainties of the adjusted power for each element is influenced by proximity of that element to an element where the power was actually measured.

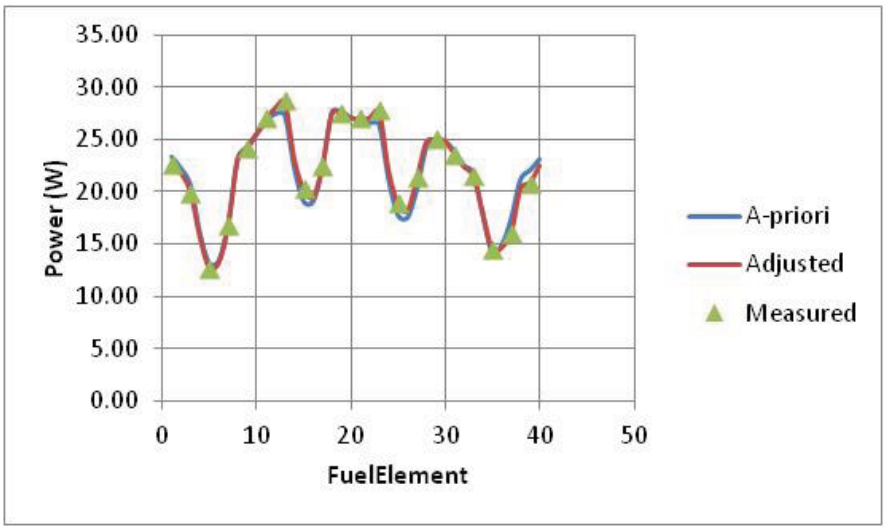

Figure 3.27. Fuel element fission rate distribution for ATRC Depressurized Run Support Test 12-5 (MCNP *a priori).* The *a priori* normalization uncertainty is assumed to be 5% and the *a priori* random uncertainty is assumed to be 10%. Total correlated plus uncorrelated *a priori* uncertainty =11.2%. Adjustment performed with θ=1.0 and Γ=1. The adjusted powers are computed using the measured data for only the odd-numbered fuel elements. Reduced uncertainties for the adjusted powers are in the range of 3.4% for the odd-numbered elements and 9.0% for the even-numbered elements.

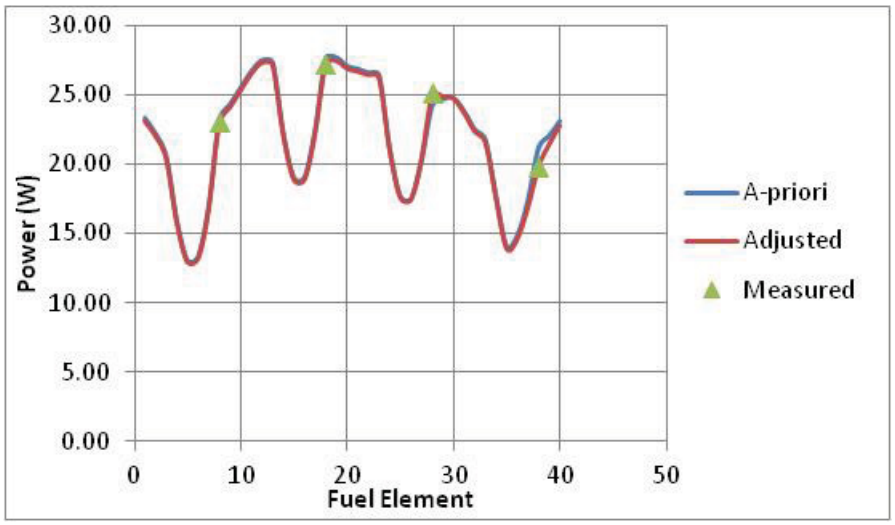

Figure 3.28. Fuel element fission rate distribution for ATRC Depressurized Run Support Test 12-5 (MCNP *a priori).* The *a priori* normalization uncertainty is assumed to be 5% and the *a priori* random uncertainty is assumed to be 10%. Total correlated plus uncorrelated *a priori* uncertainty =11.2%. Adjustment performed with θ=1.0 and Γ=1. The adjusted powers are computed using the measured data for elements 8, 18, 28 and 38 only. Reduced uncertainties for the adjusted powers are in the range of 3.4% for elements 8, 18, 28 and 38, in the range of 9.8% for the nearest neighbors to these elements, and approximately 10.7% elsewhere.

Table 3.24. Fuel element fission rate distributions for ATRC Depressurized Run Support Test 12-5 (MCNP *a priori).* The *a priori* normalization uncertainty is assumed to be 5% and the *a priori* random uncertainty is assumed to be 10%. Total correlated plus uncorrelated *a priori* uncertainty =11.2%. Adjustment performed with θ=1.0 and Γ=1.

Element	*A priori* Power (W)	% Total σ	Adjusted Power With 40 Measured Elements	% Total σ	Adjusted Power With 20 Measured Elements	% Total σ	Adjusted Power With 4 Measured Elements	% Total σ	Measured Power (W)
1	23.37	11.18	22.57	3.41	22.61	3.43	23.13	10.72	22.60
2	22.24	11.18	21.59	3.41	21.77	9.22	22.05	10.74	21.61
3	20.61	11.18	19.88	3.41	19.90	3.43	20.45	10.74	19.88
4	15.95	11.18	15.29	3.41	15.59	9.23	15.83	10.73	15.29
5	13.09	11.18	12.60	3.41	12.62	3.43	12.99	10.69	12.60
6	13.36	11.18	13.01	3.41	13.16	9.17	13.25	10.54	13.02
7	17.02	11.18	16.82	3.41	16.84	3.43	16.86	9.83	16.85
8	23.27	11.18	22.95	3.41	23.13	9.09	22.99	3.43	22.97
9	24.36	11.18	24.10	3.41	24.13	3.43	24.14	9.83	24.14
10	25.56	11.18	25.20	3.40	25.59	9.03	25.35	10.54	25.20
11	26.75	11.18	27.05	3.40	27.06	3.42	26.54	10.69	27.11
12	27.54	11.18	28.57	3.40	28.08	8.88	27.33	10.73	28.68
13	27.38	11.18	28.68	3.40	28.67	3.42	27.17	10.74	28.81
14	22.33	11.18	23.16	3.40	23.13	8.75	22.16	10.73	23.21
15	19.06	11.18	20.23	3.40	20.23	3.42	18.91	10.69	20.37
16	19.08	11.18	19.47	3.40	19.46	8.88	18.92	10.55	19.51
17	22.52	11.18	22.48	3.40	22.50	3.42	22.29	9.83	22.51
18	27.68	11.18	27.23	3.41	27.60	9.06	27.29	3.43	27.24
19	27.75	11.18	27.45	3.41	27.50	3.43	27.47	9.83	27.51
20	27.14	11.18	26.23	3.41	27.09	9.05	26.91	10.55	26.18
21	26.92	11.18	26.96	3.41	26.99	3.42	26.71	10.69	27.02
22	26.65	11.18	27.41	3.40	27.10	8.90	26.45	10.73	27.50
23	26.48	11.18	27.78	3.40	27.76	3.42	26.28	10.73	27.90
24	21.23	11.18	22.53	3.40	22.01	8.75	21.08	10.72	22.64
25	17.73	11.18	18.88	3.39	18.85	3.42	17.62	10.67	18.97
26	17.52	11.18	18.78	3.40	18.17	8.74	17.46	10.49	18.89
27	20.28	11.18	21.32	3.40	21.29	3.42	20.37	9.69	21.40
28	24.27	11.18	25.00	3.40	24.76	8.87	24.86	3.43	25.07
29	24.74	11.18	25.01	3.40	25.02	3.42	24.84	9.69	25.07
30	24.83	11.18	24.53	3.40	24.85	9.03	24.75	10.49	24.54
31	23.87	11.18	23.60	3.41	23.61	3.43	23.73	10.67	23.62
32	22.55	11.18	22.65	3.41	22.39	9.10	22.39	10.72	22.72
33	21.79	11.18	21.52	3.40	21.52	3.43	21.62	10.74	21.52
34	17.75	11.18	17.70	3.40	17.83	9.01	17.60	10.74	17.72
35	14.12	11.18	14.40	3.41	14.46	3.43	13.98	10.72	14.53
36	14.88	11.18	13.12	3.41	14.62	9.19	14.66	10.62	13.01
37	17.42	11.18	15.98	3.42	16.05	3.43	16.96	10.01	15.97
38	21.23	11.18	19.77	3.42	20.32	9.41	19.98	3.43	19.75
39	22.09	11.18	20.83	3.42	20.88	3.43	21.51	10.01	20.83
40	23.15	11.18	21.63	3.41	22.51	9.28	22.82	10.62	21.58
Total	875.56	1.80	873.97	0.55	877.68	1.10	867.73	1.60	875.54

Figure 3.29 shows the results of an adjustment of the MCNP *a priori* element powers based on the measured lobe powers for each of the five lobes. The same thing could be done using any of the other modeling codes. In this case, the first five rows of the matrix on the left-hand side of Equation 33 describe the measured lobe powers. These rows each contain entries of 1.0 for the elements included in the lobe corresponding to that row and zero elsewhere. The right hand side of each of these first five rows contains the sum of the measured powers for the lobe represented by that row. For example the first row (Lobe 1) contains entries of 0.125 for elements 2 through 9, and the average of the measured powers for elements 2 through 9 appears on the right hand side. This simulates a situation where, for example, the powers for each lobe that are measured online by the N-16 system could be entered into Equation 33 periodically, and an online estimate for all of the element powers could immediately be produced. Of course the *a priori* power vector would need to be recalculated regularly as the core depletes, control drums rotate, and neck shims are pulled during a cycle. This could however be automated to a large extent, and it should ultimately be quite practical, for example, to update the HELIOS *a priori* power vector daily, and to update the element power estimates more or less continuously during the day using the N-16 online lobe power measurements. Finally, Tables 3.25 and 3.26 show the element powers and the lobe powers corresponding to Figure 3.29.

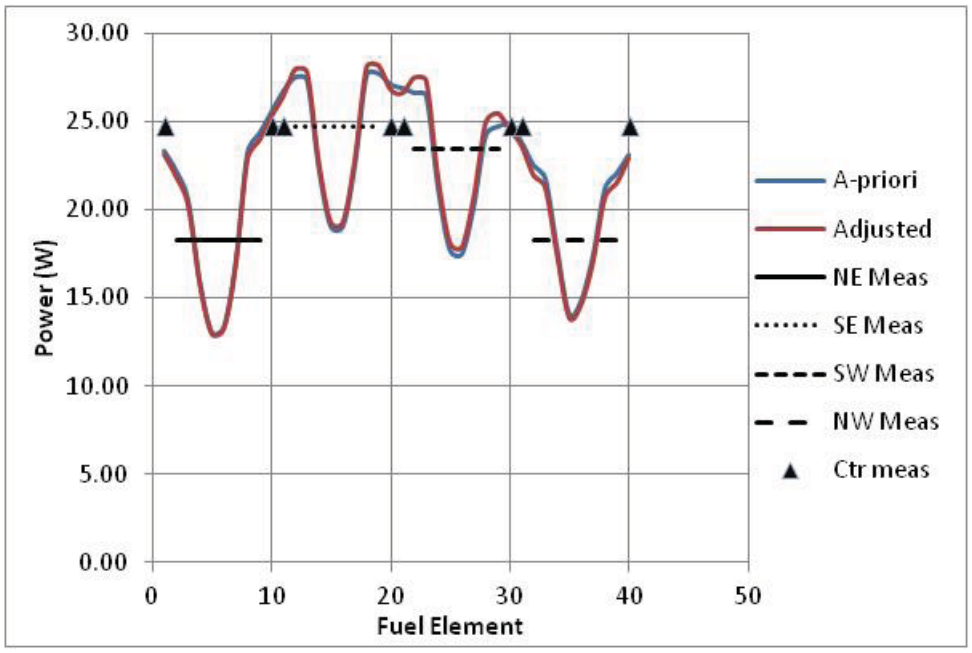

Figure 3.29. Fuel element fission rate distribution for ATRC Depressurized Run Support Test 12-5 (MCNP *a priori).* The *a priori* normalization uncertainty is assumed to be 5% and the *a priori* random uncertainty is assumed to be 10% Total correlated plus uncorrelated *a priori* uncertainty =11.2%. Adjustment performed with θ=1.0 and Γ=1. The adjusted powers are computed using the measured data for the average element power in each lobe. Reduced uncertainties for the adjusted powers are in the range of approximately 10% for all elements.

Table 3.25. Fuel element fission rate distribution for ATRC Depressurized Run Support Test 12-5 (MCNP *a priori).* The *a priori* normalization uncertainty is assumed to be 5% and the *a priori* random uncertainty is assumed to be 10% Total correlated plus uncorrelated *a priori* uncertainty =11.2%. Adjustment performed with θ=1.0 and Γ=1. The adjusted powers are computed using the measured data for the average power in each lobe.

Element	*A Priori* Power (W)		Adjusted Power using 5 Measured Lobe Powers	% Total σ	Measured Power (W)
1	23.37	11.18	23.10	9.99	22.60
2	22.24	11.18	21.85	9.83	21.61
3	20.61	11.18	20.27	9.90	19.88
4	15.95	11.18	15.74	10.07	15.29
5	13.09	11.18	12.94	10.15	12.60
6	13.36	11.18	13.21	10.14	13.02
7	17.02	11.18	16.78	10.03	16.85
8	23.27	11.18	22.85	9.78	22.97
9	24.36	11.18	23.90	9.73	24.14
10	25.56	11.18	25.24	9.92	25.20
11	26.75	11.18	26.40	9.89	27.11
12	27.54	11.18	27.92	9.59	28.68
13	27.38	11.18	27.75	9.60	28.81
14	22.33	11.18	22.57	9.79	23.21
15	19.06	11.18	19.22	9.90	20.37
16	19.08	11.18	19.24	9.90	19.51
17	22.52	11.18	22.76	9.79	22.51
18	27.68	11.18	28.06	9.59	27.24
19	27.75	11.18	28.13	9.59	27.51
20	27.14	11.18	26.79	9.88	26.18
21	26.92	11.18	26.57	9.88	27.02
22	26.65	11.18	27.45	9.41	27.50
23	26.48	11.18	27.27	9.42	27.90
24	21.23	11.18	21.73	9.66	22.64
25	17.73	11.18	18.07	9.81	18.97
26	17.52	11.18	17.85	9.82	18.89
27	20.28	11.18	20.73	9.71	21.40
28	24.27	11.18	24.93	9.53	25.07
29	24.74	11.18	25.43	9.51	25.07
30	24.83	11.18	24.53	9.95	24.54
31	23.87	11.18	23.59	9.97	23.62
32	22.55	11.18	21.92	9.92	22.72
33	21.79	11.18	21.20	9.95	21.52
34	17.75	11.18	17.35	10.09	17.72
35	14.12	11.18	13.86	10.18	14.53
36	14.88	11.18	14.59	10.17	13.01
37	17.42	11.18	17.03	10.10	15.97
38	21.23	11.18	20.67	9.97	19.75
39	22.09	11.18	21.49	9.94	20.83
40	23.15	11.18	22.88	9.99	21.58
Total	875.56	1.80	873.88	1.58	875.54

Table 3.26. Lobe fission rate distribution for ATRC Depressurized Run Support Test 12-5 (MCNP *a priori).* The adjusted powers are computed using the measured data for the total power in each lobe.

Lobe	A priori	%σ	Adjusted	%σ	Measured	%σ
NE	149.90	6.17	147.56	3.01	146.36	3.61
SE	193.34	6.15	195.65	3.01	197.84	3.61
SW	178.90	6.15	183.46	3.01	187.44	3.61
NW	151.83	6.15	148.12	3.00	146.05	3.61
Center	201.59	6.13	199.10	3.00	197.85	3.61
Sum	875.56	5.25	873.88	2.19	875.54	2.42

3.6 Discussion and Future Work

As noted earlier, the computational and experimental results reported here are parts of a larger ongoing code validation effort associated with the ATR Core Modeling Update campaign. The results of the experiments conducted so far have already been very useful for model refinement and improvement. For the longer term, fabrication of an additional set of foil and wire positioning devices was also recently completed for use in the SE IPT. Two additional spectral measurements will be conducted with this new apparatus, along with the NW LIPT apparatus, in place. In both of the additional irradiations still to be conducted, the experiment hardware and, in the second of the two remaining experiments, the core fuel elements, will also be heavily instrumented with Au/Cu and U/Al wires. Various least-squares techniques for statistically combining the ^{235}U fission rate with the Au and Cu capture rates at each instrumented flux trap and core fuel location to produce an improved estimate for the adjusted neutron flux spectrum at these positions that is statistically tied to the local fission rate will be explored. Taken together the six currently-planned irradiations will form the basis for a relatively simple, robust, and repeatable validation experiment protocol that can be extended to all of the transport codes and associated models that are included in the new suite of ATR core physics modeling tools.

3.7 References

ASTM (American Society for Testing and Materials), "Standard Guide for Application of Neutron Spectrum Adjustment Methods in Reactor Surveillance", ASTM-E944-08 (2008)

Auterinen, I., Serén, T., Uusi-Simola, J., Kosunen, A., Savolainen, S., A Toolkit for Epithermal Neutron Beam Characterization in BNCT, Radiation Protection Dosimetry, **110:**587-593 (2004)

J.D. Bess, "Preliminary Assessment of ATR-C Capabilities to Provide Integral Benchmark Data for Key Structural/Matrix Materials that May be Used for Nuclear Data Testing and Analytical Methods Validation", INL/EXT-09-15591, Idaho National Laboratory, USA (2009).

Draper Jr., E.L., Integral Reaction Rate Determinations - Part I: Tailored Reactor Spectrum Preparation and Measurement, Nuclear Science and Engineering, **48**:22-30 (1971).

Durney, J. L. and N.C. Kaufman, Calculating Reactor Power from Activation Techniques as Applied to Unusual Fuel Geometry (ATRC), IN-1047, January, 1967

P.J. Griffin and R. Paviotti-Corcuera, "Summary Report of the Final Technical Meeting on "International Reactor Dosimetry File: IRDF-2002", International Atomic Energy Agency, INDC(NDS)-448 (2003)

Harker, Y.D., Anderl, R.A., Becker, G.K., Miller, L.G., Spectral Characterization of the Epithermal Neutron Beam at the Brookhaven Medical Research Reactor, Nuclear Science and Engineering **110:**355-368 (1992).

S.S. Kim, B.G. Schnitzler, "Advanced Test Reactor: Serpentine Arrangement of Highly Enriched Water-Moderated Uranium-Aluminize Fuel Plates Reflected by Beryllium" HEU-SOLTHERM-022, *International Handbook of Evaluated Criticality Safety Benchmark Experiments*, NEA/NSC/DOC(95)03, OECD-NEA (2008).

McElroy, W.N. and Berg, S., SAND-II Neutron Flux Spectra Determination by Multiple Foil Activation Iterative Method", AWRL-TR-67-41, Vol 1-4 (1967).

Meyer, S.L., Data Analysis for Scientists and Engineers, John Wiley and Sons, 1975.

D.W. Nigg, C.A. Wemple, R. Risler, J.K. Hartwell, Y.D. Harker, G.E. Laramore, "Modification of the University of Washington Neutron Radiography Facility for Optimization of Neutron Capture Enhanced Fast-Neutron Therapy, *Medical Physics* **27:**359-367 (2000).

D.W. Nigg, K. Steuhm (Editors), Advanced Test Reactor Core Modeling Update Project Annual Report for Fiscal Year 2011, INL/EXT-11-23348, September 2011.

Organization for Economic Cooperation and Development (OECD), Nuclear Energy Agency, "International Handbook for Evaluated Reactor Physics Benchmark Experiments", NEA/NSC/DOC (2012).

Perey, F.G. , "Least-Squares Dosimetry Unfolding: The Program STAY'SL", Oak Ridge National Laboratory, ORNL/TM-6062, ENDF-254 (1977).

Perey, F.G. "Contributions to Few-Channel Spectrum Unfolding", Oak Ridge National Laboratory, ORNL-TM-6267, ENDF-259 (1978).

Rhoades W.A., and Childs R.L., The DORT Two-Dimensional Discrete-Ordinates Transport Code, Nuclear Science and Engineering **99**:88-89 (1988).

JW Rogers, R.A. Anderl, "ATR Neutron Spectral Characterization", INEL-95/0494, Idaho National Laboratory, USA (1995).

R.W. Roussin, "BUGLE-80 Coupled 47-Neutron, 20 Gamma-Ray P3 Cross Section Library", DLC-75, Radiation Shielding Information Center, Oak Ridge National Laboratory, USA (1980).

Schmittroth, F., "FERRET Data Analysis Code", Hanford Engineering Development Laboratory, HEDL-TME 79-40, UC-79 (1979).

Stallmann, F.W., LSL-M2: A Computer Program for Least Squares Logarithmic Adjustment of Neutron Spectra, NUREG/CR-4349, ORNL/TM-9933, Oak Ridge National Laboratory, USA (1986).

Wheeler, F.J., Parsons, D.K., Rushton, B.L., Nigg, D.W., Epithermal Neutron Beam Design for Neutron Capture Therapy at the PBF and BMRR Reactor Facilities, Nuclear Technology, **92**:106-118 (1990)

Williams J.G. “The Role of the Prior Covariance Matrix in Least-Squares Neutron Spectrum Adjustment”, Trans. ANS. **106:**881-883 (2012)

Williams J.G. “Least-Squares Data Adjustment with Rank-Deficient Data Covariance Matrices”, Proceedings of the 14th International Symposium on Reactor Dosimetry, American Society for Testing and Materials (2011).

4.0 VALIDATION EXPERIMENTS IN THE ATRC

David W. Nigg, Kevin A. Steuhm

As noted earlier, a total of six LEP-specific code and model validation experiments are envisioned as part of the ATR Modeling Upgrade Project, in addition to the 2012 depressurized run in ATR and the supporting experiments in ATRC that are not explicitly associated with the LEP. These latter experiments were in fact not anticipated at the beginning of the Methods Update project, but they have also provided valuable useful data. Four of the six LEP-specific experiments have been completed and detailed statistical analyses of these four were presented in the previous chapter. Additionally, some initial analysis of physics data from the ATRC experiments that support the 2012 depressurized run was presented in that chapter.

During 2013, analysis of all experimental physics data associated with the depressurized run, both from the ATRC supporting experiments as well as from experiments in the ATR itself, will be completed. It is also anticipated that the fifth planned LEP-specific validation experiment will be conducted in the ATRC. This fifth experiment (referred to here as "Irradiation 5") will use the same NW LIPT hardware and the same core fuel flux wires in the NW and SE lobes as were used for Irradiation 4, described previously, with minor changes in specific loading of the NW LIPT hardware. In addition, detailed neutron spectrum measurements will be made in the Southeast IPT using additional new hardware inserts fabricated for this purpose during 2011.

Figure 4.1 shows the loading of the NW LIPT foil positioning strips for Irradiation 5. In this case the foil packages consisted only of duplicate bare and cadmium –covered gold foils to provide a simple 2-group confirmation of the neutron spectrum in the NW LIPT. Au/Cu flux wires were also loaded positioning strips as before, but only on one side of each foil positioning strip. Each corresponding wire position on the other side of each positioning strip (see Figure 3.3 for detail) contained a uranium-aluminum flux wire, with 10% by weight ^{235}U. These latter wires were identical to the wires used for the core fuel element fission power distribution measurements described previously. The foil positioning strips were then loaded into the NW LIPT insert in the same manner as for Irradiations 1 and 2, with solid dummy strips in the other 8 positions.

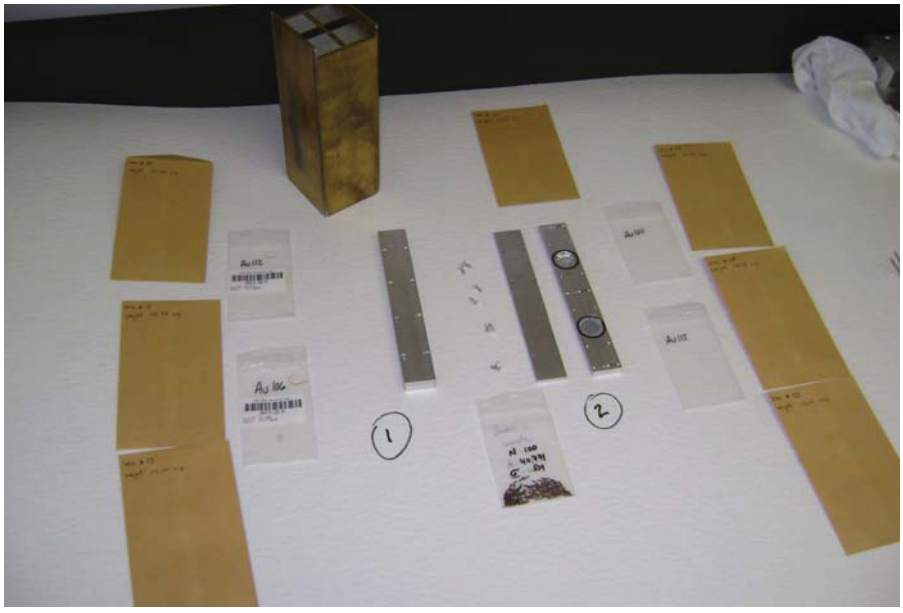

Figure 4.1. Northwest Large In-Pile Tube Fittings and Foil Positioning Strips for Irradiation 5.

Figure 4.2 shows the new SE IPT insert with a new solid aluminum fitting designed to hold a single foil positioning strip. This strip was loaded with a set of cadmium-covered indium, gold, tungsten, manganese, copper, titanium, nickel, zinc, iron and niobium foils in one foil position and a set of bare gold and manganese foils in the other foil position, without duplicates in this case. This arrangement is intended to test the ability of the threshold foils (In, Ti, Ni, Zn, Fe, Nb) to detect the high-energy part of the spectrum without the use of the boron sphere to suppress resonance interactions.

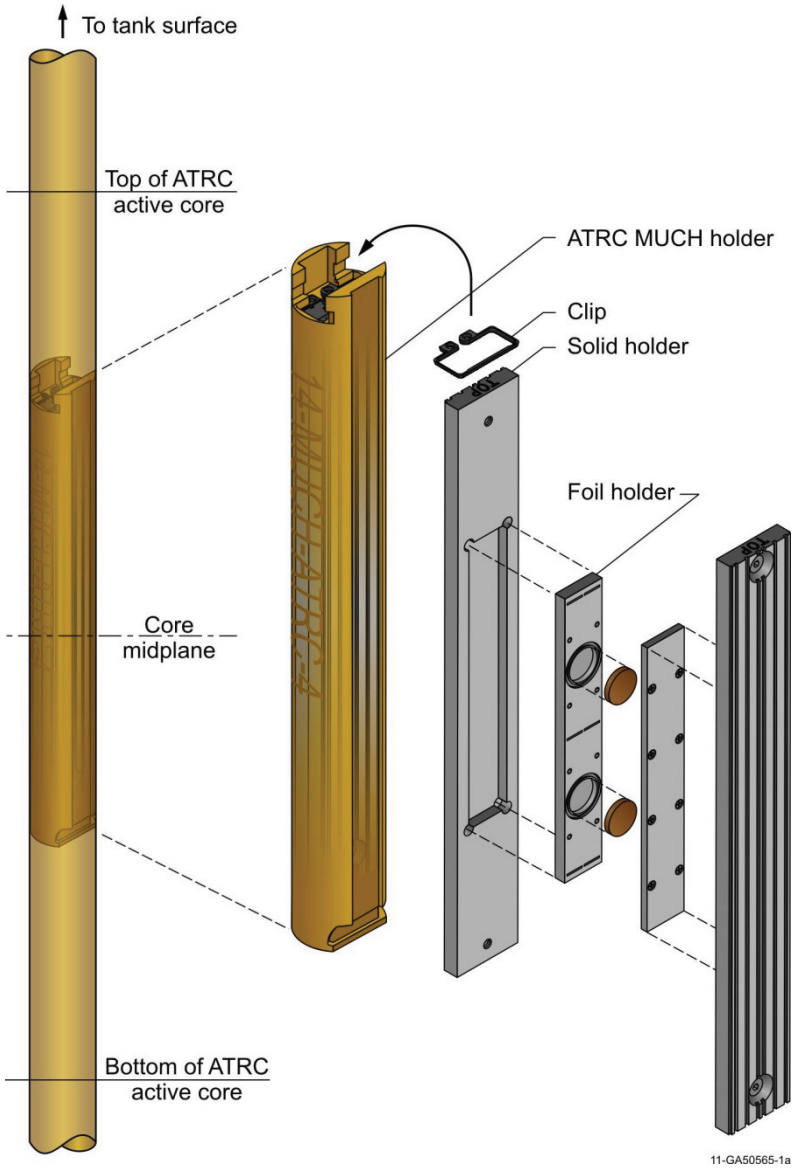

Figure 4.2. Southeast In-Pile Tube Insert Assembly (Low Water Fraction).

Figure 4.3 shows some additional detail of the foil positioning strip and the solid insert fitting for the SE IPT. Figure 4.4 shows a close up of the foil positioning strip, with the Au/Cu and the ^{235}U/Al wires in place at each of the three axial locations. Figure 4.5 shows the assembled insert fitting as it slides into the cylindrical SE IPT insert.

Figure 4.3. Foils, Foil Positioning Strip, and Insert Fitting for Southeast in-Pile Tube – Irradiation 5.

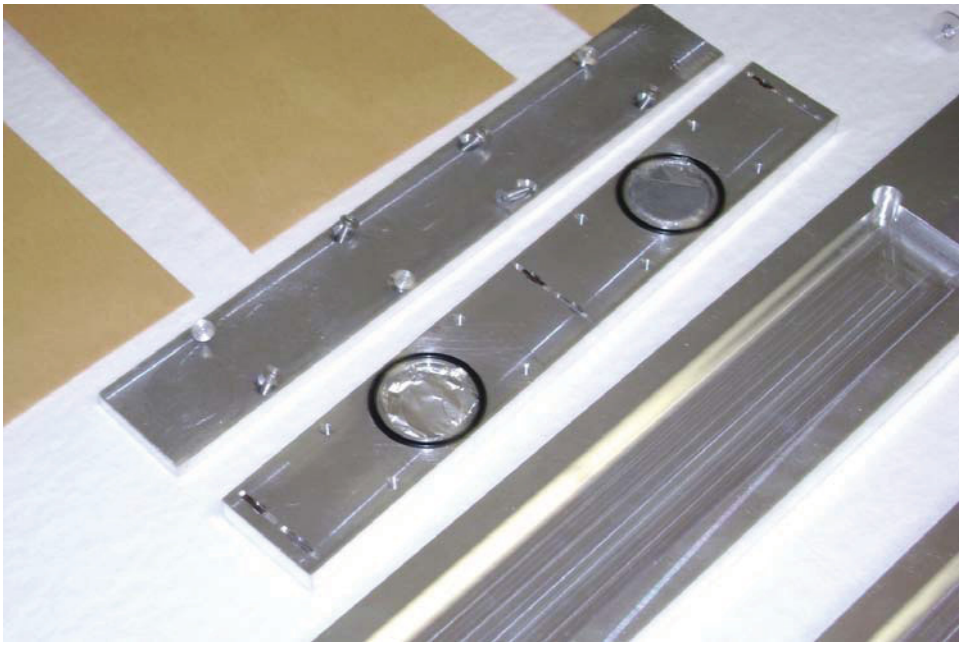

Figure 4.4. Detail of Foil and Flux Wire Positioning Strip for Southeast In-Pile Tube – Irradiation 5.

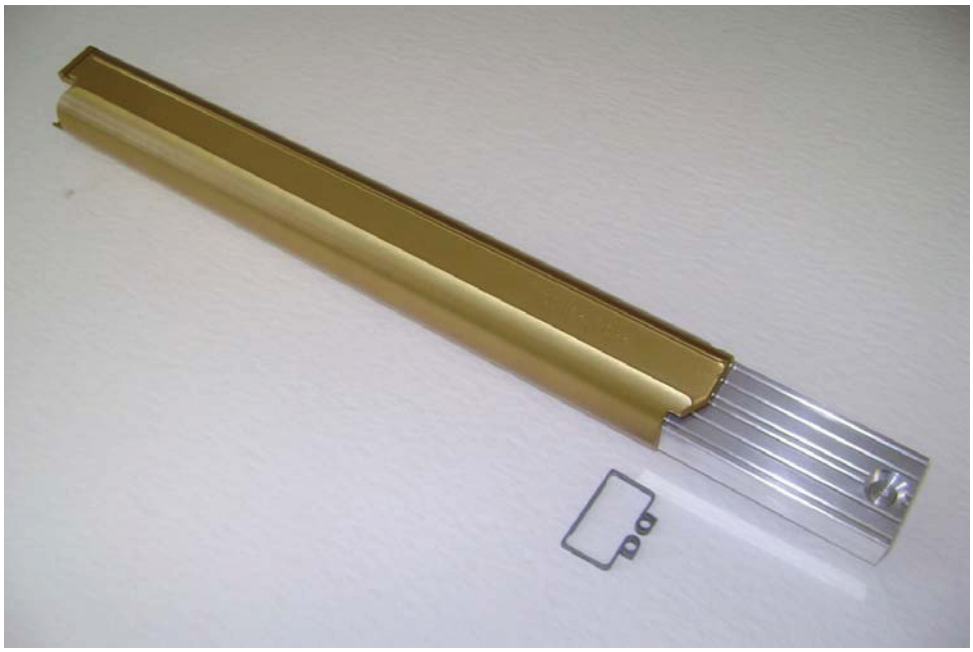

Figure 4.5. Assembled Hardware for Southeast In-Pile Tube – Irradiation 5

The Irradiation 5 experimental hardware for both the NW LIPT and the SE IPT was assembled in early Fiscal Year 2012 and it is anticipated that Irradiation 5 will be conducted during the first half of Fiscal Year 2013. Core fuel elements 12,14,16,18, 32, 34, 36, and 38, will be instrumented with three Au/Cu wires each, along the central rib, just as was done for Irradiation 4. As noted earlier, Irradiation 5 is intended to provide confirmatory spectral data for the NW LIPT as well as detailed spectral data for the SE IPT. In addition it will provide some experience with pairing of the Cu/Au wires with the ^{235}U/Al wires for the purpose of exploring techniques for statistically combining the ^{235}U fission rate with the Au and Cu capture rates to produce an improved estimate for the adjusted neutron flux spectrum at these positions that is statistically tied to the local fission rate.

Finally, Figure 4.6 shows a variation of the SE IPT hardware that will be used in Irradiation 6, which is scheduled for Fiscal Year 2014. In this case the insert fitting that holds the foil positioning strip will be a light aluminum framework with approximately 80% water in the same volume as the solid holder used for Irradiation 5. The NW LIPT insert fitting will contain only the two foil positioning strips for Irradiation 6 - the dummy strips will be removed, producing a water fraction of approximately 80% in this fitting as well. Allowing a large water fraction makes these flux trap positions more uniform in the axial dimension, with much less axial streaming and attenuation of thermal neutrons than is the case for the solid insert fittings used in Irradiations 1-3 and Irradiation 5. In turn this should make Irradiation 6 more suitable as a validation benchmark for the two-dimensional transport codes in the suite. As with Irradiation 5, core fuel elements 12,14,16,18, 32, 34, 36, and 38, will be instrumented with three Au/Cu wires each, but each Au/Cu wire will be paired with an adjacent ^{235}U/Al wire in each of the 24 fuel element wire locations, using modified flux wire positioning wands that have been fabricated for this purpose. Again, this should provide a mechanism for statistically combining the fission rate with the gold and copper neutron capture rates to produce improved spectral and fission distribution information at each core fuel element location.

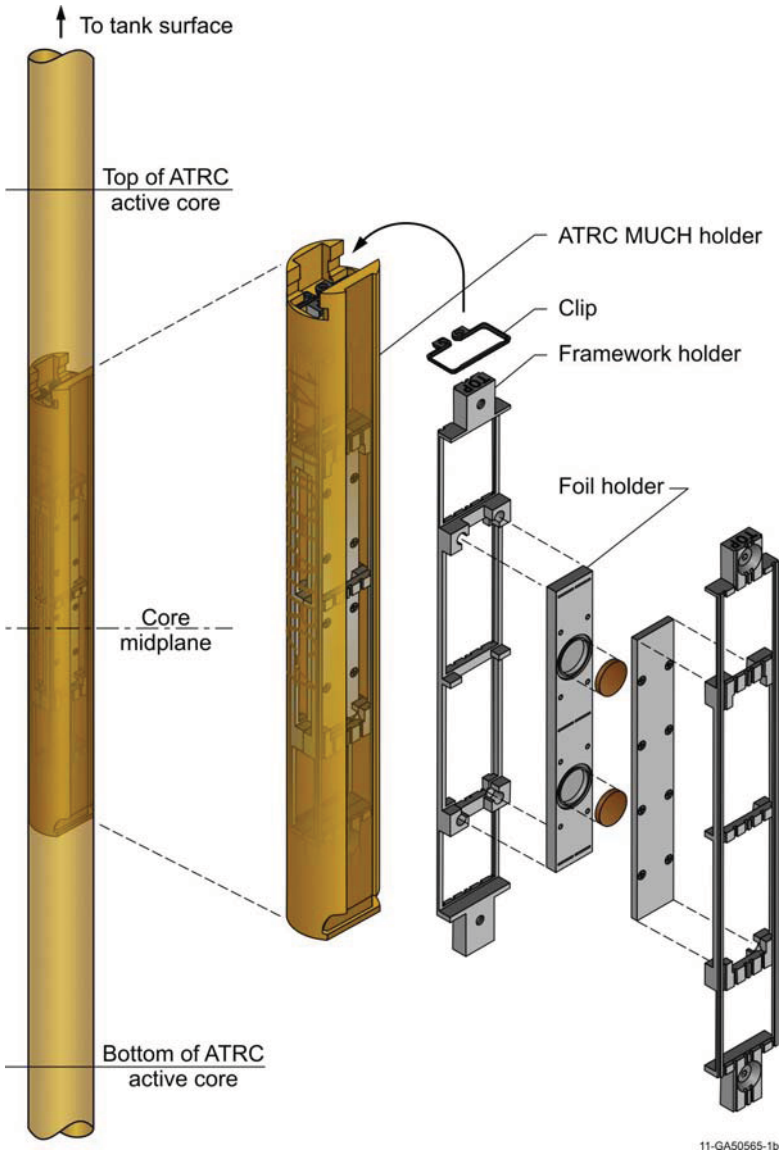

Figure 4.6. Southeast In-Pile Tube Insert Assembly (High Water Fraction).

5.0 FEASIBILITY TESTING FOR AN ATR FUEL BURNUP MEASUREMENT SYSTEM

Rahmat Aryaeinejad (INL) and Jorge Navarro (University of Utah)

State of the art neutronics modeling tools currently being phased into use for computational support of Advanced Test Reactor (ATR) operations and safety analysis will require fuel element isotopic and burnup validation data. Although this information may be retrievable from existing records to some extent, confirmatory burnup measurements for the large inventory of used fuel elements stored in the canal will be required for optimal validation of the codes and models. A suitable non-invasive fuel burnup measurement system will also permit validation measurements for new fuel elements as an ongoing tool for quality assurance of the new models as they come into general use for ATR operations support.

5.1 Introduction

In FY-10, feasibility measurements were carried out on some selected spent or irradiated fuel elements in the ATR canal to determine whether it is possible to get a meaningful gamma-ray spectrum of very hot fuels, identify the fission isotopes, establish a method for burnup calibration for long cooling times (1-3 years), and investigate the best way to measure burnup for short cooling times (< 6 months) fuels. A combination of these two calibrations can, in principle, be used to determine the burnup for fuels between these two cooling times (6-12 months). The study consisted of measuring very short, short, and long cooling time fuel elements in the ATR canal. Three different types of gamma-ray detectors of HPGe, $LaBr_3$, and High Pressure Xenon gas (HPXe) and two system configurations (above and under water) were used in this feasibility study. The idea was to investigate which detector and system configuration would be better suited for different scenarios and how to establish burnup and cooling time calibrations using experimental isotopic ratio and ORIGEN 2.2 (Croff et al., 1980) burnup calculations.

The results of the feasibility study in FY-10 (Aryaeinejad et al., 2010) and follow-on studies in FY-2011 (Nigg and Steuhm, 2011) far exceeded expectations and established the proof-of-concept for non-invasive measurement of burnup for ATR fuel elements. It was found that several isotopic ratios and absolute measurements could be used to predict ATR fuel burnup and cooling times. We have determined the burnup calibrations for three different types of HPGe, $LaBr_3$, and HPXe detectors. The results also showed the linear relationship between the $^{134}Cs/^{137}Cs$ ratio and the burnup for all three detectors. For the first time, we also found a new activity ratio of $^{134}Cs/^{144}Ce$ that has a linear relationship with the burnup. Although, our detection system was not setup for absolute activity measurement, we looked at the activity of some fission products. Among them ^{134}Cs and ^{137}Cs isotopes found to have linear relationship with the burnup and therefore they can be used as burnup monitors for the ATR fuel. We also investigated to see which other isotopic ratios or absolute activities can be used to determine the fuel element cooling time. The $^{144}Ce/^{137}Cs$ ratio, ^{144}Ce, ^{95}Zr, and ^{95}Nb showed a linear relationship as a function of cooling time. The comprehensive data analysis of these data was continued in FY-11and the results indicated that the burnup measurement system is performing well and that using the above the water configuration is the right way to design a permanent system. This configuration also makes the design simpler and less expensive. In addition, the results of the study clearly showed that a permanent system would improve the quality of data tremendously with much smaller uncertainty, and therefore would be able produce better results that can be compared with the results of calculations from the ORIGEN code as well as the new reactor models that are currently being developed in the overall Core Modeling Update project.

In the first half of FY-11, we completed the analysis of all the data taken during the previous year and also completed the conceptual design of a permanent burnup monitor system. A proposed Project Execution Plan to build this system was submitted to DOE-HQ on January 31, 2011. The second half of FY-11 was dedicated to measurements on the two short cooling time fuel elements from Cycle 145a that

were set aside for us. However, in order to establish the burnup calibration reference we also needed to do measurements on several other fuel elements that we used before for this purpose. Monitoring these fuel elements every six months provided us with valuable information about the fission product decay and also led to shortening the length of the project by 6-12 months. This is because there was no need to wait months to measure the long half-life fission product yields. All measurements were done with both HPGe and $LaBr_3$ detectors in an above the water configuration during April and May 2011. The data definitely confirmed the results obtained in the feasibility studies. We found new isotopic ratios for burnup and cooling time determination. We also found new fission product isotopes that can be used to determine burnup for short cooling time fuels between six to twelve months.

5.2 Activities Completed during FY-2012

The focus during FY-2012 included the investigation of laser and ultrasonic techniques to determine the optimal approach for non-invasively measuring the distance between the detector and the fuel element under examination. This capability was needed for refining methods for deconvolution of spectra taken with low resolution $LaBr_3$ and HPXe gas detectors.

5.2.1 Distance Measurement Techniques

We had several ultrasonic transducers in our lab but not a laser unit. We contacted Acuity Laser Measurement Company and they sent us a loan laser unit to do our measurements and compare the results with the ones obtained from the transducer measurements in terms of accuracy. Our measurement results clearly showed the laser was more accurate measuring the distance. Another advantage of using a laser is being able to see the exact location of the laser spot hitting the fuel element. This was not possible in the case of the ultrasound method. This is important because the ATR fuel plates are curved and knowing the location toward which the detector is pointed is crucial. In November 2011, we procured a small but very accurate AR-700 laser unit from Acuity. This is a Class 3B laser. The unit consists of a laser box, a controller box, and a display as shown in Figure 5.1 below.

Figure 5.1 Acuity AR-700 laser system for remote source-detector distance measurements.

The AR700 is a triangulation sensor that measures distance using a laser beam, miniature cameras, and a microprocessor. Different models can be used for different measurement ranges. They vary in range from 0.1 to 50 inches and the accuracy is generally 0.1% with linearity of around 0.03%. A variety of configuration settings can be selected via serial port or by using the function button and function display LEDs. The sample rate can be specified and the sensor has capability above 9400 samples per seconds. Sampling can be turned on and off and can be triggered using an input signal or serial port commands. Measurement outputs can be in the form of serial data (RS-232), Analog output, and Limit outputs using two switches. Figure 5.2 shows the laser unit inside the waterproof housing. As mentioned above, the unit uses a triangulation method to measure the distance. The laser beam is projected from the red circle's aperture at the bottom onto a target surface, where it is focused to a small spot. From there the laser light is scattered in all directions. These scattered beams are collected by three camera lenses located on the top window. The position of the laser spots imaged in these lenses is then processed to measure the distance.

Figure 5.3. Waterproof housing for the AR700 laser unit.

Distance calibrations were performed in air as well as in the water. The following two Figures (5.3 and 5.4) show two setup configurations. A dummy fuel element made of aluminum to resemble the actual ATR fuel element is used in our measurements. The laser system was mounted on a 3" pipe so that the laser beam and the center axis of the pipe are parallel and 2.5" apart. This means the detector is viewing a spot on the fuel element that is along the length of the fuel element 2.5" from the laser spot. Both measurements in the air and water were determined to be within an accuracy of 0.1 inches.

Figure 5.3 Measurement configuration in air.

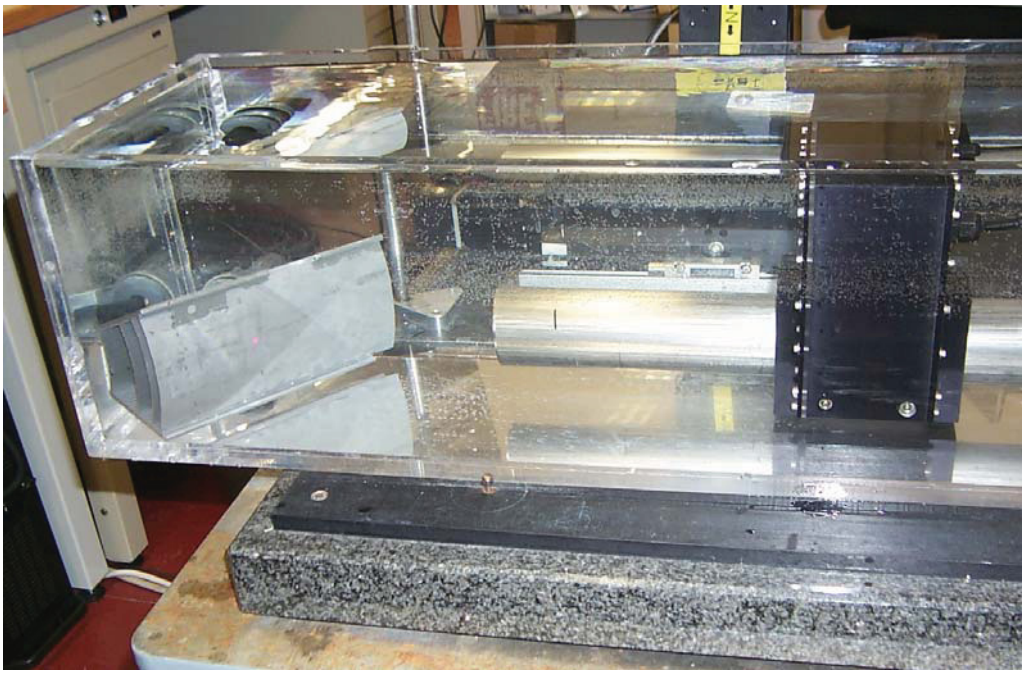

Figure 5.4 Measurement configuration in water.

5.2.2. Spectrum Deconvolution and Enhancement Technique

Starting in the second half of November and until the end of December 2011 we worked on determining the response function of the 1"x1" $LaBr_3$ and HPXe detectors used in our fuel burnup measurements. This response function can then be used to deconvolute the spectra taken with these two detectors and therefore to enhance the quality of the spectra. If this technique is developed successfully, it will eliminate the need for using an expensive and cumbersome, cooled HPGe detector.

Spectra-deconvolution methods such as Maximum Likelihood Expectation Maximization (MLEM) have been used in the past to enhance the quality of the spectrum provided by a NaI, CsI, or any scintillation counter. This technique, when used on raw spectrum data, drastically improves the energy resolution by moving counts appropriately from the Compton region into the photo-peaks.

The enhancement technique can be applied to a broad range of gamma-ray scintillation and gas detectors of different sizes and shapes. Generally, this method can play an important role in simple, accurate, and rapid radiation detection and isotope identification. It would be advantageous if one could use simpler, less expensive, and more efficient scintillators and gas counters. Successful implementation of a spectrum deconvolution process depends on accurately predicting the detector response function as a function of incident gamma-ray energy. The detector energy-dependant response function is obtained from experimental data and modeled with Monte Carlo simulations. There are several deconvolution techniques such as Single-Value Decomposition, Linear Regularization, Maximum Entropy, and Maximum Likelihood Expectation Maximization that are being used for deconvolution of low-resolution gamma-ray spectra.

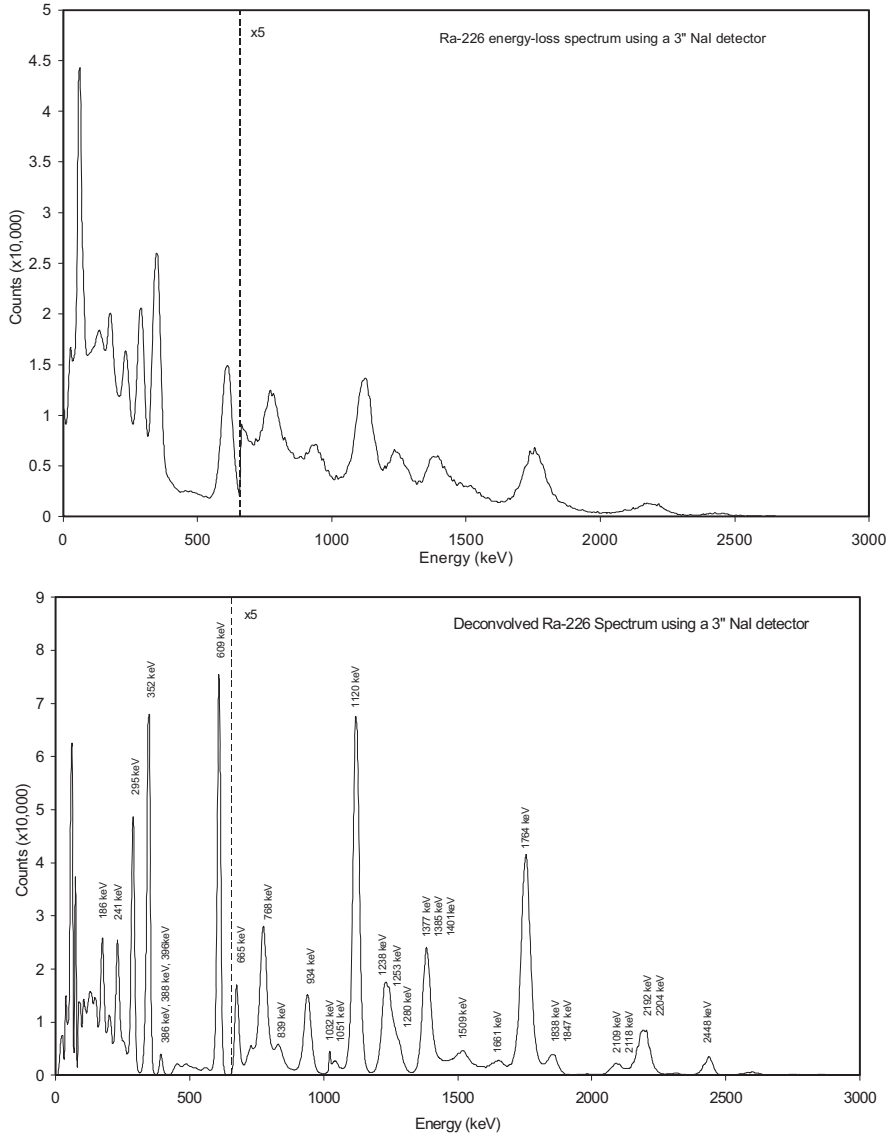

Figure 5.5. Comparison between the raw spectrum taken with 3"x3" NaI detector using a Ra-226 point source (top) and the deconvolved spectrum using ME-LM algorithm (bottom).

For most applications that are required to have an accurate estimate of counts in a full-energy peak, the Maximum Likelihood method has been shown to be superior. The best energy resolution was also achieved using the MLEM algorithm. In addition, this method provides a very accurate estimate of the peak area within 0.5%, the best peak-to-Compton (P/C) ratio, and the narrowest peak-width. The MLEM method is proven to be very effective in medical imaging applications particularly when dealing with low signal-to-noise ratio data in order to enhance PET images. In the past, we have used the enhancement technique on a 3"x3" NaI detector. Figure 5.5 shows the raw spectrum taken using a Ra-226 point source (top) and the Deconvolved spectrum using the MLEM technique (bottom). One can clearly see the power of enhancement technique in resolving all gamma rays emitted from this source (especially the weak peaks), which covers the energy ranges of up to 2.5 MeV. The energy resolution is improved from 7% to around 3% at 662 keV. In the case of $LaBr_3$ and HPXe detectors that are going to be used in this project, we expect much better spectral enhancement with an energy-resolution of around 1.5% at 662 keV.

We also performed the same method on 3"x3" NaI spectra taken with enriched uranium samples ranging from 10 % to 90% and compared the results to high-resolution spectra taken with the 40%-efficient HPGe detector. The results showed that the deconvolved spectra and the relative line intensities are in very good agreement with those derived from the germanium spectra within the limits of the detector efficiency calibration. These results showed that relatively inexpensive scintillation detectors, used in conjunction with a deconvolution technique would be able to provide better results that are comparable with an expensive HPGe detector for some applications.

The spectrum enhancement technique has not been used for $LaBr_3$ and HPXe detectors as far as we know. In this work, we will ultimately obtain the response functions for both detectors and develop the MLEM enhancement algorithms specifically for them. Some initial efforts for $LaBr_3$ are described in the following section. If it is possible, this work should be carried out in collaboration with Professor David Ramsden from the University of Southampton in England. At an IEEE conference we had a chance to talk to Professor Ramsden, who is an expert in spectrum enhancement techniques. We asked him about the latest algorithms that he uses. He told us that he improved the algorithms substantially and showed a lot of interest in collaborating with us to develop the same algorithms to enhance the quality of the spectrum for the 1"x1" $LaBr_3$ detector used in fuel burnup measurements.

5.2.3 LaBr3 Response Function and MCNP Model Calculations

The response function for a 1"x1" $LaBr_3$ detector was calculated using MCNPX and Matlab programs. The process to obtain the response function consisted of:

- Setting up an experiment, calibrating the detector with the calibration sources,
- Taking measurements of several gamma radiation sources for a long period of time (9 hours)
- Using the energy and FWHM to calculate the Gaussian Energy Broadening parameters as a function of gamma-ray energy needed in MCNPX
- Create a model of the experimental setup in MCNPX.

The detector used in the experiment was a 1"x1" Labr3 detector with an aluminum outside crystal housing of 30.4 mm and a total detector height of 140.5 mm. The detector was placed on top of a stainless steel table. The radioactive sources were placed 25 cm from the detector for each measurement.

Radioactive Sources used and experimental setup. There were four radioactive sources used for obtaining the $LaBr_3$ response function with MCNPX. The counting time of each experimental measurement was 68,400 seconds; a background measurement was also taken in order to subtract it from the source spectra and to make sure that there was no shift due to temperature changes. The radioactive sources used are shown in table 1. The spectra results were used as a comparison to the MCNPX calculation and also to calculate the parameters needed by MCNPX in order to create a simulation with Gaussian shaped energy peaks.

Table 1.-Gamma Energy Sources Measured

Gamma Energy Sources
Cs-137
Eu-152
Ra-226
Co-60

Detector Response Function using a Monte Carlo Calculations. In order to create an energy calibration for the 1"x1" $LaBr_3$ detector, the spectra for each source was analyzed using SPEX. Once the energy calibration of the detector was determined, a table (Table 2) containing the energy of the peaks used in the calibration and their respective FWHM was created. The table was imported into Matlab in order to run a least square analysis to determine the Gaussian Energy Broadening (GEB) parameters for MCNPX.

Table 2.-Gamma Energy Sources and FWHM used for GEB parameters.

Nuclide	**Energy (KeV)**	**FWHM (keV)**
Cs-137 (Ba Xray)	32.29	8.25
Eu-152	121.52	9.23
	244.8	12.88
	344.45	15.39
	778.98	24.8
	867.08	27.47
	964.01	26.96
	1408.01	39.17
Cs-137 (662 peak)	659.32	22.51

The Gaussian Energy Broadening (GEB) is a special tally treatment included in MCNPX to better model the physical detector and to give the energy lines a Gaussian shape. In order to obtain the GEB the experimental data shown in Table 2 were fitted to the following equation:

$$FWHM = a + b\sqrt{E + cE^2}$$

Where the fitting parameters a, b, and c are determined by a least-squares regression analysis.

Once the GEB parameters were obtained, a detailed model of the experiment set up was created in MCNPX (Figure 5.6 below). Models for each radioactive source measured experimentally were simulated with 10^8 and 10^9 particles cases.

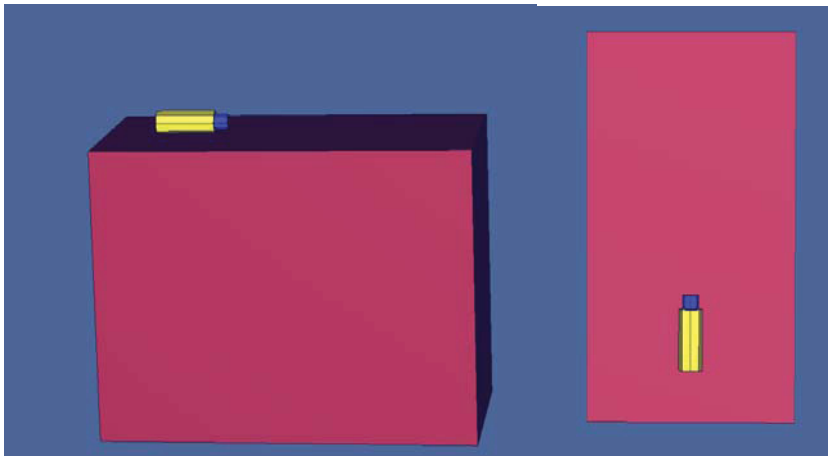

Figure 5.6 MCNPX 3-Dimensional View of Measurement Geometry

Results and Conclusions. Before the simulation results could be compared to the experimental measurements, the background spectrum was subtracted from the gamma source spectra. Once the background was subtracted the results of the simulated gamma sources were compared to the experimental results. The simulations show good agreement with the measured sources as it can be seen in Figure 5.7 below. This figure shows the simulation and the experimental measurement of the multi-energy source Radium-226. It can be seen that even at lower energies the agreement between the experimental spectrum and simulated spectrum is very good.

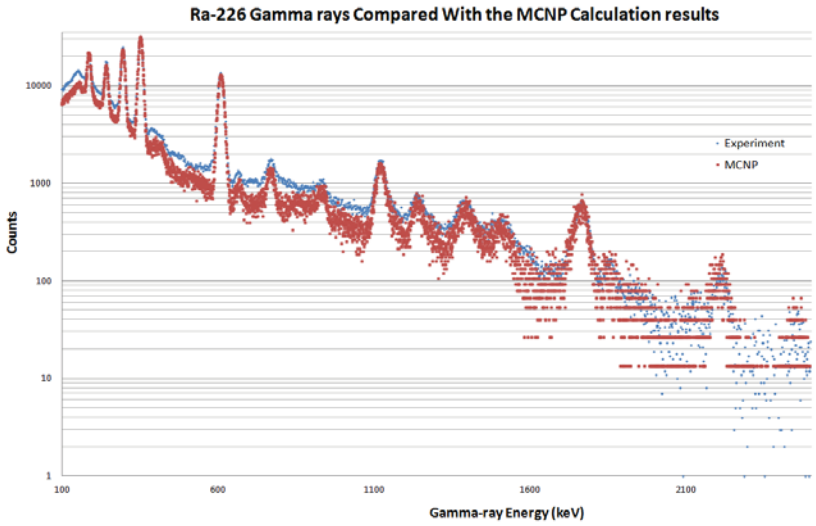

Figure 5.7. Ra-226 Experimental and Simulated MCNP Spectra

5.3 References

Croff, A.J. "ORIGEN2 -- A Revised and Updated Version of the Oak Ridge Isotope Generation and Depletion Code," ORNL-5621, July 1980.

Aryaeinejad, R., Crawford, D.S., Griffith, G.W., Gross, B.J., Lucas, D.S., Nielsen, J.W., Navarro, J., Parry, J.R., Petersom, J., Steuhm, K., Advanced Test Reactor Core Modeling Update Project Annual Report for Fiscal Year 2010,INL/EXT-10-19940, Edited by David W. Nigg, September 2010.

Nigg. D.W. and Steuhm, K.A., Project Plan for the ATR Core Modeling Update, PLN-2852, Revision 2, Idaho National Laboratory, September 2011.

Appendix A. MCNP/MRTAU Depletion Validation of AFIP-3

Steven Logan, RPI, INL Student Intern

1. Introduction

When material is subjected to a flux of neutrons, the isotopes that make up that material become depleted. This means that those isotopes undergo nuclear reactions with the neutrons and transmute into different isotopes. Thus, there is a deficiency of the isotopes that underwent the nuclear reactions. When designing experiments and fuel to be put into nuclear reactors, it is important to know how the materials will be depleted over time. In order to do this, depletion methodology is developed. These methodologies normally involve the use of two types of codes in order to simulate the depletion of the material in question.

One of these codes is the nuclear physics code that simulates how the particles interact with the material. These interactions are captured by outputting the reaction rate for each isotope that is being depleted. The other type of code handles how the mass of the isotopes changes due to the reported isotope reaction rate, which is translated into a nuclear reaction cross section. The newly computed composition of the material is reflected in the nuclear physics code, and the cycle is repeated until the appropriate amount of time has elapsed in this burn cycle.

Current depletion simulations are mainly carried out using ORIGEN2 based methodology coupled to MCNP. The goal of this research was to develop an alternative to these methodologies using a depletion code other than ORIGEN2. An additional goal was to broaden the capability of the isotopes that could be depleted. The end product was the Coupled Reactor Instrument with Automated Controls (CRDIAC). This paper will focus on the components that make up CRDIAC, the code's validity, the results from running the code, what those results mean, and what the future of CRDIAC is.

2. The Components of CRDIAC

In CRDIAC, the chosen nuclear physics code was Monte Carlo N-Particle (MCNP). Specifically, MCNP5 version 1.60 was used. CRDIAC's depletion code was the Multi-Reactor Transmutation Analysis Utility (MRTAU). The link between the two codes was developed in Python 2.7 to transform and transfer the data from one code to the other between each run. This Python script is run as a combination of a number of different modules. Figure A-1 shows how CRDIAC runs the codes together.

This methodology and others like it that use this back-and-forth, iterative way of modeling the way the material depletes have an inherent flaw that will keep them from obtaining the most accurate possible results. This is due to the fact that each burnup time step is based on the nuclide concentrations at the beginning of the time step. This type of fully-explicit coupling means that the simulation will never be perfectly reflective of reality, so this must be kept in mind when evaluating the results.

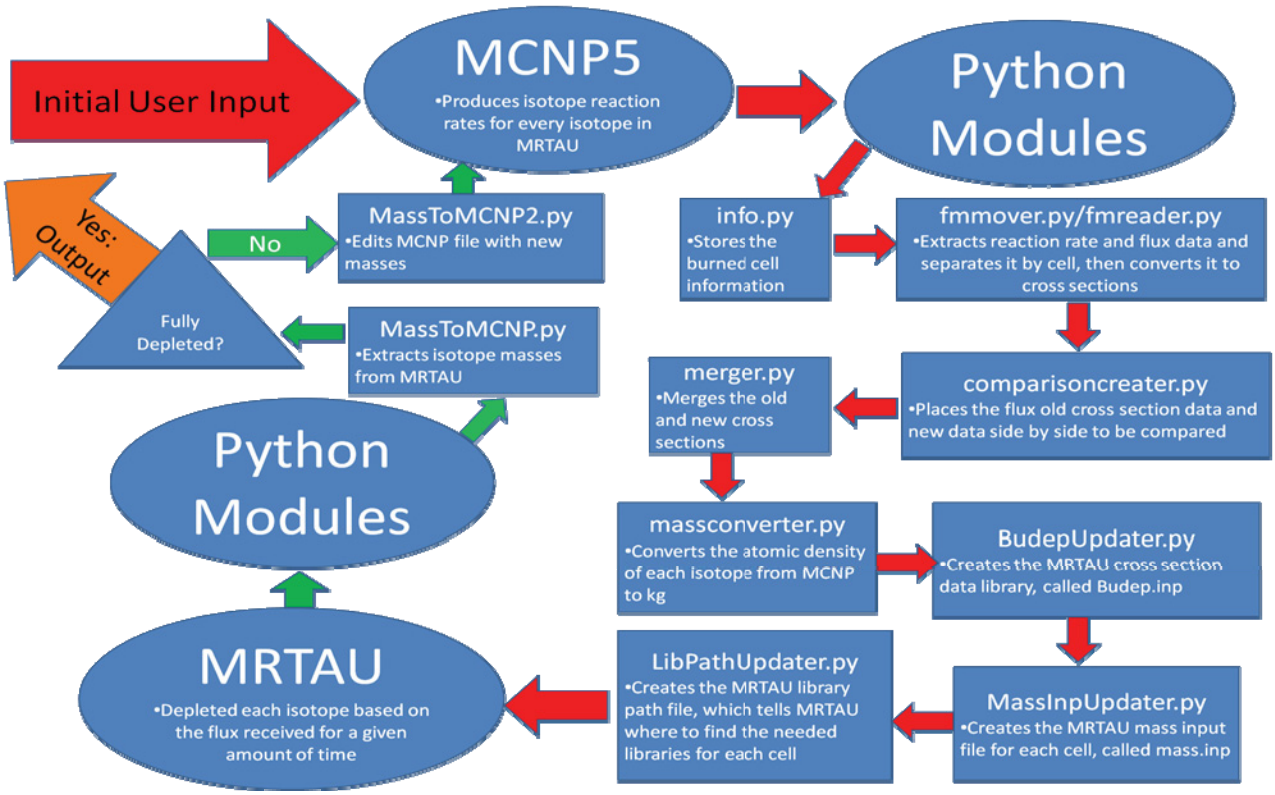

Figure A-1 CRDIAC Flow of Information Chart

a. MCNP

The nuclear physics code in CRDIAC, MCNP5 version 1.60, was developed by Los Alamos National Laboratory (LANL) and is based on reactor transport theory. It uses Monte Carlo methods to solve the transport equation, which means that many particles are introduced into the system and the path of each particle is tracked and recorded, forming a picture of what would happen in the real-system (X-5 Team, 2008). MCNP includes many options for tracking many different types of reactions with materials using different tallies.

In CRDIAC, volume based neutron flux tallies (f4 tallies) for each depleted, or burned, cell are used to generate the normalized neutron flux. Flux multiplier cards for each isotope in each cell are used to determine the reaction rate for each isotope, which can be transformed into a cross section to be used in the depletion code. Additionally, the criticality eigenvalue calculation (kcode) is also used for the power scaling when determining the true neutron flux, along with a neutron heating tally (f7 tally) for the different lobes of the reactor.

b. MRTAU

MRTAU, the depletion code in CRDIAC, was initially developed by S. Bays as part of his PhD work and was further developed at Idaho National Laboratory (INL) as part of the Parallel and Highly Innovative Simulation for INL Code System (PHISICS). MRTAU currently has 49 actinides and 182 fission products that are tracked (Alfonsi et al., 2012). When used in CRDIAC, almost all of the cross sections for these isotopes are replaced by the ones calculated from MCNP. In this way, the calculation more accurately reflects reality than calculations that do not replace in such a high level of detail. An additional feature of MRTAU is that the user, with proper nuclear data, can add other isotopes to MRTAU for depletion if they are not already present. The output from MRTAU is a table of the new concentrations of the isotopes.

c. Python

In order to automate the process of coupling MCNP to MRTAU, a series of Python modules were developed to carry out the transformation and translation of the resulting data. Python was chosen because, as a scripting language, it was relatively easy to pick up. Python also easily edits the text of the various input and output files and is a very portable code, so it can easily be switched to different operating systems. Currently, the process is not fully automated and requires some user interaction between running MCNP and MRTAU. Right now, the user would be required to:

1. Run the properly formatted MCNP input file/ put the burn information into info.py
2. Run python on the MCNP output file
3. Transfer the MRTAU input files to the appropriate directories
4. Run MRTAU for each cell
5. Update the MCNP input file with the MRTAU output masses
6. Start the cycle again

3. Verification and Validation

After CRDIAC's components were in place, it was important to verify that the code returned similar values when compared to another code that did the same task and to validate the code's results against experimental data. The verification was performed against the MCNP Coupled with ORIGEN2 (MCWO) methodology currently used at INL to simulate the depletion of the fuel in an experiment irradiated in the ATR (Lilo and Chang, 2011). The validation was performed against the data taken from the Post Irradiation Examination (PIE) of the same experiment (Robinson, 20111). In this case, the experiment chosen to do the verification and validation was the Advanced Test Reactor Full Size Plate in Center Flux Trap Position (AFIP) experiment, AFIP-3. AFIP-3 was a reduced enrichment plate-type fuel tested in the ATR and located in the center flux trap, as shown in Figure A-2. It was run for ATR Cycles 143B and 144A, where it shared the AFIP assembly with AFIP-1 in the former and a dummy plate in the latter.

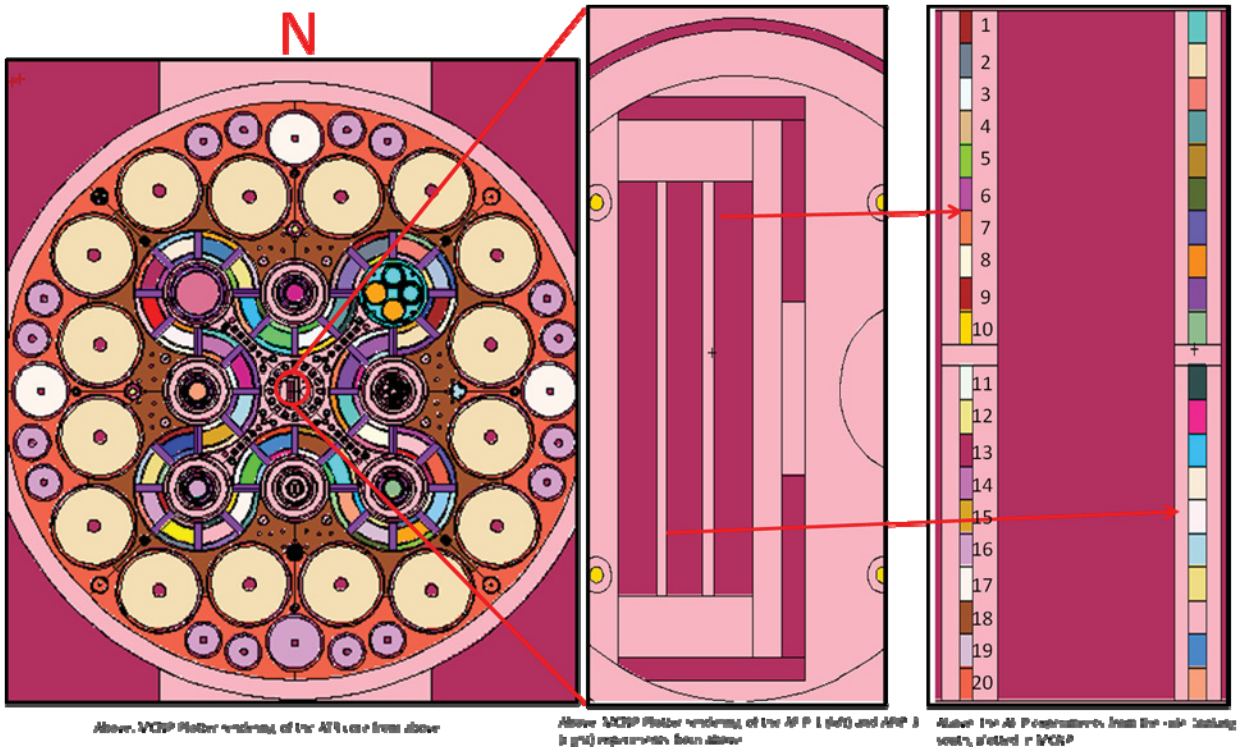

Figure A-2 From left to right, top view of ATR, top view of the AFIP-1 (left) and -3 (right) experiments, side view of the AFIP-1 and -3 experiments.

4. Results

After running CRDIAC for the same experiment and the as-run simulation performed with MCWO, the results from CRDIAC were compared. Figure A-3 shows the comparison of the MCWO and CRDIAC U-235 concentrations present in the first region during Cycle 144A, illustrating the verification results. Table A-1 shows the difference in the atomic percents of U-235, U-238, and the Cs-134/Cs-137 ratio at the end of life calculated in CRDIAC and from the PIE chemical analysis (Holm, 1978), illustrating the validation results. The gamma scans and CRDIAC mass data were normalized to produce a comparative representation of the whole plate's isotopic concentration. Figure A-4, below, illustrates the ability for CRDIAC to show how the U-235 concentration and the Cs-134/Cs-137 ratio look at the end of life for the fuel. From the figure, it is evident that the cells that experience a higher burnup (toward the center) had lower concentrations of U-235 and higher Cs-134/Cs-137 ratios, which is what one would expect. Figures A-5 and A-6 show the gamma scan of the AFIP-3 plates compared to the CRDIAC concentrations for Cs-137 and Nb-95, respectively.

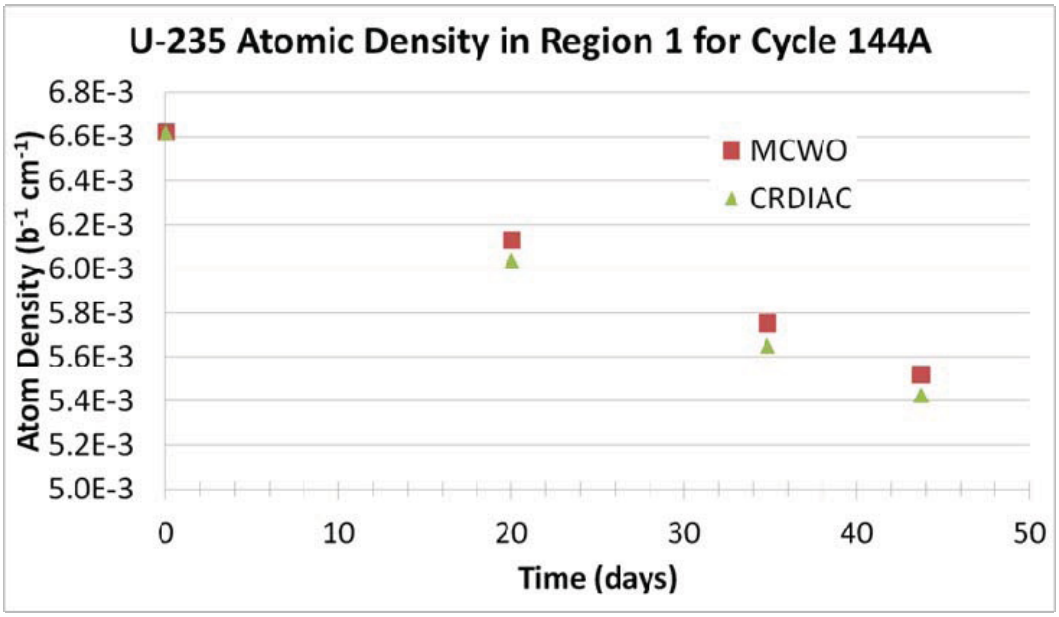

Figure A-3 Verification of CRDIAC compared to MCWO for AFIP-3 (Mesina et al., 2002)

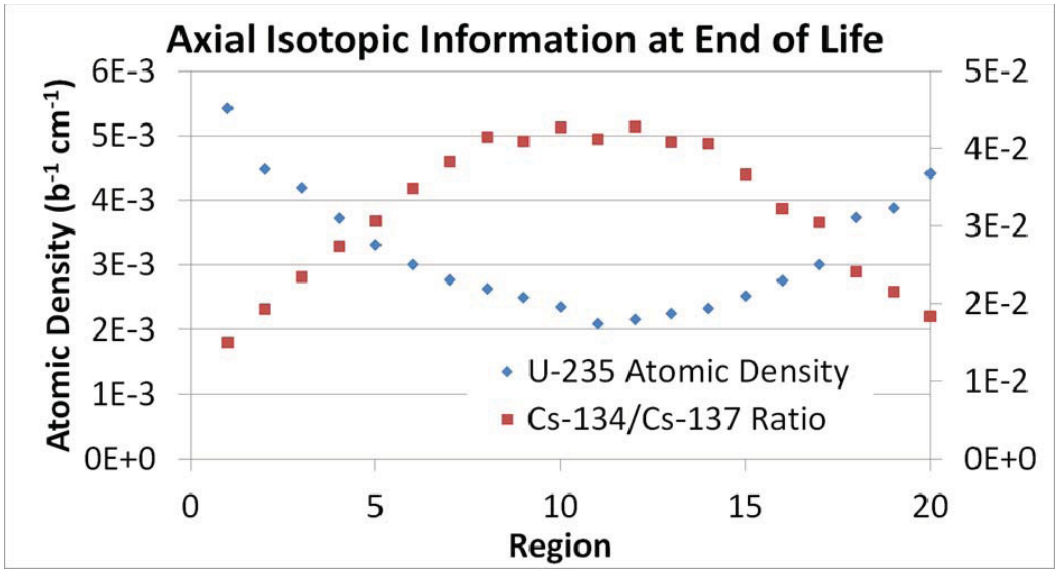

F

Figure A-4 CRDIAC output used to show the axial difference of U-235 (left axis) and the Cs-134/Cs-137 ratio (right axis) at end of life for AFIP-3.

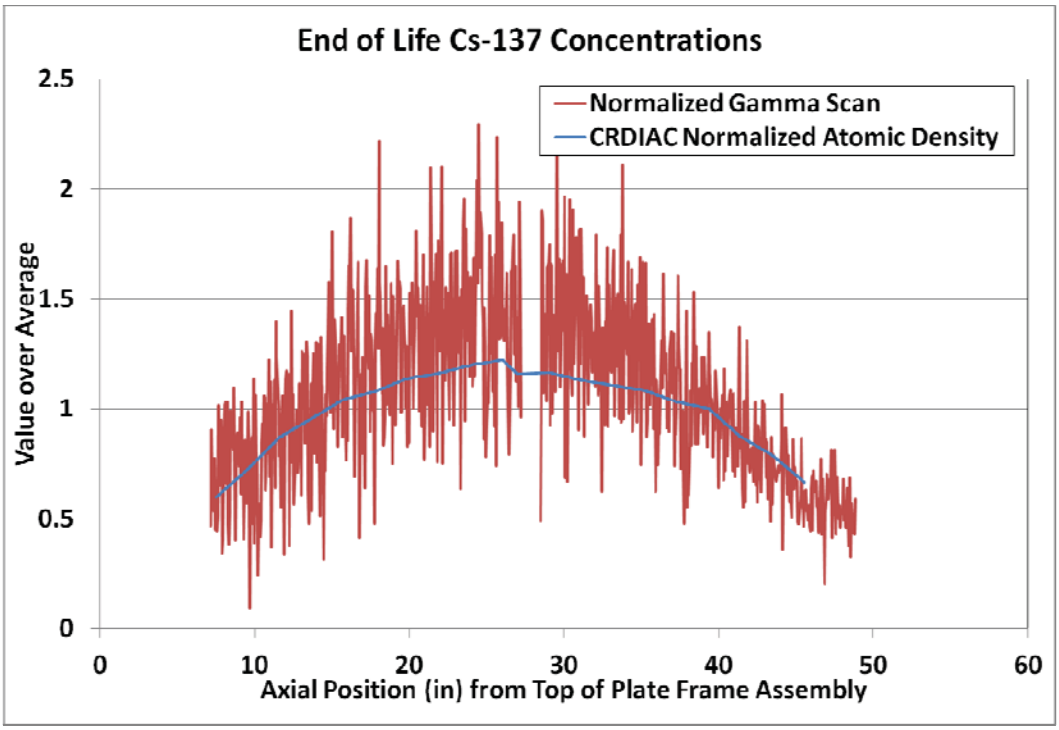

Figure A-5 CRDIAC Cs-137 profile compared against axial gamma scan of AFIP-3.

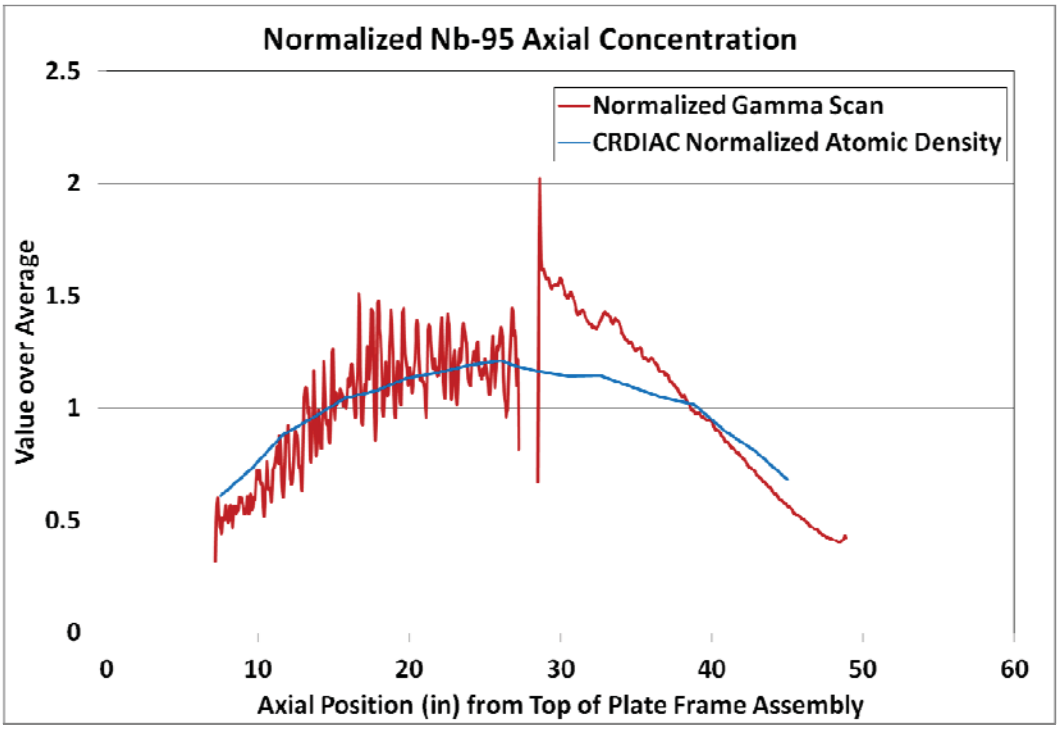

Figure A-6 CRDIAC Nb-95 profile compared against axial gamma scan of AFIP-3.

Table A-1 Validation of CRDIAC against PIE data (Robinson, 2011). Region numbers are given in Figure A-2.

Isotope	CRDIAC	PIE	C/E	Bias
Region 7				
U-235	8.34%	9.23%	90.31%	9.69%
U-238	90.00%	88.39%	101.82%	-1.82%
Cs-134/Cs-137	3.84%	3.76%	102.03%	-2.03%
Region 3				
U-235	11.2%	11.2%	100.2%	-0.2%
U-238	87.1%	86.8%	100.3%	-0.3%
Cs-134/Cs-137	3.0%	3.1%	96.3%	3.7%
Region 14				
U-235	7.3%	7.1%	103.2%	-3.2%
U-238	90.2%	90.2%	100.1%	-0.1%
Cs-134/Cs-137	4.4%	4.9%	90.6%	9.4%
Region 18				
U-235	9.2%	9.5%	96.9%	3.1%
U-238	88.7%	88.2%	100.6%	-0.6%
Cs-134/Cs-137	3.8%	4.1%	92.6%	7.4%

5. Conclusions

After comparing the MCWO and CRDIAC data for U-235 concentration in Region 1 throughout Cycle 144A (Figure A-3), the standard deviation between the data points at each time in the cycle was about 1.2% on average, so this was concluded to pass the verification step. The comparison of CRDIAC to the chemical analysis for the different regions varied in bias, as the Region 3 sample yielded about a 0.2% bias and the Region 7 sample yielded about a 9.7% bias, while the other two regions yielded about 3% biases. Taken together, the average bias was about 4%. The biases may be reduced if the cell volumes were decreased in the MCNP model of the experiment, which would lead to more cells being burned and more MRTAU calculations. It is evident by the above graphics that CRDIAC produces results that follow a similar shape as the experimental data. In conclusion, CRDIAC provides a versatile and user-customizable method to deplete fuel or even other materials present in a neutron flux and an alternative to ORIGEN-based methods.

6. **References**

Alfonsi, Andrea, et al., PHISICS Toolkit: Multi-Reactor Transmutation Analysis Utility- MRTAU. Knoxville : American Nuclear Society, 2012.

M. Holm, "Lumped Fission Product Cross Sections for the ATR CSAP PDQ Model," Idaho National Laboratory, RE-P-78-016, (February 1978).

Lillo, Misti A. and Chang, Gray S. As- Run Neutronic Analysis for the AFIP-3 Experiment Irradiated in the Center Flux Trap of the ATR, Cycles 143B and 144A. Idaho Falls : INL, 2011. ECAR-1441

G. Mesina, T. Jensen, R. McCracken, S. Smith, "LPCIS N-16 Lobe Power Calculation, Theory and Programming," Idaho National Laboratory, TRA-ATR-1821, (2002).

Robinson, Adam B. AFIP-3 Post-Irradiation Examination Summary Report. Idaho Falls : INL, 2011. INL/LTD-11-22367.

X-5 Monte Carlo Team. MCNP- A General Monte Carlo N-Particle Transport Code, Version 5. s.l. : Los Alamos National Laboratory, 2008. LA-UR-03-1987.

Appendix B. Detailed Description of As-Run Cycle Analysis

Sam Bays, INL

Cycle 145A

This cycle was loaded with the second cycle irradiation of the fourth experiment in the ATR Full-sized-plate in the center flux trap Position experiment series (AFIP-4) in the Center Flux Trap (CFT). AFIP-4 contained two plate frame assemblies, each containing six plates stacked axially within the plate frame assembly. The plates consisted of Low Enriched Uranium (20 w/o ^{235}U/U) in molybdenum alloy. The South Flux Trap (SFT) contained the first irradiation of the Advanced Graphite Creep (AGC-1) experiment, essentially graphite cylinders and instrumentation tubes, all within in a graphite matrix. The East Flux Trap (EFT) contained a Standard Irradiation Housing Assembly containing three Advanced Fuel Cycle experiments (AFC-2C, -2D, -2E) comprised of metal and oxide transuranic fuels representative of transuranic-burning Sodium-cooled Fast Reactors. The EFT also contained two National Scientific User Facility (NSUF) capsules containing advanced alloy reactor steels. The Northwest Flux Trap (NWFT) contained the Large In-Pile Tube (LIPT) with Dual Holder (DH). The Northeast Flux Trap (NEFT) contained the Multiple Irradiation Capsule Experiment (MICE) loaded with two Medium Reactivity Worth (MRW) Backups (BU). Both the NWFT and NEFT are loaded with Naval Reactor experiments. The Southeast, Southwest, and North Flux Traps contained a Standard In-Pile Tube (SIPT) loaded with Naval Reactor experiments. The West Flux Trap was loaded with the Maximum Useful Capacity Holder (MUCH) loaded with a Naval Reactors experiment.

Note: For almost all 13 cycles, the in-board and out-board large A-positions (A-1 to A-12) were loaded with High Specific Activity Cobalt (HSACo). In the current ATR HELIOS model As-Run analysis, the A-positions contained Solid Flow Restrictors Outboard A-Position (SFROP) (A-1 to A-12) and Long Solid Flow Restrictors (LSFR) (A-13 to A-16). This is a potential source of neutron poisoning not accounted for in the current ATR HELIOS As-run models.

Cycle 145A (cont.)

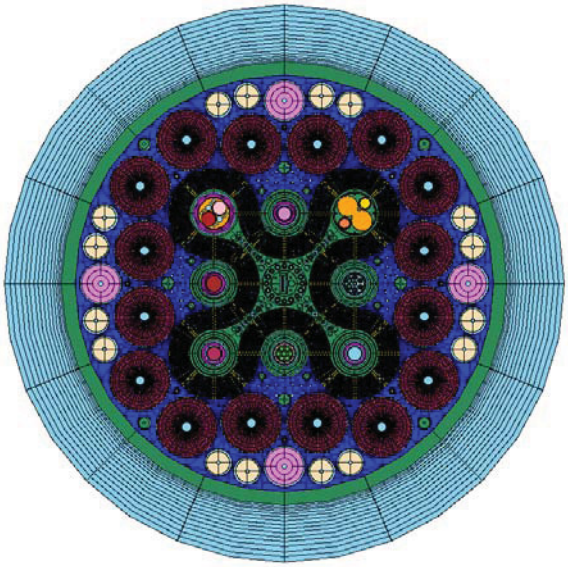

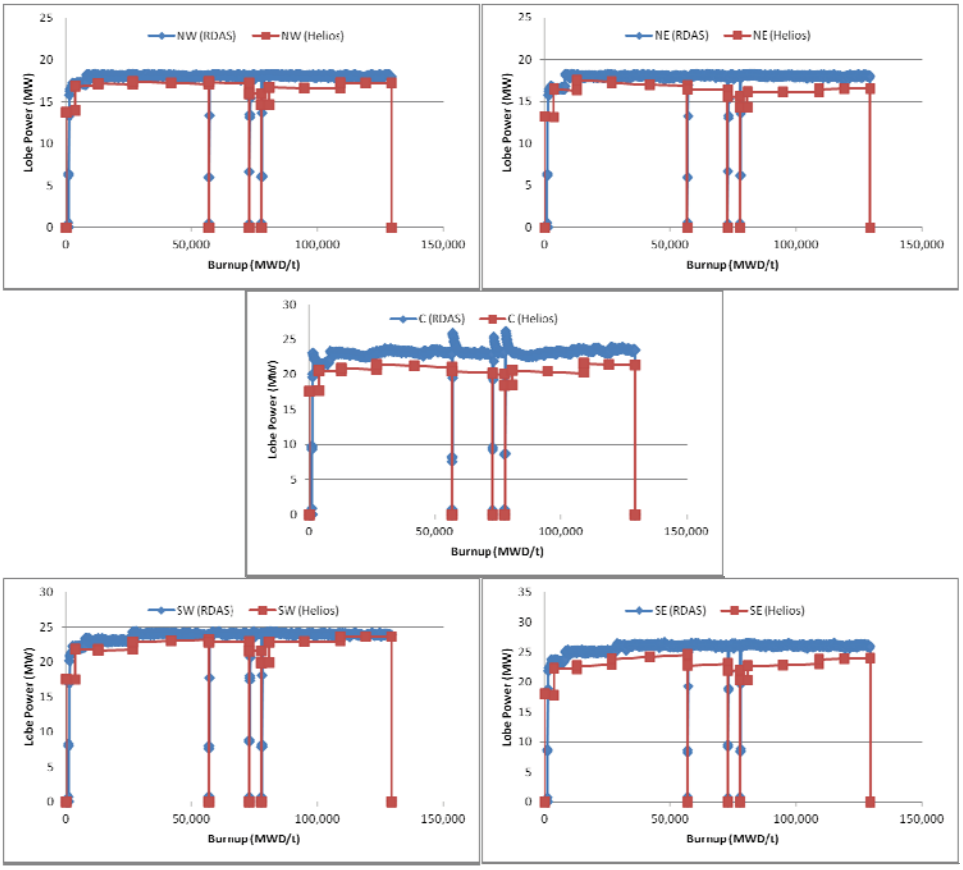

Cycle 145B

This cycle was loaded with the AFIP-BU in the CFT. The AGC-1 experiment was in the SFT. The AFC and NSUF capsules continued to be irradiated in the EFT. The NFT was loaded with the SIPT-BU, a homogenization of water and stainless steel. The WFT contained a MUCH experiment. The LIPT-DH was loaded into the NWFT. The MICE-MRW-BU was loaded in the NEFT. The SWFT and SEFT were loaded with SIPTs.

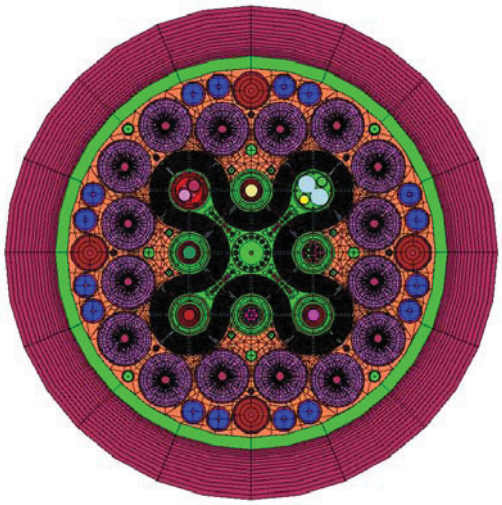

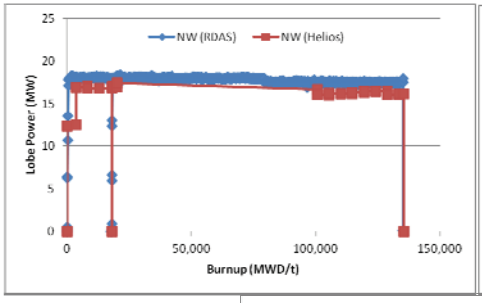

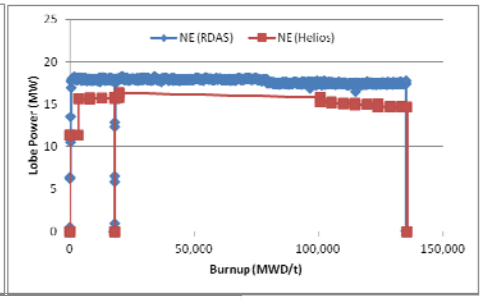

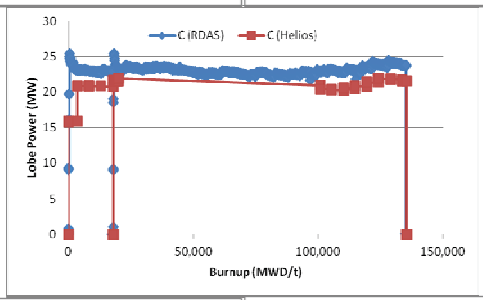

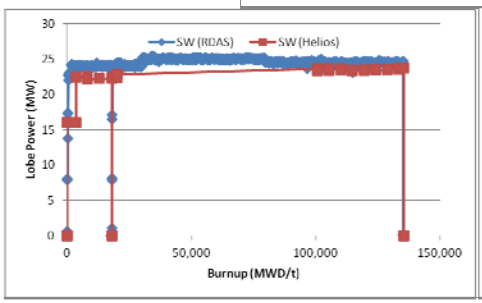

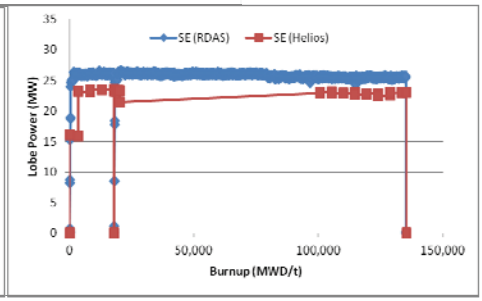

Cycle 146A

This cycle was loaded with the AFIP-BU in the CFT. The AGC-1 experiment was in the SFT. The AFC and NSUF capsules continued to be irradiated in the EFT. The Gas Fast Reactor – 1 (GFR-1) capsule was added to the EFT. One NSUF capsule was removed. The NFT was loaded with a MUCH experiment. The WFT contained a MUCH experiment. The LIPT-BU was loaded into the NWFT, a homogenization of water and stainless steel. The MICE-MRW-BU was loaded in the NEFT. The SWFT and SEFT were loaded with SIPTs.

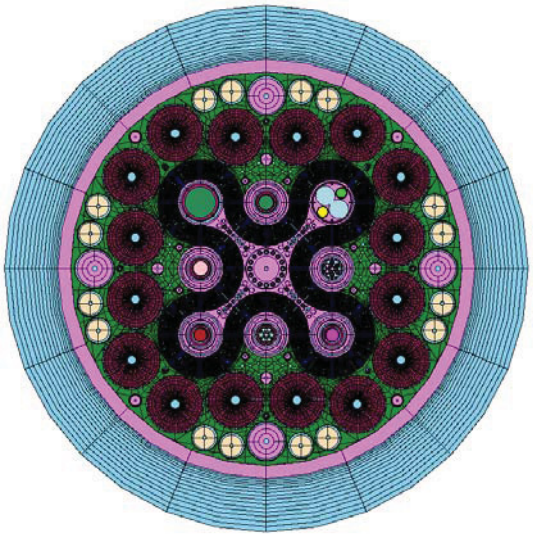

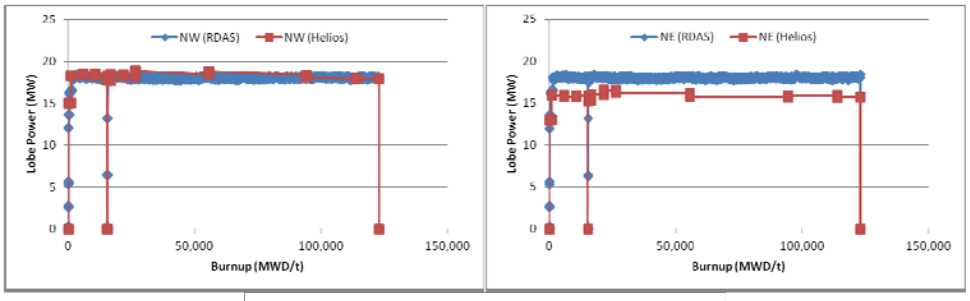

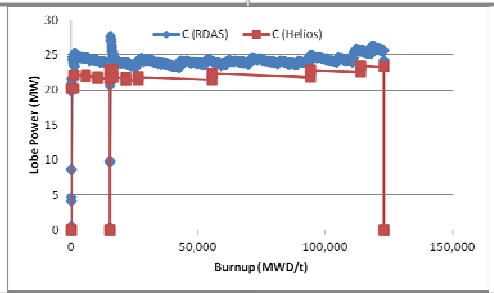

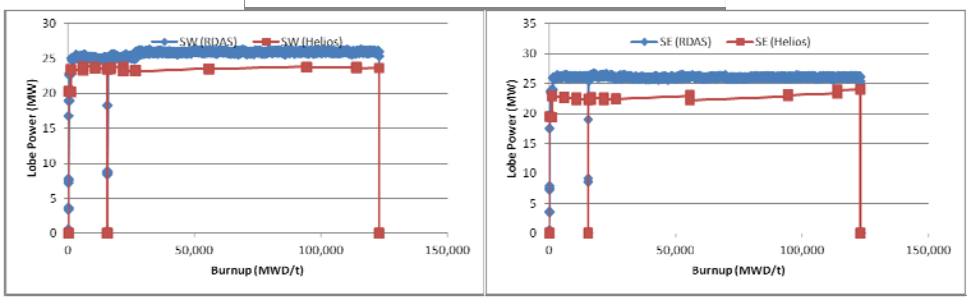

Cycle 146B

This cycle was loaded with the AFIP-6 experiment, one plate per plate frame assembly. The AGC-1 experiment was in the SFT. The AFC, GFR and NSUF capsules continued to be irradiated in the EFT. The NFT was loaded with a MUCH experiment. The WFT contained a MUCH experiment. The LIPT-DH was loaded into the NWFT. The MICE-MRW-BU was loaded in the NEFT. The SWFT and SEFT were loaded with SIPTs.

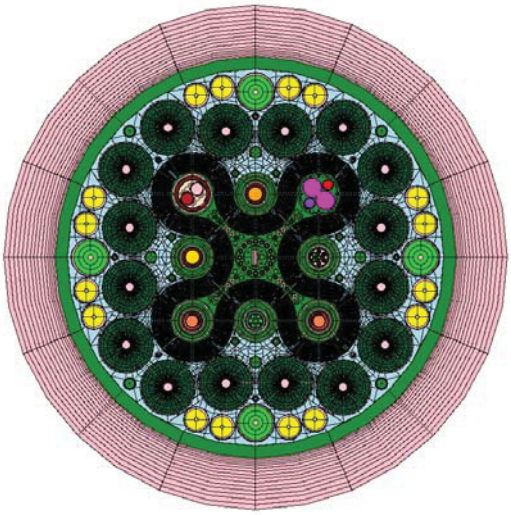

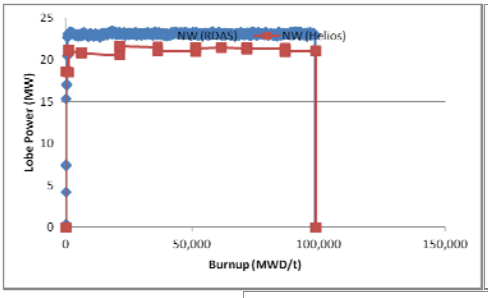

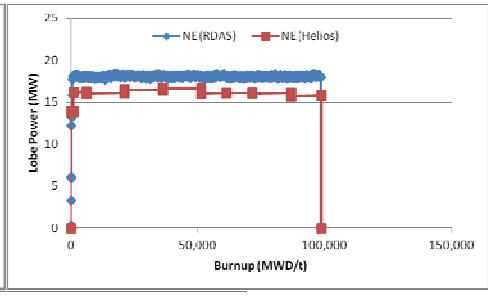

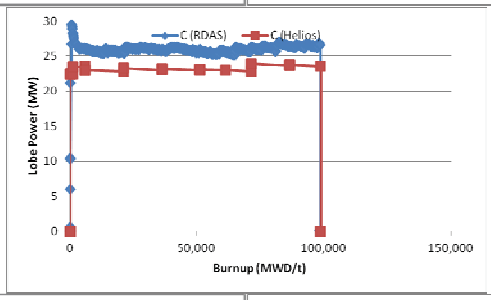

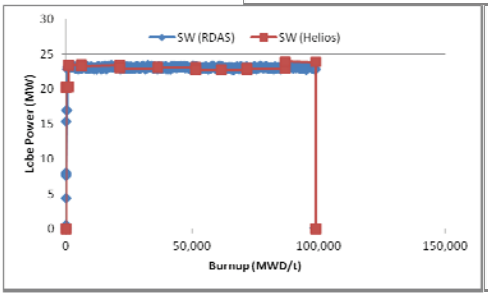

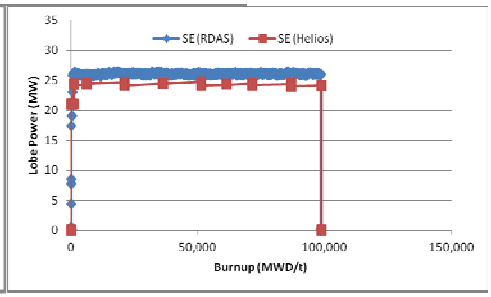

Cycle 147A

This cycle was loaded with the AFIP-BU in the CFT. The AGC-1 experiment was in the SFT. The AFC, GFR and NSUF capsules continued to be irradiated in the EFT. The NFT was loaded with a MUCH experiment. The WFT contained a MUCH experiment. The LIPT-DH was loaded into the NWFT. The MICE-MRW-BU was loaded in the NEFT. The SWFT and SEFT were loaded with SIPTs. The roughly 3 MW discrepancies in NW and NE lobe are currently unresolved. The LIPT-DH experiment for this cycle had no fissile material. The AGR-2 experiment was irradiated in the B-12 position starting in this cycle but this large B-position is on the west side of the ATR where it is unexpected to have a significant reactivity effect on the NE lobe power.

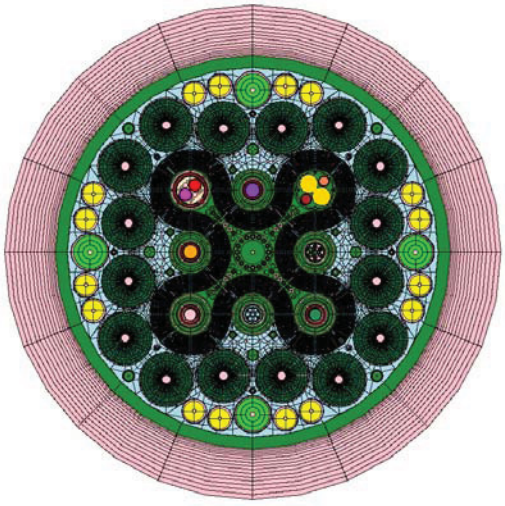

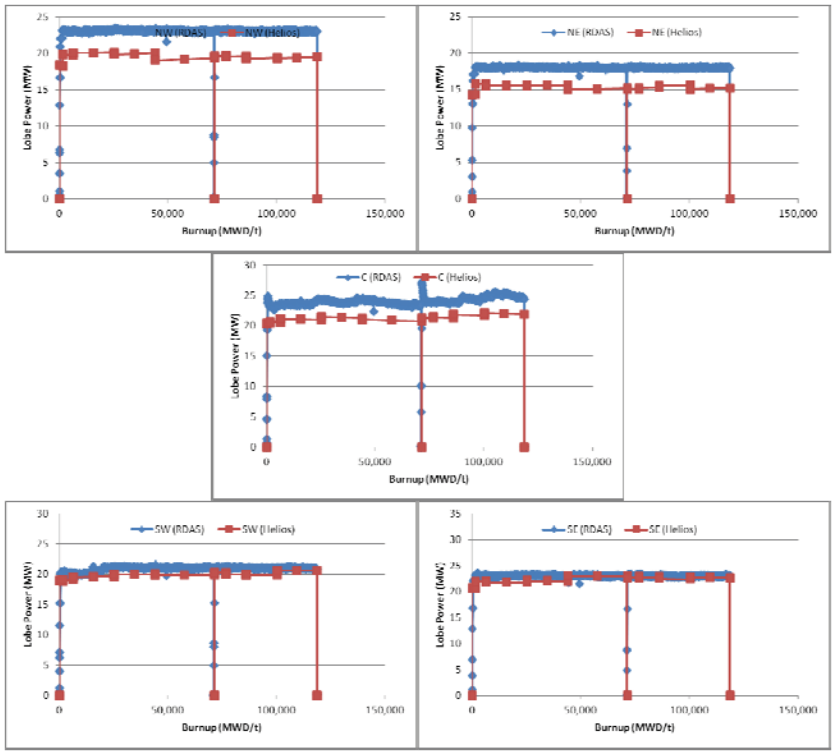

Cycle 148A

This cycle was loaded with the Center Irradiation Housing Assembly (CIHA) with seven aluminum fillers in the CFT. The AGC-1 experiment was in the SFT. The AFC, GFR and NSUF capsules continued to be irradiated in the EFT. The NFT was loaded with a MUCH experiment. The WFT contained a MUCH experiment. The LIPT-BU was loaded into the NWFT. The MICE-MRW-BU was loaded in the NEFT. The SWFT and SEFT were loaded with SIPTs.

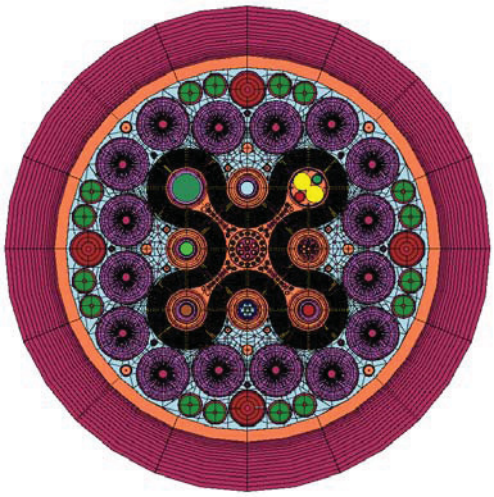

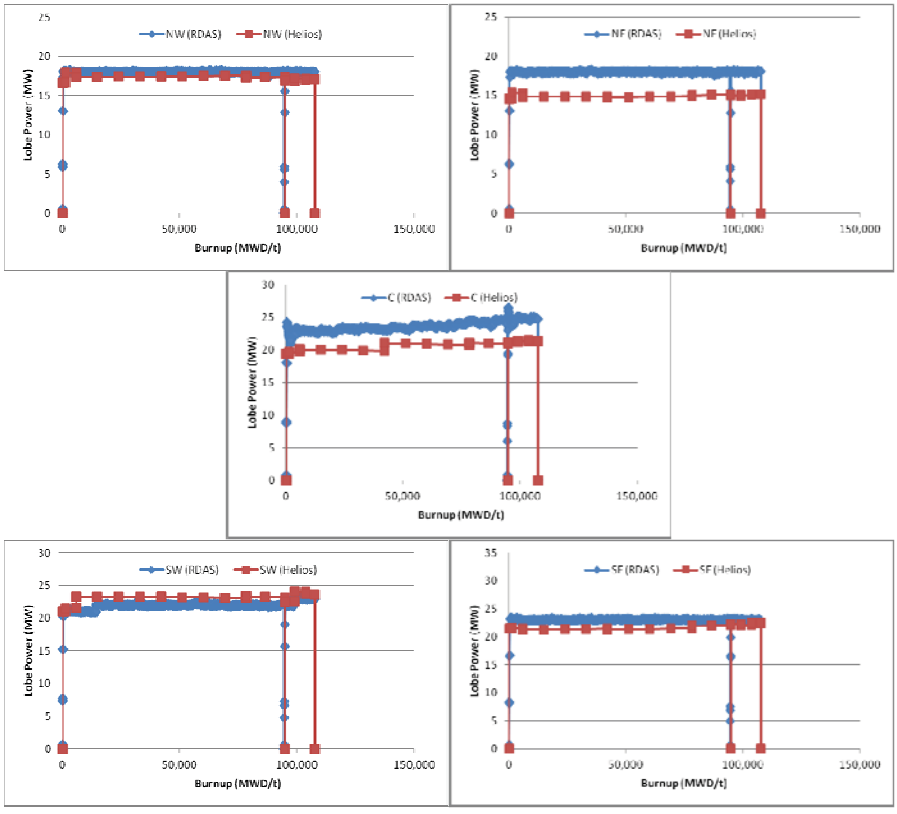

Cycle 148B

This cycle was loaded with the CIHA with seven aluminum fillers in the CFT. The AGC-1 experiment was in the SFT. The AFC, GFR and NSUF capsules continued to be irradiated in the EFT. The NFT was loaded with a SIPT experiment. The WFT contained a MUCH experiment. The LIPT-BU was loaded into the NWFT. The MICE-MRW-BU was loaded in the NEFT. The SWFT and SEFT were loaded with SIPTs.

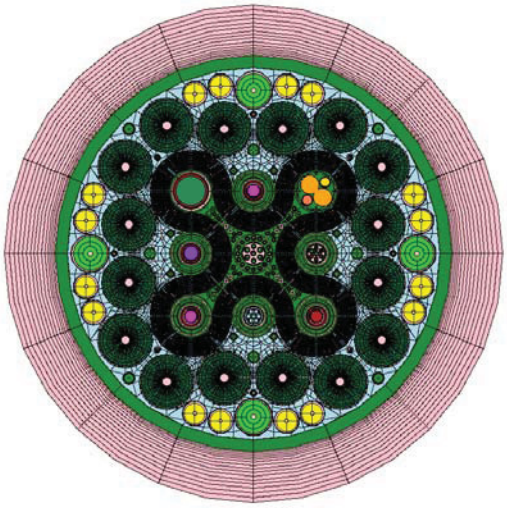

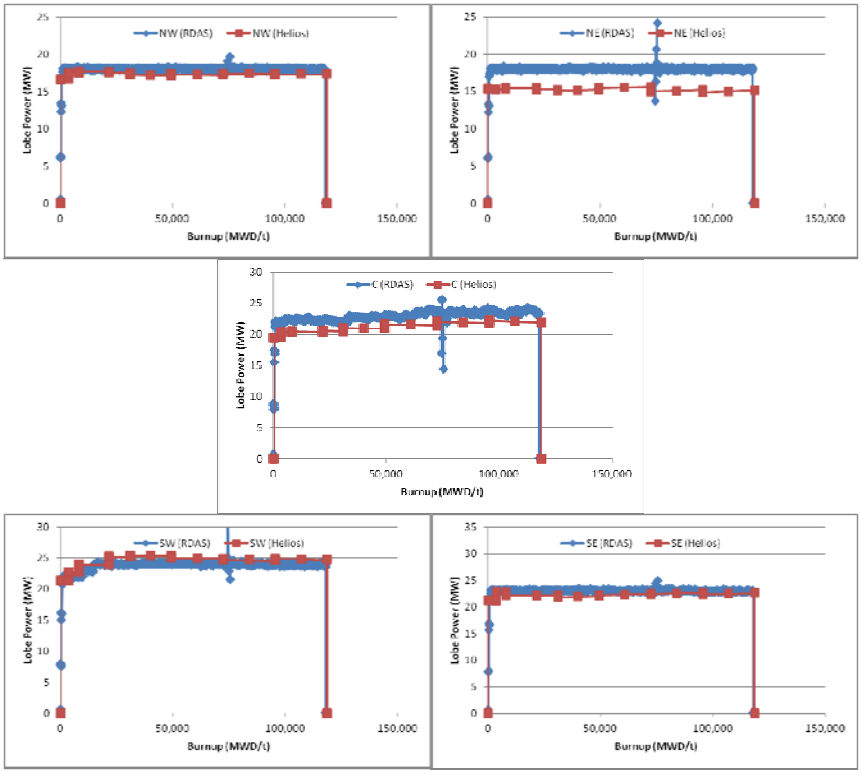

Cycle 149A

This cycle was loaded with the CIHA with seven aluminum fillers in the CFT. The AGC-2 experiment was in the SFT. The AFC, GFR and NSUF capsules continued to be irradiated in the EFT. The NFT was loaded with a SIPT experiment. The WFT contained a MUCH experiment. The LIPT-DH was loaded into the NWFT. The MICE-MRW-BU was loaded in the NEFT. The SWFT and SEFT were loaded with SIPTs. Note: The Electric Power Research Institute (EPRI) series of experiments in the small outboard A-positions were beginning to be irradiated in this cycle. LSFR (i.e., flow restrictors) are modeled instead. The EPRI experiment capsules contain pre-hydrated specimens of zirconium alloys within a stainless steel sample holder. This could either add or remove moderation in the outboard area of the neck arms depending on how much water is replaced by the capsule or how much moderation is inserted with the hydrated zirconium.

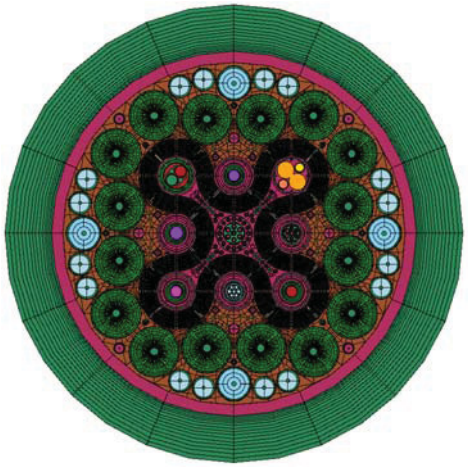

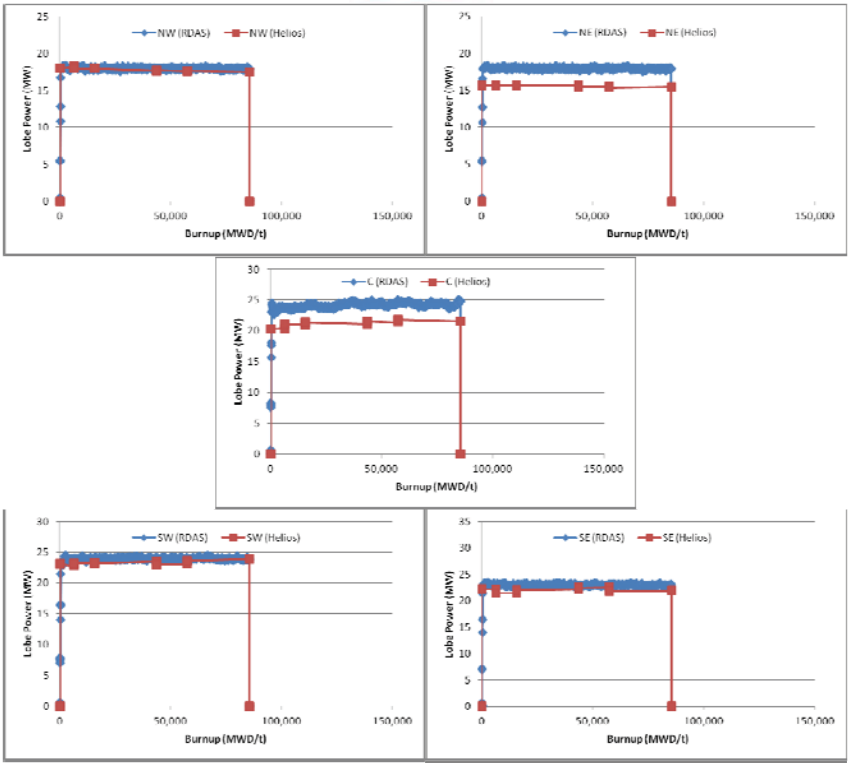

Cycle 149B

This cycle was loaded with the AFIP-7 experiment in the CFT, four curved 40% ^{235}U/U enriched uranium in molybdenum alloy plates. The AGC-2 experiment was in the SFT. The AFC and NSUF capsules continued to be irradiated in the EFT. The NFT was loaded with a SIPT experiment. The WFT contained a MUCH experiment. The LIPT-DH was loaded into the NWFT. The MICE-MRW-BU was loaded in the NEFT. The SWFT and SEFT were loaded with SIPTs.

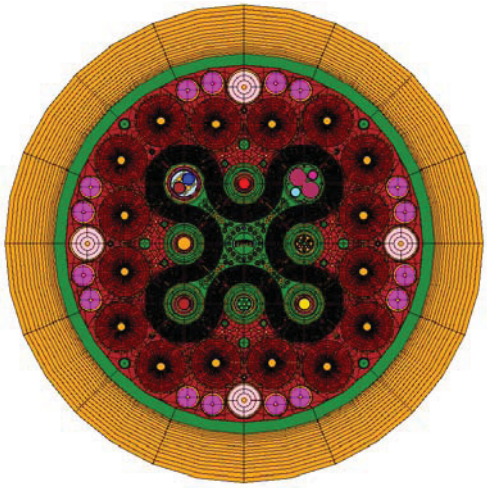

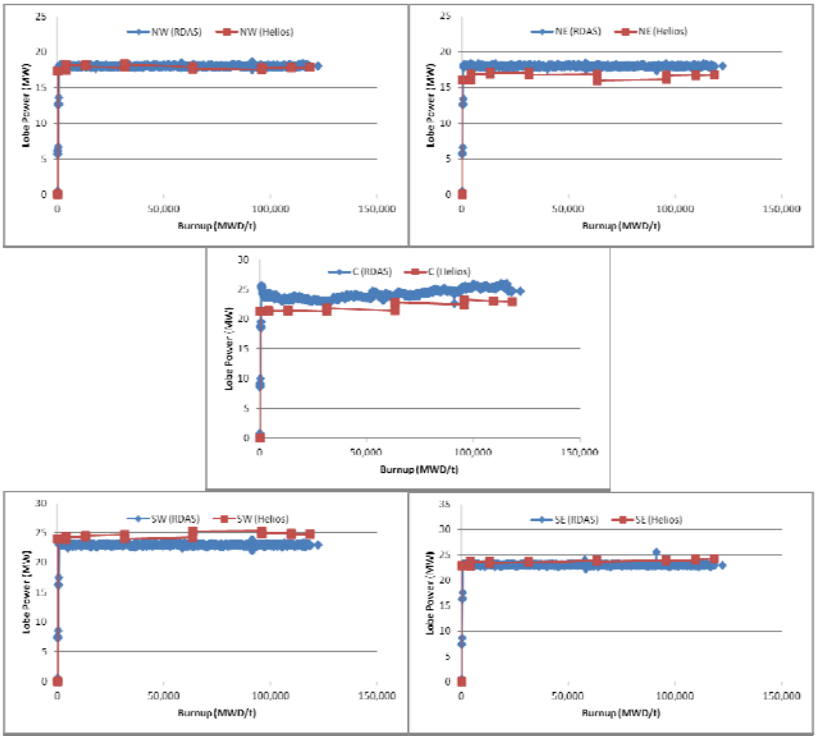

Cycle 150A

This cycle was a Powered Axial Locating Mechanism (PALM) cycle. The civilian experiments are removed from the core. A PALM mechanism was loaded into a SIPT and used to initiate ramp tests in a Navy experiment in the beginning of the cycle. The PALM mechanism moves a Navy experiment into and out-of the flux trap. The EFT and SFT both contained a Standard Irradiation Housing Assembly loaded with Low Specific Activity Cobalt Capsules (LSACo). The CFT was loaded with six aluminum fillers and one LSACo. The NFT was loaded with a SIPT experiment. The WFT contained a MUCH experiment. The LIPT-BU was loaded into the NWFT. The MICE-MRW-BU was loaded in the NEFT. The SEFT was loaded with SIPTs. The SWFT was loaded with a SIPT-BU.

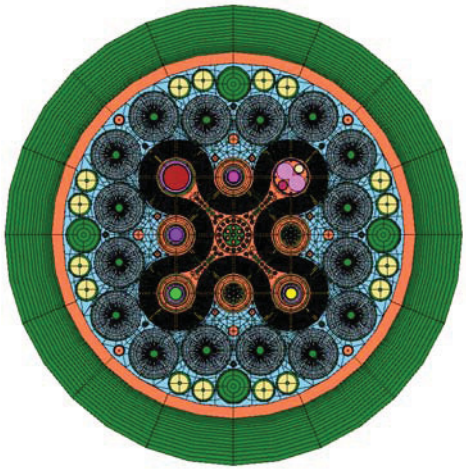

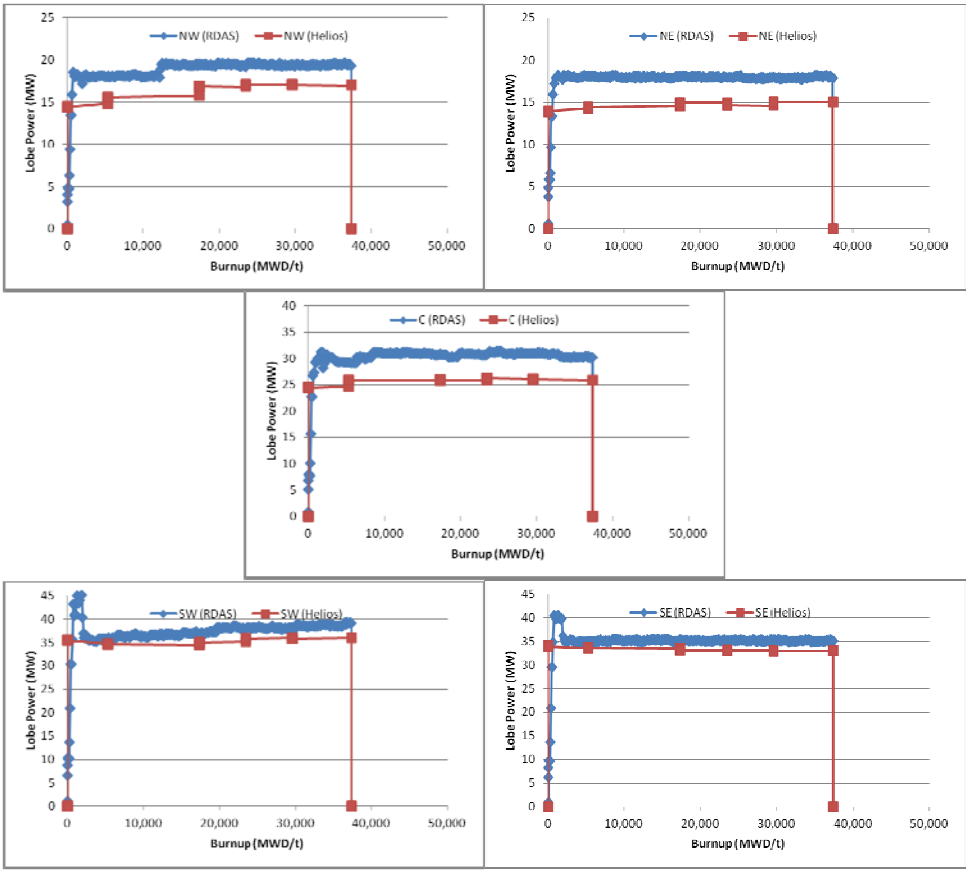

Cycle 150B

This cycle was loaded with the AFIP-7 experiment in the CFT. The AGC-2 experiment was in the SFT. The AFC and NSUF capsules continued to be irradiated in the EFT. The NFT was loaded with a SIPT experiment. The WFT contained a MUCH experiment. The LIPT-DH was loaded into the NWFT. The MICE-MRW-BU was loaded in the NEFT. The SWFT and SEFT were loaded with SIPTs.

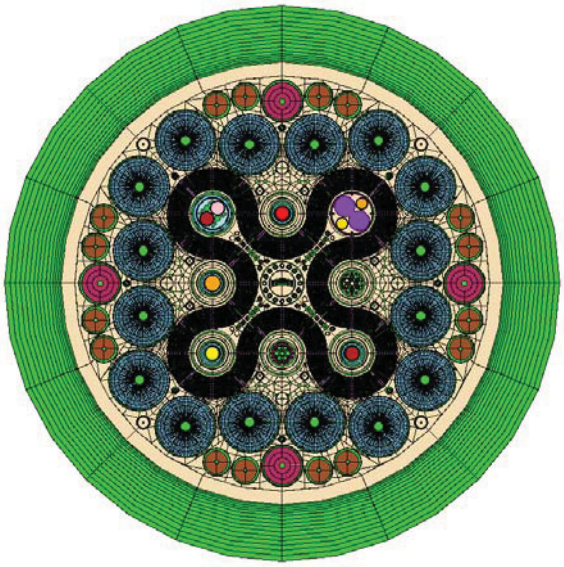

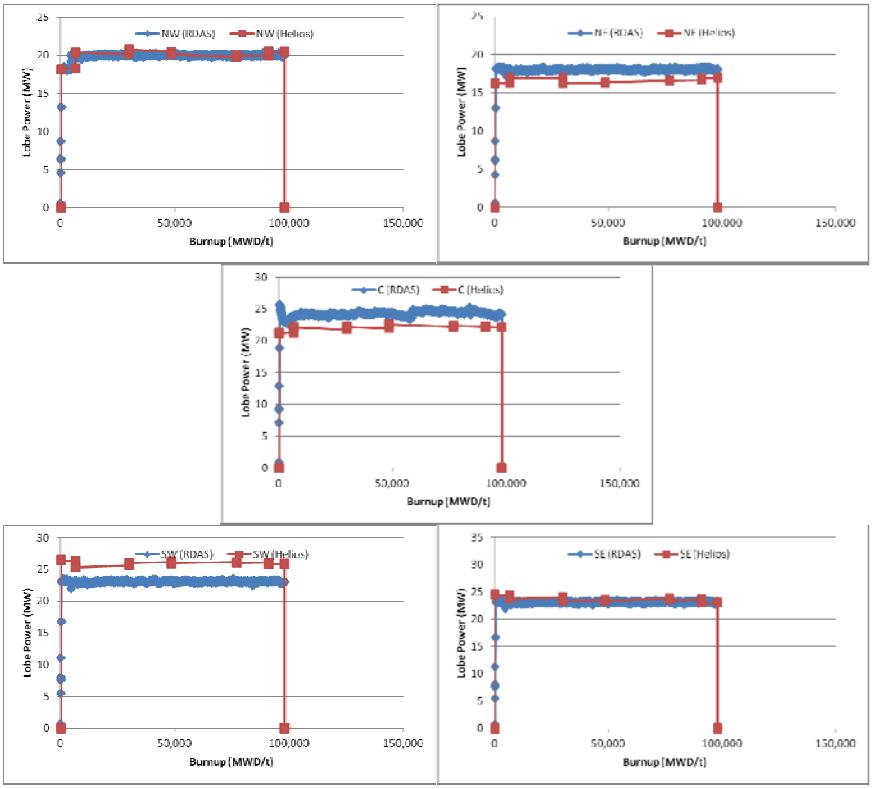

Cycle 151A

This cycle was loaded with the AFIP-6 (Mk II) experiment in the CFT. The AGC-2 experiment was in the SFT. The AFC and NSUF capsules continued to be irradiated in the EFT. The NFT was loaded with a SIPT experiment. The WFT contained a MUCH experiment. The LIPT-DH was loaded into the NWFT. The Advanced Gas Reactor – 3/4 (AGR-3/4) instrumented test capsule was loaded in the NEFT. The SWFT and SEFT were loaded with SIPTs.

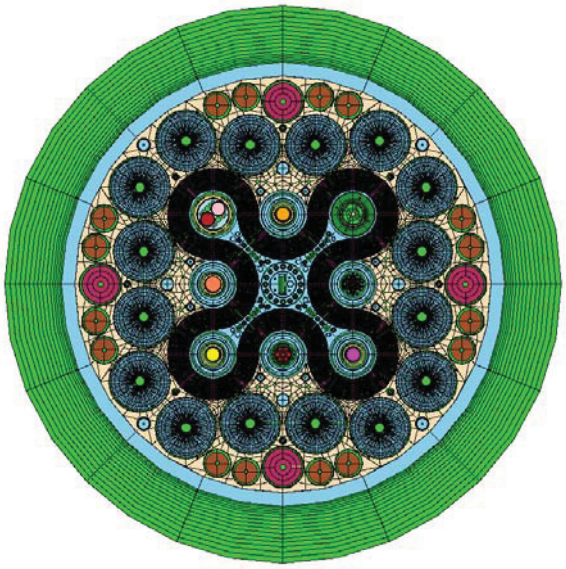

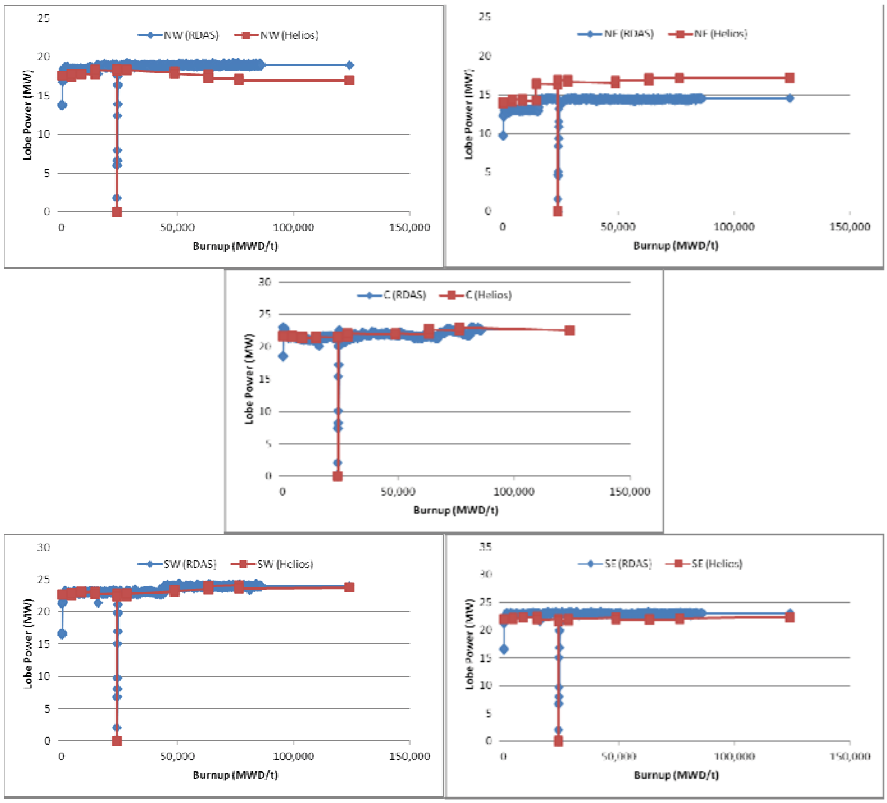

Cycle 151B

This cycle was loaded with the AFIP-6 (Mk II) experiment in the CFT. The AGC-2 experiment was in the SFT. The AFC, GFR and NSUF capsules continued to be irradiated in the EFT. The NFT was loaded with a SIPT experiment. The WFT contained a MUCH experiment. The LIPT-DH was loaded into the NWFT. The AGR-3/4 was loaded in the NEFT. The SWFT and SEFT were loaded with SIPTs.

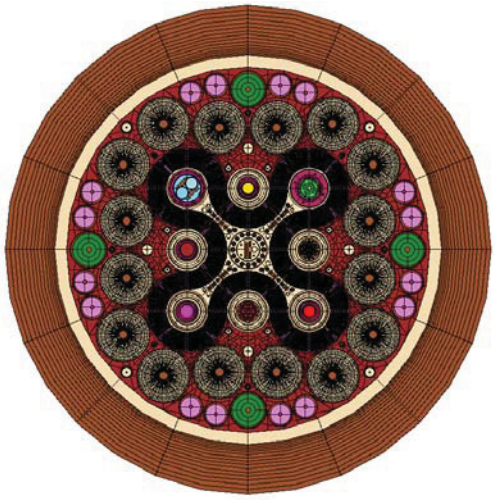

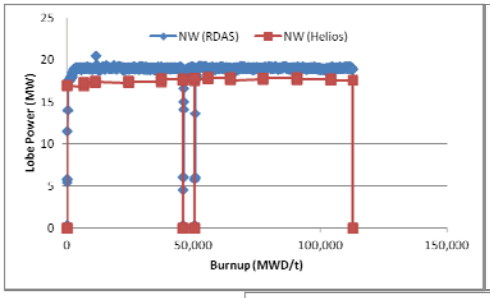

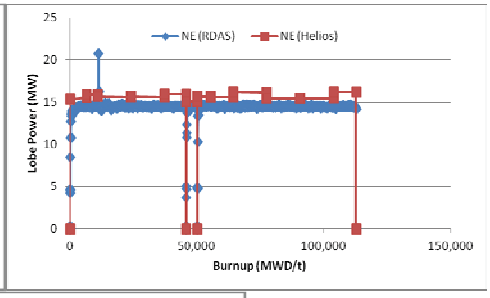

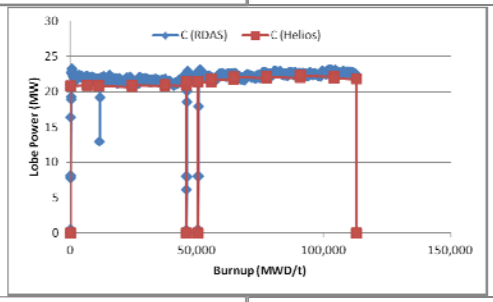

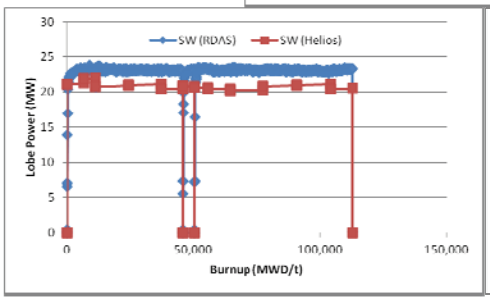

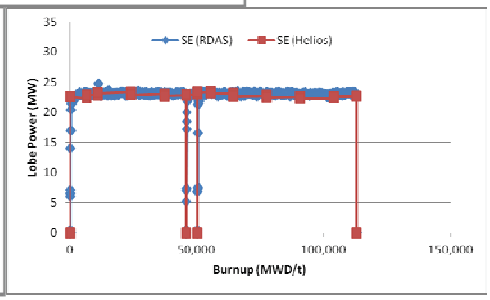

Appendix C. Post-Processing Calculation Protocols

Emily Swain, INL

A detailed review of the neutronic post-processing calculations currently performed within the PDQ-based methodology has been performed [Swain, 2011]. An overview of the requirements-driven calculations that are to be duplicated within the Helios-based methodology is presented below with brief descriptions of the simplifications and alternate methods expected to be used in this new methodology. For complete descriptions of these calculations as performed by the PDQ-based methodology, the interested reader is referred to Swain, 2011.

Power density ratios are the basis for many of the UFSAR requirements that are fulfilled by the current PDQ-based methodology. The point-to-core power density ratios are calculated by Equation 1 below using the in-house program GOPP. This calculation applies normalization factors to each plate so that various approximations in the model can effectively be removed from the results. The calculation of the power density normalization factors is performed within the PDQ-based methodology via Equation 2 below. Due to the methodology change associated with the change in geometric representation of fuel elements, the smoothing function term in Equation 1 is completely eliminated. Thus, the Helios-based methodology will replace Equation 1 with an equation that merely multiplies the power obtained from each region by its associated normalization factor.

$$\textit{Point-to-Core Power Density Ratio}_{\textit{point, plate}} = (\textit{Pwr}_{\textit{interpolated, PDQ mesh}})\text{x} \\ (\textit{Power Density Normalization}_{\textit{plate traverse, ROSUB}})\,(\textit{Smoothing Function}_{\textit{point, traverse}}) \quad (1)$$

$$\textit{Power Density Normalization}_{\textit{plate}} = (\textit{Power Peaking Axial Correction})\,(\textit{Nominal Power Division}_{\textit{lobe}})\text{ x} \\ \textit{Homogenized Cell-to-Matrix Correction}_{\textit{fuel plate}}) \,/\, \textit{Average Relative Power Density}_{\textit{PDQ}} \quad (2)$$

The first term in Equation 2 used to calculate the needed normalization factors is an axial correction currently calculated by the in-house program ROSUB that will likely be entirely replaced within the Helios-based methodology by a correction determined from one of the 3D codes in the Methods Update suite. However, duplication of part or all of the current calculation can be expected as the Helios-based methodology is developed and compared against the current methodology results. The second term is in place to correct approximations in the OSCC positions needed to obtain the specified lobe powers via Equation 3 below, as calculated by ROSUB. This overall correction is expected to be smaller using the Helios-based methodology, while remaining a necessary part of the new methodology. Due to the lack of homogenization associated with the geometric representation of fuel elements, the homogenization correction term in Equation 2 is completely eliminated, creating a three-term equivalent to Equation 2 in the Helios-based methodology.

$$\textit{Nominal Power Division}_{\textit{lobe}} = (\textit{Pwr}_{\textit{lobe, goal}} \,/\, \textit{Pwr}_{\textit{lobe, calculated}}) \,/\, (\textit{Pwr}_{\textit{total, goal}} \,/\, \textit{Pwr}_{\textit{total, calculated}}) \quad (3)$$

The final term of Equation 2 is the average power density relative to the associated PDQ regions as defined by Equation 4 below. The homogenization term discussed above and the relative power density term are used in combination to form the calculation of the average power density relative to the fuel meat volume. The Helios-based methodology will calculate average power density by directly determining the total power in the core and the total volume of fuel meat in the core. Thus, the equivalent calculation of Equation 2 using the Helios-based methodology will contain three multiplication terms, but only one of those terms (namely the nominal power division) will be calculated in the same manner as the PDQ-based methodology.

$$Average\ Relative\ Power\ Density_{PDQ} = Pwr_{total,\ calculated} / V_{fueled\ cells,\ total} \quad (4)$$

The calculation of Effective Plate Power (EPP) and Effective Point Power (EPtP) is necessary to satisfy many requirements designed to ensure safe operation of the fuel. The density ratio calculated by Equation 1 provides the data for the first term of the EPtP calculation (Equation 5 below). The second term is the power ratio calculated by Equation 6 below that is used to determine the approximate power obtained by each region if the lobe is operated at its maximum allowed power, despite the model utilizing nominal lobe powers during its calculations. The final two terms are the instrument error and plate restrictions that are obtained from operational data.

$$EPtP_{plate,\ time\ step} = (Point\text{-}to\text{-}Core\ Power\ Density\ Ratio_{plate,\ time\ step})\ (Power\ Ratio_{lobe})\ x$$
$$(Instrument\ Error_{lobe,\ lobpwr})\ /\ Plate\ Restrictions_{plate,\ recinv.t24} \quad (5)$$

$$Power\ Ratio_{lobe} = (Total\ Pwr_{lobpwr})\ (Lobe\ Pwr_{Maximum,\ lobpwr} / Lobe\ Pwr_{Nominal,\ lobpwr}) \quad (6)$$

Once the in-house program RPCR2 calculates EPtP, Equation 7 below is used to determine the EPP values by multiplying the EPtP results by an axial peaking factor calculated by ROSUB. The calculation of EPtP via Equation 5, excluding the power density ratio discussed above, is expected to remain the same for the Helios-based methodology. The axial peaking factor term in Equation 7 will likely be entirely replaced within the Helios-based methodology by a correction determined from one of the 3D codes in the Methods Update suite, much like the axial correction factor discussed above.

$$EPP_{plate,\ time\ step} = (EPtP_{plate,\ time\ step})\ (Axial\ Peaking\ Factor_{element,\ time\ step}) \quad (7)$$

Additional UFSAR restrictions require the calculation of the fission density in various plates in the core. Equation 8 below is used in the in-house program GOPP to calculate normalized fission density values. The Cumulative Fissioned Atom Density (CFAD) normalization factors are calculated using Equation 9 below. The first two terms of Equation 9 form a unit conversion, and thus will not change with changes to the methodology. The axial correction term in Equation 9 will likely be entirely replaced within the Helios-based methodology by a correction determined from one of the 3D codes in the Methods Update suite, much like the axial correction factor and axial peaking factor discussed above. Due to the lack of homogenization associated with the geometric representation of fuel elements, the homogenization correction term in Equation 9 is completely eliminated in the Helios-based methodology.

$$Fission\ Density_{point,\ time\ step} = (Fission\ Density_{interpolated,\ PDQ\ mesh})\ (CFAD\ Normalization_{plate,\ ROSUB}) \quad (8)$$

$$CFAD\ Normalization_{plate} = (\text{fissions/barn-cm}) / (10^{21}\ \text{fissions/cm}^3)\ x$$
$$(Axial\ Peak\text{-}to\text{-}Average\ CFAD\ Correction)\ (Cell\ Homogenization\ Correction_{plate}) \quad (9)$$

In order to avoid violation of EOC fission density limits, projections of these densities are calculated via the use of the fission buildup rate. The in-house program LMFIS calculates the buildup rate using Equation 10 below. The results of this calculation are then used in Equation 11 to determine a burnup limit for each position in the core. This burnup limit is used to determine the maximum cycle length and the limiting element in a lobe. The burnup rate is also used to predict the maximum fission density allowed in each position at the beginning of the next cycle via Equation 12.

$$\textit{Fission Build-up Rate}_{\textit{position}} =$$

$$(\textit{Peak Fission Density}_{\textit{last time step, position}} - \textit{Peak Fission Density}_{\textit{next to last time step, position}}) \div (\textit{Lobe Exposure}_{\textit{last time step}} - \textit{Lobe Exposure}_{\textit{next to last time step}}) \quad (10)$$

$$\textit{Burnup Limit}_{\textit{position}} = \textit{Lobe Exposure}_{\textit{last time point}} +$$

$$(\textit{Fission Density Limit}_{\textit{EOL}} - \textit{Peak Fission Density}_{\textit{last time point, lobe}}) / \textit{Fission Build-up Rate}_{\textit{position}} \quad (11)$$

$$\textit{BOL Fission Density}_{\textit{maximum, position}} = \textit{Fission Density Limit}_{\textit{EOL}} -$$

$$(\textit{EOL Exposure}_{\textit{lobe, nominal}}) (\textit{Fission Build-up Rate}_{\textit{position, maximum}}) \quad (12)$$

Appendix D. HELIOS Semi-Analytical Benchmarks for ATR Code Verification

B. D. Ganapol
Visiting Scientist, University of Arizona
and
D. S. Crawford
University Space Research Associates, INL Student Intern

1.0 INTRODUCTION

Core modeling of the Advanced Test Reactor (ATR) at INL is currently undergoing a significant update through the Core Modeling Update Project (Nigg and Steuhm, 2011). The intent of the project is to bring ATR core modeling in line with today's standard of computational efficiency and verification and validation practices. The **HELIOS-2** lattice physics code (Wemple et al., 2008) is the lead candidate code of several reactor physics codes to be dedicated to modernize ATR core analysis. This investigation is concerned with an independent verification of the **HELIOS-2** spectral representation including the slowing down and thermalization algorithm and its data dependency. Here, we describe and demonstrate a recently developed **S**imple **S**pectral **M**odel (**SSM1**) based entirely on analytical multigroup parameters for both the slowing down and thermal spectra. The new independent capability features fine group detail to assess the flux and multiplication factor dependencies on cross section data sets for a fundamental infinite medium example.

2.0 CRITICALITY AND EIGENSTATE: A Spectral Study of an Infinite Medium

In a typical thermal reactor, after neutron birth at high energy (1-2 Mev), neutrons lose energy from collisions (slow down) until they reach energies near the temperatures of the surrounding material. At this point, neutrons become thermalized after surviving the fuel resonance region, and are available to generate fission to restart the cycle. The following slowing down equation describes the self-sustaining neutron life cycle in an infinite medium:

$$\Sigma(E)\phi(E) = \int_0^{E_0} dE' \Sigma_s(E' \to E)\phi(E') + \\ + \frac{\chi(E)}{k} \int_0^{E_0} dE' \nu(E') \Sigma_f(E') \phi(E') \tag{1}$$

The Σs represent macroscopic cross sections; ν is the number of neutrons per fission appearing at energy E with distribution χ; and ϕ is the neutron flux distribution. The highest neutron energy is E_0 at 20 *Mev*. One introduces the multiplication factor k to maintain a sustained neutron population, therefore Eq(1) defines an eigenvalue problem.

3.0 THE MULTIGROUP FORMULATION

In multigroup form for N_G total groups, Eq(1) is (Bell and Glasstone, 1970)

$$\Sigma_g \phi_g = \sum_{g'=1}^{N_G} \Sigma_{gg'} \phi_{g'} + \frac{\chi_g}{k} \sum_{g'=1}^{N_G} \nu\Sigma_{fg'} \phi_{g'}, \quad g = 1,\ldots,N_G, \qquad (2a)$$

where $\Sigma_{gg'}$ is the isotropic scattering transfer cross section from group g' to g,

$$\phi_{g'} \Sigma_{gg'} \equiv \int_{\Delta E_g} dE \int_{\Delta E_{g'}} dE' \, \Sigma_s \left(E' \to E \right) \phi \left(E' \right), \qquad (2b)$$

which is appropriate for elastic slowing down and thermal scattering alike. Σ_g is the group g cross section [i = total (blank), scattering (s) or fission(f)]

$$\phi_g \Sigma_{ig} \equiv \int_{\Delta E_g} dE \Sigma_i \left(E \right) \phi \left(E \right)$$

and ϕ_g is the group flux

$$\phi_g = \int_{\Delta E_g} dE \phi \left(E \right). \qquad (2c)$$

The multigroup form comes about by first partitioning the entire energy range into N_G subintervals

$$\Delta E_g = \left[E_g, E_{g-1} \right], \quad g = 1,2,\ldots,N_G, \qquad (3)$$

and decomposing the scattering integral, by isotope j, according to

$$\int_0^{E_0} dE' \Sigma_{sj} \left(E' \to E \right) \phi \left(E' \right) = \sum_{g'=1}^{N_G} \int_{\Delta E_{g'}} dE' \Sigma_{sj} \left(E' \to E \right) \phi \left(E' \right).$$

Based on the experimental nature of cross section data, i.e., interval measurement uncertainty, the group partition is made practical by assuming a flux weighting across each (measurement) interval

$$\phi \left(E \right) = f_g \left(E \right) \phi_g \qquad (4a)$$

and requiring

$$\int_{\Delta E_g} dE f_g(E) \equiv 1. \qquad (4b)$$

By introducing Eqs(4) into Eq(1), and after integrating over group *g* with

$$\Sigma_g \equiv \int_{\Delta E_g} dE f_g(E)\Sigma(E) \qquad (5a)$$

$$\Sigma_{sjgg'} \equiv \int_{\Delta E_g} dE \int_{\Delta E_{g'}} dE'\Sigma_{sj}(E' \to E) f_g(E'), \qquad (5b)$$

we arrive at Eq(2a).

3.1 Neutron Slowing Down: Elastic Scattering

Basic neutron elastic scattering is assumed for the homogeneous mixture while neutrons slow down above the thermal region [0,E_T] or $1 \le g \le N_T$. A simple thermal model based on a free hydrogen gas will be developed in § 3.2.

In general, if one assumes piecewise constant cross sections in interval ΔE_g,

$$\Sigma_g \equiv \Sigma_{g-1/2}; \qquad (6a)$$

and, if in addition, the weighting function is the common 1/*E* weighting for neutron slowing down, the weighting function becomes

$$f_g(E) \equiv \frac{\alpha_{0g}}{E}, \quad \alpha_{0g} \equiv \left[\ln\left(\frac{E_{g-1}}{E_g}\right)\right]^{-1}, \qquad (6b)$$

then, for elastic scattering for the j^{th} material

$$\Sigma_{sjgg'} \equiv \frac{\alpha_{0g'}\Sigma_{sjg'}}{1-\alpha} \int_{\Delta E_g} dE \int_{\Delta E_{g'}} dE' \frac{\rho_j(E', E)}{E'^2}, \qquad (7)$$

where

$$\rho_j\left(E',E\right)\equiv\left\{\begin{array}{ll} 1, & \alpha_j E'\le E\le E' \\ 0, & \text{otherwise}\end{array}\right\}=\Theta\left(E-\alpha_j E'\right)-\Theta\left(E-E'\right).$$

Θ is the unit step function and α_j is the scattering parameter for isotope *j*

$$\alpha_j\equiv\left[\frac{A_j-1}{A_j+1}\right]^2.$$

On substitution and after some manipulation, the group to group transfer cross section therefore becomes (Ganapol, 2009)

$$\Sigma_{sjgg'}\equiv$$

$$\equiv\frac{\alpha_{0g'}\Sigma_{sg'}}{1-\alpha_j}\left\{\begin{array}{l}\Theta\left(E_{g-1}-\alpha_j E_{g'-1}\right)T_{3j}\left(E_{g-1}/\alpha_j,E_{g'-1}\right)+\Theta\left(E_{g-1}-\alpha_j E_{g'}\right)T_{3j}\left(E_{g'},E_{g-1}/\alpha_j\right)- \\ -\Theta\left(E_g-\alpha_j E_{g'-1}\right)T_{4j}\left(E_g/\alpha_j,E_{g'-1}\right)-\Theta\left(E_g-\alpha_j E_{g'}\right)T_{4j}\left(E_{g'},E_g/\alpha_j\right)- \\ -\Theta\left(E_{g-1}-E_{g'-1}\right)T_{1j}\left(E_{g-1},E_{g'-1}\right)-\Theta\left(E_{g-1}-E_{g'}\right)T_{1j}\left(E_{g'},E_{g-1}\right)+ \\ +\Theta\left(E_g-E_{g'-1}\right)T_{2j}\left(E_g,E_{g'-1}\right)+\Theta\left(E_g-E_{g'}\right)T_{2j}\left(E_{g'},E_g\right)\end{array}\right\} \tag{8a}$$

for $1\le g'\le N_T,\ 1\le g\le N_G$ with

$$T_{kj}\left(x,y\right)\equiv\beta_{kj}\left[\frac{1}{x}-\frac{1}{y}\right]-\gamma_{kj}\ln\left(\frac{y}{x}\right). \tag{8b}$$

Table 1 gives the appropriate constants for $T_{kj}\left(x,y\right)$.

Table 1: $T_{kj}\left(x,y\right)$

k	β_{kj}	γ_{kj}
1	E_{g-1}	1
2	E_g	1
3	E_{g-1}	α_j
4	E_g	α_j

We emphasize that the particular advantage of Eqs(8) is that they represent multigroup slowing down entirely analytically.

3.2 Neutron Thermalization: Thermal Scattering

A spectral model is truly not complete without consideration of neutron thermalization. For this reason, we now consider the simplest of thermal scattering models-- the hydrogen gas (H-gas) model (Bell and Glasstone, 1970). In this formulation, hydrogen is the primary scattering element and does so in its free gas molecular form. Hence, a thermal region is created with N_G-N_T groups where the H-gas model applies, apart from the slowing down region. E_T is the slowing down/thermal boundary, where the only coupling between the regions will be through the incoming scattering source from slowing down as discussed below.

The H-gas model assumes the following form for the differential scattering cross section:

$$\Sigma_{sjT}\left(E'\to E\right)\equiv\Sigma_{sj}\left(E'\right)\begin{cases}\dfrac{F\left(\varepsilon\right)}{\varepsilon'}, & \varepsilon'\geq\varepsilon\\ \dfrac{F\left(\varepsilon'\right)}{\varepsilon'}e^{\left(\varepsilon'-\varepsilon\right)}, & \varepsilon'<\varepsilon,\end{cases} \tag{9a}$$

where

$$\begin{aligned}&F\left(\varepsilon\right)\equiv erf\left(\sqrt{\varepsilon}\right)\\ &\varepsilon\equiv E/kT\end{aligned} \tag{9b}$$

and kT is the average thermal neutron energy of $0.025ev$. Here, k is Boltzmann's constant.

The multigroup form uses a Maxwellian

$$f_g\left(E\right)\equiv f_{0g}\varepsilon e^{-\varepsilon} \tag{10a}$$

as the normalized weight, where the normalization is

$$f_{0g}\equiv\left[\int_{E_g}^{E_{g-1}}dE\,\varepsilon e^{-\varepsilon}\right]^{-1}=\frac{1}{kT}\frac{1}{\left[\left(\varepsilon_g+1\right)e^{-\varepsilon_g}-\left(\varepsilon_{g-1}+1\right)e^{-\varepsilon_{g-1}}\right]}. \tag{10b}$$

Thus, the multigroup transfer cross section becomes

$$\Sigma_{sjTgg'}=\int_{\Delta E_g}dE\int_{\Delta E_{g'}}dE'\,\Sigma_{sjT}\left(E'\to E\right)f_{g'}\left(E'\right)$$

to give

$$\Sigma_{sjTgg'} = f_{0g'} \int_{\Delta E_g} dE \int_{\Delta E_{g'}} dE' \, \Sigma_{sj}\left(E'\right) F\left(\varepsilon\right) e^{-\varepsilon'}; \quad N_T + 1 \le g' \le g - 1 \le N_G \tag{11a}$$

$$\Sigma_{sjTgg'} = f_{0g'} \int_{\Delta E_g} dE \int_{\Delta E_{g'}} dE' \, \Sigma_{sj}\left(E'\right) F\left(\varepsilon'\right) e^{-\varepsilon}; \quad N_G \ge g' \ge g + 1 \ge N_T + 1 \tag{11b}$$

and

$$\Sigma_{sjTgg} = f_{0g} \int_{\Delta E_g} dE' \left[\begin{array}{l} \displaystyle\int_{E_g}^{E'} dE \, \Sigma_{sj}\left(E'\right) F\left(\varepsilon\right) e^{-\varepsilon'} + \\ \displaystyle + \int_{E'}^{E_{g-1}} dE \, \Sigma_{sj}\left(E'\right) F\left(\varepsilon'\right) e^{-\varepsilon} \end{array} \right]. \tag{11c}$$

where $N_G \equiv N_T + N_S$. Since the cross sections are assumed to be constant in the interval, Eqs(11) simplifies to

$$\Sigma_{sjTgg'} = f_{0g'} \Sigma_{sjg'} \int_{\Delta E_{g'}} dE' e^{-\varepsilon'} \int_{\Delta E_g} dE \; F\left(\varepsilon\right); \quad N_T + 1 \le g' \le g - 1 \le N_G \tag{12a}$$

$$\Sigma_{sjTgg'} = f_{0g'} \Sigma_{sjg'} \int_{\Delta E_g} dE e^{-\varepsilon} \int_{\Delta E_{g'}} dE' \, F\left(\varepsilon'\right) \; ; \; N_G \ge g' \ge g + 1 \ge N_T + 1 \tag{12b}$$

$$\Sigma_{sjTgg} = f_{0g} \Sigma_{sjg} \int_{\Delta E_g} dE' \left[e^{-\varepsilon'} \int_{E_g}^{E'} dE \; F\left(\varepsilon\right) + F\left(\varepsilon'\right) \int_{E'}^{E_{g-1}} dE \; e^{-\varepsilon} \right] \tag{12c}$$

In this form, detailed balance,

$$f_{0g} \Sigma_{sjg} \Sigma_{sjTgg'} = f_{0g'} \Sigma_{sjg'} \Sigma_{sjTg'g}, \tag{13}$$

is evident also the double integration in Eqs(12) has conveniently decoupled for $g' \neq g$.

With the aid of integration by parts, all the above integrals can be expressed analytically to give the following expressions (after some algebra):

$$I_{Fg} \equiv \int_{\Delta E_g} dE\, F(\varepsilon)$$

$$= kT\left[\begin{array}{r}\left(\varepsilon_{g-1}-1/2\right)F\left(\sqrt{\varepsilon_{g-1}}\right)-\left(\varepsilon_g-1/2\right)F\left(\sqrt{\varepsilon_g}\right)- \\ -\frac{1}{\sqrt{\pi}}\left(\sqrt{\varepsilon_g}e^{-\varepsilon_g}-\sqrt{\varepsilon_{g-1}}e^{-\varepsilon_{g-1}}\right)\end{array}\right], \quad (14a)$$

which, in turn, gives

$$\Sigma_{sjTgg'} = f_{0g'}\Sigma_{sjg'}kT\left(e^{-\varepsilon_{g'}}-e^{-\varepsilon_{g'-1}}\right)I_{F_g}; \quad g' \le g-1. \quad (14b)$$

Then from detailed balance

$$\Sigma_{sjTg'g} = \left[\frac{f_{0g}\Sigma_{sjg}}{f_{0g'}\Sigma_{sjg'}}\right]\Sigma_{sjTgg'}, \quad g' \ge g+1. \quad (15)$$

For within group scatter, we have

$$\Sigma_{sjTgg} = 2f_{0g}\Sigma_{sjg}\left[I_1 - kTe^{-\varepsilon_{g-1}}I_{Fg}\right] \quad (16a)$$

with

$$I_1 \equiv kT\left[\begin{array}{l}e^{-\varepsilon_g}F\left(\sqrt{\varepsilon_{g-1}}\right)-e^{-\varepsilon_{g-1}}F\left(\sqrt{\varepsilon_g}\right)+ \\ +\frac{1}{\sqrt{2}}\left(F\left(\sqrt{2\varepsilon_g}\right)-F\left(\sqrt{2\varepsilon_{g-1}}\right)\right)\end{array}\right] \quad (16b)$$

Similarly, to slowing down, the multigroup parameters are found analytically, hence eliminating errors originating from error in the group parameters.

4.0 CROSS SECTIONS: NUMERICAL IMPLEMENTATION

The implementation of Eq(2a) requires resolution of several issues, including choice of the group structure to give the multigroup parameters, neutron conservation, and an inversion strategy for the flux. Here, we consider generation of the transfer cross sections.

4.1 Slowing Down Scattering Kernel and Conservation

The ENDF/B VII.1 library will be the source of the nuclear data, which is found at the following website: www.nndc.bnl.gov/exfor/endf00.jsp.

Spectral coverage for the materials for this study will be $10^{-5} ev \leq E \leq 20 Mev$. All that is required to determine the elastic scattering transfer cross sections is the scattering total (integrated) cross sections. The procedure to prepare the transfer cross sections in the multigroup setting begins by bringing the **ENDF/B** data local to be processed by a multigroup cross section generation code called **ENDFPR.f**. The primary function of **ENDFPR.f** is to interface with the **ENDF/B** data library. The **ENDFPR.f** program interrogates the relevant **ENDF/B** data files to determine the number of entries on each as well as the energy range, which can vary across the various isotopes.

The information presented in Chart 1 displays on the monitor upon execution of **ENDFPR.f** and introduces the sample case we consider here. The desired energy range is indicated for a U235/water homogeneous mixture. The material cross sections are on 7 files (**nfl**) with the number of entries (**nei**) and the available energy interval indicated for each. Finally, if the calculation is successful, the number of groups in the cross section set is specified (in this case 8 groups)

The secondary function of **ENDFPR.f** is to assemble the cross section set. This is done by imposing the widest possible available boundaries over all isotopes and then forming equal lethargy groups within the chosen boundaries. All cross sections are then interpolated through a Padé interpolation with the interpolated values formally attached to the group centers.

An interpolation of degree ***m*** (usually ***m*** = 2) is applied to all data files to obtain the total, scattering and fission cross sections within the group boundaries now common to all isotopes. The results are output to file **o62.dat**-- an 8-group example of which is included in Chart 2. Also included are degree 2 polynomial and degree 4 Padé interpolations, which are in relatively close agreement with the degree 2 interpolation. Hence, the interpolation seems stable (about 4-place agreement); however, it should be noted that higher Padé interpolations can lead to negative cross sections and subsequent instability in *k*. In addition, Chart 2 indicates that for any benchmark comparisons, we should not expect more than 4-place agreement.

File **o62.dat** is next input into the **x2.f** code to determine the slowing down transfer cross sections from Eq(8a) to prepare file **o71.dat** for the final calculation. This file provides the integrated and transfer scattering cross section data for the *k*- calculation to follow.

Chart 1: **ENDFPR.f** output sample

```
endfpr.f output ****************************
 ************************************
Energy range: 20000000.00000000
1.000000000000000E-05
u235.tot.dat
u235.sct.dat
u235.fis.dat
H.tot.dat
H.sct.dat
O.tot.dat
O.sct.dat

Number of files
nfl= 7
------------------------------

Number of entries on files
     nei= 107650
     nei= 16991
     nei= 45164
     nei= 374
     nei= 157
     nei= 2730
     nei= 1590

Energy interval on files
 1.0000E-05  2.0000E+07
 1.0000E-05  2.0000E+07
 1.0000E-05  2.0000E+07
 1.0000E-05  2.0000E+07
 1.1024E-05  2.0000E+07
 1.0000E-05  1.5000E+08
 1.0000E-05  1.5000E+08

min/max energies:  1.1024E-05  2.0000E+07

     8-group set generated
```

Chart 2: **o62.dat** degrees 2 and 4 interpolations

Chart 2: Interpolation Comparison

Degree 2 Padé interpolation

E	*UT*	*US*	*UF*	*HT*	*HS*	*OT*	*OS*
2.000000E+07	6.169680E+00	3.216440E+00	2.020630E+00	4.827840E-01	4.827570E-01	1.638960E+00	9.987240E-01
5.870751E+05	7.817606E+00	5.039435E+00	1.118598E+00	5.633424E+00	5.633385E+00	3.177389E+00	3.177389E+00
1.723286E+04	1.482244E+01	1.174663E+01	2.293389E+00	1.839052E+01	1.838718E+01	3.816828E+00	3.814964E+00
5.058491E+02	3.431867E+01	1.074259E+01	1.922773E+01	2.009382E+01	2.009075E+01	3.851117E+00	3.851054E+00
1.484857E+01	2.340014E+01	1.129382E+01	8.426088E+00	2.017740E+01	2.016366E+01	3.852708E+00	3.852701E+00
4.358612E-01	1.291769E+02	1.410651E+01	1.004111E+02	2.088133E+01	2.080066E+01	3.861392E+00	3.861351E+00
1.279416E-02	1.010802E+03	1.520860E+01	8.432305E+02	3.797851E+01	3.750940E+01	4.094496E+00	4.094113E+00
3.755567E-04	6.104437E+03	1.739933E+01	5.114513E+03	1.924756E+02	1.897363E+02	9.640211E+00	9.638518E+00
1.102400E-05	3.562580E+04	5.568290E+01	2.989550E+04	1.117820E+03	1.101910E+03	5.237200E+01	5.236290E+01

Degree 2 Polynomial interpolation

2.000000E+07	6.169680E+00	3.216440E+00	2.020630E+00	4.827840E-01	4.827570E-01	1.638960E+00	9.987240E-01
5.870751E+05	7.817903E+00	5.043710E+00	1.118613E+00	5.639250E+00	5.639211E+00	3.177637E+00	3.177637E+00
1.723286E+04	1.482246E+01	1.174669E+01	2.293825E+00	1.839162E+01	1.839121E+01	3.816829E+00	3.816830E+00
5.058491E+02	3.431899E+01	1.074429E+01	1.922797E+01	2.009382E+01	2.009148E+01	3.851117E+00	3.851114E+00
1.484857E+01	2.340015E+01	1.129510E+01	8.426091E+00	2.017740E+01	2.016366E+01	3.852708E+00	3.852701E+00
4.358612E-01	1.292093E+02	1.410951E+01	1.004597E+02	2.088138E+01	2.080133E+01	3.861392E+00	3.861352E+00
1.279416E-02	1.011112E+03	1.520864E+01	8.437788E+02	3.798031E+01	3.751303E+01	4.094520E+00	4.094252E+00
3.755567E-04	6.105397E+03	1.739965E+01	5.116609E+03	1.925484E+02	1.898221E+02	9.640603E+00	9.639045E+00
1.102400E-05	3.562580E+04	5.568290E+01	2.989550E+04	1.117820E+03	1.101910E+03	5.237200E+01	5.236290E+01

Degree 4 Padé interpolation

2.000000E+07	6.169680E+00	3.216440E+00	2.020630E+00	4.827840E-01	4.827570E-01	1.638960E+00	9.987240E-01
5.870751E+05	7.824718E+00	5.042715E+00	1.118127E+00	5.631178E+00	5.631139E+00	3.176602E+00	3.176692E+00
1.723286E+04	1.482256E+01	1.174701E+01	2.294803E+00	1.840289E+01	1.838270E+01	3.816829E+00	3.787974E+00
5.058491E+02	3.432292E+01	1.073734E+01	1.923761E+01	2.009374E+01	2.006974E+01	3.851118E+00	3.852556E+00
1.484857E+01	2.339973E+01	1.129258E+01	8.424502E+00	2.017740E+01	2.015283E+01	3.852709E+00	3.852108E+00
4.358612E-01	1.291909E+02	1.391847E+01	1.003975E+02	2.088133E+01	2.078228E+01	3.861392E+00	3.858878E+00
1.279416E-02	1.011342E+03	1.520676E+01	8.430007E+02	3.799141E+01	3.750458E+01	4.094525E+00	4.091530E+00
3.755567E-04	6.105762E+03	1.739675E+01	5.113450E+03	1.925834E+02	1.896907E+02	9.636446E+00	9.638053E+00
1.102400E-05	3.562580E+04	5.568290E+01	2.989550E+04	1.117820E+03	1.101910E+03	5.237200E+01	5.236290E+01

4.1.1. Necessary "dump group"

In preparation for a demonstration, we now investigate conservation of the multigroup approximation for elastic scattering. Since the total (integrated) scattering cross section is conservative, all scattered neutrons must be accounted for, therefore

$$\Sigma_{sj}\left(E'\right)=\int_0^{E_0} dE\Sigma_{sj}\left(E'\rightarrow E\right). \qquad (17)$$

Theoretically, one can verify this expression easily, but the multigroup approximation must also be considered. In that case, conservation means

$$\Sigma_{sjg'}\equiv\sum_{g=1}^{N_G}\int_{\Delta E_g} dE\Sigma_{sj}\left(E'\rightarrow E\right)=\int_{E_L\equiv E_{N_G}}^{E_0} dE\Sigma_{sj}\left(E'\rightarrow E\right),$$

where E_L is the top boundary of the bottom group to give

$$\Sigma_{sg'} \equiv \frac{\Sigma_{sjg'}}{1-\alpha} \int_{E_L}^{E_0} dE \, \frac{\rho\left(E', E\right)}{E'}.$$

From this expression, we find

$$I\left(E'; E_L, E_0\right) \equiv \frac{1}{\left(1-\alpha\right)E'} \int_{E_L}^{E_0} dE \rho\left(E', E\right)$$

$$= \frac{1}{\left(1-\alpha\right)E'} \int_{\max(E_L, \alpha E')}^{\min(E_0, E')} dE = \frac{\min(E_0, E') - \max(E_L, \alpha E')}{\left(1-\alpha\right)E'}$$

which must be unity

$$I\left(E'; E_L, E_0\right) = 1. \qquad (18)$$

Equation (18), of course, is only strictly true if

$$E_L / \alpha \le E' \le E_0,$$

but not so in general for $0 \le E' < E_L / \alpha$. In this case,

$$I\left(E'; E_L, E_0\right) = \frac{1}{\left(1-\alpha\right)}\left(1 - \frac{E_L}{E'}\right) < 1 \qquad (19)$$

and conservation fails. If a "dump group" [0,E_L] is included allowing neutrons to scatter all the way to near zero energy, conservation now holds for nearly all $E' > 0$ since E_L is replaced by 10^{-10}*ev*. The cross sections in the last group are set to near zero since they are not used.

4.2. Thermal Scattering Kernel and Conservation

The thermal scattering kernel simply requires the integrated scattering cross sections found from **ENDF/B** and normalization. The normalization maintains conservation similar to elastic scattering through

$$\Sigma_{sg'} = \int_0^{E_T} dE \Sigma_{sT}\left(E' \to E\right) = \sum_{g=N_T+1}^{N_G} \int_{\Delta E_g} dE \Sigma_{sT}\left(E' \to E\right) \qquad (20)$$

for each isotope in the thermal energy region. Thus, applying conservation from Eqs(12) to (16), summing over all the thermal groups

$$\sum_{g=N_T+1}^{N_G} \Sigma_{sTgg'} = kTf_{0g'}\left(e^{-\varepsilon_{g'}} - e^{-\varepsilon_{g'-1}}\right)\sum_{g=g'+1}^{N_G} I_{F_g} +$$

$$+ kTf_{0g'} I_{F_{g'}} \sum_{g=N_T+1}^{g'-1}\left(e^{-\varepsilon_g} - e^{-\varepsilon_{g-1}}\right) + 2f_{0g}\left[I_1 - kTe^{-\varepsilon_{g-1}} I_{Fg}\right],$$

we find the normalized thermal transfer scattering cross section

$$\Sigma_{sTgg'} \to \Sigma_{sTgg'}\left[\sum_{g=N_T+1}^{N_G} \Sigma_{sTgg'}\right]^{-1}. \qquad (21)$$

4.3. Overall Neutron Balance and the Fission Spectrum

For the particular elastic and thermal scattering models assumed, the neutron spectral equation is now

$$\Sigma(E)\phi(E) = \int_{E_T}^{E_0} dE'\Sigma_s(E' \to E)\phi(E') +$$

$$+ \int_0^{E_T} dE'\Sigma_{sT}(E' \to E)\phi(E') + \qquad (22a)$$

$$+ \frac{\chi(E)}{k}\int_0^{E_0} dE'\nu(E')\Sigma_f(E')\phi(E'),$$

where, nominally, elastic scattering is not initiated below the thermal cutoff

$$\Sigma_s(E' \to E) = 0, \quad E' < E_T \qquad (22b)$$

and thermal up/down scattering initiates at the thermal region boundary, hence

$$\Sigma_{sT}(E' \to E) = 0, \quad E', E \geq E_T \ . \qquad (22c)$$

By integrating over all energy $[0, E_0]$

$$\int_0^{E_0} dE\Sigma(E)\phi(E) = \int_{E_T}^{E_0} dE'\left[\int_0^{E_0} dE\Sigma_s(E'\to E)\right]\phi(E') +$$
$$+ \int_0^{E_T} dE'\left[\int_0^{E_T} dE\Sigma_{sT}(E'\to E)\right]\phi(E') +$$
$$+ \frac{1}{k}\left[\int_0^{E_0} dE\chi(E)\right]\int_0^{E_0} dE'\nu(E')\Sigma_f(E')\phi(E'),$$

where the terms in square brackets have been normalized to one to give the proper overall balance, we find

$$\int_0^{E_0} dE\Sigma(E)\phi(E) = \int_{E_T}^{E_0} dE'\Sigma_s(E')\phi(E') + \int_0^{E_T} dE'\Sigma_s(E')\phi(E') +$$
$$+ \frac{1}{k}\int_0^{E_0} dE'\nu(E')\Sigma_f(E')\phi(E'),$$

or

$$\int_0^{E_0} dE\Sigma_a(E)\phi(E) = \frac{1}{k}\int_0^{E_0} dE'\nu(E')\Sigma_f(E')\phi(E') \qquad (23)$$

for an overall balance of loss and production from neutron birth to reproduction.

To complete the analysis, the following Watt fission spectrum has been assumed:

$$\chi(E) = Ce^{-E/a}\sinh\left(\sqrt{bE}\right) \qquad (24)$$

where

$$C = \left(\frac{\pi b}{4a}\right)^{1/2}\frac{e^{-b/4a}}{a}$$

with constants $a = 0.988,\ b = 2.249$ and E is in *Mev*. Note that the fission section does not play a role in the balance of Eq(23).

5. EIGENVALUE AND EIGENFLUX: SIMPLE SPECTRAL MODEL 1 (SSM1)

Our goal is to independently find the eigenvalue and spectral variation of the eigenflux in an infinite medium and to compare to the corresponding **HELIOS** values. For this purpose, the initial version of a Simple Spectral Model (Version 1) has been developed by coupling the analytical group parameters outlined above with the **ENDF/B** data library in the **FORTRAN** code **SSM1.f**.

Our first determination of the multiplication factor and eigenflux comes from Eq(2a) written as

$$\sum_{g'=1}^{N_G}\left[\Sigma_g\delta_{gg'}-\left(\Sigma_{g'g}+\frac{\chi_g}{k}\nu\Sigma_{fg'}\right)\right]\phi_{g'}=0\,. \tag{25}$$

More appropriately, in a vector form, Eq(25) becomes

$$\boldsymbol{H}\boldsymbol{\phi}=\frac{1}{k}\boldsymbol{\chi}\boldsymbol{f}^T\boldsymbol{\phi}\,, \tag{26}$$

where

$$\boldsymbol{H}\equiv\left\{\Sigma_g\delta_{gg'}-\Sigma_{g'g},\ g,g'=1,...,N_G\right\}$$
$$\boldsymbol{\phi}\equiv\left\{\phi_g\right\}$$
$$\boldsymbol{\chi}\equiv\left\{\chi_g\right\}$$
$$\boldsymbol{f}\equiv\left\{\nu\Sigma_{fg}\right\}.$$

Formally solving this equation gives

$$\boldsymbol{\phi}=\frac{1}{k}\boldsymbol{H}^{-1}\boldsymbol{\chi}F\,, \tag{27a}$$

where the scalar fission source is

$$F\ =\ \boldsymbol{f}^T\boldsymbol{\phi}\,. \tag{27b}$$

Then, multiplying Eq(27a) by $\boldsymbol{f}^T$

$$\boldsymbol{f}^T\boldsymbol{\phi}=F=\frac{1}{k}\boldsymbol{f}^T\boldsymbol{H}^{-1}\boldsymbol{\chi}F\,,$$

and canceling the scalar F gives the following explicit representation of the eigenvalue:

$$k = \boldsymbol{f}^T \boldsymbol{H}^{-1} \boldsymbol{\chi} \,. \tag{28a}$$

It should be mentioned that this is one of the few instances of an explicit determination of an eigenvalue in transport/diffusion theory and results from the rank one matrix $\boldsymbol{\chi}\boldsymbol{f}^T$ appearing in Eq(26).

Once k has been determined, the normalized flux (normalized to $F = 1$) comes from Eq(27a)

$$\boldsymbol{\phi} = \frac{1}{k} \boldsymbol{H}^{-1} \boldsymbol{\chi} \,, \tag{28b}$$

and is again given explicitly. For comparison purposes, the flux is further normalized with the first flux component set to unity.

To find the flux in a second independent confirmation, we write Eq(26) as a generalized eigenvalue problem

$$\boldsymbol{H}\boldsymbol{\phi} = \frac{1}{k} \boldsymbol{B}\boldsymbol{\phi} \tag{29a}$$

giving

$$\left[\boldsymbol{H}^{-1}\boldsymbol{B} - k\boldsymbol{I} \right] \boldsymbol{\phi} = 0 \,. \tag{29b}$$

Thus, k is also the eigenvalue of the matrix $\boldsymbol{H}^{-1}\boldsymbol{B}$. The normalized scalar flux with $\phi_1 \equiv 1$ is found by first letting $\phi_{N_G} \equiv 1$ and from Eq(2a) solving

$$\sum_{\substack{g'=1 \\ g' \neq l}}^{N_G} \left[\Sigma_g \delta_{gg'} - \left(\Sigma_{g'g} + \frac{\chi_g}{k} \nu\Sigma_{fg'} \right) \right] \phi_{g'} = - \left[\Sigma_g \delta_{gl} - \left(\Sigma_{lg} + \frac{\chi_g}{k} \nu\Sigma_{fl} \right) \right], \tag{30a}$$

and finally renormalizing to

$$\phi_g \rightarrow \frac{\phi_g}{\phi_1} \,. \tag{30b}$$

A third confirmation comes directly from Eq (31)

$$k = \frac{\sum_{g=1}^{N_G} \nu_g \Sigma_{fg} \phi_g}{\sum_{g=1}^{N_G} \Sigma_{ag} \phi_g} , \qquad (31)$$

since we have two estimates of the flux. We are now in position to verify the **HELIOS-2** code for an infinite medium.

6. HELIOS SPECTRAL VERIFICATION FOR AN INFINITE MEDIUM

The nuclear system used for benchmarking will be a simple homogeneous U235/water mixture

6.1. Data Confirmation

The first step in the benchmarking procedure is to explicitly display the data used for inspection to ensure reliability. The relevant material properties are given in the following table:

Table 2
Material Properties

Material	Density(gm/cm^3)	At. Wt.
U235	19	235
H2O	1	18

We will exercise both primary group sets found in the **HELIOS-2** code of N_G = 49 and 177 groups. Table 3 provides the number of thermal groups assumed for each set and the fast/thermal cutoff. We now begin the inspection for each set used with **SSM1**.

Table 3
Group Structure

Total	thermal	Cutoff
49	7	0.11157ev
177	14	0.11157ev

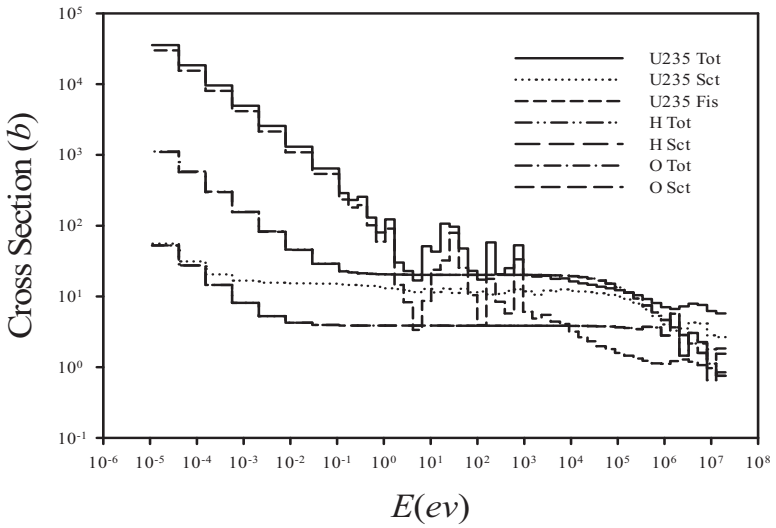

Fig. 1a. Isotope (total) cross sections as processed by **ENDFPR.f** for 49 Groups.

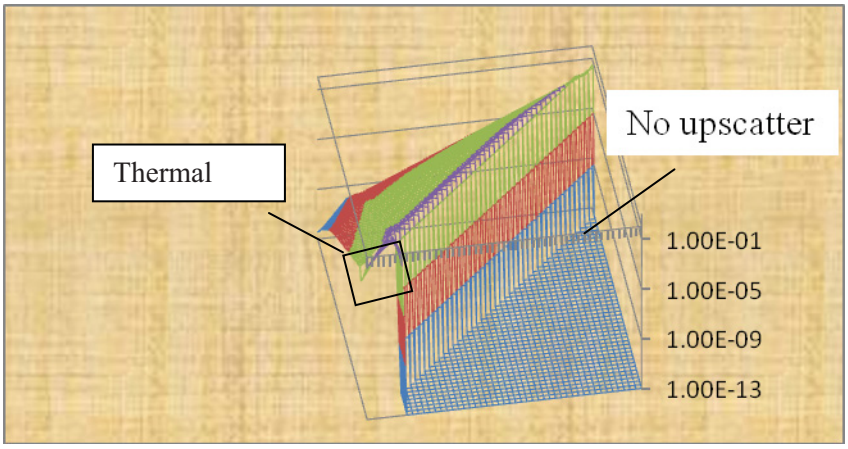

Fig. 1b. Transfer cross section processed by **x2.f** for 49 Groups.

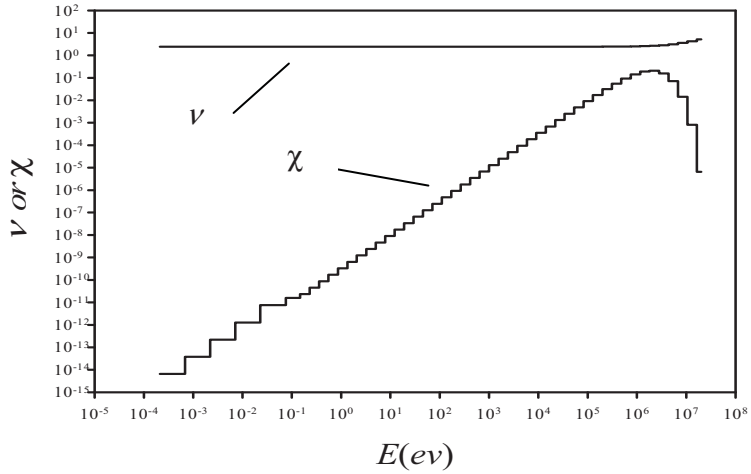

Fig. 1c. ν and χ processed by **ENDFPR.f** and **SSM1.f** for 49 Groups.

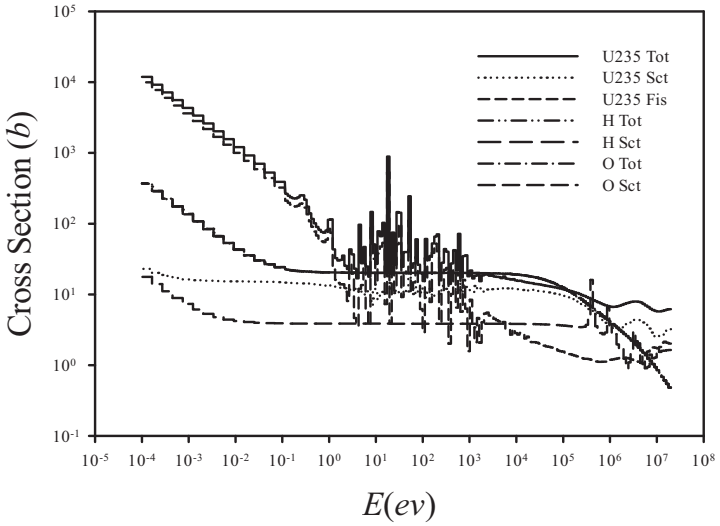

Fig. 2a. Isotope (total) cross sections processed by **ENDFPR.f** for 177 Groups.

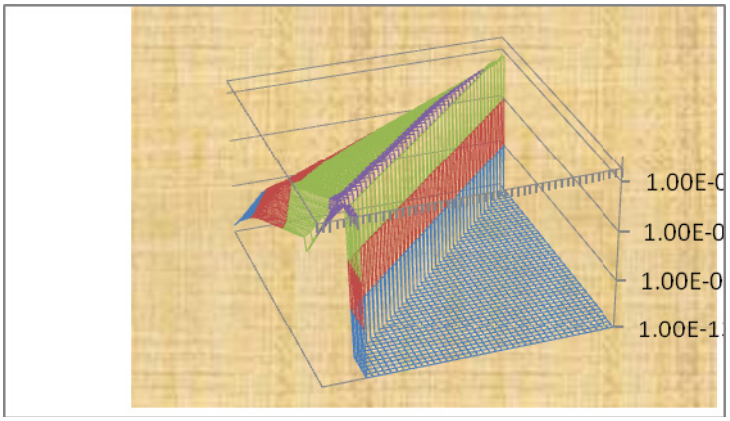

Fig. 2b. Transfer cross section processed by **x2.f** for 177 Groups.

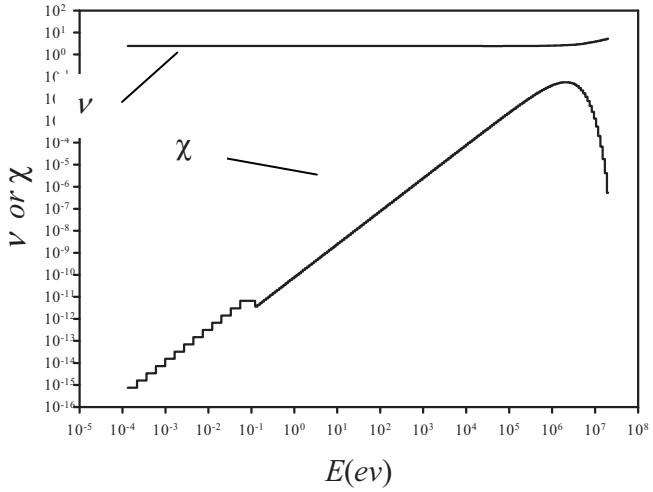

Fig. 2c. ν and χ processed by **ENDFPR.f** and **SSM1.f** for 177 Groups.

6.1.1. $\underline{N_G = 49}$ and $\underline{N_G = 177}$ Groups

The cross section data after processing to 49 groups from **ENDF/B** library is shown in Fig. 1a for the individual isotopes. Both the fuel and oxygen resonances can be observed. The transfer cross sections are displayed in Fig. 1b, where the forbidden upscatter region while slowing down and the thermal regions are identified. The "diagonal ridge" is also very prominent. Finally, Fig. 1c shows expected and reasonable ν and χ values.

The identical data for the 177 group set are shown in Figs. 2a-c.

6.2. Comparisons for SSM1/HELIOS-2

Calculations were performed for the two cross section sets initiated by a data comparison of **SSM1/HELIOS** for the mixed constituents given in Figs. 3a-d. The **HELIOS** data compare well with that generated by direct **ENDF/B**, which is smoother and has greater coverage of the resonance region. A plot of the energies at the same group number for both models for the two group sets is given in Fig. 4. It seems that **HELIOS** focuses greater attention on the region [0.1*ev*,100*ev*] for the 49 set; while, **SSM1** focuses attention on the region [0.1*ev*,10^5*ev*] For the 177 group set, the two transport models sample similar groups.

A comparison of multiplication factors for the two transport models is given in Table 4. Given that these are two entirely independent spectral models with entirely independent data, the agreement of 1000 *pcm* is quite reasonable.

Table 4
***k*- Comparison**

Model	*k*	*Difference in (pcm)*
Simple(49)	1.2268	…
Simple(177)	1.2216	…
Helios(49)	1.2279	110
Helios(177)	1.2317	1001

If the scattering source is reconfigured as

$$Q_{scat} = \alpha \int_{E_T}^{E_0} dE' \Sigma_s(E') \phi(E') + (1-\alpha) \int_{0}^{E_T} dE' \Sigma_s(E') \phi(E')$$

such that the thermal region is shared in part (α - fraction) by the slowing down scattering source, then for 177 groups the multiplication factor becomes 1.2301 for α = 0.025. The difference now is only 150 *pcm* for this reasonable physical assumption. For 49 groups the **SSM1** estimation is 1.2350— within 80 *pcm*. Obviously, through adjustment of α, the two models can be made to agree exactly for this one number. While such variability is the essence of modeling and brings about the concern that the models do not truly represent first principles, variability also speaks to the fact that the models initially agreed so well without any parameter adjustments.

Figure 5a shows a comparison of the normalized group fluxes [ϕ_g] for the two cross section sets simulated by **SSM1.** The thermal region is distinguished by the approximate Maxwellian distribution with a peak near 0.025*ev* and the fission spectrum by the peak near 2 *Mev*. Recall that all elements are assumed to scatter like Hydrogen, which is a reasonable assumption since the majority of the scattering contribution for the mixture is from Hydrogen. The 1/*E* spectral (constant) variation is also quite evident. In addition, for the 177-group case, the high-energy Oxygen resonances are apparent.

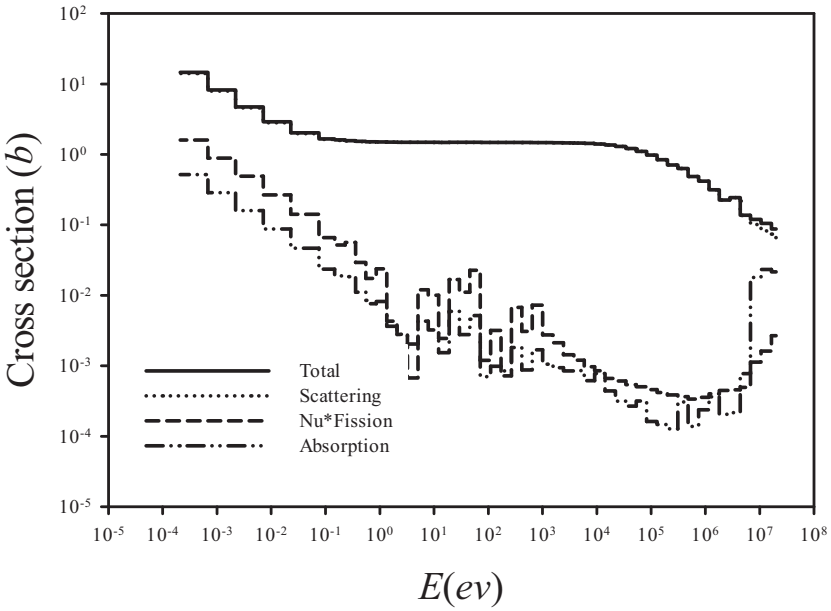

Fig. 3a. Homogeneous cross sections for N_G = 49 by **SSM1.**

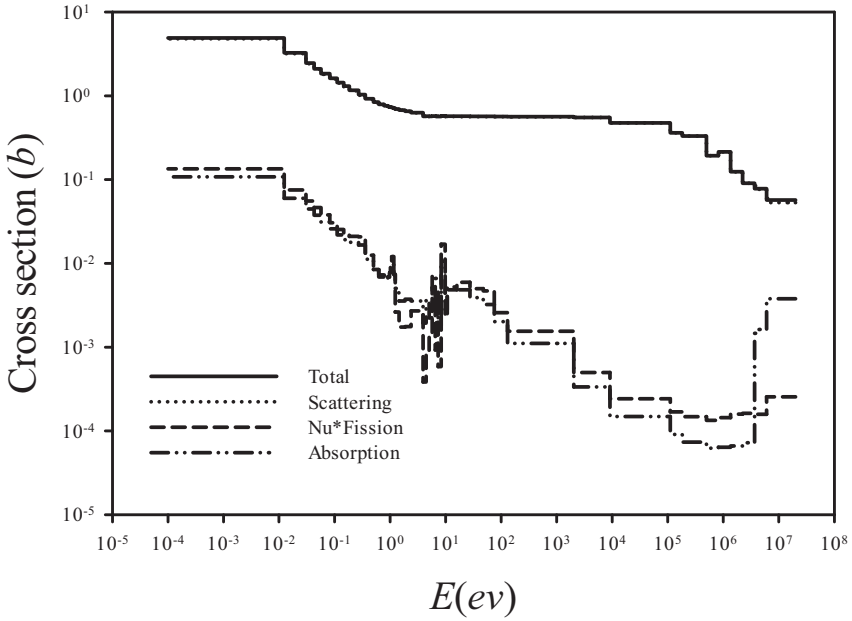

Fig. 3b. Homogeneous cross sections for N_G = 49 by **HELIOS.**

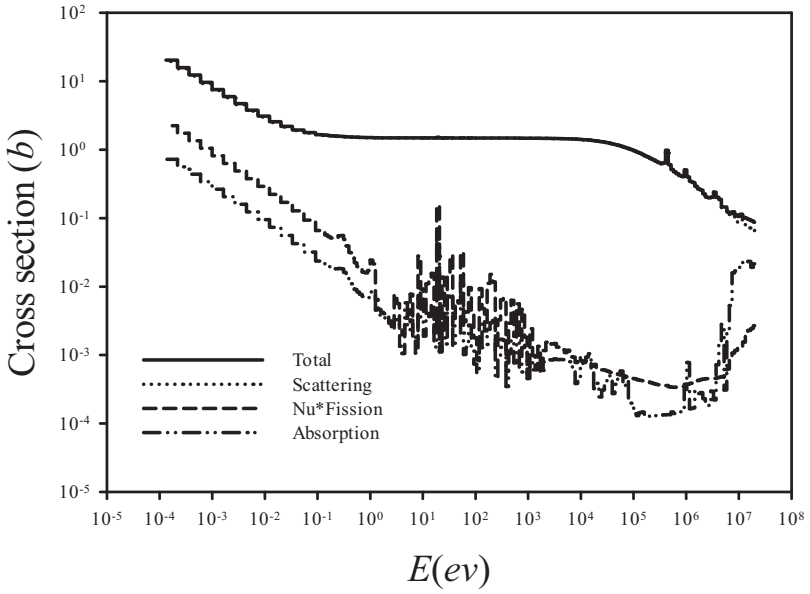

Fig. 3c. Homogeneous cross sections for N_G = 177 by **SSM1.**

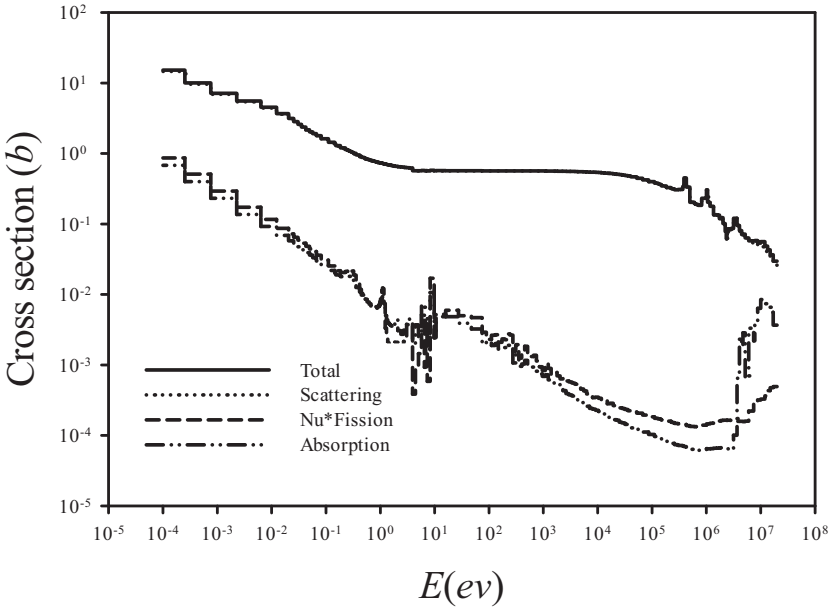

Fig. 3d. Homogeneous cross sections for N_G = 177 by **HELIOS.**

The inset in Fig. 5a confirms the excellent agreement between the two cross section sets when the fluxes are normalized to their maxima. A similar comparison is given in Fig. 5b for **HELIOS**. The rather

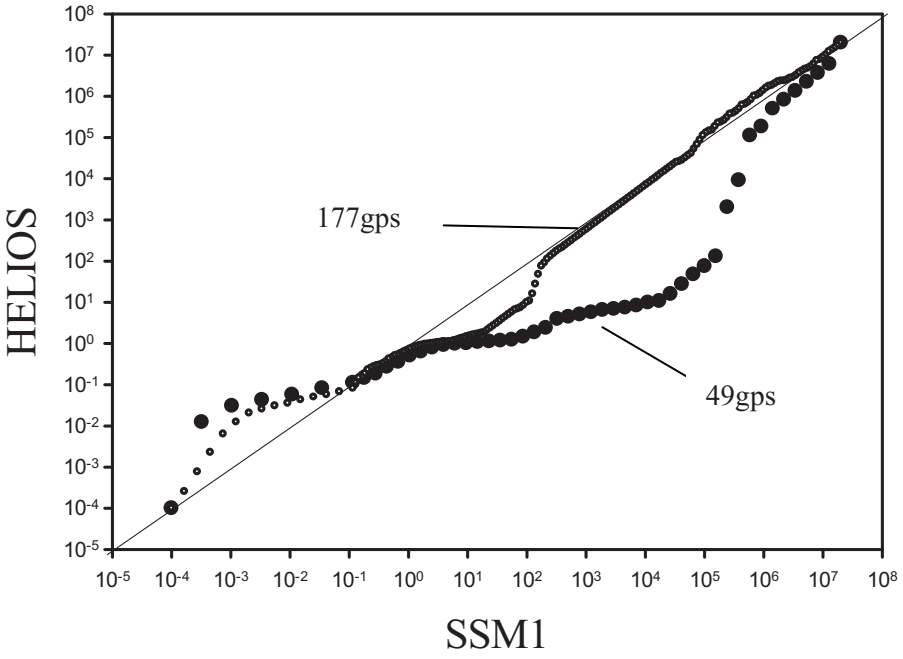

Fig. 4. Energies at the same group numbers for the two transport models

rugged nature of the **HELIOS** spectra is a plotting artifact as discussed below. The general agreement between the cross section sets for **HELIOS** is less evident than for **SSM1**. In addition, **HELIOS** has an uncharacteristic "bump' in the region 10*ev* to 100*ev*—again a consequence of a plotting artifact.

Figures 6a- d show the group flux per lethargy [or $E\phi(E)$] comparisons of **SSM1** and **HELIOS** for 177 and 49 groups respectively and are the "significant figures" of this report. Recall to this point, there has been no attempt to adjust the two models to give closer agreement. All physical parameters are estimated on a purely physical basis. Now, we take a different approach. For Figs 6a,b (177 groups), to give a better fit as can be observed, the thermal/fast boundary was adjusted upward to 0.41157*ev* (Probably a more realistic value to begin with). Remarkably, the spectra are now nearly identical. In addition, plotting the flux as $E\,\phi(E)$ eliminates the unphysical rugged nature of the **HELIOS** flux results and is the more natural dependent variable. The multiplication factor given by **SSM1** is now 1.2234—off by 830 *pcm* from the original **HELIOS**. Nearly excellent agreement is also observed for the 49-group case in Figs. 6c,d. **SSM1**, however, gives more detail in the thermal region. For this case, the multiplication is 1.2272 or 70 *pcm* from the **HELIOS** result.

As the final exercise in this section, we will drive the simple model with the **HELIOS** data. This is most easily done by capturing all the relevant data from the **HELIOS ZENITH** output file and constructing an **o71.dat** input file for **SSM1**. The first task is to capture the **HELIOS** output using the **Hls2.f** code.

We perform this operation electronically by the **htx.f** code, by searching for the following key-words in the **ZENITH** output:

```
wd(1) = ' avesgmtr'
wd(2) = '   avesgm'
```

```
wd(3) = ' avesgmnu'
wd(4) = ' avespctr'
wd(5) = ' avescttr'
wd(6) = '       fl'
```

for the *transport cross section*, *absorption cross section*, *nu times the fission cross section*, *fission spectrum*, *scattering block* and the *flux*. The **htx.f** code also requires **HELIOS**'s energy structure. This information is then arranged into appropriate columns as the **o71.dat** file to be read by a special version of **SMM1** called **SMM1H**. Note that little or no modification of the **ZENITH** output is necessary. Sometimes however, because the ZENITH output may be printed in different formats, the above key-words need to be adjusted.

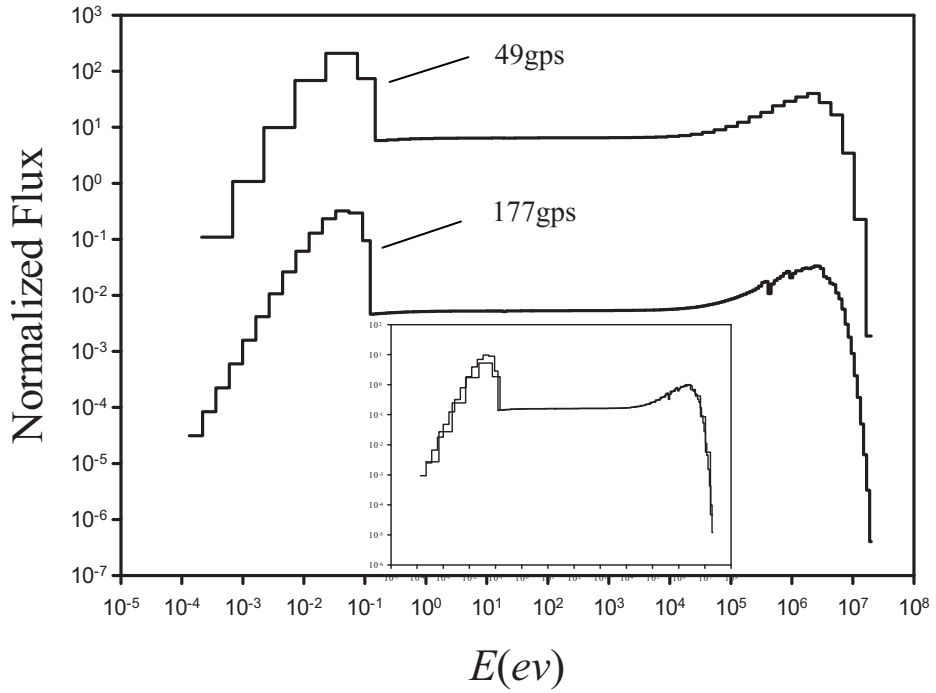

Fig.5a. Group flux [φ_g] comparison for 49 and 177 groups for **SSM1**.

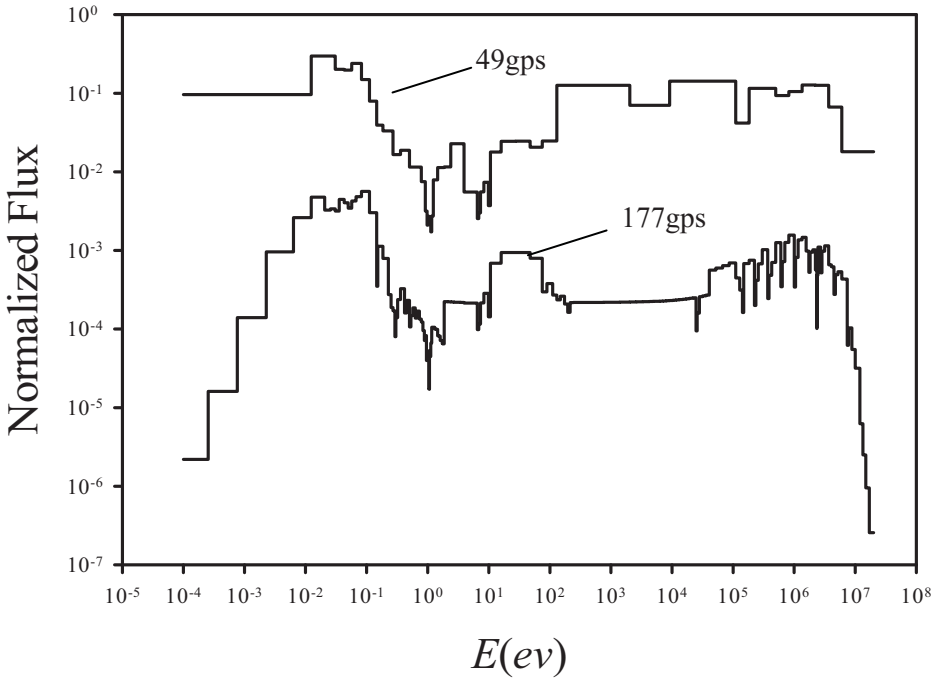

Fig.5b. Group flux [φ_g] comparison for 49 and 177 groups for **HELIOS**.

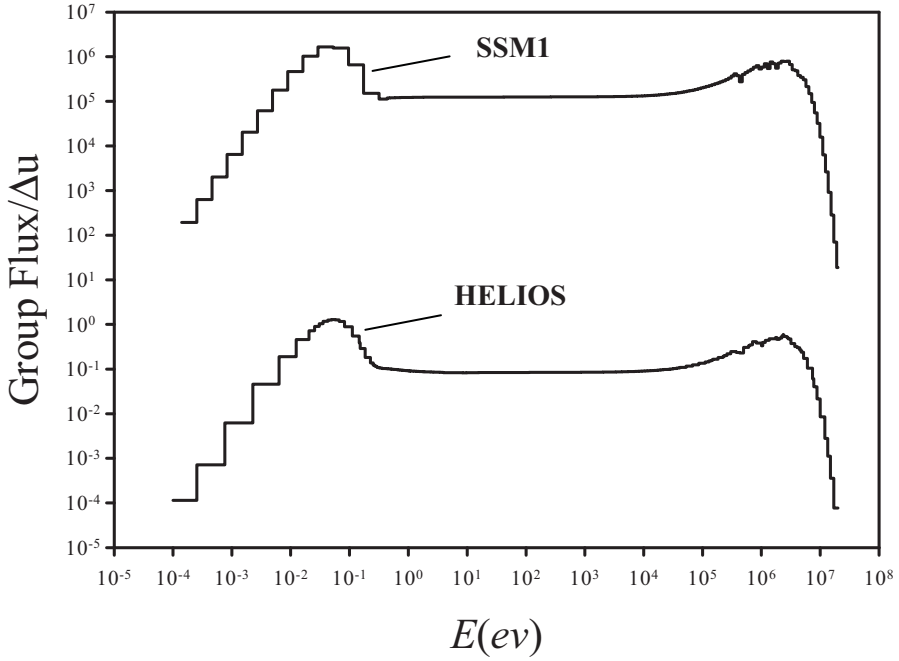

Fig.6a. Offset flux [$E\varphi(E)$] comparison between models for 177 groups.

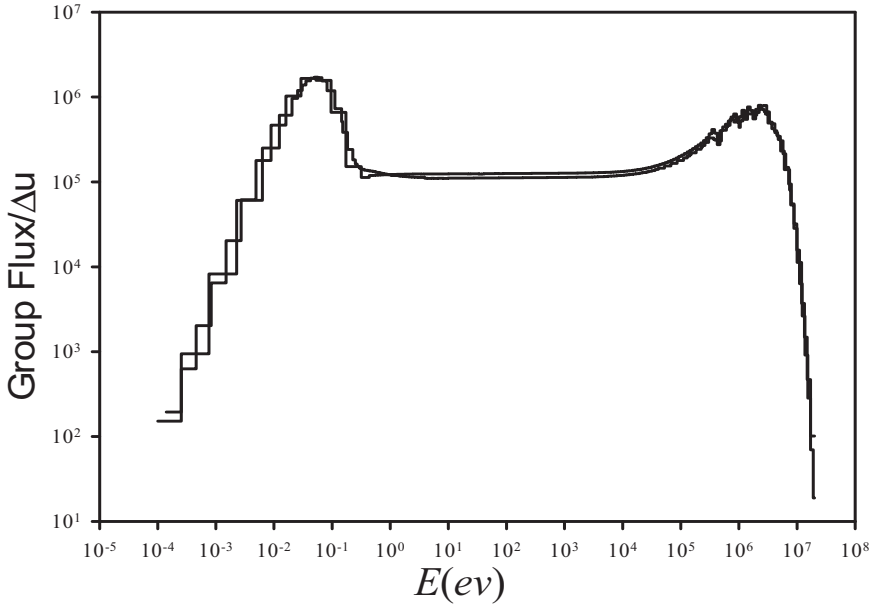

Fig.6b. Coincident flux [$E\varphi(E)$] comparison between models for 177 groups.

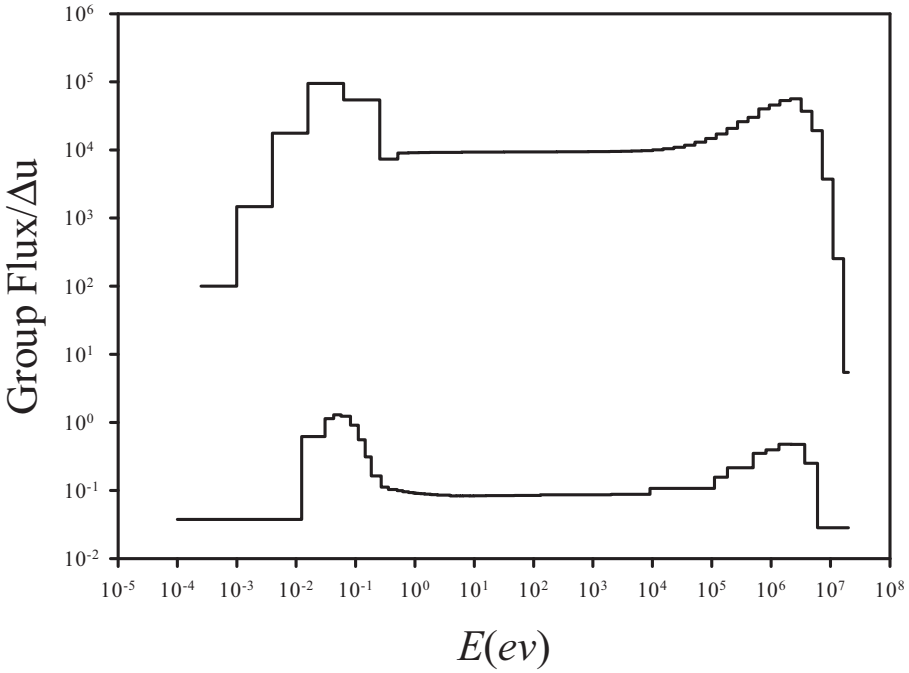

Fig.6c. Offset flux [$E\varphi(E)$] comparison between models for 49 groups.

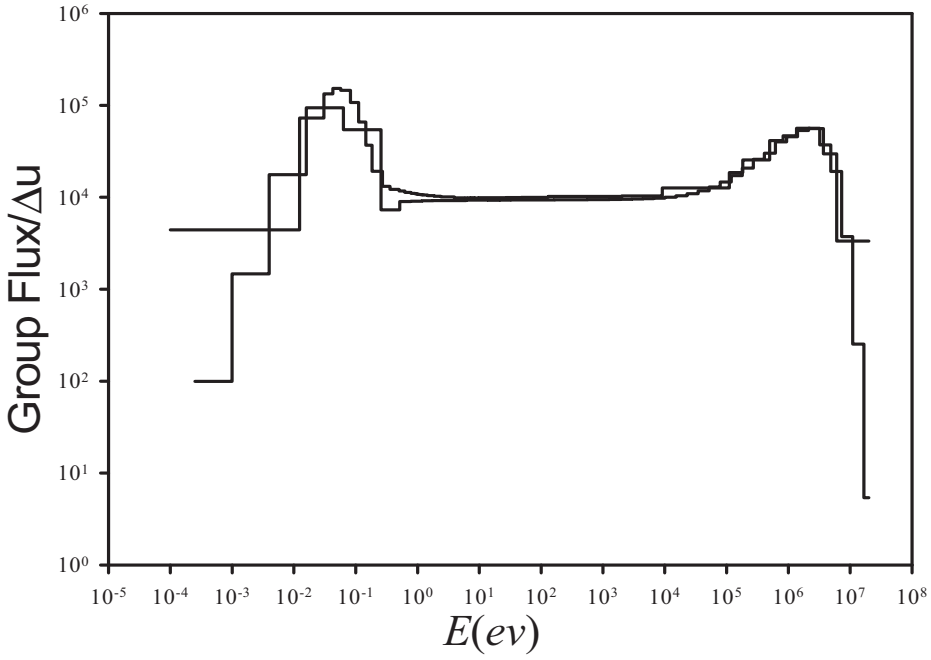

Fig.6d. Coincident flux [$E\varphi(E)$] comparison between models for 49 groups.

In the case of linearly anisotropic scattering, before generating the **o71.dat** output file, the consistent total scattering cross section, including anisotropy, is obtained from

$$\Sigma_{sg} = \frac{\Sigma_{trg} - \Sigma_{ag}}{1 - \bar{\mu}_0}, \tag{32}$$

(assuming only U235 fuel for simplicity), where

$$\bar{\mu}_0 = \frac{A_{235}\bar{\mu}_{0,U} + A_{O_2}\bar{\mu}_{0,O_2}}{A_{235} + A_{O_2}}; \quad \bar{\mu}_{0,A} \approx \frac{2}{3A}. \tag{33}$$

The total cross section then becomes $\Sigma_g = \Sigma_{sg} + \Sigma_{ag}$. The integrated cross sections input to **SSM1H** are shown in Figs. 3b and d. The fission spectrum is similar to that of Figs. 1c and 2c. The **ZENITH** input transfer is then checked by recalculating the multiplication factor KINF as found by **HELIOS** from Eq(31).

On running the **HELIOS** input through **SSM1H**, we find Figs. 7a,b for the 49 and 177 group sets respectively. The **SSM1H** and **HELIOS** fluxes are virtually graphically identical (though not exactly

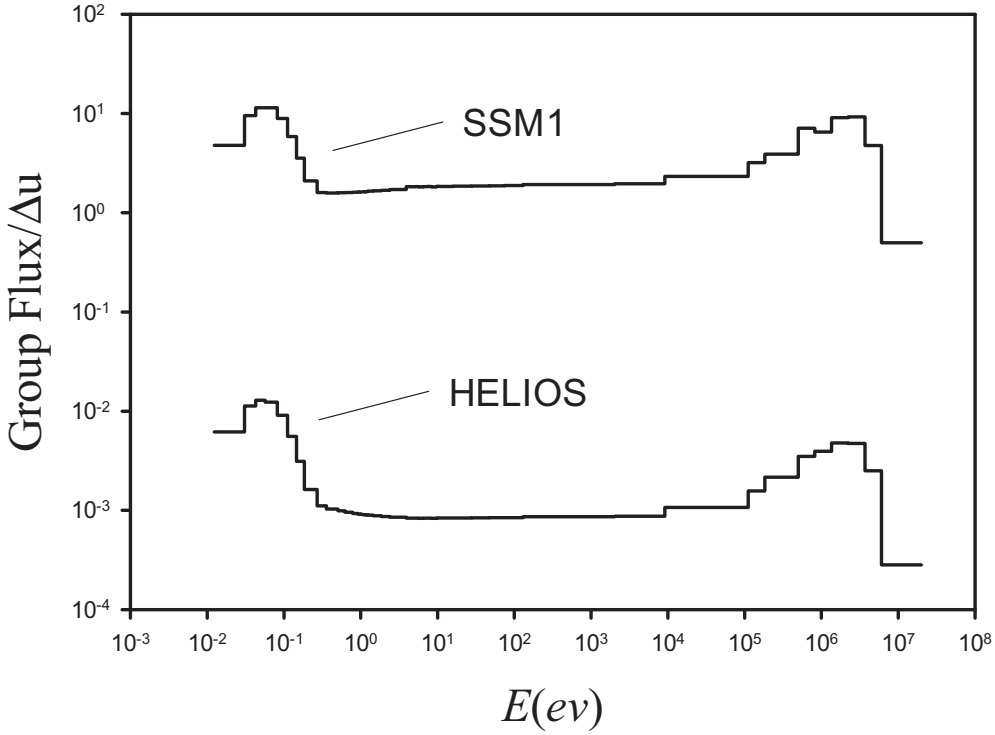

Fig. 7a. Flux [$E\varphi(E)$] **HELIOS** data in **SSM1H** for 49 group set.

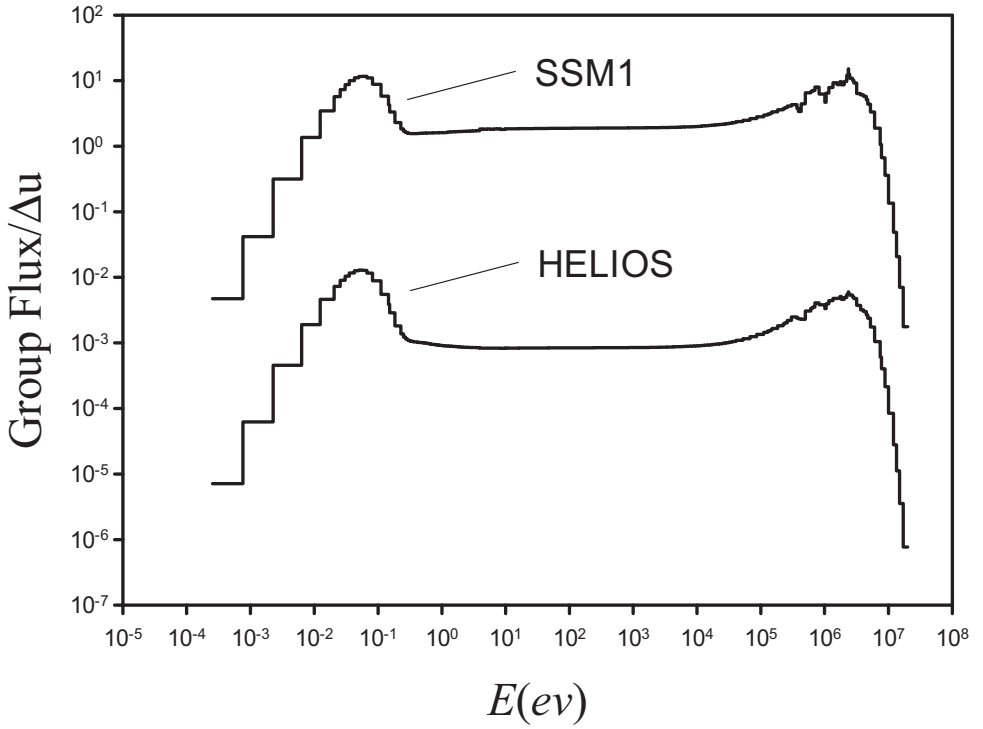

Fig. 7b. Flux [$E\varphi(E)$] **HELIOS** data in **SSM1H** for 177 group set.

identical). Even while nearly identical, **HELIOS** data as input **SSM1H** produces a k, as shown in Table 5, that is further away from the original **HELIOS** result. We believe the reason for this greater discrepancy comes from lack of normalization of the total scattering cross section as required by Eq(17) in the multigroup form

$$\Sigma_{sg'} \equiv \sum_{g'=1}^{G} \Sigma_{g'g} \qquad (34a)$$

Figure 8 shows the scattering defect

$$f_{g'} \equiv \frac{\Sigma_{sg'}}{\sum_{g'=1}^{G} \Sigma_{g'g}} \qquad (34b)$$

in the **HELIOS** data. In order to obtain the agreement observed in Figs 7a and b

Table 5*k*- Comparison SMM1/HELIOS data

Model	***k***	***Difference in (pcm)***
Simple(49)	1.2177	910
Simple(177)	1.2208	1009

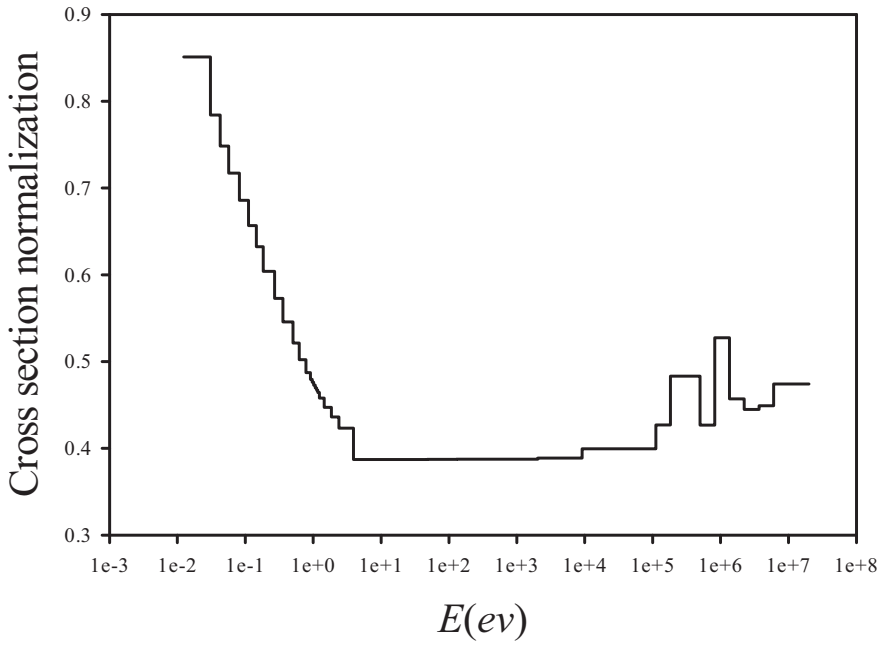

Fig. 8. **HELIOS** scattering cross section defect

.

the scattering cross section ***must*** be normalized by Eq(34a) to maintain conservation. Most likely **HELIOS-2** does this also, but this needs to be confirmed.

7. TENTATIVE CONCLUSIONS

A simple spectral model was developed from the first principles of slowing down and thermalization. The model features all group parameters determined analytically according to the multigroup approximation. Most importantly, the model was developed without regard to **HELIOS** input or results. In this sense, the simple slowing down model (**SSM1**) is entirely independent of **HELIOS** and therefore can legitimately be used as an independent check. Without any adjustment of the **SSM1** parameters, graphical comparisons indicate remarkable agreement. It must be emphasized that this is first a first principle verification based on different implementation and data input. When the **HELIOS** data is input into the **SSM1** model and with an adjustment of the thermal/fast cutoff, even better agreement is achieved.

8. REFERENCES

G. BELL AND S. GLASSTONE, Nuclear Reactor Theory, Van Norstrand Reinhold, London, 1970.

B. GANAPOL, NEUP Grant: CFP-09-807. (See NEUP website) 2009.

D.W. NIGG AND K.A. STEUHM, Advanced Test Reactor Core Modeling Update Project: Annual Report for Fiscal Year 2011, INL/EXT-11-23348.

C.A. WEMPLE, H-N.M. GHEORGHIU, R.J.J. STAMM'LER, E.A. VILLARINO, "Recent Advances in the **HELIOS** Lattice Physics Code", *Proc. PHYSOR 2008*, Interlaken, Switzerland, September 14-19, 2008.